TECHNICAL UNIVERSITY OF CATALONIA

BARCELONATECH

Modelling thermo-mechanical response of metal canister disposed in engineered barrier systems

Doctoral Thesis

Civil and Environmental Engineering Department

Universitat Politècnica de Catalunya

Author:

Peiman Khadivipanah

Supervisors:

Professor Sebastià Olivella

Professor Jean Vaunat

Barcelona, 2021

Abstract

The main objective of this thesis is to describe and implement a rate-dependent (viscoplastic) constitutive equations for copper based canister using a single internal state variable and use it for modelling disposal schemes subjected to shear conditions.

The model of Bodner and Partom (BP) is considered for this purpose (Bodner & Partom, 1975). To evaluate the copper's response to variations in strain rate throughout a temperature range, this model uses viscoplastic constitutive equations based on a single internal state variable that is a function of plastic work. The BP constitutive model has been implemented in CODE_BRIGHT computer code (DIT-UPC, 2021; Olivella et al., 1994; Olivella et al., 1996). The constitutive equation is verified against existing results and its validation is carried out by assessing the capability to reproduce experiments. For verification, the stress-strain response of a bar under uniaxial tensile conditions at a constant velocity was simulated with CODE_BRIGHT and the results compared with the solution obtained from Stealth Finite Difference Code and the semi-analytical solutions.

In addition, it is analyzed the reaction of a canister installed inside an engineered barrier which undergoes hydration and swelling until it reaches full saturation prior to shearing. The implemented elasto-viscoplastic model actually represents the behavior of the canister in yielding conditions. Although the canister is very stiff and strong compared to the clay components where it will be emplaced in a clay volume shear deformations occurring on the engineered barrier system (EBS) will have an impact on the canister (Börgesson, 1986). Finally, a repository of nuclear spent fuel is analyzed under extreme conditions as it is a long-life system and has to resist all types of environmental conditions, for instance earthquakes and glaciations.

After model implementation and verification in CODE BRIGHT this program has been used to model the canister-clay shear tests in 2D and 3D. In the Mock-up scale and Full-scale in 2D and 3D models, a comparison between the total stress method (mechanical analysis only) and the effective stress method (hydro-mechanical analysis) has been investigated. Experimental results from a canister-clay shear test (Börgesson, 1986) have been compared to the findings of the numerical model using CODE BRIGHT. Sensitivity analysis on viscosity for total stress calculations and permeability for effective stress calculations have been performed in the Mock-up scale and Full-scale. In the canister-clay shear test, a mesh

sensitivity analysis and also a comparison between the updated mesh (Lagrangian method) and the fixed mesh method have been carried out.

Finally, in two and three dimensions, the simulation of canister-clay shear tests based on impact of discontinuity (the discontinuity is in the rock and due to it, there is shearing in canister-rock system), as well as sensitivity analysis of parameters and mesh in mechanical and a coupled hydro-mechanical analysis, have been investigated.

Acknowledgments

This work would never have been done without the guidance of my supervisor, Prof. Sebastià Olivella. I am very grateful for the opportunity of developing a thesis with such a brilliant professor and for the availability, patience, and support shown towards his PhD candidates. I will be forever thankful for his teachings, his counsel, and for believing in me. I feel privileged to have had the opportunity to work with him over the last four and a half years.

I would like to express my gratitude to my co-supervisor, Prof. Jean Vaunat for all the support and for exploiting my potential, and for giving me a positive attitude and clear ideas to keep moving forward.

A sincere thanks to Dr. Xavier Pintado, for his valuable advice and kind support and guiding me at all times on what to do, reviewing my documents, and with his infinite patience sharing his deep expertise. Thanks to him for hosting me at the AINS Group company in Finland.

A deep thanks to my parents for giving me all the love, unconditional support, and freedom to take my path. This thesis would have not even commenced without them.

I gratefully acknowledge the financial support received from the CIMNE grant based on CODE_BRIGHT Project that allowed me to dedicate myself full-time to the research work presented in this thesis.

Finally, I want to thank all the friends I have met along the way or those I see daily, who in their way have helped me to finish this work.

Contents

List of Figures

List of Tables

CHAPTER

I

1 INTRODUCTION

Nuclear energy's emergence presents a desirable prospect for low-cost, high-efficiency energy sources. The proper disposal of radioactive waste (Sjöberg, 2004), on the other hand, remains a major challenge. Since spent nuclear fuel is very hazardous, it is one of the most difficult types of waste to handle. The health risks and safety concerns associated with radioactive waste are the primary barriers to widespread nuclear energy use (Deng et al., 2020). Nuclear waste must be treated or reprocessed with extreme caution due to its radioactivity and highly hazardous properties (Brunnengraeber & Schreurs, 2015).

The spent nuclear fuel components are to be buried deep underground in a repository. A multi-barrier disposal system, which consists of a system of engineered barriers (EBS) and hosts rock, essentially isolates radionuclides from the living atmosphere, and prevents the release of radionuclides (Fyfe et al., 1984; Fyfe, 1999).

The confinement or isolation of nuclear waste from the biosphere in repositories is the final step in the management of spent nuclear fuel. The repository may be a near-surface or deep geological structure, depending on the period of life and concentration of radionuclide found in the waste. The preferred option of nuclear waste management in many countries is deep geological disposal (Dvořáková et al., 2015; Sellin & Leupin, 2013), such as Argentina, Australia, Canada, Finland, France, Japan, the Netherlands, Russia, South Korea, Sweden, Switzerland, UK, and the USA (Hedin et al., 2008).

1.1 Background and motivation

Deep geological disposal (Thegerstroem & Laarouchi Engstroem, 2013) is an option for the confinement of the spent nuclear fuel in many countries. Finland and Sweden have their programs quite advanced and have decided to use the KBS-3 design (SKB, 2010a, 2010b), which involves the excavation of tunnels in crystalline rock. The fuel assemblies containing the fuel rods will be put into metal canisters (cast iron with a copper shell) (Raiko, 2012) and these canisters emplaced in vertical deposition holes. Between the canisters and host rock, there will be compacted bentonite blocks (rings around the canisters and discs above and below) and bentonite pellets filling the voids between the blocks and the host rock. This method is called the KBS-3V disposal method (Juvankoski & Marcos, 2010).

Simulation of spent nuclear fuel disposal in deep underground cavities excavated in geological structures (Figure 1-1) requires an accurate thermo-hydro-mechanical (THM)

representation of the different components. The host rock and the components of the clay engineered barrier have been extensively investigated in laboratory tests (Pintado et al., 2013), mock-up tests (Åkesson et al., 2010; Martín et al., 2014) and “in situ” tests (A. Gens et al., 2009; Johannesson et al., 2007). To be able to reproduce the clay components, different constitutive equations have been developed by different authors (Alonso et al., 1990; Gens & Alonso, 1992).

Engineered barriers undergo hydration from contact with the rock. Wetting of the initially unsaturated clay components leads to swelling. This latter is expected to close open spaces between blocks and at the contacts with rock, canister, and drift backfilling materials.

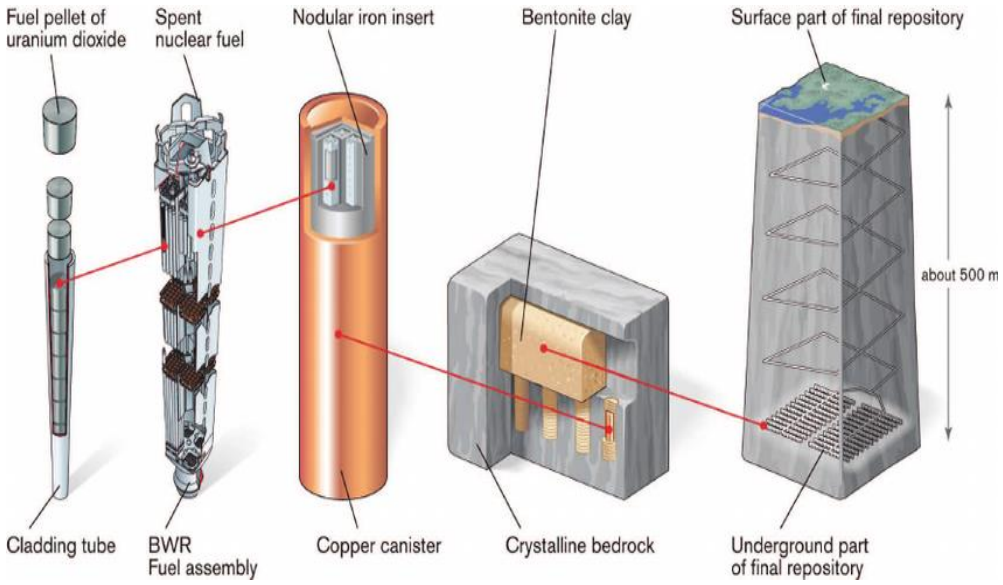

Figure 1-1 Copper canister and other elements for a radioactive waste disposal scenario (KBS-3V, Sweden)(Sellin & Leupin, 2013).

The canister will have two main components described before, the insert manufactured from cast iron and the shell, manufactured from copper. The insert will also contain steel parts like cassette tubes, the lid, and the screw for fixing the lid (see Figure 1-2). The study of the metal component's behavior has been carried out by the nuclear agencies which have planned to use the KBS-3 design. Models described in Raiko (2012) and Raiko et al. (2010) and Hernelind (2010) have been used for the canister design. Cast iron and steel were simulated with models based on the von Mises’ material model, with constant Young modulus and Poisson’s ratio in the elastic part and a dependency on shear rate for defining the hardening from the yield stress to ultimate (failure) stress. For long-term analysis, the copper constitutive model takes into account creep effects. The modeling in canister design has been performed assuming undrained conditions in buffer in some cases, so the Poisson

ratio is close to 0.5 (0.49 has been considered) and only the momentum balance equation is solved, without considering pore pressure (water balance equation is not solved). Von Mises model can be assimilated to the Drucker-Prager model (Drucker & Prager, 1952) if p (mean stress) is kept constant.

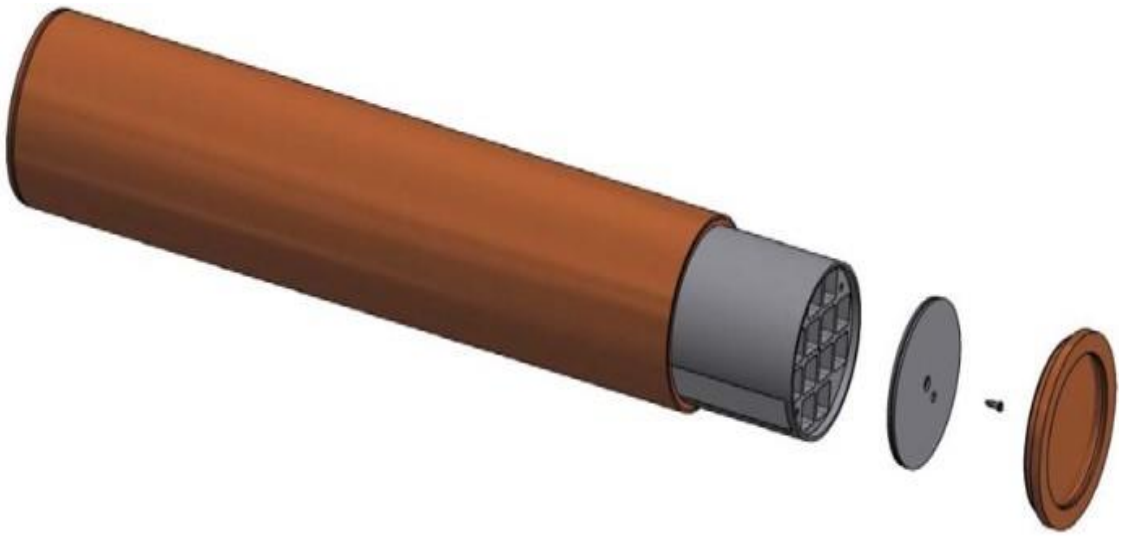

Figure 1-2 Canister components (Jonsson et al., 2018).

Since the other components of the multibarrier system are porous media (clay buffer in deposition holes, clay backfill in deposition tunnels and host rock), the usual modeling with coupled finite element models requires to assume that the canister is also a porous material (due to the CODE_BRIGHT is a computer code for porous materials). The assumption that the canister is treated as a porous material can be done provided that an extremely low porosity, permeability, and diffusivity is considered (so the code can also be used for dealing with "non-porous" materials like metals).

The thesis starts with a review of models for copper and other metals in general. Implementation of an elasto-viscoplastic nonlinear equation with hardening for copper is considered an interesting starting point. This should be followed by modeling scenarios of disposal under different geometrical configurations, boundary conditions, and time scales. Thermo mechanical modeling can be done if the clay is assumed in saturated conditions and mechanical response under undrained conditions. This is probably true if the loading is very fast and the permeability of the clay very low (bentonite). This may induce canister tilting and canister deformation. Representation of the canister with details of its internal components is important and perhaps with metallic materials that undergo different deformation rates but this is beyond of the scope of this thesis.

An adequate solution has to be found for the hydraulic equations (liquid and gas flow) that have to be solved for the engineered barrier and host rock. The obvious solution is to remove these equations for the canister. Still, there is another issue as the clay-based engineered barrier is in contact with the canister, sometimes with a gap in between the canister and the buffer.

1.2 Thesis objectives

It is known that the mechanical behavior, such as yield stresses, ductility, and strength, etc., of material changes under different strain-rate loadings and temperatures. The consideration of rate and temperature dependence of material behavior and an understanding of the deformation behavior of metals over a wide range of temperatures and strain rates in forming metal is very important in the design of structures.

According to Liang and Khan (1999), flow (or yield) stress can be a measure of the material's strength and resistance to plastic flow at any instant under any strain rate. The rate sensitivity, defined as the amount of change of flow (or yield) stress because of a change of strain rate, is the major resistance to instability. Therefore, the accurate determination and description of the rate dependence of mechanical behavior of materials, along with the temperature dependence and work hardening of those materials have attracted considerable attention from material and mechanical scientists for more than five decades (Liang & Khan, 1999).

An ideal plasticity model in general for metals should be able to describe the materials' properties such as strain-rate dependence, temperature dependence, strain, and strain-rate history dependence, work hardening, or strain-hardening behavior. Accurate modeling of deformation processes of materials over a wide range of strain rates and temperatures requires a reliable constitutive description of the stress-strain behavior.

Bodner-Partom (Bodner & Partom, 1975) model is formulated with a set of equations to represent elastic-viscoplastic strain-hardening material behavior for different strain and loading histories for copper. An important feature of the total deformation formulation rate is that it can be separated into elastic and plastic components, which are functions of state variables at all stages of loading and unloading. The authors introduced the unified theories of viscoplastic material behavior combining all aspects of plastic responses into a set of time-dependent equations with a single plastic strain rate variable. The model can be used for the simulation of the canister copper shell.

The state variable based viscoplastic theory developed by Bodner-Partom was chosen in the present work for three reasons (Bodner & Rajendran, 1995): (1) ability to predict the response of the material to a broad range of load histories, (2) adaptability to finite element analyses of structural components, and (3) ease with which the parameters in a constitutive model can be determined from high strain rate experiments.

The key aim of the present work is to build algorithms (computer subroutines) describing rate-dependent (viscoplastic) constitutive equations (Bodner & Partom, 1975; Bodner & Rajendran, 1995) based on a single internal state variable which is a function of plastic work. These algorithms are used to calculate the response of copper to changes of strain rate over a range of temperatures in CODE_BRIGHT. Once implemented, an investigation of the response of canister installed inside engineered barriers which undergo hydration and swelling until full saturation, has been carried out. Also, the effect of external events as earthquakes or glaciations can be studied at some moment of the transient or stationary thermo-hydro-mechanical phase.

CODE_BRIGHT (DIT-UPC, 2021; Olivella et al., 1994; Olivella et al., 1996); is a Finite Element Method (FEM) program capable of performing coupled thermo-hydro-mechanical (THM) analysis in geological media and has been selected for Bodner-Partom model implementation. It has been developed at the Department of Civil and Environmental Engineering of the Technical University of Catalonia and works combined with the pre/post-processor GiD, developed by the International Center for Numerical Methods in Engineering (CIMNE, www.cimne.com).

Although the models can simulate temperature evolution, without loss of generality, the simulations have been performed in isothermal conditions. This means that temperature is assumed constant and the energy balance equation has not been solved in all the different models.. However, different values of temperature have been considered depending on the simulation.

The canister should fulfill some requirements described in Jonsson (Jonsson et al., 2018) to preserve the safety of the KBS-3 repository. One of the requirements is to be able to preserve its integrity due to shear-type rock movements if a fracture intersects a deposition hole. These movements may occur due to an earthquake or due to a glacial load (Hernelind, 2010). A mock-up test was performed in Sweden during the 1980s (Börgesson, 1986) where a 30 mm shear displacement was imposed in a test set-up at 1:10 scale with different shear rates. The canister was reproduced with a copper cylinder which reached the yield

conditions after the test (Figure 1-3). To be able to simulate the stress state of the canister and the large strains expected during the shearing, it is necessary to represent the canister properly under thermo-mechanical conditions in the context of a coupled thermo-hydro-mechanical calculation using porous media tools. Elasto-viscoplastic theory can be used to represent the behavior of the canister in yielding conditions. Although the canister is very stiff and strong compared to the clay components where it will be emplaced in a clay volume, shear deformations occurring on the engineered barrier system (EBS) will have an impact on the canister as Börgesson (1986) showed. Bodner-Partom model (Bodner & Partom, 1975; Bodner & Rajendran, 1995) has been chosen for copper simulation in this work.

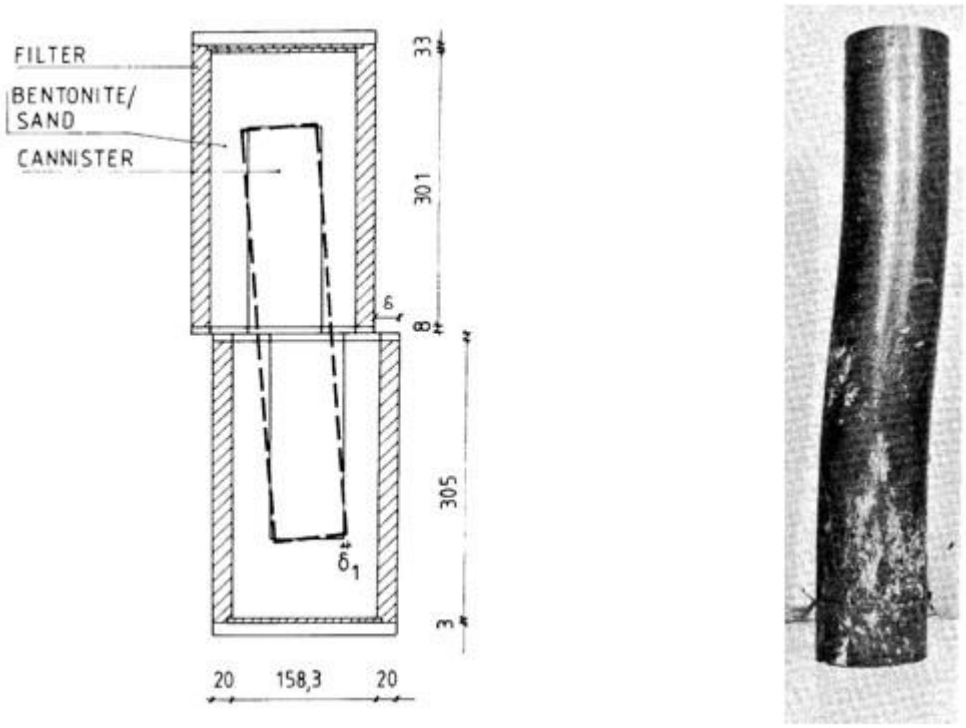

Figure 1-3 Mock-up test (Börgesson, 1986). Diagram (left, magnitudes in mm) copper cylinder after the shearing (right).

1.3 Methodology

The main objectives of this thesis are to analyze the viscoplastic behavior of copper and use this model for copper canister in nuclear waste disposal simulations and to analyze the canister-clay shear test under extreme conditions. The following items describe in detail the steps carried out in this investigation to achieve each of the specific objectives:

1. Bibliographic study and state of the art. This state of the art concentrates on the response of metal canisters to the thermo-hydro-mechanical processes that may occur in a repository.
2. Studying of Thermo-Hydro-Mechanical modeling in porous media. This is necessary as the canister is embedded in porous media under hydro-mechanical processes.
3. Learning CODE_BRIGHT. This is an important activity as the implementation of the constitutive model has to be done in this program that is used for the modeling of schemes of radioactive waste disposal.
4. Learning FORTRAN programing. CODE_BRIGHT is a program written in FORTRAN.
5. Studying of constitutive equations for copper. A series of constitutive equations are implemented in CODE_BRIGHT for rocks and soils. These equations normally include hydraulic coupling and reproduce stress-strain hardening, softening, contraction, dilatancy, etc. but are not adequate for metals as metals require work hardening and temperature dependence quite different from what is used for soils and rocks.
6. Programming of Bodner-Partom model in FORTRAN and Implementation in CODE_BRIGHT. This is a classical equation for copper which was developed to model substantially different conditions like the ones we expect in nuclear waste disposal. Validation and verification of the implemented Bodner-Partom model.
7. Undrained shear test modeling with a canister model in CODE_BRIGHT in 2D and 3D based on mock-up test in mechanical analysis and a coupled hydro-mechanical analysis. It is a shear test carried out to assess the consequences of a shear zone in a vertical deposition hole (KBS-3V nuclear spent fuel disposal concept), cylindrical samples (h = 622 mm, Ø = 158 mm) made of highly compacted MX-80 bentonite (is a granular bentonite product made out of dried bentonite clay and milled to millimeter-sized grains) (Karnland et al., 2006; Posiva, 2011; Villar, 2005) surrounding a cylindrical canister (h = 450 mm, Ø = 80 mm) made of copper were prepared (Börgesson, 1986). The shear test apparatus used had a cylindrical housing divided into two similar parts by a plane perpendicular to the cylinder axis. One of these parts was held fixed and

the other could be displaced perpendicularly to the cylinder axis. The samples were placed in the cylindrical housing of the shear apparatus. Afterward, the samples were completely saturated with water, thereby inducing a swelling pressure in the bentonite. Finally, the samples were sheared at different rates.

8. Comparison of the results of the shear test in the CODE_BRIGHT with the results obtained from the Mock-up tests (Börgesson, 1986).
9. Undrained Shear test modeling with a Canister model in CODE_BRIGHT in 2D and 3D based on Full-scale mechanical analysis and a coupled hydro-mechanical analysis.
10. Comparison of Canister-clay shear test between Mock-up test and Full-scale in 2D and 3D.
11. Sensitivity analysis of important parameters in Mock-up test and Full-scale.
12. Influence of discontinuity in canister-clay shear test with including the rock in 2D and 3D and sensitivity analysis of parameters in total stress and effective stress analysis.

1.4 Outline of thesis

Subsequently, the thesis is organized as follows:

Chapter 2 provides the theoretical basis and the equations used for a coupled thermo-hydro-mechanical analysis. General information about the soil mechanical behavior such as Barcelona Basic Model and Drucker-Prager model which is used for highly compacted MX-80 bentonite and rock and discontinuity. Explanation about equivalent parameters of discontinuity according to soil and rock properties is done.

The third chapter contains the theoretical basis and the mathematical formulation of the Bodner-Partom model considered to simulate the copper. For the validation, the numerical solutions of elasto-viscoplastic constitutive model of the copper have been compared with experimental results. For verification, the Bodner-Parton model is used to simulate the response of copper to changes of strain rate over a range of temperatures. CODE_BRIGHT with Bodner-Partom constitutive equations has been verified with Stealth Finite Difference Code and semi-analytical solutions.

Chapter 4 describes the canister-clay shear test in 2D and 3D based on the Mock-up test and full-scale and sensitivity analysis of important parameters of test and mesh and then validate the model with the canister-clay shear test. Chapter 5 explains the influence of discontinuity on canister-clay shear test with considering rock or without rock and sensitivity analysis of significant parameters and mesh. Finally, Chapter 6 presents a summary of the overall conclusions of this research project.

1.5 Research dissemination

Journal papers

Khadivipanah P., Pintado X., Olivella S., Vaunat J., (2019) Copper canister shearing in spent nuclear fuel repository using Bodner-Partom model. Published by Geomechanics for Energy and the Environment. https://doi.org/10.1016/j.gete.2019.100171

Khadivipanah P., Olivella S., Pintado X., Vaunat J., Two-dimensional model shear deformation of the canister-clay system. Nuclear material and energy journal (under review)

Khadivipanah P., Olivella S., Pintado X., Vaunat J., Analysis of shear mock-up tests in a canister-clay system for spent nuclear fuel isolation. Geomechanics for Energy and the Environment (under review)

Conferences

Khadivipanah P., Olivella S., Vaunat J., (2019). Modelling and analysis of copper canister shear test in engineered clay barrier for spent fuel isolation. VIII International Conference on Coupled Problems in Science and Engineering. Barcelona, Spain.

Khadivipanah P., Olivella S., Vaunat J., (2019). Viscoplastic constitutive equations for copper to model canister deformations and implementation in CODE_BRIGHT. XV International Conference on Computational Plasticity. Fundamentals and Applications. Barcelona, Spain.

Workshops proceedings

Khadivipanah P., Olivella S., Vaunat J., (2017). Bodner-Partom constitutive equations for the copper canister. 9th Workshop of CODE_BRIGHT USERS. Barcelona, Spain.

Khadivipanah P., Olivella S., Vaunat J., (2018). Viscoplastic constitutive equations for copper to model canister deformation. 10th Workshop of CODE_BRIGHT USERS. Barcelona, Spain.

Khadivipanah P., Pintado X., Olivella S., Vaunat J., (2019) Shear deformation analysis of canister-clay as an engineered barrier principle for spent fuel isolation. 11th Workshop of CODE_BRIGHT USERS. Barcelona, Spain.

ALERT Geomaterials workshop and doctoral school, Oct 2018, Aussois, France.

10th ALERT OLEKZIENKIEWICZ WINTER SCHOOL, Nov 2018, Bari, Italy.

Winter school on Geomechanics for energy and the environment, Jan 2019, EPFL (École polytechnique fédérale de Lausanne), Sur-Ollon, Switzerland.

Khadivipanah P., Olivella S., Vaunat J., (2019). Influence of discontinuity in the canister-clay shear test. The Short Mediterranean Ph. D School on Impacts of Climate Change and Sustainable Engineering Responses. Napoli, Italy. (I received an award from The Università degli Studi di Napoli Federico II (DICEA)).

EURAD Doctoral School (GAS & HTEC WPs), Jan 2020, Liege university, Liege, Belgium.

Advanced Virtual Course on Modeling Granular Processes for Energy and Environment. 25 February to 15 April, 2021, the Labex Numev at University of Montpellier, France.

Training

Training in A-Insinöörit Company (AINS group), (2019). Collaboration with a scientist from AINS Group Company for Canister-clay shear test. Three months stay in Helsinki, Finland (Finance support by UPC Erasmus).

CHAPTER 2

2 GENERAL CONCEPT AND GOVERNING EQUATIONS

This chapter provides an overview of the fundamental mathematical equations implemented in CODE_BRIGHT (Olivella et al., 1994; Olivella et al., 1996) required to describe a coupled thermo-hydro-mechanical analysis in nuclear waste disposal. The project and strategies have used a study of basic soil constitutive models such as the Barcelona Basic Model (BBM) (Alonso et al., 1990) and the Drucker-Prager Model (DP) (Drucker & Prager, 1952) to reflect discontinuity with soil properties.

2.1 THEORETICAL BASIS

The components and phases of soils are classified as three phases and three species, as follows:

Three phases:

- Solid-phase (s): mineral
- Liquid phase (l): water + air dissolved
- Gas-phase (g): a mixture of dry air and water vapor

Three species:

- Solid (-): The mineral is coincident with the solid phase
- Water (w): as a liquid or evaporated in the gas phase
- Air (a): dry air, as gas or dissolved in the liquid phase

In balance equations, the abbreviation would be used as follows:

ϕ = porosity

ρ = density

ω = mass fraction

j = total mass flux

$\mathbf{i_c}$ = conductive heat flux

$\omega\rho$: mass content per unit volume of phase

σ = stress tensor

i = non-advective mass flux

b = body forces

q = advective flux

u = displacements

$\mathbf{j_E}$ = energy fluxes due to mass motion

S_l, S_g: degree of saturation of liquid and gas phases i.e., a fraction of pore volume occupied by each phase.

Superscripts *w* and *a* reference to water and air, respectively.

Subscripts *s, l,* and *g* refer to solid, liquid, and gas phases, respectively.

2.2 Mass balance of solid

The following equilibrium equation will be used:

$$\frac{\partial}{\partial t}\begin{pmatrix}\text{mass or energy per unit}\\ \text{the volume of porous media}\end{pmatrix}+\nabla\cdot\begin{pmatrix}\text{fluxes of mass}\\ \text{or energy}\end{pmatrix}=\begin{pmatrix}\text{sources of a sink of}\\ \text{mass and energy}\end{pmatrix}$$

The solid mass per unit volume can be introduced as:

$$\frac{m_s}{v}=\frac{m_s}{v_s}\frac{v_s}{v}=\rho_s(1-\phi) \tag{2.2-1}$$

m_s is solid mass and v, v_s are mixture volume element and solid phase volume, respectively.

This is applied in the balanced equation and the mass balance of solid present in the medium is written as:

$$\frac{\partial}{\partial t}\left(\rho_s(1-\phi)\right)+\nabla\cdot\left(\rho_s(1-\phi)\frac{d\boldsymbol{u}}{dt}\right)=0 \tag{2.2-2}$$

$$\updownarrow$$

$$\frac{\partial}{\partial t}\left(\rho_s(1-\phi)\right)+\nabla\cdot(\mathbf{j}_s)=0$$

Where ρ_s is the mass of solid per unit volume of solid and $\mathbf{j}_s$ is the flux of solid.

The variation in porosity caused by volumetric deformation and solid density variation is expressed by the following equation:

$$\frac{D\phi}{dt}=\rho_s(1-\phi)\frac{D\rho_s}{dt}+(1-\phi)\nabla\cdot\left(\frac{d\mathbf{u}}{dt}\right)=0 \tag{2.2-3}$$

Volumetric strain equals: $\nabla\cdot\frac{d\boldsymbol{u}}{dt}=\frac{d\varepsilon_x}{dt}+\frac{d\varepsilon_y}{dt}+\frac{d\varepsilon_z}{dt}$

In continuous, the material derivative concerning the solid has been used and its definition is:

$$\frac{D_s(\blacksquare)}{Dt}=\frac{\partial}{\partial t}+\frac{d\mathbf{u}}{dt}\cdot\nabla(\blacksquare)$$

2.3 Mass balance of water

Water is present in liquid gas phases. The mass balance of water in the liquid and the gas phase is expressed as:

$$\frac{\partial}{\partial t}\left(\omega_g^w\rho_g S_g\phi\right)+\nabla\cdot\left(\mathbf{j}_g^w\right)=f^{evaporation}+f^w \tag{2.3-1}$$

$$\frac{\partial}{\partial t}\left(\omega_l^w\rho_l S_l\phi\right)+\nabla\cdot\left(\mathbf{j}_l^w\right)=f^{condensation}+f^w \tag{2.3-2}$$

Where f^w is an external supply of water and the internal source terms that represent phase change are:$f^{condensation} + f^{evaporation} = 0$

When you combine the two mass balance equations, you get:

$$\frac{\partial}{\partial t}\left(\omega_l^w \rho_l S_l \phi + \omega_g^w \rho_g S_g \phi\right) + \nabla \cdot \left(j_l^w + j_g^w\right) = f^w \tag{2.3-3}$$

Since the total mass balance within the medium is taken into account in this equation, there is no internal production term.

The fixed framework and solid skeleton are used to describe flux equations, which are presented in (Figure 2-1):

A fixed framework is referred to as the flux:

$$\mathbf{j}_g^w = \mathbf{i}_g^w + \omega_g^w \rho_g \mathbf{q}_g + \phi S_g \omega_g^w \rho_g \, d\mathbf{u}/dt = \mathbf{j}_{\boldsymbol{g}}^{\boldsymbol{w}} + \phi S_g \omega_g^w \rho_g \, d\mathbf{u}/dt \tag{2.3-4}$$

The solid skeleton is also referred to as flux.:

$$\mathbf{j}_{\boldsymbol{g}}^{\boldsymbol{w}} = \mathbf{i}_g^w + \omega_g^w \rho_g \mathbf{q}_g \tag{2.3-5}$$

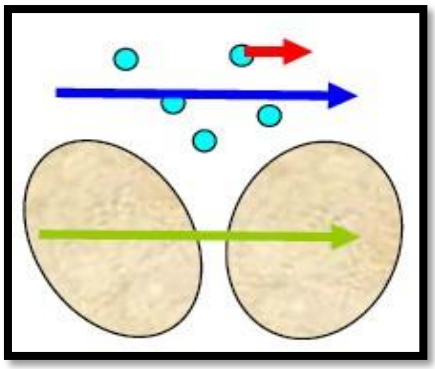

Figure 2-1 Flux relates to the mass balance of water.

The use of the material derivative results in:

$$\phi \frac{D_s(\omega_l^w \rho_l S_l + \omega_g^w \rho_g S_g)}{Dt} + \left(\omega_l^w \rho_l S_l + \omega_g^w \rho_g S_g\right) \frac{D_s \phi}{Dt} + \left(\left(\omega_l^w \rho_l S_l + \omega_g^w \rho_g S_g\right)\phi\right) \nabla \cdot \frac{d\mathbf{u}}{dt} + \nabla \cdot \left(\mathbf{j}_{\boldsymbol{l}}^{\boldsymbol{w}} + \mathbf{j}_{\boldsymbol{g}}^{\boldsymbol{w}}\right) = f^w \tag{2.3-6}$$

The main objective is to calculate the unknowns from the governing equations. As a result, the dependent variables must be tied to the unknowns in some way. The degree of saturation, for example, would be calculated using a retention curve that can express it in terms of temperature, liquid pressure, and gas pressure.

Porosity is described in Equation (2.3-6) as:

- A coefficient in storage terms.
- In a term involving its variance caused by various processes.
- Concealed in variables that are affected by porosity (e.g. intrinsic permeability).

2.3.1 Retention curve

This law is concerned with capillary pressure and the degree of saturation. One of the commonly used models in the van Genuchten model (Van Genuchten, 1980), which can be written as:

$$S_e = \frac{S_l - S_{min}}{S_{max} - S_{min}} = \left(1 + \left(\frac{P_g - P_l}{P}\right)^{1/(1-\lambda)}\right)^{-\lambda} \quad (2.3\text{-}7)$$

This equation contains the parameters *λ* and *P.* The first *(λ)* essentially controls the curve's shape while the second *(P)* controls its height, so the latter can be viewed as a measure of the capillary pressure used to initiate soil desaturation. Since surface tension can scale capillary pressure (Milly, 1982; Olivella & Gens, 2000), it seems that *P* can as well.

This can be shown using Laplace's law:

$$P_g - P_l = \frac{2\sigma}{r} \quad (2.3\text{-}8)$$

Where σ is surface tension and *r* is the curvature radius of the meniscus.

The retention curve can also be written as:

$$P_g - P_l = P\left(S_e^{-1/\lambda} - 1\right)^{(1-\lambda)} \quad (2.3\text{-}9)$$

Then, assuming the constant water content means all S_e and *r* constants, the following follows:

$$P = P_o \frac{\sigma(T)}{\sigma(T_o)} \quad (2.3\text{-}10)$$

at temperature T_o, Where P_o is the corresponding parameter. Since surface tension decreases with temperature, P will decrease as well. As a result, for a given degree of saturation, capillary pressure decreases with temperature (Olivella & Gens, 2000).

The following formula is used to measure surface tension (Pruess, 1987):

$$\sigma(T) = (1 - 0.625a)(0.235a^{1.256}) \qquad a = \frac{374.15 - T}{647.3} \qquad T < 360^{\circ}C$$

$$\sigma(T) = 0.0019106\exp(0.05(360 - T) \qquad T > 360^{\circ}C$$

2.3.2 Darcy's law

Advective fluxes of liquid and gas are generally determined by Darcy's law:

$$\mathrm{q}_{\alpha} = -\frac{\mathbf{k}k_{r\alpha}}{\mu_{\alpha}}(\nabla P_{\alpha} - \rho_{\alpha}\mathbf{g}) \tag{2.3-11}$$

Where α = l, g whether liquid or gas phase laws are being used. It is necessary to quantify intrinsic permeability (**k**), relative permeability ($k_{r\alpha}$), and viscosity (μ_{α}). These variables exhibit a variety of dependencies, which are discussed further below.

2.3.3 Intrinsic permeability

This parameter depends primarily on the porous medium structure. Typically, a simple function of the medium form and porosity (Kozeny's model) is used:

$$\mathbf{k} = \mathbf{k}_o \frac{\phi^3}{(1-\phi)^{\mathbf{2}}} \frac{(1-\phi_o)^2}{{\phi_o}^3} \tag{2.3-12}$$

Where φ_o represents a reference porosity and $\mathbf{k_o}$ represents the intrinsic permeability at the reference porosity. Since the soil undergoes changes in porosity, implying a change in permeability, this dependence is particularly important for modeling the hydraulic behavior of the clay barrier.

2.3.4 Relative permeability

A relative permeability function can be calculated using the van Genuchten model (Van Genuchten, 1980):

$$k_{rl} = \sqrt{S_e}\left(1 - \left(1 - S_e^{1/\lambda}\right)^{\lambda}\right)^2 \tag{2.3-13}$$

Which is written in terms of the same effective saturation that was defined for the retention curve and employs the same parameters λ that are responsible for the retention curve's form. This rule has the benefit of avoiding the determination of relative permeability experimentally, which is very difficult.

A generalized power function of the degree of saturation is another function for measuring liquid relative permeability:

$$k_{rl} = AS_e^{\lambda} \tag{2.3-14}$$

This power function is independent of the retention curve assumed and has been shown to be sufficient for modeling clay soils when experimental data is available (FEBEX, 1999). When desaturation occurs, the van Genuchten model correlated with relative permeability usually indicates an unexpected drop. For bentonite clays, power law provides for a less pronounced slope, which is more realistic.

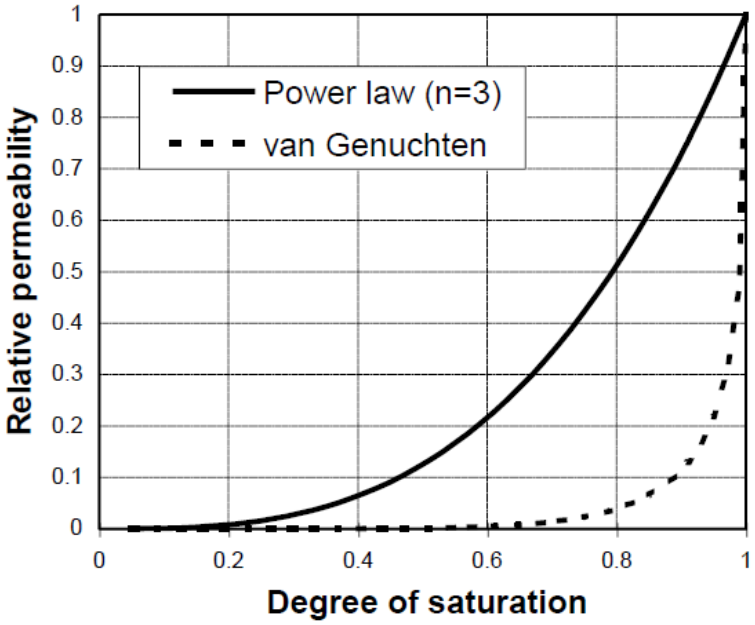

Figure 2-2 In the relative permeability-degree of saturation curve, the Power law, and van Genuchten are compared (Olivella & Gens, 2000).

Relative permeability is a function of the degree of saturation. With n = 3, the power law was determined, and the van Genuchten model was calculated with λ = 0.36 (Figure 2-2).

In the gas phase, relative permeability is normally determined by:

$$k_{rg} = 1 - k_{rl} \qquad \text{or} \qquad k_{rg} = AS_{eg}^{\lambda}$$

2.3.5 Liquid viscosity

Darcy's law requires the viscosity of water. Temperature fluctuations cause changes in viscosity, which can be measured as follows:

$$\mu_l = Aexp(\frac{B}{273.15 + T}) \tag{2.3-15}$$

Where A = 2.1×10^{-2} MPa and B = 1808.5 K^{-1}.

2.3.6 Gas viscosity

Gas viscosity can be estimated as a first approximation as (k: intrinsic permeability):

$$\mu_g = \frac{A\sqrt{273 + T}}{\left(1 + \frac{B}{273 + T}\right)} \frac{1}{1 + \frac{b_k}{P_g}} \qquad b_k = C - Dk \geq 0 \tag{2.3-16}$$

Where A = 1.48×10^{-2} MPa s. and B= 119.5 K^{-1}, C =0.14 and D= 1.2 ×10^{15}. A reduction coefficient considers the probability of Knudsen diffusion (Klinkenberg effect). As the mean free path of the gas particles becomes comparable to the pore size (low permeability material) slip effects (nonlaminar flow) may result in an apparent lower viscosity (apparent higher gas conductivity).

$$\begin{aligned} \mathrm{q}_\alpha &= -\frac{\mathbf{k}k_{r\alpha}}{\mu_{\mathrm{g}}^o}\left(1 + \frac{b_k}{P_g}\right)(\nabla P_\alpha - \rho_\alpha \mathrm{g}) \\ &= -\frac{\mathbf{k}k_{r\alpha}}{\mu_{\mathrm{g}}^o}(\nabla P_\alpha - \rho_\alpha \mathrm{g}) - \left(\frac{\mathbf{k}k_{r\alpha}}{\mu_{\mathrm{g}}^o}\frac{b_k}{P_{\mathrm{g}}}\right)(\nabla P_\alpha - \rho_\alpha \mathrm{g}) \end{aligned} \tag{2.3-17}$$

2.4 Momentum balance for the medium

When the inertial terms are disregarded (where the mechanical equilibrium conditions have been used), the momentum balance decreases to the equilibrium of stress:

$$\nabla \cdot \boldsymbol{\sigma} + \mathbf{b} = 0 \tag{2.4-1}$$

Where **σ** is the stress tensor and **b** is the vector of body forces.

2.5 Discontinuities

In general, the flow can be calculated using lower dimension elements in a program that only solves water, heat flow, and transport (i.e. triangles combined with tetrahedral elements for 3D problems).

CODE BRIGHT (DIT-UPC, 2021; Olivella et al., 1994; Olivella et al., 1996) has specific implementations for segments in 2D and triangles in 3D to account for flow in fractures. This can also be used in a hydro-mechanical coupled problems if the mechanical deformations of the discontinuity are minor and the transmissivity remains constant (for instance, rock fractures with constant transmissivity).

When a discontinuity with its mechanical properties must be represented, and the geometric representation is finite, properties must be determined with regard to the thickness of the finite zone representing the discontinuity.

2.5.1 Estimating strength based on geomaterial properties

In comparison to a rock, the strength of a discontinuity varies (Figure 2-3). Direct measures of discontinuity cohesion and friction angle (Mohr-Coulomb constitutive model) may be used specifically for interface elements simulated with a finite thickness or nil thickness. If these interface properties are unknown, a reduction factor R may be used to reduce them. In fact, the Mohr-Coulomb parameters for discontinuities in geotechnical models can be calculated as follows:

$$c' = c'_{\text{rock}} R \qquad (2.5\text{-}1)$$

$$\phi' = \text{atan}\,(R \tan \phi'_{\text{rock}}) \qquad (2.5\text{-}2)$$

Where R ≤ 1 is a reduction coefficient that represents the different strengths of discontinuities.

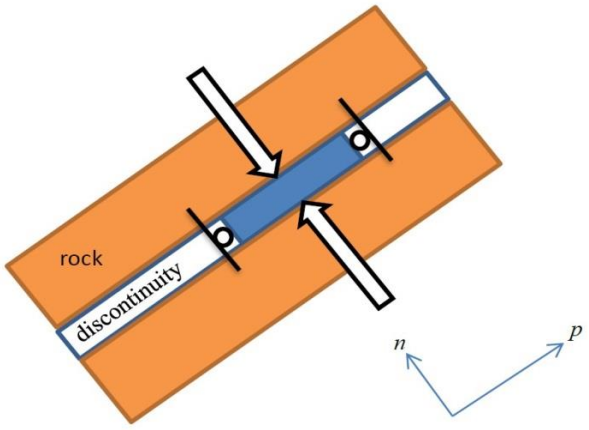

Figure 2-3 Schematic of discontinuity in rock with axial deformation.

2.5.2 Equivalence of stress-strain parameters in a discontinuity when using a finite thickness representation

Equivalent parameters are needed where a zone of thickness t is used to describe a discontinuity (Figure 2-4). When using a finite thickness representation, the aim is to suggest parameters for discontinuities. Equivalent parameters can be calculated using discontinuity parameters (k_n, k_s) and a finite thickness (t). The assumption would be that:

$$\Delta\sigma_n = k_n \Delta u_n \tag{2.5-3}$$

$$\Delta\tau = k_s \Delta u_s \tag{2.5-4}$$

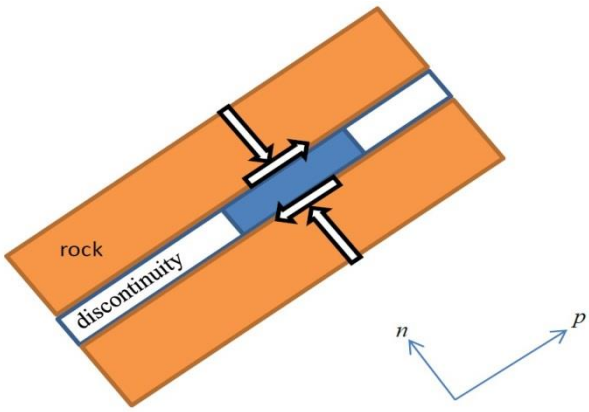

Figure 2-4 Schematic of discontinuity in rock with equivalent parameters

The following relation can be written on a discontinuity with an arbitrary thickness of t in the case of shear deformation:

$$G = k_s t \tag{2.5-5}$$

This is conveniently shown when substituting (2.5-5) in equation (2.5-4) results in:

$$\Delta\tau = k_s \Delta u_s = \frac{G\Delta u_s}{t} = G\Delta\varepsilon_s \tag{2.5-6}$$

This means that *G* can be measured for a zone of a given thickness that represents the discontinuity. It can, however, be adjusted if the thickness of the equivalent continuum zone is changed. As a result, it is determined by the thickness.

The normal deformation modulus can be determined in the case of normal deformation as:

$$E_n = k_n t \tag{2.5-7}$$

This is easily shown because substituting (2.5-7) in equation (2.5-3) results in:

$$\Delta\sigma_n = k_n \Delta u_n = \frac{E_n \Delta u_n}{t} = E_n \Delta\varepsilon_n \tag{2.5-8}$$

The following equation (Equation 2.5-9) can be used to link the normal deformation modulus E_n to Young's modulus:

$$E = \frac{(1+\nu)(1-2\nu)}{(1-\nu)} E_n \tag{2.5-9}$$

By imposing the deformation in the transversal two directions be zero, this finding can be deduced from elastic equations. Since it is obtained in the same manner, the parameter E_n is also known as the oedometric modulus (PLAXIS (2019) uses this term).

The Poisson ratio can be calculated as follows:

$$\nu = \frac{E_n - 2G}{2E_n - 2G} \tag{2.5-10}$$

Eventually, if the elastic properties of a discontinuity (k_n, k_s) are defined, the elastic parameters for a zone of the equivalent thickness (t) can be calculated:

$$G = k_s t \tag{2.5-11}$$

$$\nu = \frac{E_n - 2G}{2E_n - 2G} = \frac{k_n - 2k_s}{2k_n - 2k_s} \tag{2.5-12}$$

$$\mathrm{K} = \frac{(1+\nu)}{3(1-\nu)} k_n t \tag{2.5-13}$$

$$E = \frac{(1+\nu)(1-2\nu)}{(1-\nu)} E_n = \frac{(1+\nu)(1-2\nu)}{(1-\nu)} k_n t \tag{2.5-14}$$

For the equivalent discontinuity, any of the pairs $(E, \nu), (\mathrm{K}, G)$ or (K, ν) can be used. Except for the Poisson ratio, all parameters are dependent on the thickness selected.

Notice that for the case of very high normal stiffness $(k_n \gg k_s)$ equation (2.5-12) implies $\nu \to 0.5$ (which means that ν ≠ 0.5 because when the calculations are performed, the program fails due to infinite values of the bulk modulus) i.e. incompressible material, in this case, the elastic modulus can be determined using $E = 2G(1+\nu)$.

2.6 Equivalent parameters for discontinuities

Conditions	The equation for elastic parameters	Other
Normal and shear stiffness of the rock are known	$\nu_d = \frac{k_n - 2k_n}{2k_n - 2k_s}$ $E_d = \frac{(1+\nu_d)(1-2\nu_d)}{(1-\nu_d)} k_n t$	Normal and shear stiffness of the rock is defined as: $\Delta\sigma_n = k_n \Delta u_n$ $\Delta\tau = k_s \Delta u_s$ *t* is the element thickness
Shear stiffness of the rock (G) is known and fracture does not deform in volume	$G_d = R^2 G$ $\nu_d = 0.45$ $E_d = 2(1+\nu_d)G_d$	*R* is a parameter for the reduction of strength. Bulk modulus can be calculated as well: $K_d = \frac{2G_d(1+\nu_d)}{3(1-2\nu_d)}$
Discontinuity assumed like clay without swelling (kappa and shear modulus given)	$\mathrm{K_d} = \mathrm{K} = \frac{p'(1+e)}{\kappa}$ $G_d = R^2 G$ Where κ is the elastic compression index in the Cam-Clay model	Young and Poisson moduli can be calculated as: $\nu_d = \frac{3\mathrm{K_d} - 2G_d}{2(3\mathrm{K_d} + G_d)}$ $E_d = \frac{9\mathrm{K_d} G_d}{3\mathrm{K_d} + G_d}$
Discontinuity assumed like clay without swelling (kappa and Poisson's ratio given)	$\mathrm{K_d} = \mathrm{K} = \frac{p'(1+e)}{\kappa}$ $\nu_d = \frac{1+\nu - R^2(1-2\nu)}{2\left(1+\nu+R^2(1-2\nu)\right)}$	Young and shear modulus can be calculated as well: $E_d = 3\mathrm{K_d}(1-2\nu_d)$ $G_d = \frac{E_d}{2(1+\nu_d)}$

Conditions	The equation for plastic parameters	Other
Cohesion and friction angle are known	$c'_d = Rc'_{soil}$ $\phi'_d = atan(Rtan\phi'_{soil})$	*R* is a reduction factor for strength properties
The slope of the critical state line and tensile strength term are known	$M_d = RM$ $p_{s_d} = R(p_{s0} + ks)$	

In general, if the transmissivity is known, the corresponding intrinsic permeability can be calculated using the equation $k = \frac{T}{t}$. Where k is the hydraulic conductivity, T is the transmissivity, and t is the fracture thickness.

2.7 Barcelona Basic Model for soil

The Barcelona Basic Model (BBM) (Alonso et al., 1990) is often used to simulate the thermo-hydro-mechanical (THM) behavior of engineered barrier components including buffer and backfill blocks (Åkesson et al., 2010; Chen et al., 2009; Gens et al., 2009; Toprak et al., 2013). The thermo-elastoplastic (TEP) model is used in CODE BRIGHT to execute this model. This section discusses the model's formulation.

Effective stress is characterized as $\sigma' = \sigma - \max(p_g, p_l)$ (for positive compressions), which is a modification of the normal effective stress considered for saturated soils. The effective mean stress p' can be calculated as $p' = p - \max(p_g, p_l)$. The mechanical constitutive equation is as follows:

$$d\boldsymbol{\sigma}' = \mathbf{D}d\boldsymbol{\varepsilon} + \mathbf{h}ds \tag{2.7-1}$$

is generated from $\mathrm{d}\boldsymbol{\varepsilon} = \mathrm{d}\boldsymbol{\varepsilon}^{\mathrm{e}} + \mathrm{d}\boldsymbol{\varepsilon}^{\mathrm{p}} = (\mathbf{D}^{\mathrm{e}})^{-1}\mathrm{d}\boldsymbol{\sigma}' + \alpha\mathbf{I}\mathrm{d}s + \Lambda\frac{\partial \mathrm{G}}{\partial \boldsymbol{\sigma}'}$ and the volumetric strain is defined as $\varepsilon_v = \varepsilon_x + \varepsilon_y + \varepsilon_z$.

Volumetric strains that are elastic, isotropic, or non-isothermal are described as follows:

$$d\varepsilon_v^e = \frac{\kappa_i(s)}{1+e}\frac{dp'}{p'} + \frac{\kappa_s(p',s)}{1+e}\frac{ds}{s+0.1} + (\alpha_0 + 2\alpha_2\Delta T)dT \tag{2.7-2}$$

With the following parameter dependency on suction and stress:

$$\kappa_i(s) = \kappa_{i0}(1 + \alpha_i s + \alpha_{il} ln\left(\frac{s+0.1}{0.1}\right)) \tag{2.7-3}$$

$$\kappa_s(p',s) = \kappa_{s0}\left(1 + \alpha_{sp}\ln\frac{p'}{p_{ref}}\right)exp(\alpha_{ss}s) \tag{2.7-4}$$

Where e is the void ratio, p' is the mean effective stress, s is the suction, k_{io} and α_i are parameters for elastic volumetric compressibility against mean stress change, and k_{so}, α_{sp}, p_{ref} and α_{ss} are parameters for elastic volumetric compressibility against suction change. The parameters α_i, α_{il}, α_{sp} and α_{ss} do not belong to the original BBM model and were later introduced for swelling clays using the model BBM. The model is quite sensitive to these parameters.

The elastic properties are defined using two constants: κ and ν, respectively, elastic compressibility and Poisson ratio although the original BBM model considers constant shear modulus. The effective bulk modulus *K* depends on the mean effective stress *p'*, and the shear modulus is calculated as:

$$\mathrm{K} = \frac{1+\mathrm{e}}{\kappa} p', \qquad G = \frac{3\mathrm{K}(1-2\nu)}{2(1+\nu)} \tag{2.7-5}$$

The yield surface $F = F(\sigma', \varepsilon_v^p, s) = F(p', J, \theta, \varepsilon_v^p, s)$, where ε_v^p is the plastic volumetric strain, which depends on stresses and suction and can be illustrated using stress invariants:

Mean effective stress: $p' = \frac{1}{3}(\sigma_x' + \sigma_y' + \sigma_z') = p - \max(P_g, P_l)$

Deviatoric stress: $J = \sqrt{\frac{1}{2}(\mathbf{s}:\mathbf{s})}$ $\mathbf{s} = \boldsymbol{\sigma}' - p'\mathbf{I}$

Lode's Angle: $\theta = -\frac{1}{3}\sin^{-1}\left(1.5\sqrt{3}\det\mathbf{s}/J^3\right)$

For the sake of convenience, a modified Cam-Clay model is used as the reference isothermal saturated constitutive law, and the yield surface is as follows:

$$F = q^2 - M^2(p' + p_s)(p_0 - p') \tag{2.7-6}$$

With *M* as a critical state line parameter and p_0 as a suction-dependent parameter:

$$p_0 = p^c \left(\frac{p_0^*(T)}{p^c}\right)^{\frac{\lambda(0)-\kappa_{io}}{\lambda(s)-\kappa_{io}}} \tag{2.7-7}$$

$$p_0^*(T) = p_0^* + 2(\alpha_1 \Delta T + \alpha_3 \Delta T|\Delta T|)$$

$$\lambda(s) = \lambda(0)[(1-r)\exp(-\beta s) + r] \tag{2.7-8}$$

$$p_s = p_{s0} + ks\exp(-\rho\Delta T) \tag{2.7-9}$$

Where p^c is the reference stress; p_0^* is the initial preconsolidation stress for saturated conditions; $\lambda(0)$ is the slope of void ratio in saturated conditions; *r* defines the maximum soil stiffness; β controls the rate of increase of soil stiffness with suction; α_1 and α_3 are parameters for elastic thermal strain, p_{s0} is the tensile strength in saturated conditions; *k* takes into account the increase of tensile strength due to suction, and ρ provides for the decrease in tensile strength caused by temperature.

According to the following, hardening is influenced by plastic volumetric strain:

$$dp_0^* = \frac{1+e}{\lambda(0)-\kappa_{i0}} p_0^* d\varepsilon_v^p \tag{2.7-10}$$

The plastic potential G is calculated as follows:

$$G = q^2 - \alpha M^2 (p' + p_s)(p_0 - p') \tag{2.7-11}$$

Where α is a non-associativity parameter.

2.8 Drucker-Prager Model for soil

The Drucker-Prager (DP) model, also known as the extended Von Mises model, is a classical constitutive model that has been widely used in geotechnical engineering to simulate yield strength.

Drucker-Prager (DP) shear strength criteria based on Mohr-Coulomb (MC) is widely used in soil and rock mechanics in CODE BRIGHT, and the viscoplasticity Drucker-Prager model is used in the current work, and viscosity may be good for further research assuming improvements in parameters due to the strain rate.

An attempt has been made to achieve the stress-strain response under the undrained loading path. It is widely used because of the simplicity and easily determinable model parameters and in principal stresses, the $\sigma_1 \geq \sigma_2 \geq \sigma_3$ are assumed for material (with a positive sign for compressive stresses).

A linear combination of two other stresses can be used to express intermediate principal stress:

$$\sigma_2 = (1-b)\sigma_1 + b\sigma_3 \tag{2.8-1}$$

Where:

$$b = \frac{\sigma_1 - \sigma_2}{\sigma_1 - \sigma_3} \in (0,1) \tag{2.8-2}$$

And it is called the principal stress ratio. The lower bound of *b* (*b*=0) stands for the $\sigma_1 = \sigma_2$ case (triaxial extension, TXE), while the upper bound of *b* (*b*=1) stands for $\sigma_2 = \sigma_3$ case (triaxial compression, TXC). In particular, when *b*=0.5 (Lode angle $\theta = 0$), Drucker-Prager strength criteria are equivalent to Mohr-Coulomb strength criteria, without depending on the friction angle of the material.

As stress paths are plotted using the Mohr-Coulomb strength criterion, the mean normal stress (s) and maximum shear stress (*t*) are described in the following equations:

$$s = \frac{\sigma_1 + \sigma_3}{2} \tag{2.8-3}$$

$$t = \frac{\sigma_1 - \sigma_3}{2} \tag{2.8-4}$$

They are classified as stress invariants and using the parameters *s* and t are often simple when the parameter of intermediate principal stress (σ_2), for example, is not investigated.

The octahedral normal effective stress σ'_{oct} and the octahedral shear stress τ'_{oct} are invariants of stress state and they are introduced by

$$\sigma'_{oct} = \frac{1}{3}\left(\sigma'_x + \sigma'_y + \sigma'_z\right) \tag{2.8-5}$$

$$\tau'^{2}_{oct} = (1/9)\left[\left(\sigma'_x - \sigma'_y\right)^2 + \left(\sigma'_y - \sigma'_z\right)^2 + (\sigma'_z - \sigma'_x)^2 + 6\left(\tau^2_{xy} + \tau^2_{yz} + \tau^2_{zx}\right)\right] \tag{2.8-6}$$

Or, in terms of principal stress,

$$\sigma'_{oct} = {}^1\!/_3\,(\sigma'_1 + \sigma'_2 + \sigma'_3) \tag{2.8-7}$$

$$\tau'_{oct} = {}^1\!/_3\,[(\sigma'_1 - \sigma'_3)^2 + (\sigma'_2 - \sigma'_3)^2 + (\sigma'_3 - \sigma'_1)]^{1/2} \tag{2.8-8}$$

The state of effective stress at M' set out by a distance O'N' along the diagonal O'R with a distance N'M' normal to O'R; the vector O'N' is equal to $\sqrt{3}\sigma'_{oct}$ and the vector N'M' is equal to $\sqrt{3}\tau'_{oct}$.

For the particular case of $\sigma'_2 = \sigma'_3$, we have:

$$\sigma'_{oct} = {}^1\!/_3\,(\sigma'_1 + 2\sigma'_3) \tag{2.8-9}$$

$$\tau'_{oct} = \left(\sqrt{2}/3\right)[(\sigma'_1 - \sigma'_3)] \tag{2.8-10}$$

In order to avoid the repetition of the $\sqrt{2}/3$ value, the new invariants *q'* and *p'* are introduced in the following:

$$p' = {}^1\!/_3\,(\sigma'_1 + 2\sigma'_3) = \sigma'_{oct} \tag{2.8-11}$$

$$q' = (\sigma'_1 - \sigma'_3) = \left(3/\sqrt{2}\right)\tau'_{oct} \tag{2.8-12}$$

The Drucker-Prager parameters determined based on Mohr-Coulomb parameters into *p-q* space are described in the following relation based on stress state invariants and parameters from the direct shear test (a classical soil mechanic test):

$$F(0) = q - \eta p - C \tag{2.8-13}$$

$$\eta = \frac{6\sin\phi}{3 - \sin\phi} \tag{2.8-14}$$

$$C = \frac{6c\cos\phi}{3 - \sin\phi} \tag{2.8-15}$$

CHAPTER 3

3 Bodner-Partom Model

The Bodner-Partom model has been used for modeling the elastic-viscoplastic hardening of some materials and it was proposed by Bodner and Partom (Bodner & Partom, 1975). This model is applied in many engineering applications, which are briefly described in this section.

A unified constitutive model of Bodner and Partom has been applied for finite-element structural analysis of turbine engine hot section parts by Chan (Chan et al., 1988). The unified theory developed avoids simplifying the assumption of classical theory and should simulate more accurately the behavior of superalloy materials under cyclic loading conditions and high-temperature environments. This class of constitutive theory is defined by the use of kinetic equations and internal variables with appropriate evolution equations for stress relaxation. Model development is directed toward isotropic, cast nickel-base alloys used for air-cooled turbine blades and vanes. Also, the unified model has been adjusted to the MARC finite element structural code (https://www.mscsoftware.com/) and utilized for stress analysis of notched bar and turbine blade geometries.

The Bodner-Partom model was used for the simulation of HY100 steel in a wide range of high strain-rate experiments, encompassing some stress states and strain rates presented by Rajendran (Rajendran & Bless, 1986). Data were obtained for compressive and tensile one-dimensional stress loading with a split Hopkinson bar, and one-dimensional strain loading with plate-impact experiments.

Bodner and Rajendran (Bodner & Rajendran, 1995) presented the Bodner-Partom viscoplastic equations for improved prediction of strain rate and temperature effects on the plastic flow behavior of metals. The thermal softening and strain hardening features widely differ from metal to metal. For example, experimental results using the Kolsky apparatus (split Hopkinson bar) show that the shapes of flow stress vs. temperature curves substantially differ between aluminum and copper. Ávila and Krishina (1999) expressed an integrated micro/macro-mechanical study of the elastic-viscoplastic behavior of unidirectional metal matrix composites (MMC). The micromechanical analysis of the elastic moduli was based on the Composites Cylinder Assemblage model (CCA). These "homogenization" techniques were later combined with the Vanishing Fiber Diameter (VFD) model and a new formulation was offered. The concept of a smeared element procedure

was used in conjunction with two different versions of the Bodner-Partom elastic-viscoplastic constitutive model for the associated macroscopic analysis.

Rubin (1989) used the Bodner-Partom model as a numerical solution for time integration of the flow rule for large plastic deformation and arbitrary loading histories of an elastic-viscoplastic metal and then the comparison of the numerical solution of simple shear with the analytical solution that predicts the value of the Cauchy shear stress even for extremely large integration steps.

3.1 Constitutive equations of Bodner-Partom model

The Bodner-Partom constitutive equations (Bodner & Merzer, 1978; Bodner & Partom, 1975) are presented in detail. Starting with the flow law (Von Mises) of isotropic plasticity:

$$\frac{d\boldsymbol{\varepsilon}^{\boldsymbol{p}}}{dt} = \lambda \mathbf{s} \tag{3.1-1}$$

Where $\boldsymbol{\varepsilon}^{\boldsymbol{p}}$ and $\mathbf{s}$ are the plastic strain and the deviatoric stress, respectively. Equation (3.1-1) can be written in terms of stress and strain invariants:

$$D_2^p = \lambda^2 J_2 \tag{3.1-2}$$

$$D_2^p = D_0^2 \exp\left(\left(-\frac{z^2}{3J_2}\right)^n \left(\frac{n+1}{n}\right)\right) \tag{3.1-3}$$

Where D_2^{P} is the second invariant of the deviatoric plastic strain rate, and J_2 is the second invariant of the deviatoric stress. Combining equation (3.1-1) through (3.1-2), the plastic strain rate is defined in the following form:

$$\frac{d\boldsymbol{\varepsilon}^{\mathbf{p}}}{dt} = D_0 \exp\left(-\left(\frac{z^2}{3J_2}\right)^n \left(\frac{n+1}{2n}\right)\right)\frac{\mathbf{s}}{\sqrt{J_2}} \tag{3.1-4}$$

Where D_0 is the limiting strain rate and changes with the strain velocity:

$\dot{\varepsilon}^p$ [s^{-1}]	< 10	$10 - 10^3$	$> 10^3$
D_0 [s^{-1}]	10^4	10^6	10^7

n is the strain rate sensitivity parameter and temperature-dependent constant.

$$n = (835 + 5T(\mathrm{K}))/T(\mathrm{K}) \tag{3.1-5}$$

$$T(\mathrm{K}) = T(^{\circ}\mathrm{C}) + 273.15$$

m is a material constant that controls the rate of work hardening. *Z* is resistant to plastic flow and loading history dependency. Z_0 and Z_1 are the initial and saturated values of the internal state variable *Z*. It is noted that Z_0 could take any value between 0 and Z_1.

$$Z = Z_1 - (Z_1 - Z_0)\exp(-mw_p) \tag{3.1-6}$$

And w_p is the plastic work in following which is calculated by integration of the following differential equation:

$$dw_p = \boldsymbol{\sigma} d\boldsymbol{\varepsilon}^{\boldsymbol{p}} \tag{3.1-7}$$

In addition, for materials that exhibit strong strain hardening, m has been made a function of w_p. The expression for m is:

$$m = m_0 + m_1\exp\left(-\alpha w_p\right) \tag{3.1-8}$$

This is a classical model and most of the references are based on applications with conditions (temperatures and strain rates) far from repository conditions. It is necessary to demonstrate whether these models apply to repository conditions.

3.2 Implementation in CODE_BRIGHT

In FORTRAN's programming, the algorithm of the Bodner-Partom constitutive equations is written based on the finite element method and then released in CODE_BRIGHT. In the Bodner-Partom model, the invariant of plastic work is chosen as a history variable. w_p^k is the plastic work at time k and w_p^{k+1} is the plastic work at time k+1. The history variable is applied in the convergence of the Bodner-Partner solution. A factor, epsilon, is used to weigh the previous w_p estimates with the current W_p in order to obtain improved values for the next iteration, as follow:

$$w_p = w_p^k(1 - \varepsilon) + w_p^{k+1}\varepsilon \tag{3.2-1}$$

$$w_p^{k+1} = w_p^k + dw_p \tag{3.2-2}$$

When $\varepsilon = 1$, the new estimates are equal to the current values, and when $\varepsilon = 0.5$, the new estimates are simply the averages of the previous estimates and the new values. Generally,

$\varepsilon = 1$ works well; sometimes, however, ε must be reduced (to 0.75 or 0.5) in order to improve the accuracy of the solution.

Analytical (Tangent) and approximate (Secant) derivatives methods can be used in constitutive equations of Bodner-Partom in FORTRAN. According to the equation (3.1-1), both methods are implied for calculating the plastic strain rate with respect to the second invariant of deviatoric stress and temperature. In general, the derivative of the plastic strain rate with respect to stress is in the form of the following equation.

$$\frac{\partial \dot{\boldsymbol{\varepsilon}}^{\mathbf{p}}}{\partial \boldsymbol{\sigma}} = \lambda \frac{\partial \mathbf{s}}{\partial \boldsymbol{\sigma}} + \left(\frac{\partial \lambda}{\partial J_2}\right)\left(\frac{\partial J_2}{\partial \boldsymbol{\sigma}}\right)\mathbf{s} \tag{3.2-3}$$

$$\frac{\partial J_2}{\partial \boldsymbol{\sigma}} = \mathbf{M}\boldsymbol{\sigma} \tag{3.2-4}$$

The matrix **M** is:

$$\begin{bmatrix} \mathbf{M}_a & \mathbf{0_{3x3}} \\ \mathbf{0}_{3x3} & \mathbf{M}_b \end{bmatrix}$$

$$\mathbf{M}_a = \begin{bmatrix} \frac{2}{3} & -\frac{1}{3} & -\frac{1}{3} \\ -\frac{1}{3} & \frac{2}{3} & -\frac{1}{3} \\ -\frac{1}{3} & -\frac{1}{3} & \frac{2}{3} \end{bmatrix}; \mathbf{M}_b = \begin{bmatrix} 2 & 0 & 0 \\ 0 & 2 & 0 \\ 0 & 0 & 2 \end{bmatrix}$$

Secant and tangent methods are used for calculating the derivative of λ with respect to the second invariant of deviatoric stress. The derivative of plastic strain rate with respect to temperature is computed in the equation below.

$$\frac{\partial \dot{\boldsymbol{\varepsilon}}^{\mathbf{p}}}{\partial T} = \left(\frac{\partial \lambda}{\partial T}\right)\mathbf{s} \tag{3.2-5}$$

For the implementation in CODE_BRIGHT, the analytical derivatives (tangent method) have been considered.

3.3 Comparison with tensile test in copper

A comparative study of the elasto-viscoplastic behavior of copper is presented here. The stress-strain response of copper in a uniaxial tensile test has been reported by Yao (Yao & Sandström, 2000). This test is simulated in CODE_BRIGHT with the copper model implemented and the results of the test and modeling are compared.

3.3.1 Geometry, initial and boundary conditions, and model parameters

The geometry of the copper sample tested was a cylinder with a radius of 5 millimeters and a height of 100 millimeters ((Yao & Sandström, 2000); Figure 3-1). The mesh used in this model is the quadratic tetrahedra element and the number of nodes and elements are 633 and 390 in respectively (Figure 3-2).

As it has been commented before, the model is elasto-viscoplastic. In elasticity, a linear elastic model is used in which the Young modulus is 120 GPa and the Poisson ratio is 0.308. The boundary conditions are fixed displacements on top and at the bottom. The vertical displacement rate in the upper surface is 10^{-4} m/s and non-displacement at the bottom. Radial stresses are zero.

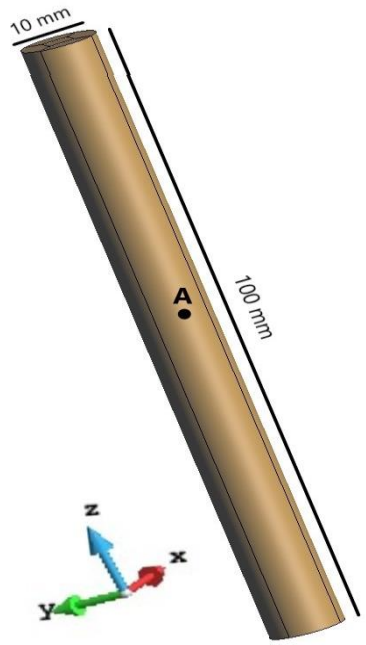

Figure 3-1 Dimension of copper (Yao & Sandström, 2000).

Figure 3-2 Quadratic tetrahedral mesh in copper (Yao & Sandström, 2000).

3.3.2 Results

After the calculations, the results of CODE_BRIGHT (a finite element analysis) are related to experimental data (Yao & Sandström, 2000). Comparison between the CODE_BRIGHT modeling in small strain setting and experiments is shown at the end of the test in Figure 3-3. Point A is chosen in Figure 3-1 for analysis of stress-strain response in copper. It is necessary to say that the validation has been carried out with the tests performed at room temperature (20ºC).

Elongating the sample and measuring the stress variation with strain provides a stress-strain curve for the material. The vertical stress is applied to the vertical axis, whereas the vertical strain is set to the horizontal axis. Two types of stress (Engineering stress and True stress) are considered for the test measurements. True stress is defined as the applied load divided by the material's actual (instantaneous) cross-sectional area (which changes over time). Engineering stress is calculated by dividing the applied load by the initial cross-sectional area (original area of cross-section) of the material. Nominal stress is another term for Engineering stress. CODE_BRIGHT considers the engineering stress in small strains setting.

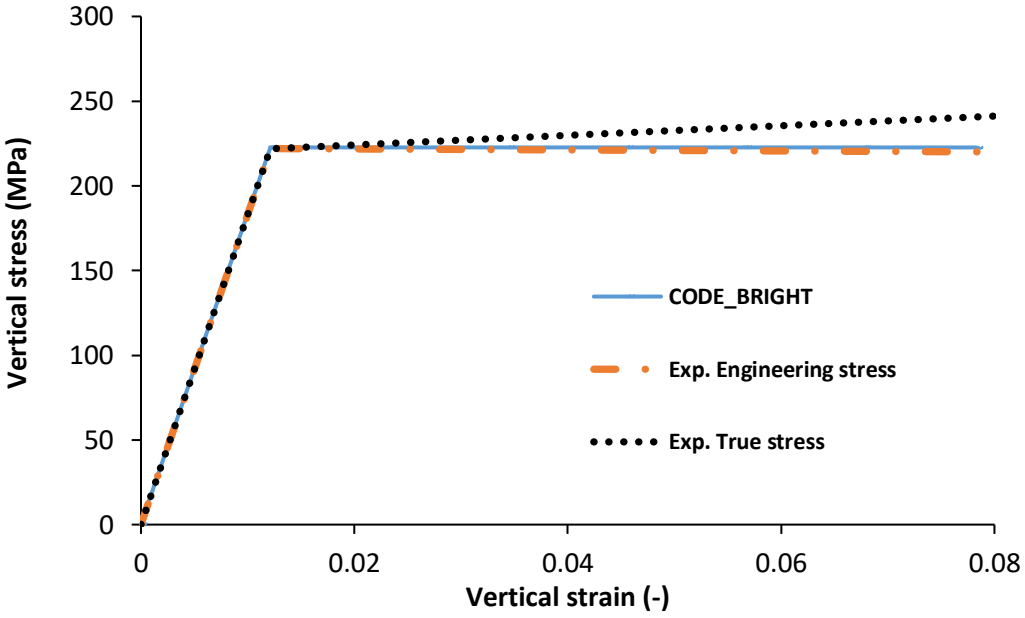

Figure 3-3 Stress-Strain curves (Point A) (Yao & Sandström, 2000).

Engineering stress is lesser than the corresponding True stress in tension conditions. In tension, the current area decreases. In compression, it is reversed, Engineering stress is greater than the corresponding True stress. The experiment under cold worked conditions has been performed. The results in CODE_BRIGHT approximately are the same as the results obtained from experiments for copper (Yao & Sandström, 2000).

3.4 Comparison with Stealth Finite Difference Code

The new subroutines that describe the Bodner-Partom constitutive equations must be checked for their verification. For this purpose, the stress-strain response of a uniaxial tensile experiment on a prismatic sample at constant velocity under cold worked conditions (Rajendran & Grove, 1987) was computed in CODE_BRIGHT and the results compared with the results from Stealth Finite Difference Code.

3.4.1 Geometry, initial and boundary conditions, and model parameters

The geometry of the sample is prismatic, with bases length of 0.01 meters (thin thickness) and a height of 1 meter. The boundary condition on top of the geometry is a vertical displacement rate of -100 m/s and fixed at the bottom of the geometry. The stresses orthogonal to lateral boundaries are zero (uniaxial tensile experiment). The mesh used is three-dimensional with linear hexahedra elements using numerical integration (selective) with 8 points. The number of nodes and elements are 425 and 256 respectively.

In elasticity, a linear elastic model is used in which the Young modulus is 200 MPa and the Poisson ratio is 0.3. The viscoplastic model is used by the Bodner-Partom model, and the material parameters are shown in Table 3-1. This is a synthetic case for model verification, so these parameters are not relating to any special material.

Table 3-1 Input parameters of the material (Rajendran & Grove, 1987).

Parameter	Value	Unit
D_0	10^8	s^{-1}
Z_0	1500	MPa
Z_1	1500	MPa
m_0	0.002	$(MPa)^{-1}$
m_1	0	$(MPa)^{-1}$
α	0.50	$(MPa)^{-1}$

3.4.2 Results

The results confirm that the Bodner-Partom model has been implemented in CODE_BRIGHT correctly. Figure 3-4 presents the 3-D geometry with the display vector of displacements.

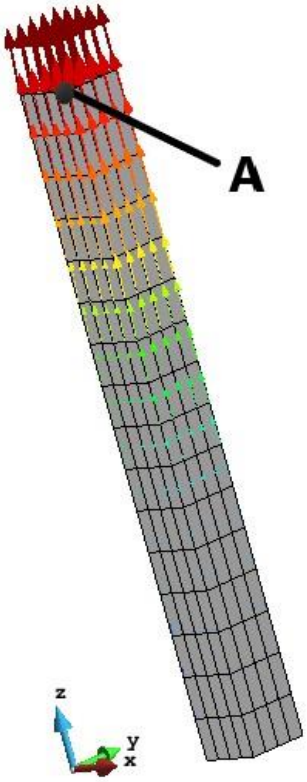

Figure 3-4 Point A and display vector of displacement.

The evolution of the stresses is studied in point A (described in Figure 3-4) in Figure 3-5. This figure shows the stress-strain curve obtained in CODE_BRIGHT and it is compared with the curve obtained with Stealth Finite Difference (Rajendran & Grove, 1987) when the same synthetic test is simulated. The two curves are identical, which proofs that the model has been correctly implemented. Note that this case does not include hardening because the original results did not include this feature.

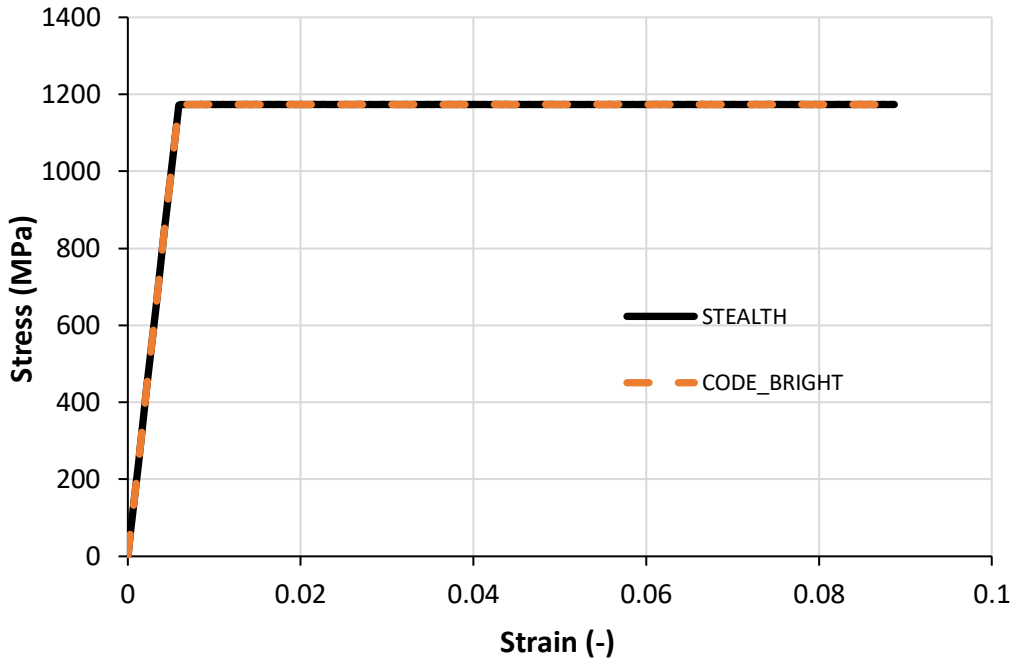

Figure 3-5 Comparison between the stress-strain curve obtained from Code_Bright with the stress-strain curve of Stealth Finite Difference Code (Rajendran & Grove, 1987).

3.5 Comparison with semi-analytical solutions

The implementation of the Bodner-Partom model for solving the simulation of the uniaxial tensile stress (Figure 3-1) and simple shear test (Figure 3-6) is considered in two cases of the semi-analytical and numerical methods. The semi-analytical solution is calculated by Excel and it is called a semi-analytical solution there is not an explicit solution of the ordinary differential equations (ODE). The ODE can be solved numerically by the Euler method. The deformation of the shear test at end of the test is shown in Figure 3-7 after 30 seconds. According to Figure 3-8 and Figure 3-9. The evaluation of two cases are verified and CODE_BRIGHT and semi-analytical solution show the same results.

The viscoplastic behavior of the Bodner-Partom model in a uniaxial tensile test is obtained in the following equation:

$$\frac{d\varepsilon_z^p}{dt} = D_0 \exp\left(-\left(\frac{z^2}{3J_2}\right)^n \left(\frac{n+1}{2n}\right)\right)\frac{s_{zz}}{\sqrt{J_2}}$$

$$J_2 = \frac{1}{3}\sigma_z^2 \quad , \quad s_{zz} = \sigma_z - p = \frac{2}{3}\sigma_z \quad \text{and} \quad p = \frac{1}{3}\sigma_z$$

In conclusion, the plastic strain rate is equal to:

$$\frac{d\varepsilon_z^p}{dt} = D_0 \exp\left(-\left(\frac{z^2}{3 * \frac{1}{3}\sigma_z^2}\right)^n \left(\frac{n+1}{2n}\right)\right) \frac{\frac{2}{3}\sigma_z}{\frac{1}{\sqrt{3}}\sigma_z}$$

So

$$\frac{d\varepsilon_z^p}{dt} = D_0 \exp\left(-\left(\frac{z}{\sigma_z}\right)^{2n} \left(\frac{n+1}{2n}\right)\right) \frac{2}{\sqrt{3}}$$

In addition, the plastic strain rate for the shear test is approached in the following way:

$$\frac{d\varepsilon_p}{dt} = D_0 \exp\left(-\left(\frac{z^2}{3J_2}\right)^n \left(\frac{n+1}{2n}\right)\right) \frac{\tau_{xy}}{\sqrt{J_2}}$$

$J_2 = \tau_{xy}^2$, $q = \sqrt{3}\,\tau_{xy}$

Then:

$$\frac{d\varepsilon_p}{dt} = D_0 \exp\left(-\left(\frac{z}{\sqrt{3}\tau}\right)^{2n} \left(\frac{n+1}{2n}\right)\right)$$

Table 3-2 The material parameters of the uniaxial tensile test.

Parameter	Value	Unit
D_0	10^{-3}	s^{-1}
Z_0	237	MPa
Z_1	350	MPa
m_0	0.15	$(MPa)^{-1}$
m_1	0.25	$(MPa)^{-1}$
α	0.50	$(MPa)^{-1}$

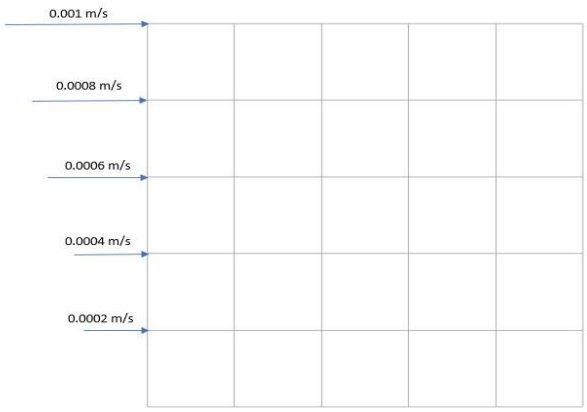

Figure 3-6 Different displacement rates are used in a simple shear test in the X-direction.

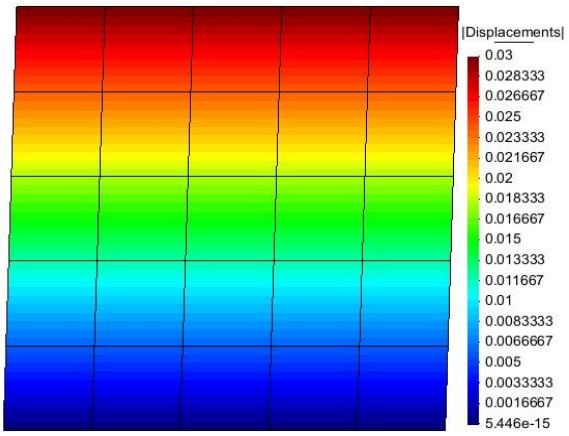

Figure 3-7 Contour fill of displacements in simple shear test at the end of the test.

The material parameters for the uniaxial tensile test and simple shear test are depicted in Table 3-2 and Table 3-3.

Table 3-3 The material parameters of the simple shear test.

Parameter	Value	Unit
D_0	10^{-3}	s^{-1}
Z_0	237	MPa
Z_1	237	MPa
m_0	0.15	$(MPa)^{-1}$
m_1	0.25	$(MPa)^{-1}$
α	0.50	$(MPa)^{-1}$

In conclusion, the comparison between the semi-analytical with Euler method and numerical modeling in CODE_BRIGHT for two tests are manifested in the following figures:

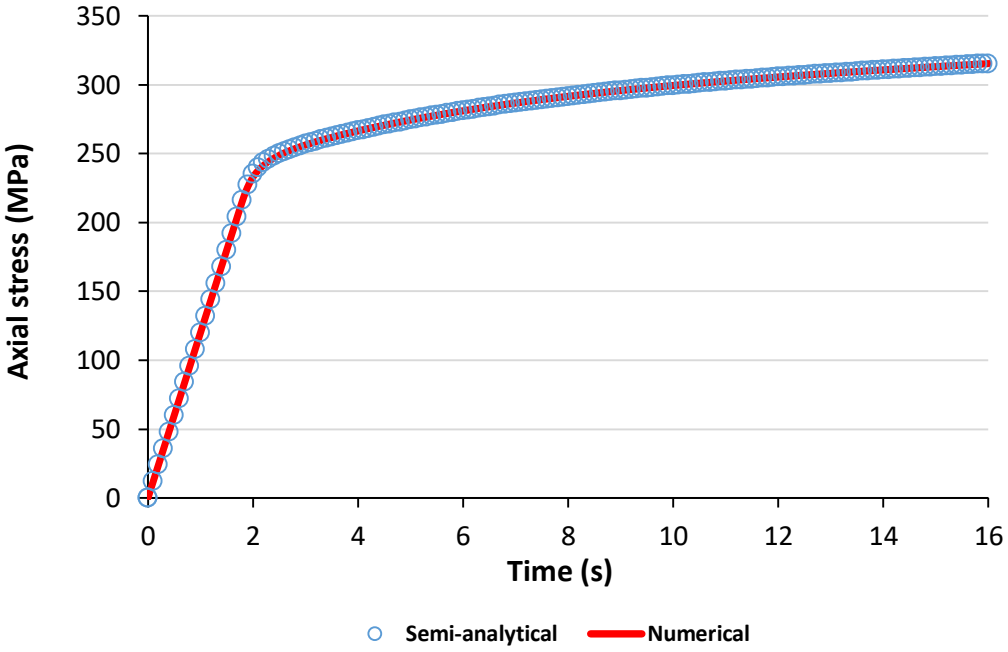

Figure 3-8 Comparisons between the semi-analytical and numerical solutions in the uniaxial tensile test.

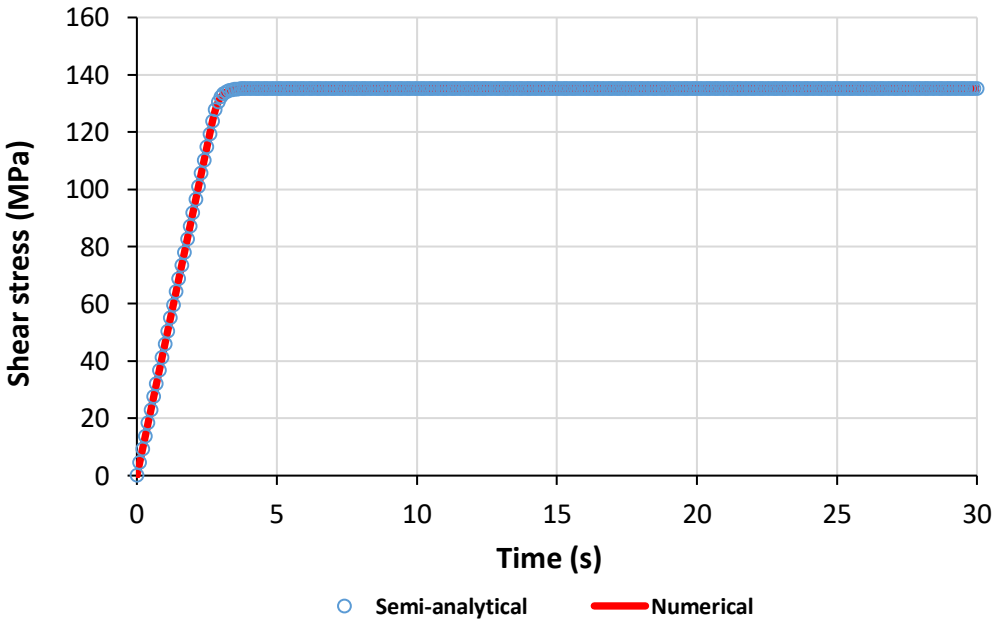

Figure 3-9 Comparisons between the semi-analytical and numerical solutions in the simple shear test.

CHAPTER 4

4 Canister-clay shear test analysis with CODE_BRIGHT

Spent nuclear fuel produced in nuclear power plants should be stored in safe conditions for thousands of years. Some countries have proposed to dispose of the spent nuclear fuel in deep geological repositories. Spent nuclear fuel will be encapsulated in metal canisters (Raiko et al., 2010; Raiko, 2005) and disposed of safely several hundreds of meters deep in stable geological formations that guarantee intact storage for the long term. In the KBS-3V disposal concept (Wimelius & Pusch, 2008), copper canisters are going to be placed in vertical deposition holes. Surrounding the canister, bentonite will be used to isolate the canisters and delay any potential radionuclide migration (Juvankoski & Marcos, 2010). Bentonite is also used to backfill the deposition tunnels, preventing the formation of preferential pathways, which could assist radionuclide migration. Figure 4-1 shows a schematic of the KBS-3V disposal concept. The selected geological formation must provide a stable thermo-hydro-mechanical-chemical (THMC) environment at the repository depth.

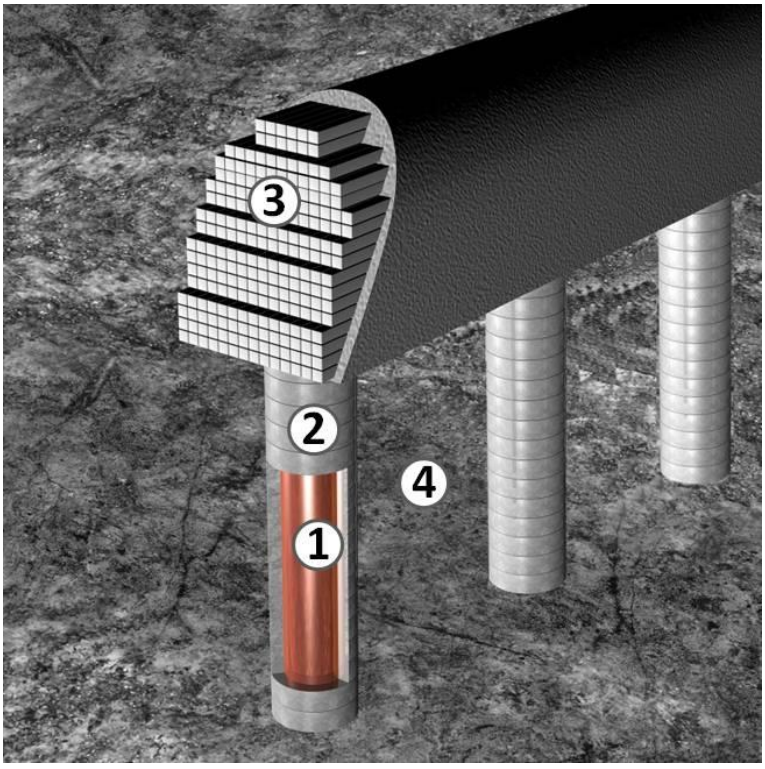

Figure 4-1 KBS-3V type repository concept (www.Posiva.fi). 1: Canister, 2: Buffer, 3: Backfill, 4: Host rock.

In porous media, subjected to thermal, hydraulic, and mechanical conditions, relevant thermo-hydro-mechanical (THM) phenomena take place (Åkesson et al., 2010; Chen et

al., 2009; A. Gens et al., 2009; Toprak et al., 2013). In fact, there exist a number of mutual interactions that must be taken simultaneously into account in the analyses. It is necessary to represent adequately the canister under thermo-mechanical coupling in the context of a thermo-hydro-mechanical calculation. Elastic-visco-plastic theory can be used to represent the behavior of the canisters. The canister is designed to maintain the spent nuclear fuel isolated from the surrounding environment for at least 100,000 years (Jonsson et al., 2018; Raiko, 2005).

Bodner and Partom (Bodner & Merzer, 1978; Bodner & Partom, 1975; Bodner & Rajendran, 1995) formulated a set of constitutive equations to represent Elastic-viscoplastic strain-hardening material behavior for large deformations and arbitrary loading histories. This model has been chosen for copper simulation. An essential feature of the model is that the total deformation rate is considered to be separable into elastic and inelastic components, which are functions of state variables at all stages of loading and unloading. The canister was reproduced with a copper cylinder which reached the yield conditions after the test.

Different constitutive equations for clay have been proposed by different authors (e.g. (Alonso et al., 1990; Börgesson et al., 1995; François & Laloui, 2008; François et al., 2008; Gallipoli et al., 2003; Gens & Alonso, 1992)). Drucker–Prager viscoplasticity model (Drucker & Prager, 1952) and Barcelona Basic Model (Alonso et al., 1990) have been considered for the clay simulation.

For a hydro-mechanical calculation, it is necessary to solve the water balance equation and the equilibrium equation. It is possible to avoid the solution of the water balance equation when the water does not flow because the load is quite fast and the porous media has low permeability. In geotechnics, this is referred to as undrained conditions (Terzaghi, 1925). Undrained triaxial tests can be carried out for the characterization of clay in undrained conditions (Börgesson et al., 1995; Dueck et al., 2010; Dueck & Nilsson, 2010).

The shear test that is modeled in this work happened quickly enough, so the bentonite did not have time for pore pressure dissipation, and therefore, it can be considered under undrained conditions. Actually, for low permeability materials, the assumption of undrained conditions that permits us to avoid solving water balance equation, then, the hydraulic boundary conditions are not considered.

The opposite of undrained conditions happens if it is possible to consider that the water pressure reaches equilibrium very rapidly. This occurs because the loading is slow and the

porous media has relatively high permeability. Pore pressure reaches equilibrium conditions during the loading phases (e.g. the construction of a building on sandy soil). This is referred to as “drained conditions”. The concepts “undrained conditions” and “drained conditions” are defined concerning permeability and loading velocity. Since bentonite has very low permeability, it is unlikely to do the mock-up test in drained conditions. Even if flow through the sample boundaries is permitted, pressure dissipation takes place very slowly.

In this section, simulations will be referred to as “total stress analysis” and “effective stress analysis”. The description of the two alternatives follows:

- Total stress analysis: it is assumed that undrained conditions are satisfied, so water does not move at all (permeability close to 0). This requires the use of specific parameters: undrained young modulus (E_u), undrained Poisson ratio (ν_u close to 0.5), undrained shear strength (c_u).
- Effective stress analysis: it corresponds to a hydro-mechanical coupled analysis. The permeability of the bentonite is a key parameter. As the boundary is assumed the pore pressure remains fixed, some internal flows (and deformations) may take place. If permeability is low enough, the previous case should be recovered.

As indicated, the total stresses approach uses parameters for undrained conditions. Young modulus should be measured or estimated in undrained tests. Poisson ratio can be simply set to ~0.5 which indicates incompressibility (bulk modulus $K = \frac{E}{3(1-2\nu)}$). The undrained shear strength (c_u) can be either determined experimentally or analytically from standard strength parameters (friction angle for Mohr-Coulomb or M for BBM or Cam-Clay models). Undrained strength is not a parameter because it depends on the initial effective stress state. This parameter is determined in the appendix, so the value considered is consistent with the BBM parameters for bentonite.

In effective stress calculation, the mechanical problem is solved in a coupled way with water flow, i.e. hydro-mechanical analysis. Parameters correspond to effective stress constitutive equations.

An understanding of the total stress analysis and the effective stress analysis is essential in geotechnical engineering, and these two methods are practical in the evaluation of all types of geotechnical projects, such as engineered barrier systems, slope stability, earth pressure calculations, and foundation design.

CODE_BRIGHT (DIT-UPC, 2021; Olivella et al., 1994; Olivella et al., 1996) is the reference computer code for the design of the spent nuclear fuel repository in Sweden and Finland. It is a Finite Element Method (FEM) program capable of performing coupled hydro-mechanical (HM) analysis in geological media. It has been developed at the Department of Civil and Environmental Engineering of the Technical University of Catalonia (UPC) and works combined with the pre/post-processor GiD, developed by the International Center for Numerical Methods in Engineering (CIMNE).

The purpose is to model the canister-clay mock-up system using total stress and effective stress approaches. Sensitivity analysis on important parameters for the two methods has been performed and finally, these two models are compared together in mock-up scale in 2D and 3D. Sensitivity analyses represent alternate models or data to those of the Base Case to develop a better understanding of the modeled system but remain within the scope of the base. Analyses of the sensitivity cases illustrate the effect of model and data uncertainties.

4.1 Test description

To assess the consequences of a shear zone in a vertical deposition hole (KBS-3V spent nuclear fuel disposal concept), small-scale tests were carried out (Börgesson, 1986). Cylindrical samples (h = 622 mm, Ø = 158 mm) made of highly compacted MX-80 bentonite surrounding a cylindrical canister (h = 450 mm, Ø = 80 mm) made of copper were prepared. The shear test apparatus used had a cylindrical housing divided into two similar parts by a plane perpendicular to the cylinder axis. One of these parts was held fixed and the other could be displaced perpendicularly to the cylinder axis. The samples were placed in the cylindrical housing of the shear apparatus. Afterward, the samples were completely saturated with water, thereby inducing a swelling pressure in the bentonite. Finally, the samples were sheared at different rates. The scope of the test was to assess the consequences of rock displacement across a deposition hole with a model test scaled 1:10 to a real deposition hole (Figure 4-2).

a) 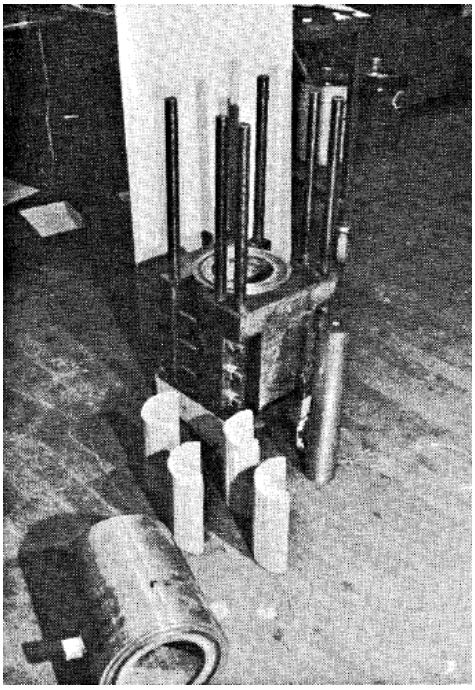

b) 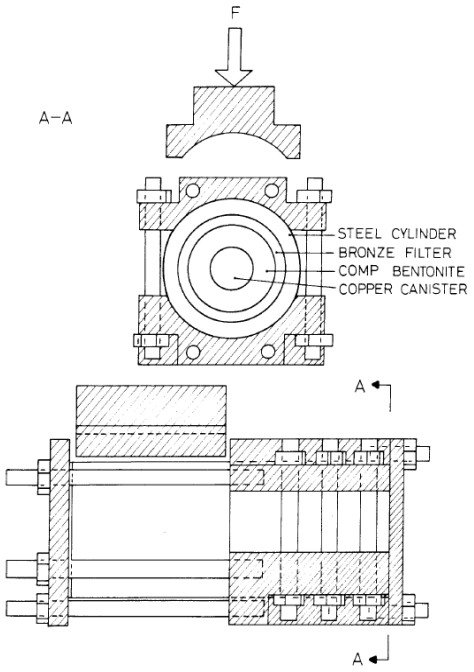

Figure 4-2 a) The shear apparatus, four of the bentonite blocks, and the canister just before mounting (Börgesson, 1986; Fig 3:7); b) Apparatus in which the filled deposition hole was simulated and sheared. The cross-hatched area is the steel frame (Börgesson, 1986; Fig 3:1).

4.2 Shear test modeling using total stress approach in 2D

4.2.1 Mock-up scale

A synthetic case that is inspired by a mock-up test (Börgesson, 1986) is presented in this section in 2D plane strain for the total stress analysis. It is simulated using two rectangles, the larger (h = 622 mm, L = 158 mm) represents the entire test set-up, and the smaller (h = 450 mm, L = 80 mm) the copper rod. MX-80 bentonite fills the space between the copper and the boundary. The mesh has 425 nodes and 384 linear quadrilateral elements. These elements are based on a numerical integration with 4 points (Figure 4-3). Selective integration by means of the modification of matrix **B** (Hughes, 1980) permits to solve the problem of locking that appears when the medium is quite incompressible and/or the volumetric strains are expected to be extremely small, like in a shearing dominated deformation.

Two different boundary conditions are applied. The lower part is fixed and the upper part can be displaced perpendicularly to the axial axis. On the upper part, corresponding to the mobile half of the shear apparatus, a horizontal displacement rate equal to -0.001 m/s is applied (the vertical displacements are kept to 0).

In the lower part, which corresponds to the fixed half of the shear apparatus, the horizontal and the vertical displacements are kept to 0. On a thin transition zone between those parts, a linear horizontal increment field (the vertical displacements were kept to 0) is considered. The shear zone thickness is 10 mm. Initial total stresses are equal to -9 MPa (compression is negative) and the pore pressure, in effective stresses analysis, is 0 MPa.

For the total stress approach, linear elasticity for bentonite and copper has been used. The parameters are compiled in Table 4-1. More information about bentonite parameters in undrained conditions can be found in Dueck (Dueck et al., 2010) and Börgesson (Boergesson & Hernelind, 2006).

Table 4-1 Elastic parameters of bentonite and copper (Börgesson & Hernelind, 2010).

Linear Elasticity		
	ν	E (MPa)
Bentonite	0.49	233*
Copper	0.33	120000

* Young modulus at a shear rate of 0.1 s^{-1} and a saturated bentonite density of 2020 kg/m^3

In Table 4-1, ν is Poisson's ratio and E is the Young modulus.

Drucker–Prager viscoplasticity (DIT-UPC, 2021; Drucker & Prager, 1952) with the Perzyna formulation (Perzyna, 1966) for bentonite and Bodner-Partom Viscoplasticity (Bodner & Partom, 1975; Khadivipanah et al., 2020) for copper have been applied and values are included in Table 4-2.

In Drucker-Prager viscoplasticity, Γ_0, m, c_u are fluidity (related with the inverse of viscosity), stress power, and undrained shear strength, respectively. In geotechnics, the undrained approach is referred to as $\phi = 0$ (note that this is not friction angle for effective but for total).

Table 4-2 Plastic parameters of bentonite and copper (Bodner & Partom, 1975; Drucker & Prager, 1952; Khadivipanah et al., 2020; Toprak et al., 2017).

Viscoplasticity models		
Bentonite	Γ_0 ($s^{-1}MPa^{-m}$)	10^3
	m (-)	3
	c_u (MPa)	3
Copper	D_0 (s^{-1})	10^4
	Z_0 (MPa)	31
	Z_1 (MPa)	237
	m_0 $(MPa)^{-1}$	0.15
	m_1 $(MPa)^{-1}$	0.25
	α $(MPa)^{-1}$	0.50

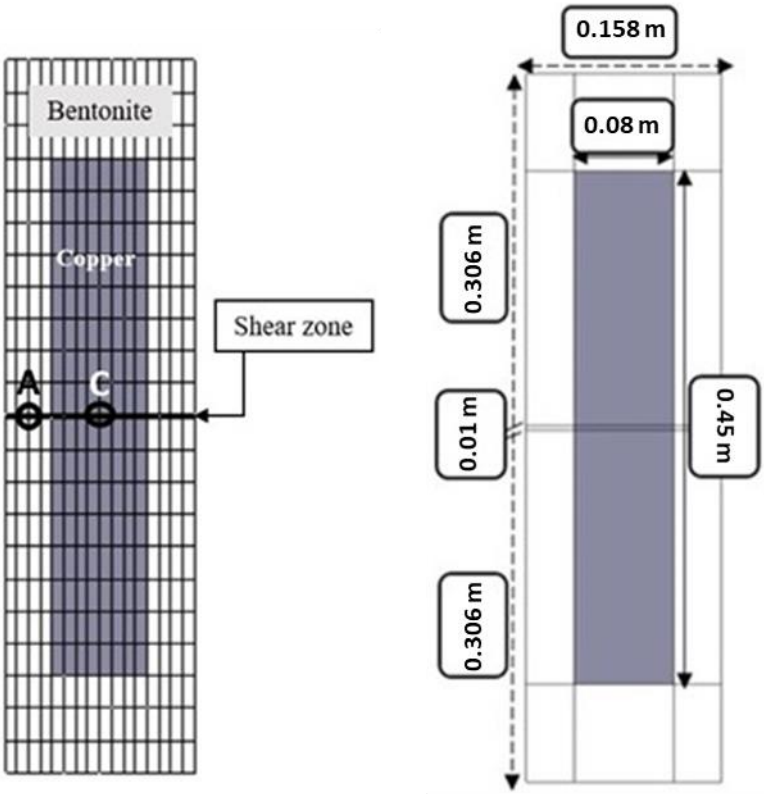

Figure 4-3 Geometry and mesh for Canister-Clay Shear Test.

The initial porosity for copper and bentonite is depicted in Figure 4-4.

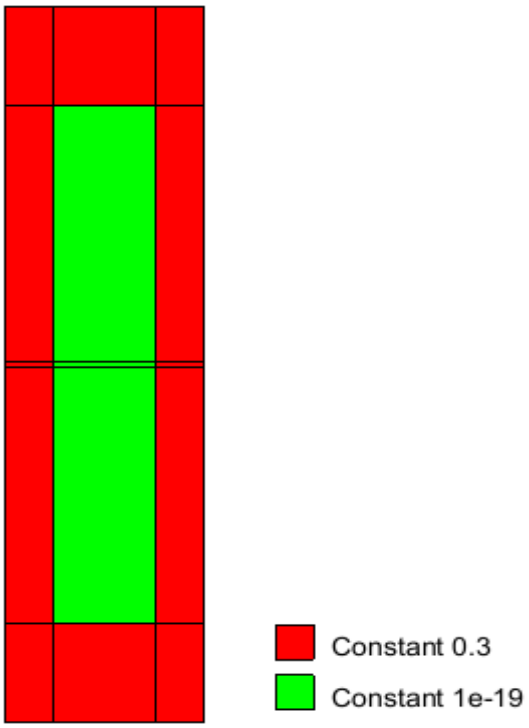

Figure 4-4 Initial total porosity.

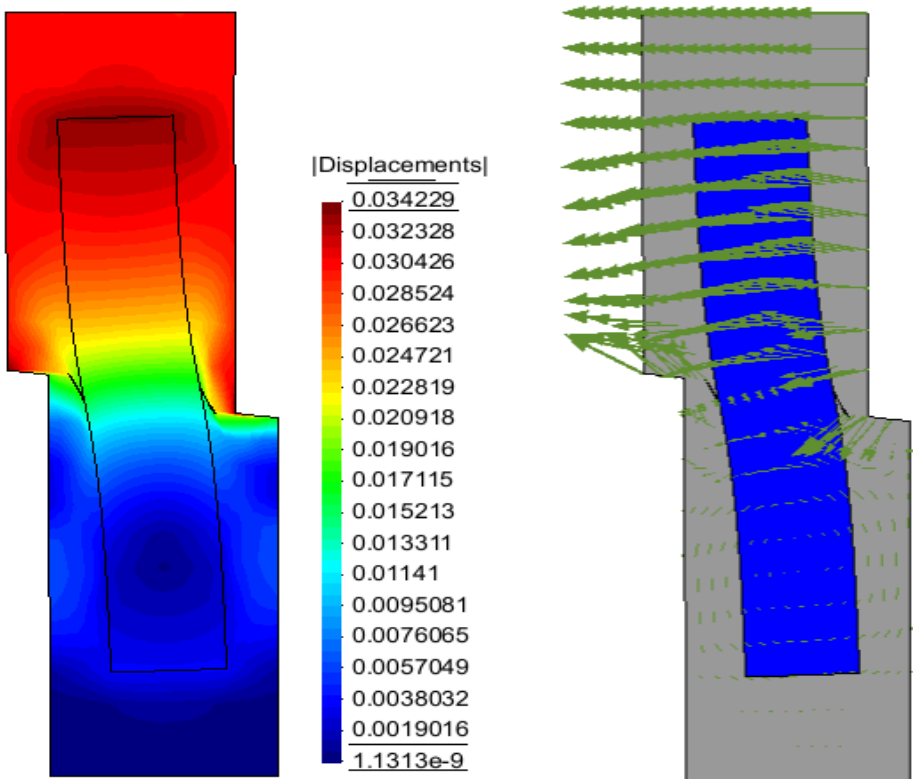

Figure 4-5 Deformation and display vector of Canister-clay shear test.

4.2.1.1 Undrained shear strength of bentonite

As indicated before, a total stress analysis requires specific parameters consistent with the total stress assumption. The undrained shear strength can be determined analytically from values of BBM parameters. This is presented in the appendix. Two different values have been used as strength parameters M in BBM. Following the parameters in Toprak (Toprak et al., 2017), undrained shear strength calculated gives a value of 3 MPa. In contrast, considering a lower strength (Börgesson et al., 1995), the calculated value falls close to 1 MPa.

The relatively simple calculation using undrained shear strength leads to the curves presented in Figure 4-6 (for bentonite) and Figure 4-7 (for copper). As shown in Figure 4-6, it is consistently obtained that deviatoric stress with respect to deviatoric strain in case of undrained shear strength of 3 MPa displays higher stress development than the case for 1 MPa. Note that $J^2 = \frac{1}{6}[(\sigma_1 - \sigma_2)^2 + (\sigma_1 - \sigma_3)^2 + (\sigma_2 - \sigma_3)^2]$, in a triaxial test $(\sigma_2 = \sigma_3)$, the deviatoric stress $q = \sigma_1 - \sigma_3$ and $J^2 = \frac{1}{3}(\sigma_1 - \sigma_3)^2$. The undrained shear strength c_u at confined pressure σ_3 in a triaxial test is $\frac{q}{2}$ at failure (Wood, 1990), so if c_u =3 MPa (see Appendix), $J = \frac{2}{\sqrt{3}} c_u = \frac{1}{1.73} \times 2 \times 3 = 3.5\ \mathrm{MPa}$ (J is the square root of the second invariant of the deviatoric stress tensor). Figure 4-7 displays the stress-strain curve for the canister copper. It can be observed that for the lower strength of the bentonite, the copper undergoes lower shear deformation. For $c_u = 1\ \mathrm{MPa}$ the canister copper undergoes less deviatoric deformation because there is more movement permitted in clay than for the case with $c_u = 3\ \mathrm{MPa}$ in small strains conditions.

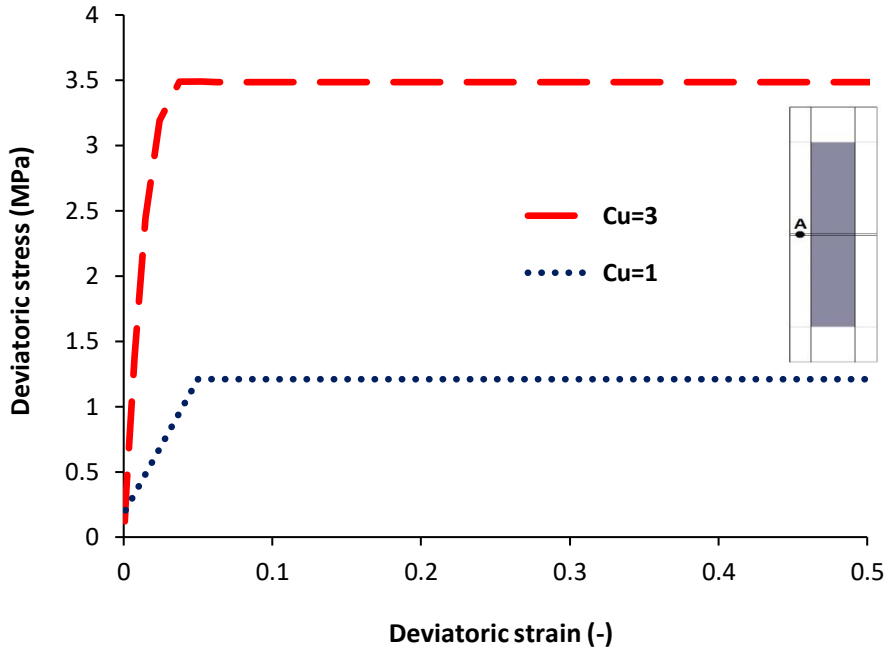

Figure 4-6 Sensitivity analysis to undrained shear strength for bentonite (Point A).

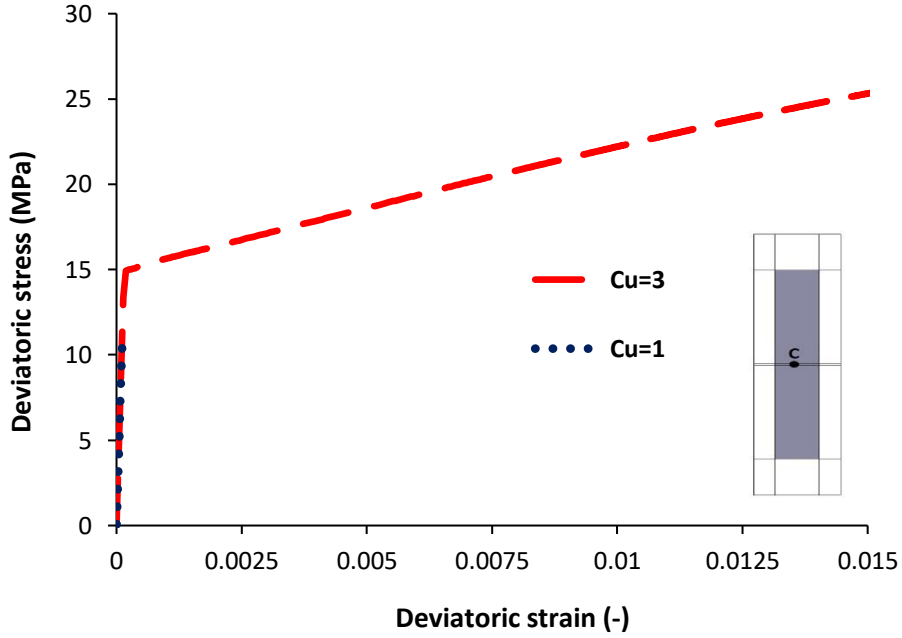

Figure 4-7 Sensitivity analysis to undrained shear strength for copper (Point C). Copper ($c_u = 1$) can rotate more because the clay is softer. So, the deviatoric deformation of the copper is much less when the clay is more deformable (less strength).

4.2.1.2 Sensitivity analysis of Γ_0

Three different values of Γ_0 (1/"viscosity") were assessed (1, $10^{-3,}$ and 10^3 s^{-1} MPa^{-3}). According to Figure 4-8, when the Γ_0 is equal to 10^{-3} s^{-1} MPa^{-3}, deviatoric stress is greater than deviatoric stress of 1 s^{-1} MPa^{-3} and 10^3 s^{-1} MPa^{-3}. When the viscosity changes from 1 s^{-1} MPa^{-3} to 10^3 s^{-1} MPa^{-3}, the variation in deviatoric stress (obtained by subtracting the hydrostatic stress from each principal stress) is very small in the bentonite. Point A in Figure 4-3 is chosen for the analysis of the bentonite. The elastic parameters for copper and bentonite are considered by Toprak, 2017 and it is depicted in Table 4-3. The plastic parameters are similar to Table 4-2.

Table 4-3 Elastic parameters of bentonite and copper (Toprak et al., 2013; Toprak et al., 2017).

Linear Elasticity		
	ν	E (MPa)
Bentonite	0.49	304
Copper	0.35	133000

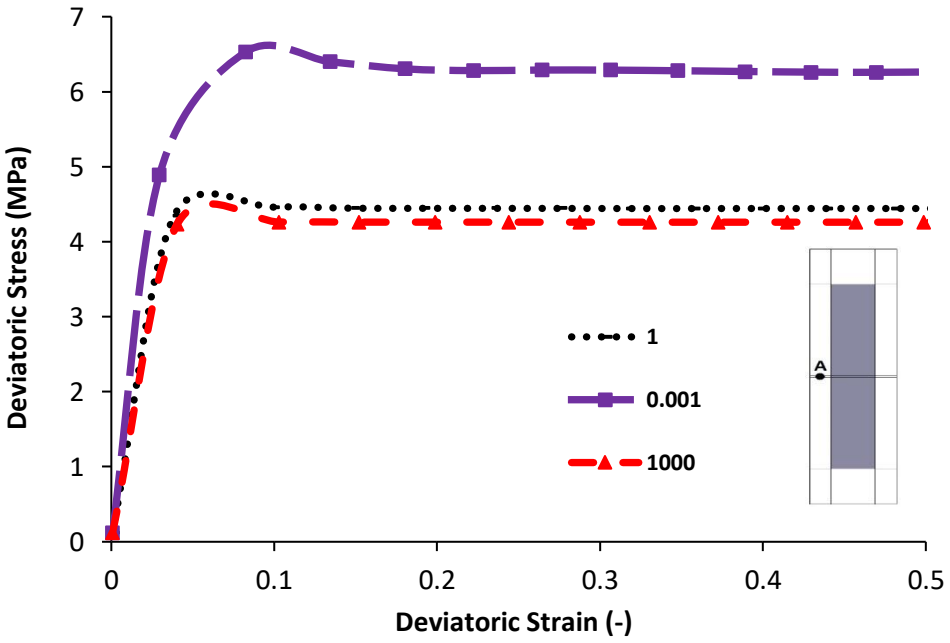

Figure 4-8 Deviatoric stress-strain curves in different Γ_0 for the bentonite (Point A).

For Copper affected by bentonite viscosity parameter:

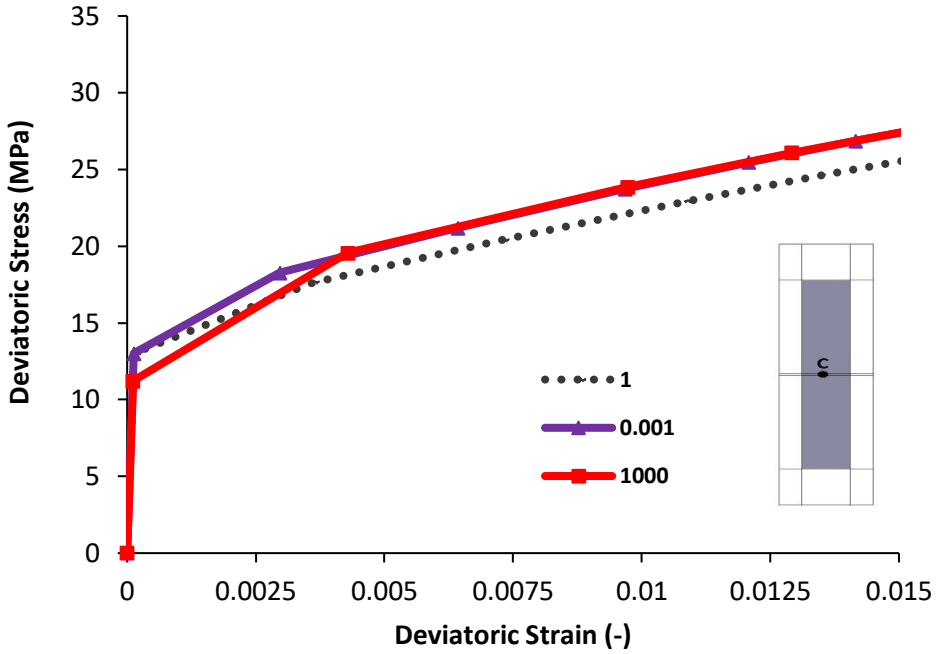

Figure 4-9 Deviatoric stress-strain curves in different Γ_0 for the copper (Point C).

Point C is selected for analysis of copper and according to Figure 4-9, the deviatoric stresses in different Γ_0 (1/"viscosity") roughly have the same elasto-viscoplastic curve. The results are consistent, so the larger Γ_0 has the larger deviatoric strain.

4.2.1.3 Sensitivity analysis of mesh

The mesh sensitivity analysis has been done. Three types of mesh such as rough, medium (the reference), and fine were considered. For all meshes, the Γ_0 is 1 s^{-1} MPa^{-3} for bentonite. The fine mesh (Figure 4-12) had 672 elements and 731 nodes and the medium mesh (Figure 4-11) had 384 elements and 425 nodes and the rough mesh (Figure 4-10) had 224 elements and 225 nodes.

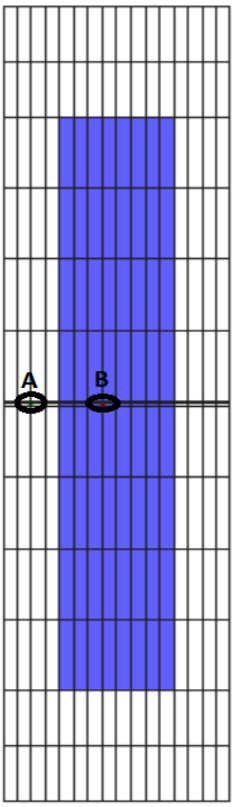

Figure 4-10 Rough mesh.

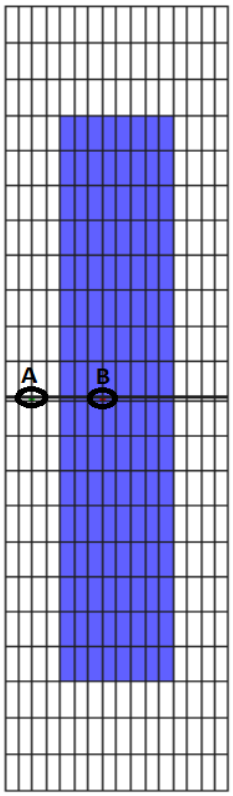

Figure 4-11 Medium mesh.

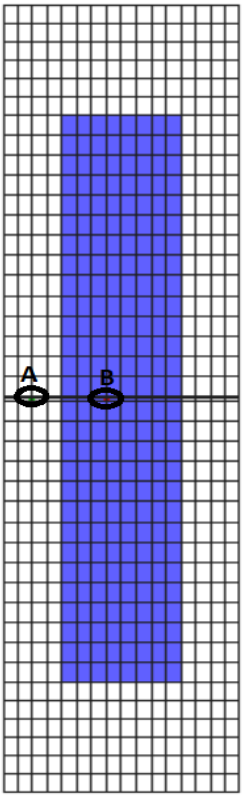

Figure 4-12 Fine mesh.

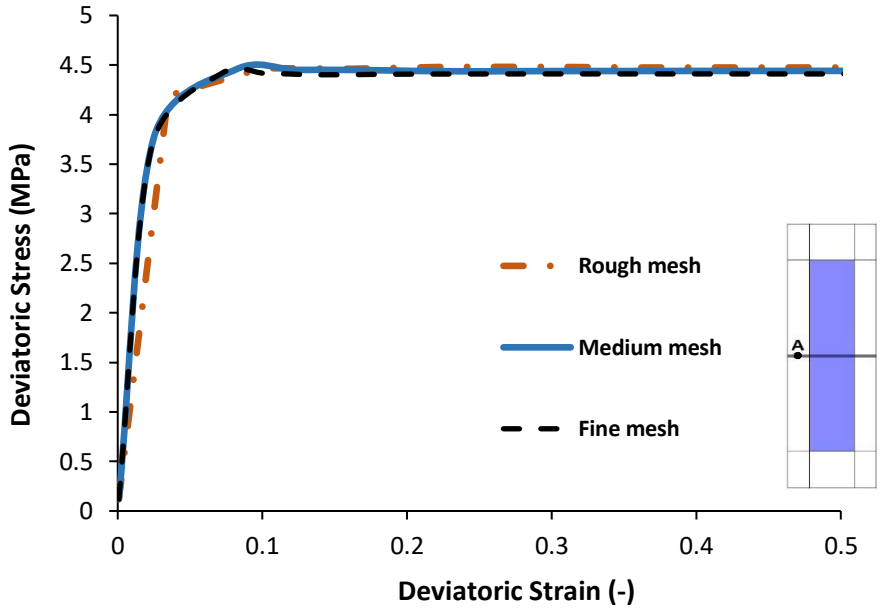

Figure 4-13 Comparison between rough, medium, and fine meshes for bentonite (Point A).

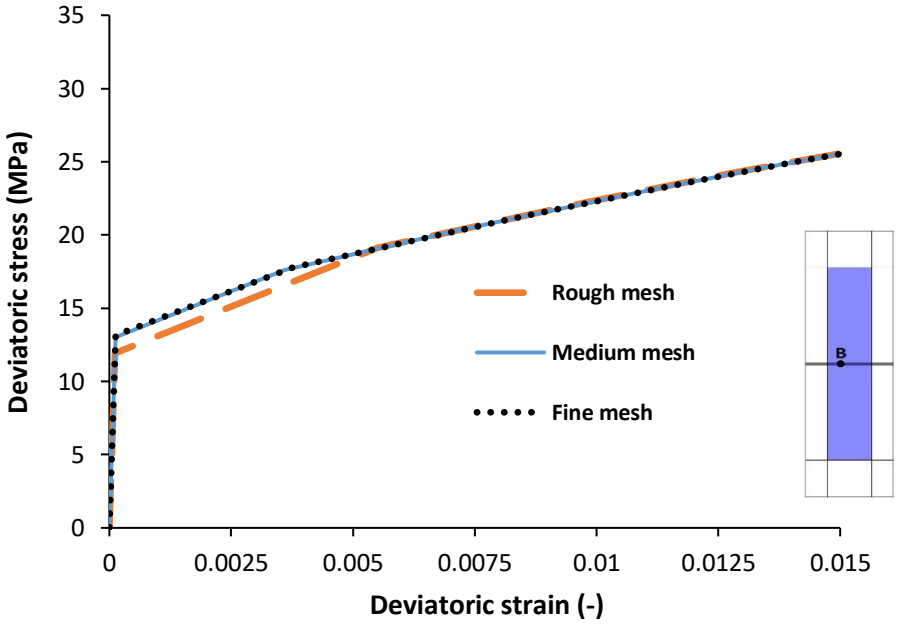

Figure 4-14 Comparison between rough, medium, and fine meshes for copper (Point B).

Points A and B in Figure 4-10, Figure 4-11, and Figure 4-12 are selected for comparison between rough, medium, and fine meshes in bentonite and copper in respectively. Deviatoric stress is the same in all three meshes as shown in Figure 4-13 and Figure 4-14.

4.2.1.4 Comparison between the updated Lagrangian method and fixed mesh method

Since the total stress analysis is simpler than the coupled hydro-mechanical analysis, the sensitivity to using the updated Lagrangian approach is done with this approach.

CODE_BRIGHT formulation was originally developed for small strains and fixed mesh. However, it includes the option to use the updated lagrangian method. This method modifies the coordinates of the mesh nodes after each time step is solved. When the formulation of CODE_BRIGHT uses updated lagrangian, it is considered that a geometrically nonlinear solution is obtained, still at small strain conditions. The model parameterization, i.e. the mesh, the boundary conditions are evaluated based on the simulated deformation, stress in the system.

The scope of this section is to compare results obtained with CODE_BRIGHT incorporating the updated Lagrangian formulation and the standard solution based on a fixed mesh.

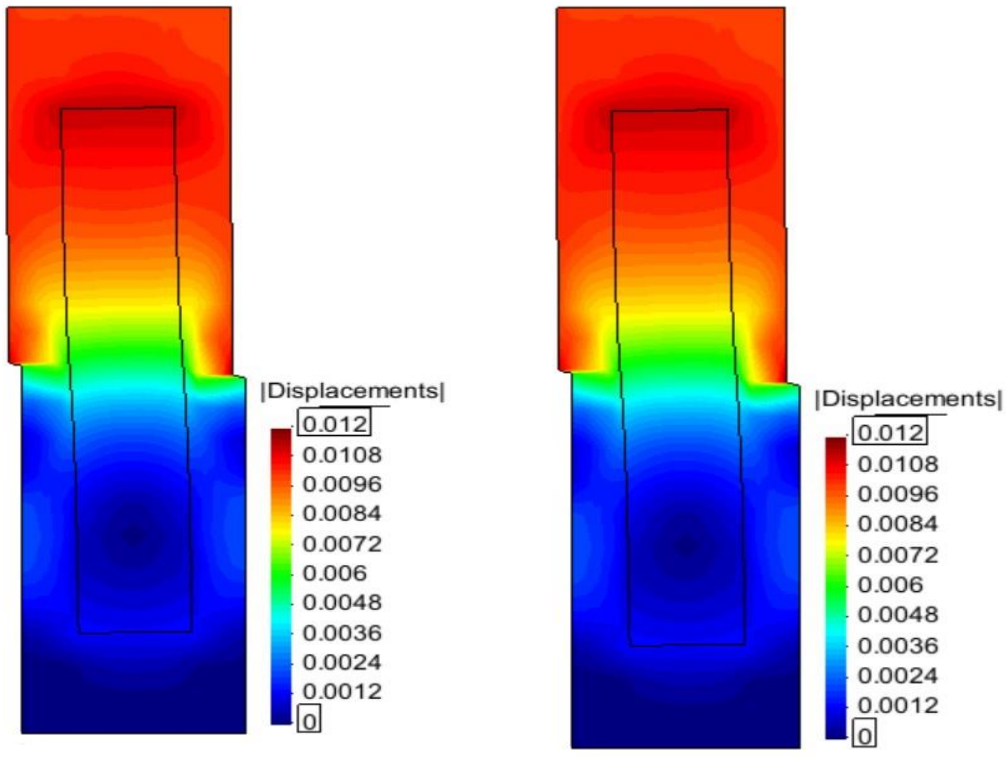

Figure 4-15 Displacements field in fixed mesh method (left) and updated Lagrangian method (right).

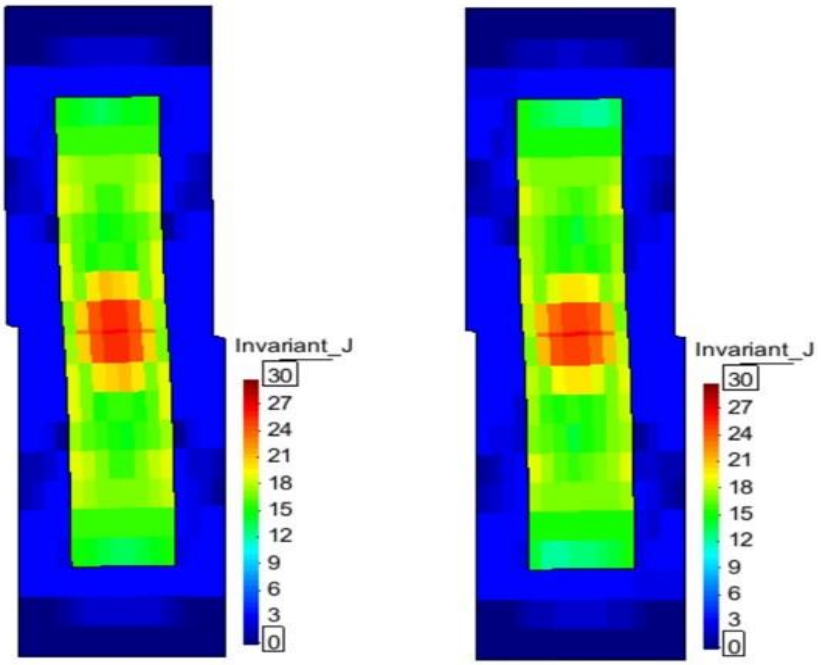

Figure 4-16 Deviatoric stress field in fixed mesh method (left) and updated Lagrangian method (right).

Figure 4-15 and Figure 4-16 show the contours fill with displacement field and deviatoric stress field for fixed mesh and updated Lagrangian method for the canister-buffer system. According to points A and C in Figure 4-3, deviatoric stress-strain curves are depicted for bentonite and copper in Figure 4-17 and Figure 4-18, respectively.

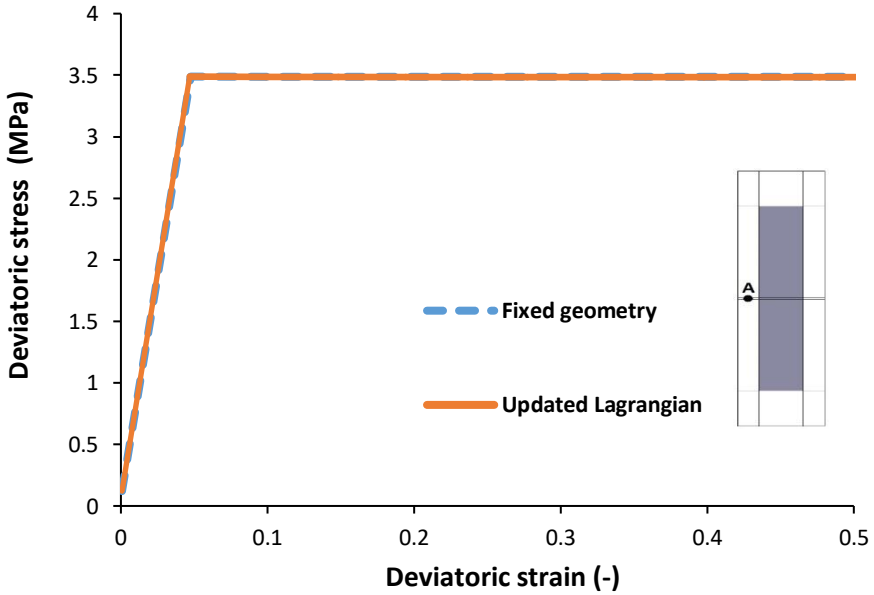

Figure 4-17 Comparison between the updated lagrangian and fixed mesh for bentonite (Point A).

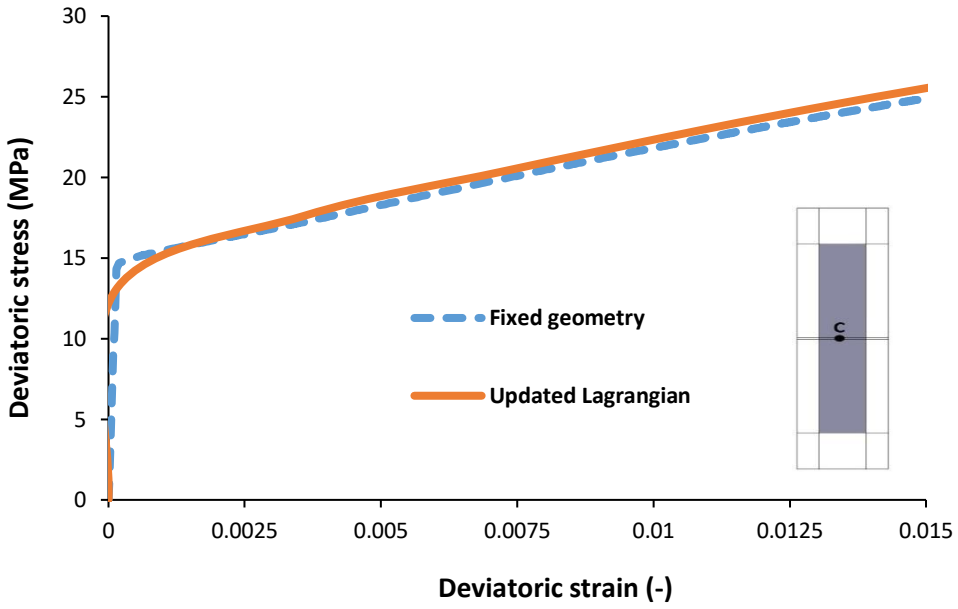

Figure 4-18 Comparison between the updated lagrangian and fixed mesh for copper (Point C).

In conclusion, at the end of the test, the difference between the fixed mesh and updated lagrangian is very small for bentonite and copper. This is because the deviatoric strains are small in large part of the mesh, so the small strains setting can be considered adequate for solving this problem due to the mesh is not suffering a significant distortion on average although there are parts of the mesh, like the shear band, which might suffer large strains. The updated lagrangian is not an objective rate but it allows to follow very well the volumetric strains if the time steps are small enough. The rotations cannot be followed as well as the volumetric strains but it should be taken into account that not all objective rates would improve the lagrangian setting. In simple shear test simulation, the Jaumann rate has a sinusoidal evolution of the stresses (Ji et al., 2013).

4.2.1.5 Sensitivity analysis of limiting plastic strain rate in Mock-up scale

According to Table 4-2, D_0 is the limiting or maximum strain rate for the copper, and the values of 10^6 s^{-1}, 10^4 s^{-1}, 10^2 s^{-1} for D_0 are considered. According to the following figures, it has no significant effect on the copper and the bentonite. The diagrams are depicted in Figure 4-19 and Figure 4-20.

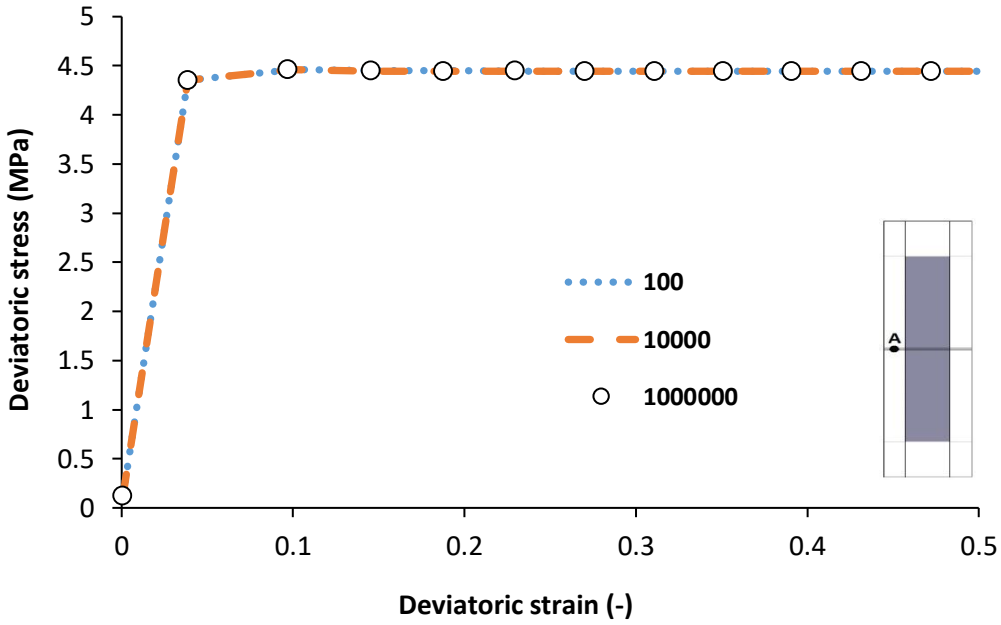

Figure 4-19 Deviator stress-strain curves for the bentonite in different D_0 (Point A).

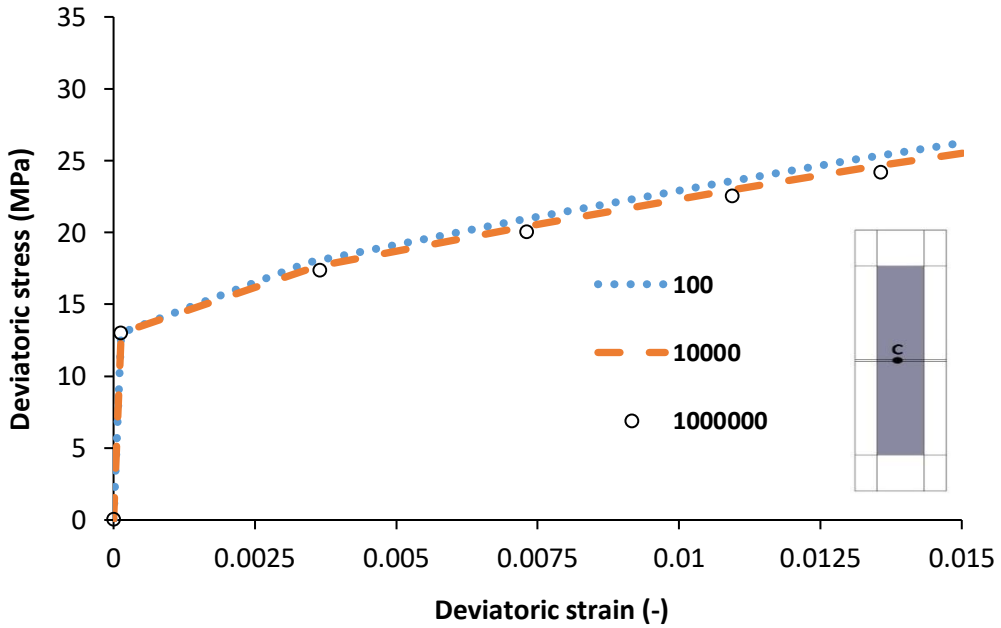

Figure 4-20 Deviator stress-strain curves for the copper in different D_0 (Point C).

4.2.2 Full-scale

The scale effect has been analyzed by comparing the results obtained in the mock-up test and a simulation performed in full-scale. In the full-scale model for shear simulation, the geometry has a height of 7.8 meters and a width of 1.75 meters, and the canister has a height of 4.8 meters and a width of 1.05 meters and it is shown in Figure 4-21. Shear thickness is 10 cm. Figure 4-22 refers to the displacement field and display vectors of the model in full-scale at the end of the test.

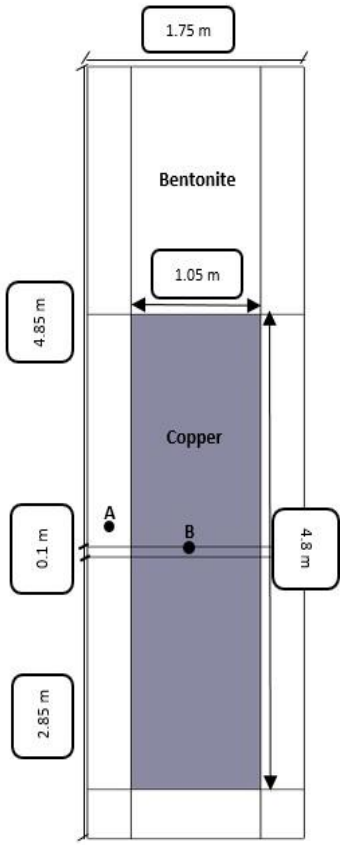

Figure 4-21 The full scale of shear testing.

It should be taken into account that the canister has been considered as a piece of copper although as it has been explained in the Introduction, has different components.

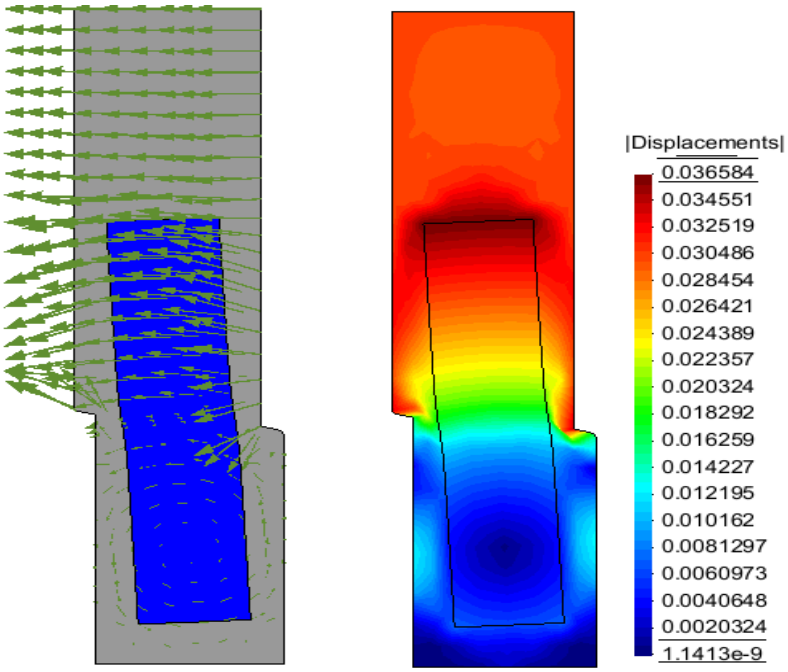

Figure 4-22 Displacement field and display vectors of the model.

4.2.2.1 Sensitivity analysis of dimension

The comparison between the full-scale model and the mock-up model was conducted for deviatoric stress-strain. For the bentonite in both models, the deviatoric stress was almost equal but in the copper, the deviatoric stress in the full-scale model was more than the mock-up model. The corresponding diagrams are shown in Figure 4-23 and Figure 4-24.

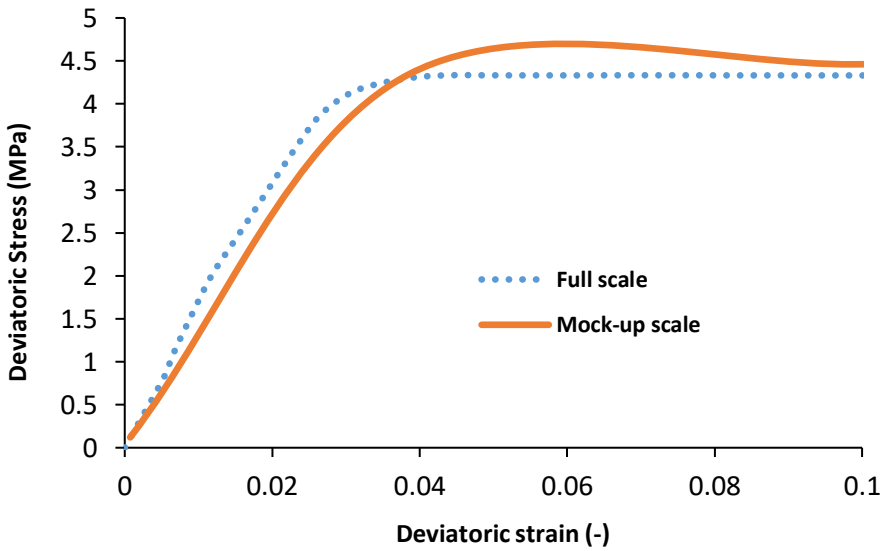

Figure 4-23 Deviator stress-strain curves in mock-up and full-scale for the bentonite (Point A).

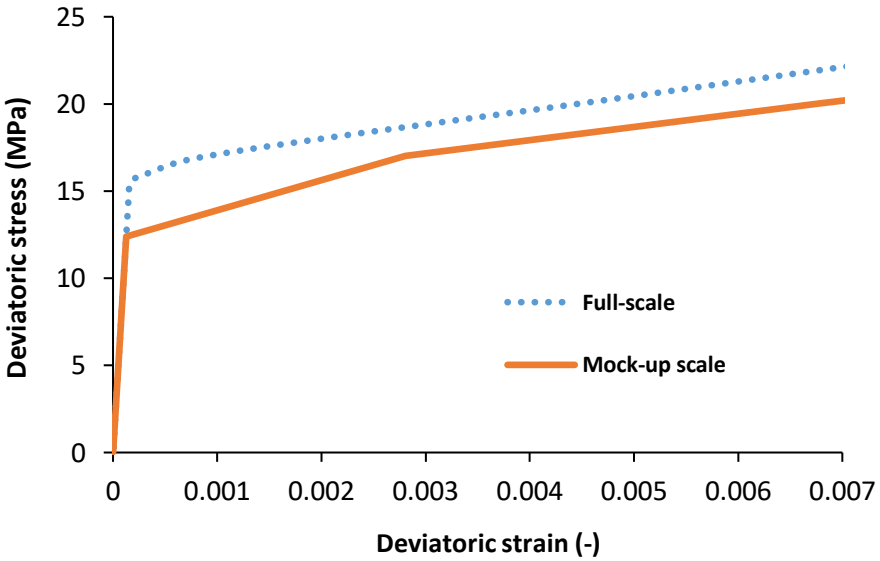

Figure 4-24 Deviator stress-strain curves in mock-up and full-scale for the copper (Point B).

4.2.2.2 Sensitivity analysis of limiting plastic strain rate in Full-scale

Sensitivity analysis of limiting plastic strain rate has been calculated in Full-scale. It is shown that deviatoric stress in different values of 10^6 $s^{-1}MPa^{-3}$, 10^4 $s^{-1}MPa^{-3}$, 10^2 $s^{-1}MPa^{-3}$ and 10^{-4} $s^{-1}MPa^{-3}$ approximately is the same for copper and bentonite. The results are presented in Figure 4-25 and Figure 4-26 for bentonite and copper, respectively.

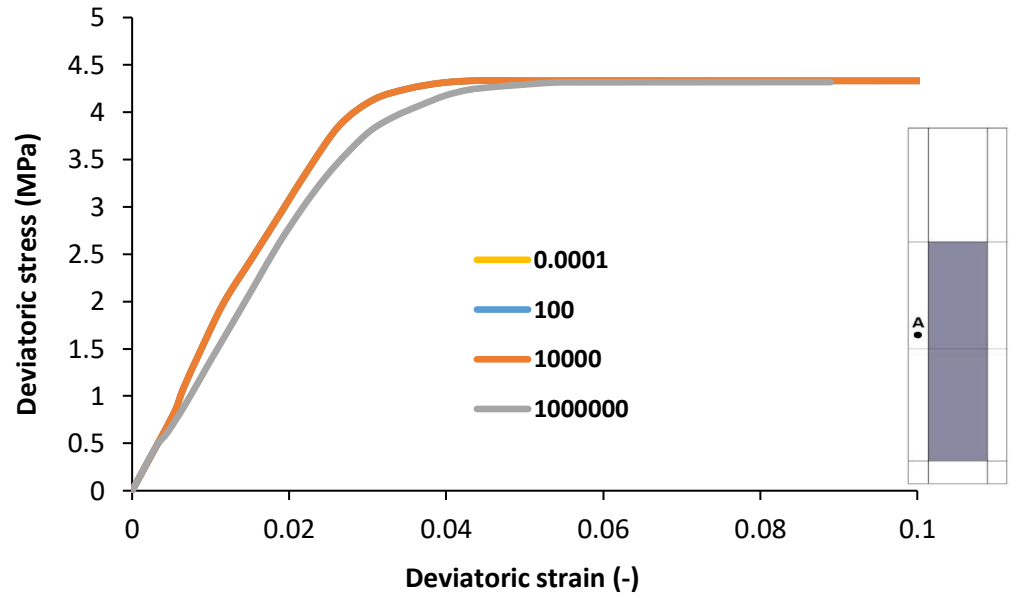

Figure 4-25 Deviator stress-strain curves for bentonite in different D_0 (Point A).

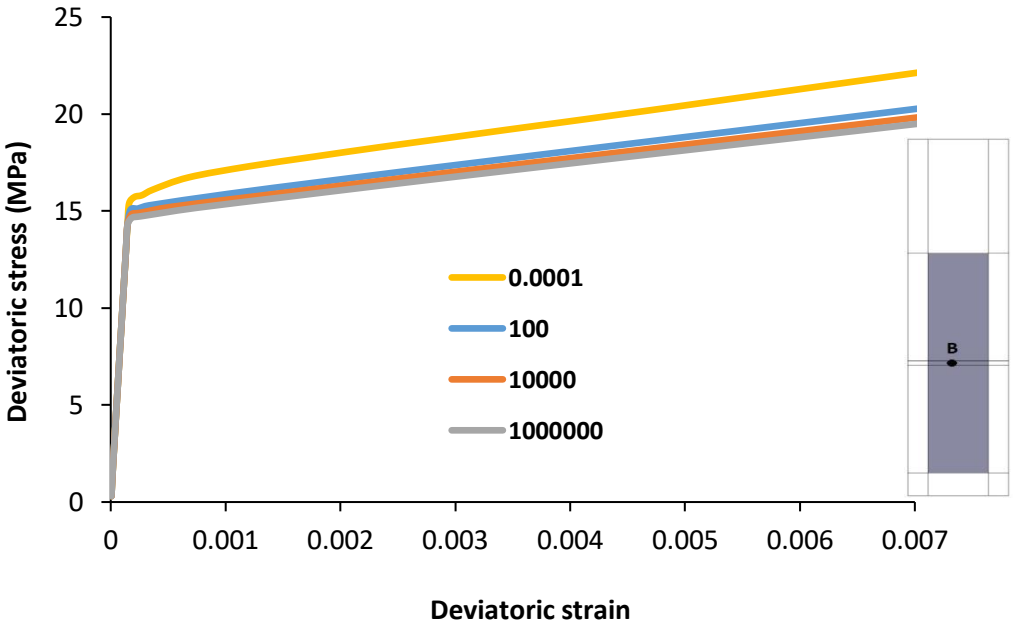

Figure 4-26 Deviator stress-strain curves for copper in different D_0 (Point B).

4.3 Shear test modeling using effective stress approach in 2D

4.3.1 Mock-up scale

The effective stress approach is presented here to study the modeling of the hydro-mechanical coupling process. It is assumed that flow in hydraulic boundary conditions is equal to zero in Figure 4-28. The initial stress is -9 MPa (compression negative) which may correspond to a realistic swelling pressure for bentonite. In spent nuclear fuel repositories, swelling stress will develop during saturation as water inflows progressively from the host rock.

Linear elastic parameters and viscoplastic model for the copper material are the same as for the total stress approach (previous section). For bentonite, Barcelona Basic Model has been employed and material parameters are referred to in Table 4-4.

In buffer design, where the saturation process and swelling pressure development are assessed, the canister is more a boundary condition than an element that should be analyzed. The canister is a source of heat, and impervious volume, and an almost rigid element without strains. This assumption can be considered exact in thermo-hydraulic analysis and almost accurate when the mechanical problem is considered because the stresses developed in the canister are still far from the yield stress of its components (copper and cast iron). In buffer shearing due to an earthquake or a relative movement between the lips of a fracture crossing a deposition hole, there could be possible to reach yield stresses in the canister, so this element should be considered as accurate as possible in order to have realistic movements on its surface that could influence the stress state of the buffer.

In effective stress, the dimensions (Figure 4-27) and boundary conditions of the shear test are similar to the dimensions and boundary conditions in the shear test in total stress. The MX-80 bentonite clay is fully saturated. The degree of saturation is directly related to water content and dry density. The porosity is related directly to the dry density and the porosity considered for non-porous materials is 0.01. In all lines of boundaries (two dimensional), hydrostatic water pressure is applied.

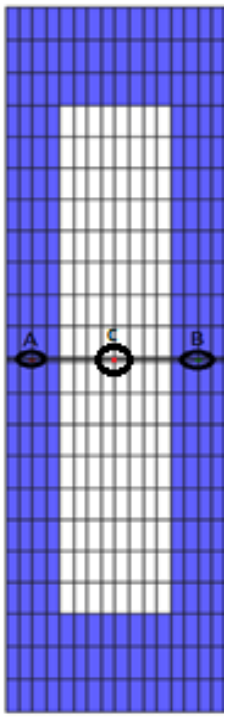

Figure 4-27 Canister-clay shear test using effective stress approach.

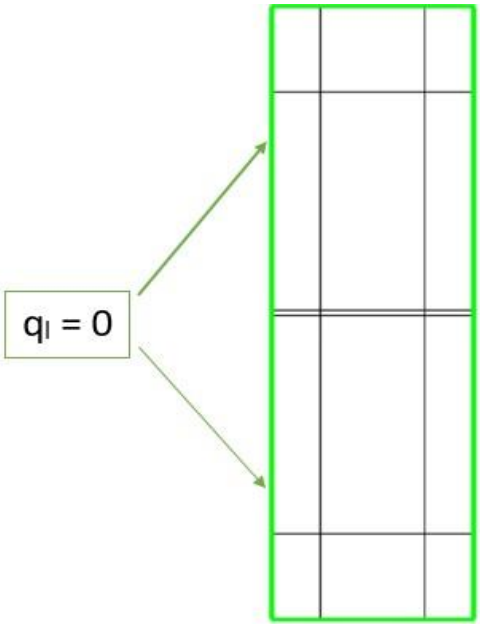

Figure 4-28 Flux boundary condition.

In an effective stress approach, BBM model (Alonso et al., 1990) is used for the bentonite and it is shown in Table 4-4. The model is saturated and has drained conditions.

Table 4-4 Input parameters of the bentonite in effective stress approach (Toprak et al., 2017).

BBM MODEL FOR BENTONITE		
ν (-)	0.3	Poisson's Ratio
K_{min} (MPa)	10	Minimum bulk modulus
κ_{i0} (-)	0.09	The initial (zero suction) elastic slope for specific volume-mean stress
$\lambda(0)$ (-)	0.15	The slope of void ratio-mean stress curve at zero suction
r (-)	0.8	Parameter defining the maximum soil stiffness
β (MPa)$^{-1}$	0.02	Parameter controlling the rate of increase of soil stiffness with suction
p_c (MPa)	0.1	Reference pressure
p_0^* (MPa)	10	Initial preconsolidation mean stress for saturated soil
M (-)	1.07	Critical state line parameter

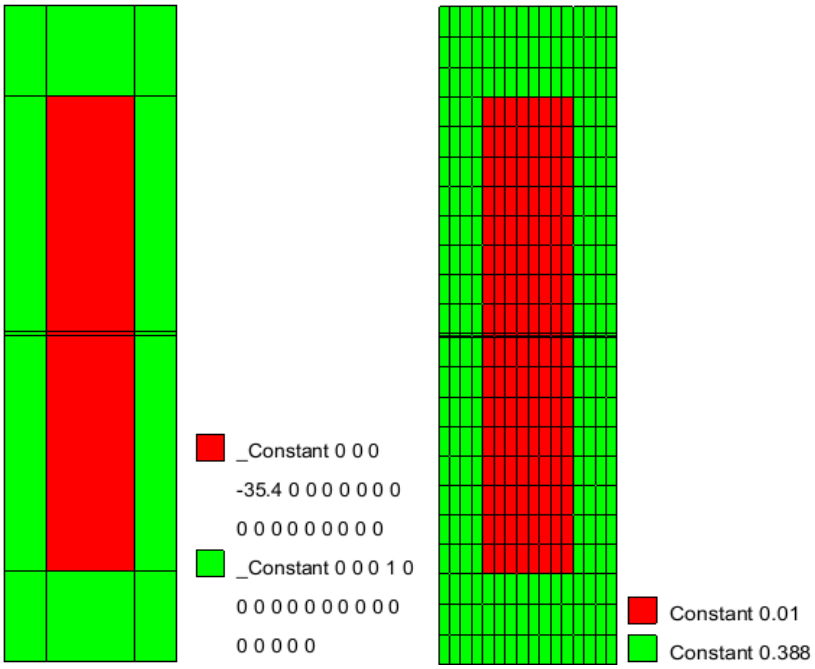

Figure 4-29 The liquid pressure (P_l) in initial unknown (left) initial Porosity (right).

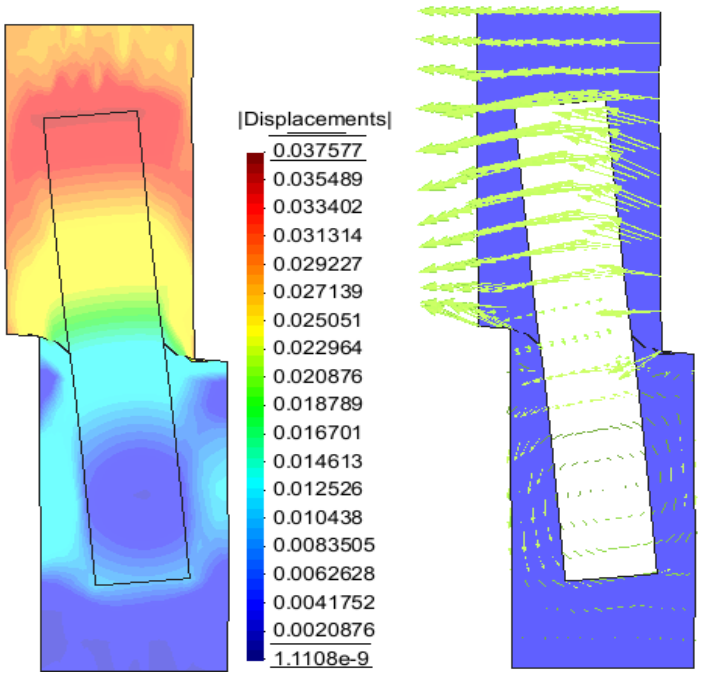

Figure 4-30 Deformation and display vector of canister-clay in hydro-mechanical modeling.

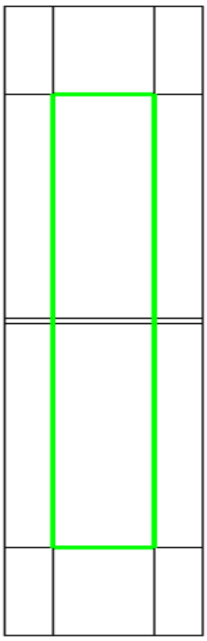

Figure 4-31 Interface of canister-clay with green color.

The liquid pressure for copper is equal to -35.4 MPa and this is due to the fact that liquid pressure could not enter the canister and liquid pressure for bentonite is equal to 1 MPa. On the other hand, the liquid pressure of the canister-clay interface is 1 MPa because the water is in out of the copper, and the copper is under the liquid pressure of the bentonite. The interface is shown in Figure 4-31.

The undrained shear strength for BBM model is calculated in the following equation:

$$C_u = P^{?} \cdot \frac{M}{2} \left(\frac{P_0^*}{2P^{?}}\right)^{\frac{\lambda-k}{\lambda}} \quad (4.3\text{-}1)$$

$$C_u = 8 * \frac{1.07}{2} * \left(\frac{10}{2*7}\right)^{\frac{0.15-0.05}{0.15}} = 3\ MPa$$

$$P^{?} = 9 - 1 = 8\ MPa$$

4.3.1.1 Effect of critical state line strength parameter

The parameter M represents the strength of the soils in the BBM. It is the slope of the critical state line (CSL) in the deviatoric stress vs mean stress diagram. For the sensitivity, the M value equal to 1.07, that was used in Toprak (Toprak et al., 2017) and the M value of 0.369, that was calculated from tests carried out by Börgesson (Börgesson et al., 1995) and Dueck (Dueck et al., 2010), are considered. Deviatoric stress-strain curves for the two values of strength considered are shown in Figure 4-32 (for bentonite) and Figure 4-33 (for copper).

In this sensitivity, permeability has been considered constant with a value of 3.67×10^{-21} m^2 (Pintado et al., 2016) for bentonite.

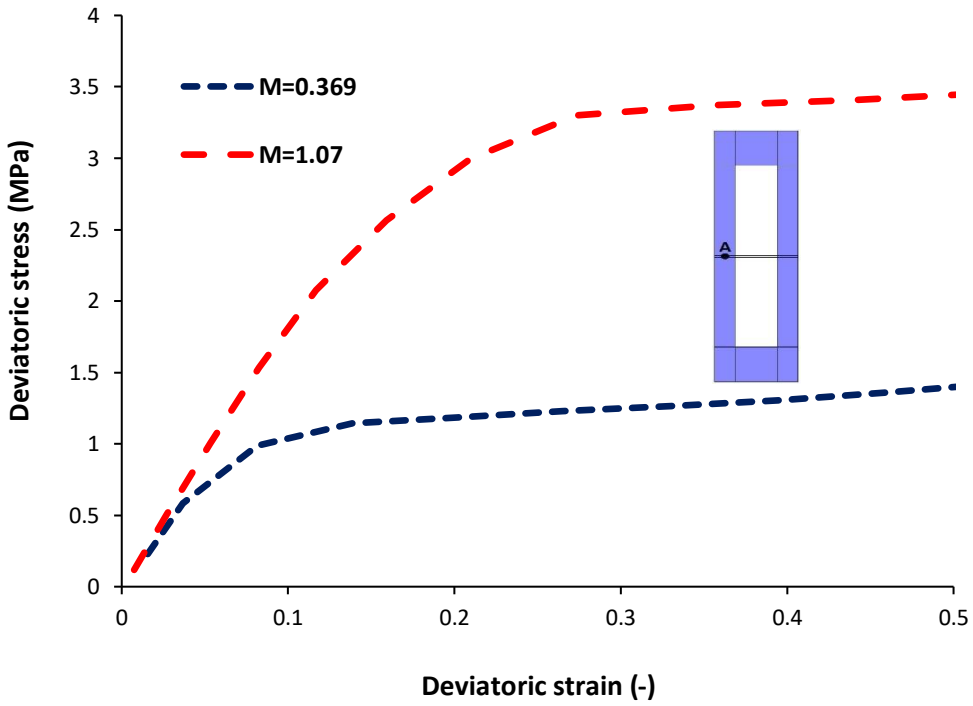

Figure 4-32 Sensitivity analysis to the slope of the critical state line for bentonite (Point A).

The decrease of M value causes a reduction in the stress development in bentonite and copper. This is shown in Figure 4-32 and Figure 4-33, at the beginning there is an elastic loading, then the hardening is reached. For lower clay strength, the deformation of the copper is lower because the clay permits more movement (solid rigid) of the canister.

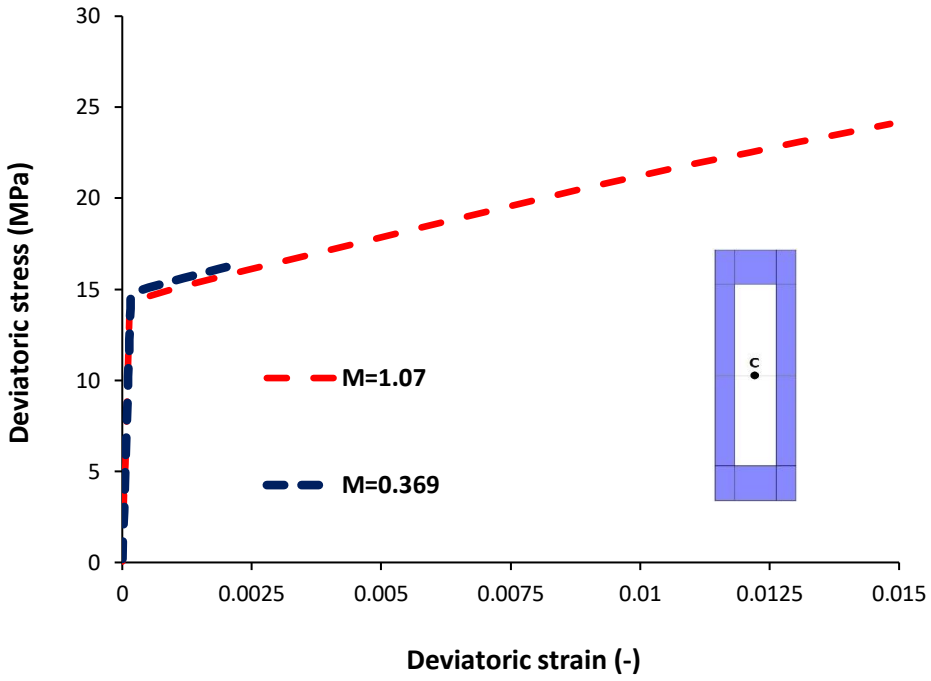

Figure 4-33 Sensitivity analysis to the slope of the critical state line for copper. Copper suffers less deformation (M =0.369) when the clay is softer. The reason is that the canister can rotate more when the clay is softer (Point C).

4.3.1.2 Sensitivity analysis of mesh

Sensitivity analysis of mesh in three types of rough, medium, and fine meshes for permeability of 3.67×10^{-20} m^2 was performed. The fine mesh has 672 elements and 731 nodes, the medium mesh has 384 elements and 425 nodes and the rough mesh has 224 elements and 225 nodes.

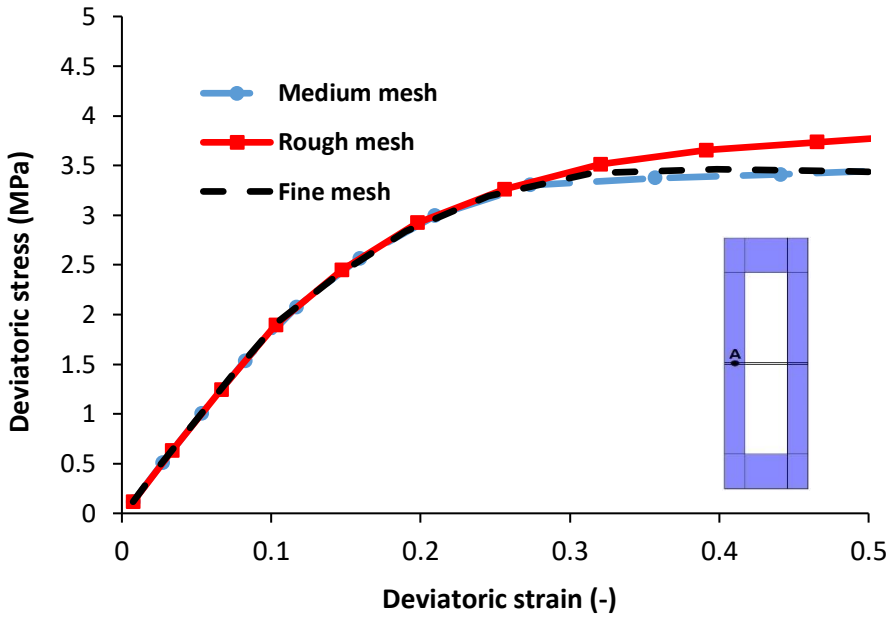

Figure 4-34 Comparison between rough, medium, and fine meshes for bentonite in effective stress approach (Point A).

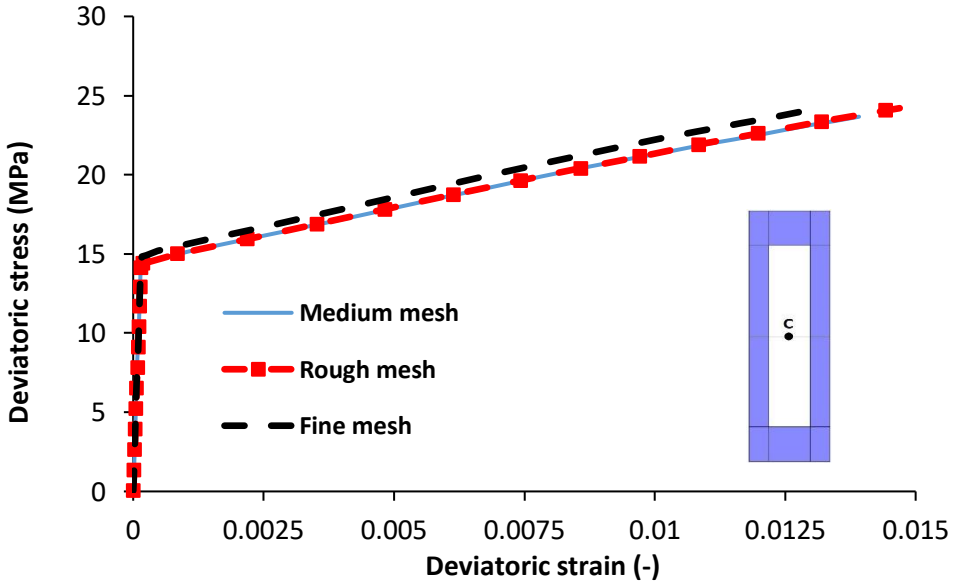

Figure 4-35 Comparison between rough, medium, and fine meshes for copper in effective stress approach (Point C).

Point A is chosen from Figure 4-27 and according to Figure 4-34, the deviatoric stress in the rough mesh is bigger than the deviatoric stress in medium and fine mesh for bentonite. Finally, point C is selected in Figure 4-27 for copper, and then it is shown in Figure 4-35 in which deviatoric stress in rough and medium meshes is the same but the deviatoric stress in the fine mesh is bigger than the other meshes. The results do not depend on the mesh in medium and fine mesh, so the non-mesh dependency is guaranteed.

4.3.1.3 Sensitivity analysis of permeability

It has been discussed that permeability of the bentonite plays a major role in the response of the system concerning internal volumetric deformations and water movement. A sensitivity analysis of the permeability in the medium mesh has been carried out. To check this sensitivity, the permeabilities of 3.67×10^{-18} m^2, 3.67×10^{-21} m^2 and 3.67×10^{-22} m^2 have been considered. The value of 3.67×10^{-21} m^2 can be calculated from the relation between the permeability and porosity presented in Pintado (Pintado et al., 2016). The saturated density in the mock-up test was around 2050 kg/m^3 (Börgesson, 1986), which is equivalent to a porosity of 0.41 assuming a solid's density of 2780 kg/m^3 (Kiviranta & Kumpulainen, 2011). The calculation has been carried out assuming an air entry value high enough for avoiding desaturation, so it is not necessary to consider neither a water retention curve nor the relative permeability. These values can be considered to produce conditions close to the undrained failure conditions. The value of deviatoric stress and preconsolidation stress in two points A and B (Figure 4-36) are approximately equal, as shown in Figure 4-37 and Figure 4-38.

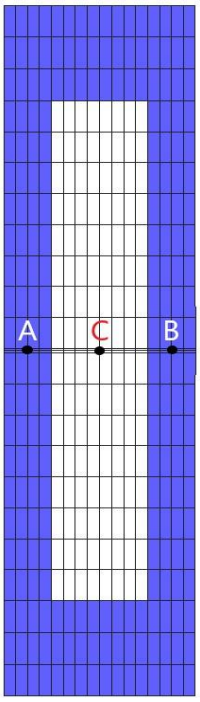

Figure 4-36 Points that are considered for comparison of results for the sensitivity analysis to permeability. The number of elements and nodes is 384 and 425, respectively.

In the deviatoric stress-deviatoric strain curves shown in Figure 4-37, deviatoric stress for the case of permeability equal to 3.67×10^{-18} m^2 is higher than deviatoric stresses for the cases of permeabilities 3.67×10^{-21} m^2 and 3.67×10^{-22} m^2. Results for permeabilities 3.67×10^{-21} m^2 and 3.67×10^{-22} m^2 are equal.

An indication of plastic volumetric deformations (linked with internal water movement) is the preconsolidation stress (it is a history variable of the BBM equations). The variation of preconsolidation stress is represented in Figure 4-38.

The preconsolidation stress for the case with the permeability of 3.67×10^{-18} m^2 increases, which means that the clay is compressed during shearing. This is due to the coupled process of deformation, plastification produces shear and contraction.

Preconsolidation stress does not change when for the cases with the permeability of 3.67×10^{-21} m^2 and 3.67×10^{-22} m^2 indicating that volumetric plastic deformations do not occur.

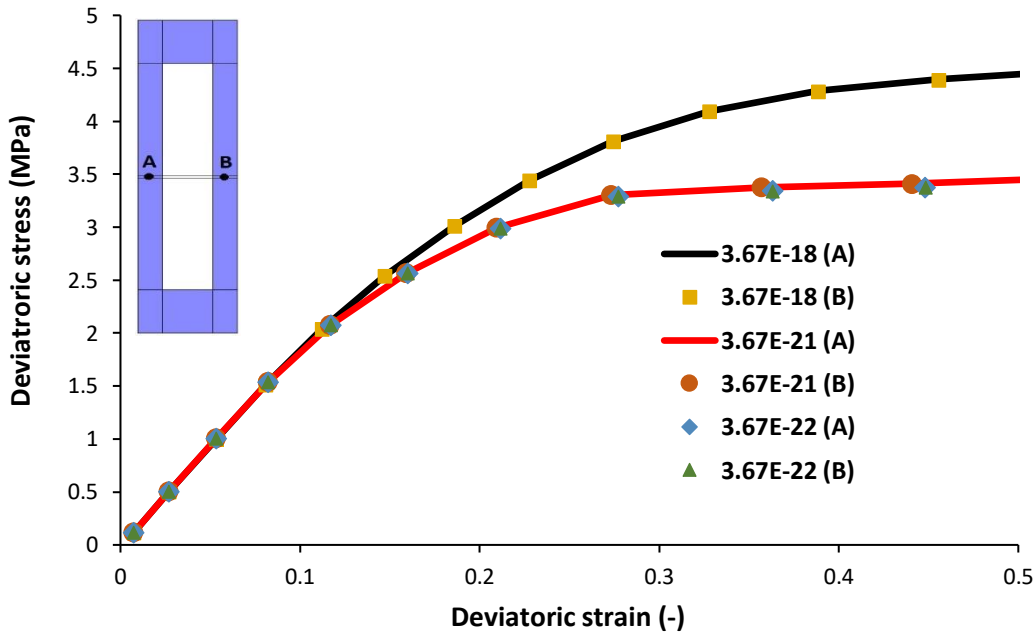

Figure 4-37 Deviator stress-strain curves for all permeabilities.

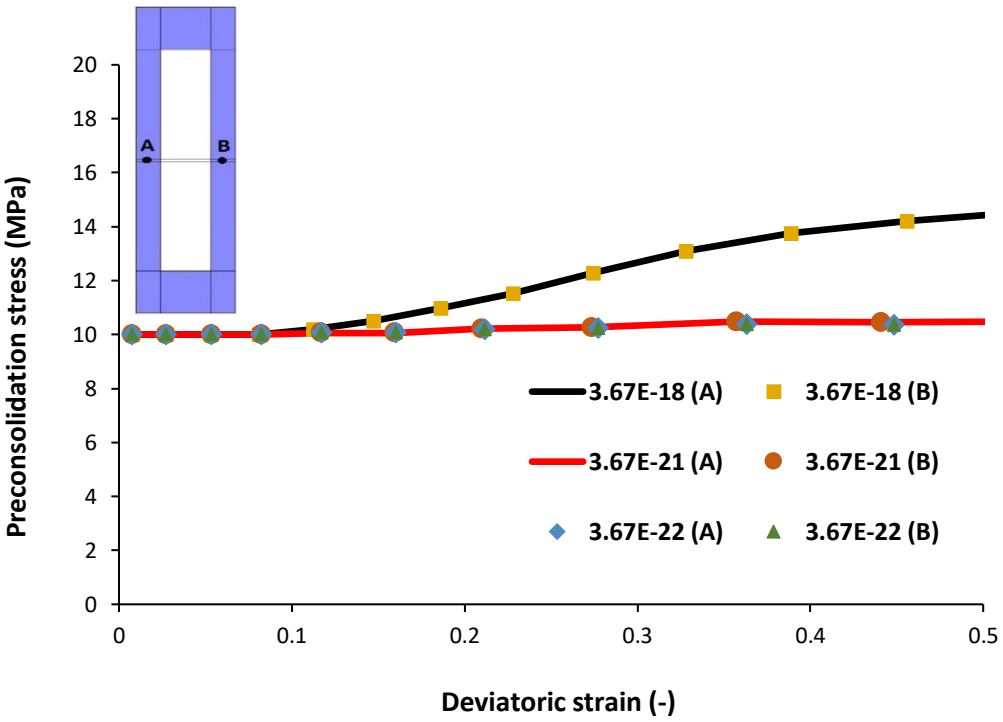

Figure 4-38 Preconsolidation stress-deviatoric strain curves for all permeabilities.

4.3.2 Full-scale

4.3.2.1 Sensitivity analysis of dimension

The comparison between the mock-up and full-scale models was made for the deviator stress-strain. For bentonite and copper in both models, the deviatoric stress is almost equal. The corresponding diagrams are depicted in Figure 4-39 and Figure 4-40.

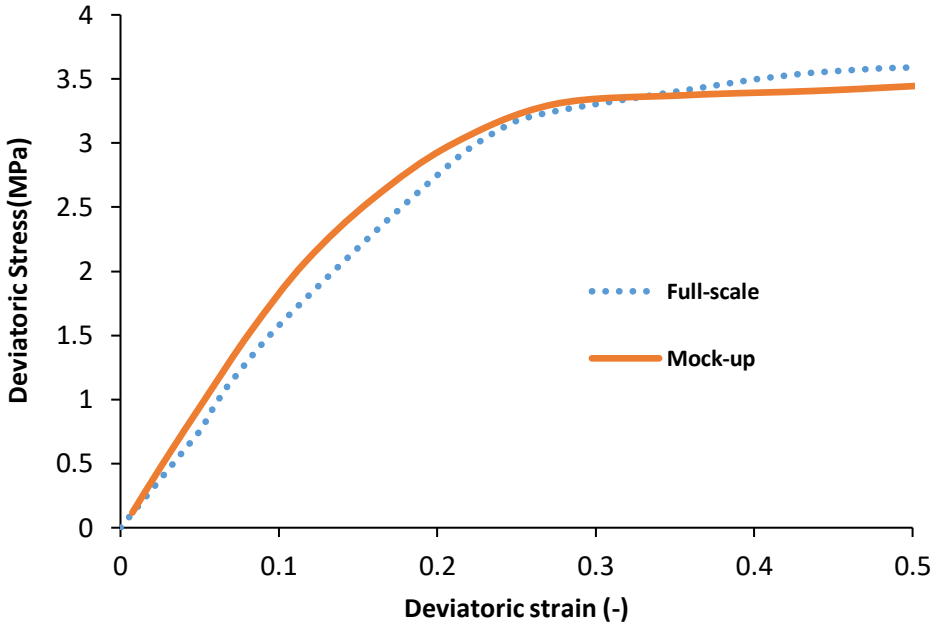

Figure 4-39 Deviator stress-strain curves in full-scale and mock-up for bentonite (Point A).

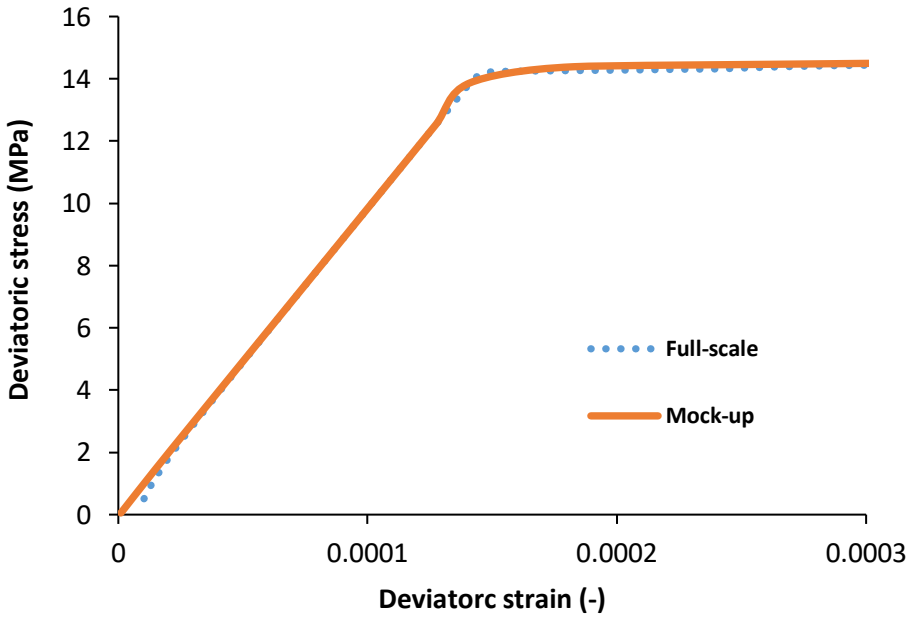

Figure 4-40 Deviator stress-strain curves in full-scale and mock-up for copper (Point B).

4.3.3 Comparison between the total stress approach and the effective stress approach

In this section, a comparison between the total stress method (undrained condition) and the effective stress method has been investigated in a mock-up scale. Total stress analysis corresponds to impermeable bentonite. The total stress is the limit case of the effective stress analysis when permeability tends to zero or is very low. Two cases with permeabilities of 3.67×10^{-21} m^2 and 3.67×10^{-22} m^2 for bentonite in effective stress analysis are considered.

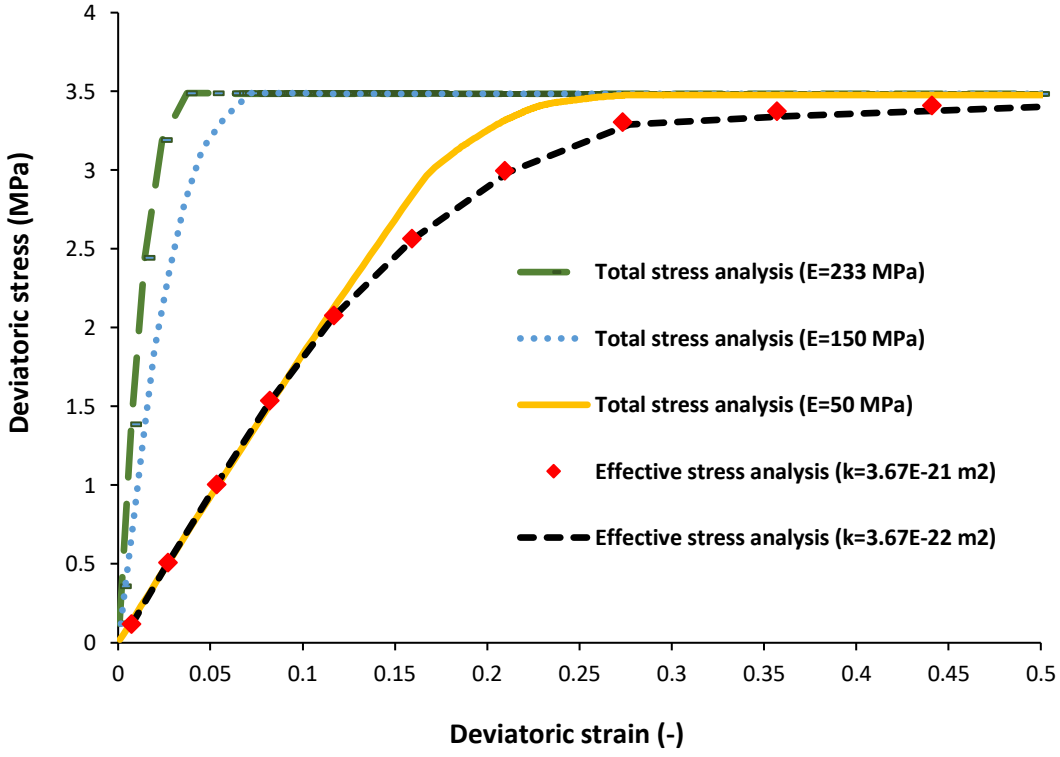

Figure 4-41 Deviatoric stress- deviatoric strain curves for bentonite (Point A)**.**

Regarding point A in Figure 4-36 for bentonite, the deviatoric stress in undrained condition until the deviatoric strain equals 0.3 is more than the deviatoric stress in the drained condition (permeabilities of 3.67×10^{-21} m^2 and 3.67×10^{-22} m^2) but after that, the results of both methods are close together (Figure 4-41).

The elastic part in Figure 4-41 is different because the total stress approach and effective stress approach do not share the same elastic parameters. In the total stress approach, linear elasticity with incompressibility has been used. While for an effective stress approach, elasticity with non-linear stiffness has been considered. Both methods display the same strength at end of the test as the undrained shear strength for the total stress analysis has

been calculated consistently using the clay strength parameters for the effective stress analysis (see Appendix).

However, the model for total stress calculated with elastic properties in Table 4-1 displays a very stiff response. In order to improve the correspondence between the two approaches, total stress analysis with lower undrained stiffness is used (elastic modulus of bentonite is 50 MPa (fitted) and 150 MPa (which corresponds to a shear rate of 10^{-6} s^{-1} and a saturated density of 2020 kg/m^3, the minimum value presented in Börgesson and Hernelind, 2010) instead of the value of 233 MPa given in Table 4-1). This stiffness reduction permits adjusting the response during the initial part of the loading.

Also, the copper in the shear test is verified and the deviatoric stress in total stress is the same as the deviatoric stress in effective stress and according to point C in Figure 4-36. Results are depicted in Figure 4-42.

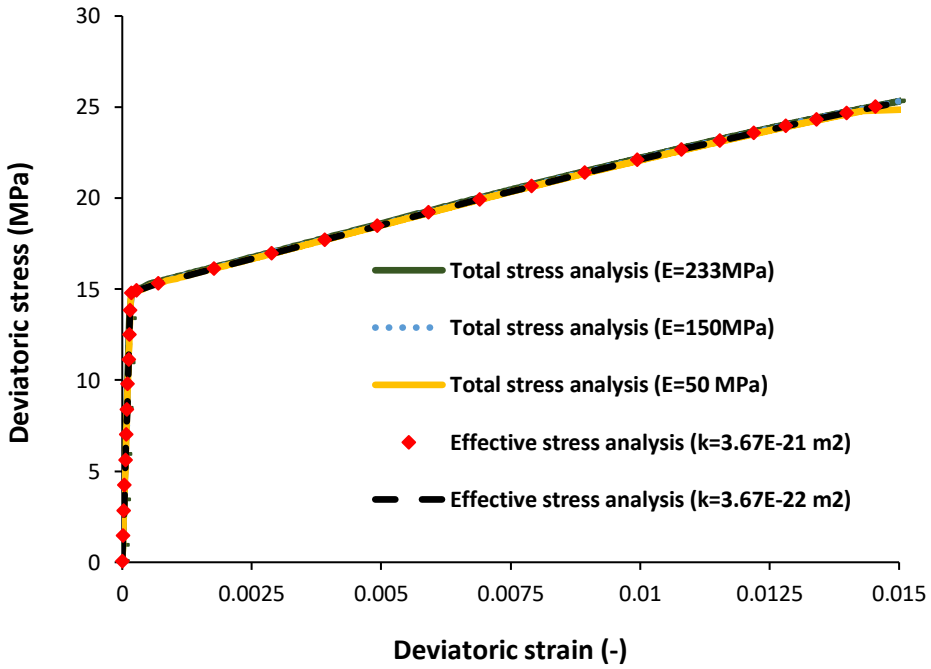

Figure 4-42 Deviatoric stress- deviatoric strain curves for copper (Point C).

4.4 Model development and validation

The scope is to validate models implemented in CODE_BRIGHT with the copper-clay shear test results. To do this, the results of the numerical model using CODE_BRIGHT in the coupled hydro-mechanical analysis were compared to the results of the copper-clay shear test with different horizontal displacement rates simulating horizontal rock shearing through a deposition hole in the center of the canister.

The slow test (Test 1) was simulated at first. This test was utilized for carrying out the complete test modeling, performing the simulation of the three-month saturation process, and shearing process of around 15 minutes. The findings were relative to the calculated results by Börgesson, 1986, providing useful knowledge about the material models and modeling technique's relevance. The assumed initial effective stresses were null and the initial porosity for bentonite was 0.41, equivalent to a dry density of 1640 kg/m^3. The initial degree of saturation considered was 36%.

The geometry of the copper element is a cylinder with a radius of 40 mm and a height of 450 mm that is surrounded by clay and has a radius of 79 mm and a height of 642 mm (Figure 4-43). It is necessary to say that the shear test was made at room temperature.

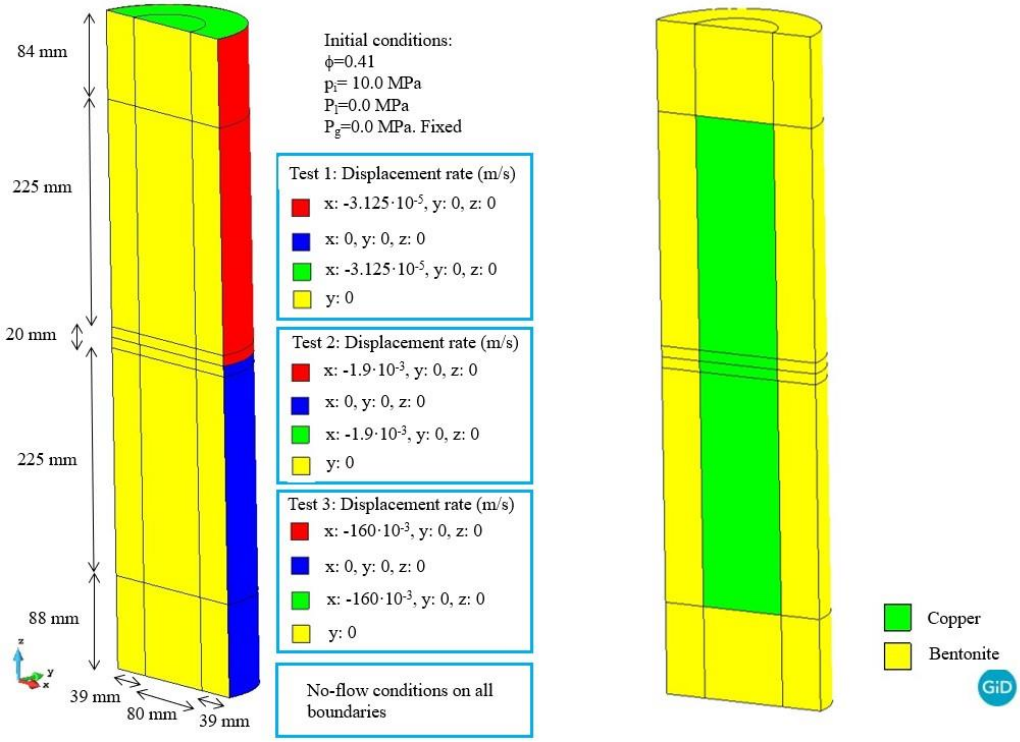

Figure 4-43 Geometry, initial conditions and boundary conditions (left) and materials (right).

The saturation process period considered was 90 days (as in Börgesson, 1986) with a liquid pressure of 0.1 MPa on the boundary, equivalent to saturation conditions of the filter. Gas pressure was considered constant and equal to 0.1 MPa (atmospheric pressure). Modeling was performed by solving the momentum and water mass balance equations.

For bentonite and copper, an elastic-viscoplastic material model was used, with stress-strain relationships obtained from laboratory experiments. Since the shear is fast, the density did not change too much during the experiments due to the low permeability. The predicted canister stresses and strains are used to evaluate plastic and creep deformation against copper shell failure criteria. The hydraulic parameters of MX-80 bentonite were calibrated from these tests and are listed in Table 4-5.

Table 4-5 Hydraulic parameter for bentonite (Pintado et al., 2016).

Equation	Parameter	MX-80 bentonite	
Van Genuchten retention curve	P_0 (MPa)	27	About the air entry value.
	λ (-)	0.45	Shape function for retention curve.
	a (-)	11	Parameter for porosity influence on retention curve.
	b (-)	4	Parameter for porosity influence on retention curve.
	ϕ_0 (-)	0.4245	Reference porosity for porosity influence on retention curve.
Advective flux (Darcy)	k (m^2)	5.59×10^{-21}	Intrinsic permeability
	ϕ_0 (-)	0.438	Reference porosity for reading intrinsic permeability.
	ϕ_{min} (-)	0.1	Minimum porosity
	b (-)	15	Parameter

The constitutive model for bentonite use a linear elastic part and an inelastic part that is viscoplastic for saturated and unsaturated soil based on Desai and Perzyna theory (Desai et al., 1987; Perzyna, 1966) (elliptical yield surface corresponding to modified Cam-Clay model) and the parameters' values are depicted in Table 4-6.

Table 4-6 Input parameters of the bentonite (Börgesson & Hernelind, 2010; Börgesson et al., 1995; A. Gens et al., 2009; Toprak et al., 2017).

Linear elasticity	ν		0.3	Poisson's Ratio
	E	MPa	233	Young modulus
Viscoplasticity model	Γ_0	s^{-1}	10^{-3}	1/"Viscosity"
	n	-	3	Power of stress function
	b	-	1	Non-associativity parameter
	λ(0)- κ	-	0.25-0.09 = 0.16	Viscoplastic compression parameter
	M	-	0.36[1)]	A critical state line parameter
	p_{s0}	MPa	0.115[2)]	Tensile strength in saturated conditions
	k	-	0.1[3)]	The parameter that takes into account the increase of tensile strength due to suction
	p_0^*	MPa	10	Preconsolidation stress

1) Börgesson et al. (1995) obtained ϕ'=9.9°. $M = \frac{6sin\phi'}{3-sin\phi'} = 0.36$

2) Börgesson et al. (1995) obtained c'=0.56 MPa. $p_{s0} = \frac{Mc'}{tan\phi'} = 0.115\ kPa$

3) Gens et al., (2009) for FEBEX bentonite.

A linear elasticity model and Bodner-Partom Viscoplasticity (Bodner & Merzer, 1978; Bodner & Partom, 1975; Khadivipanah et al., 2020) for copper have been considered and the parameters are referred to in Table 4-7.

Table 4-7 Input parameters of the copper.

Linear Elasticity	v		0.33[1]	Poisson's Ratio
	E	MPa	120000[1]	Young modulus
Bodner-Partom Viscoplasticity	D_0	s^{-1}	10^4[2,3]	Limiting strain rate
	Z_0	MPa	55[2] (31[3])	Initial value of the internal state variable
	Z_1	MPa	237[2,3]	Saturated value of the internal state variable
	m_0	$(MPa)^{-1}$	0.061[2] (0.15[3])	Initial value of hardening parameter
	m_1	$(MPa)^{-1}$	0.145[2] (0.25[3])	Saturated value of hardening parameter
	α	$(MPa)^{-1}$	0.26[2] (0.5[3])	A material constant

(1) Börgesson and Hernelind, 2010
(2) Calibrated from test (Börgesson and Hernelind, 2010)
(3) Reference model parameters (Bodner & Partom, 1975)

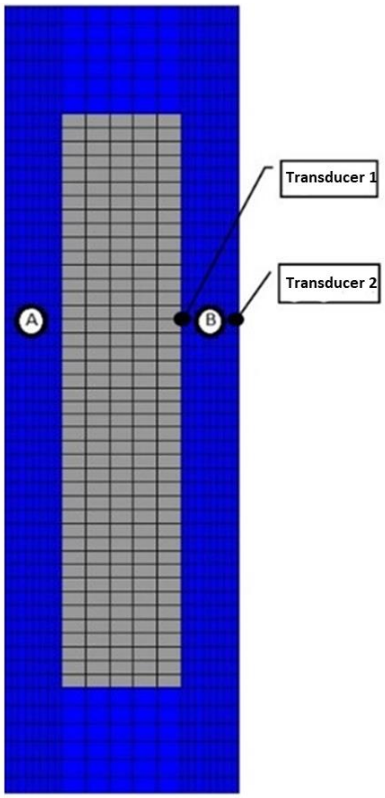

Figure 4-44 The location of pressure transducers (transducers 6 and 9 in Börgesson, 1986) and points A and B in the canister-clay system.

According to Figure 4-44, Points A and B have been chosen for the analysis of the model. The mesh is composed of 3410 nodes and 2592 elements. The element chosen was linear quadrilateral prism with selective numerical integration (8 points) by means of the modification of matrix **B.** Note that all elements are continuous elements, without using contact elements. The elements in the shear zone are smaller.

Figure 4-45 depicts the change in suction as a function of mean effective stress. Changes in suction from a high value of 90 MPa, representing the initial conditions, where the degree of saturation was 36% at a dry density of 1640 kg/m^3, to null suction, representing fully saturated conditions. At mean effective stress of 10 MPa, the path achieves the LC (Loading-Collapse curve), and in the fully saturated situation and shearing phase, the mean effective stress is reduced.

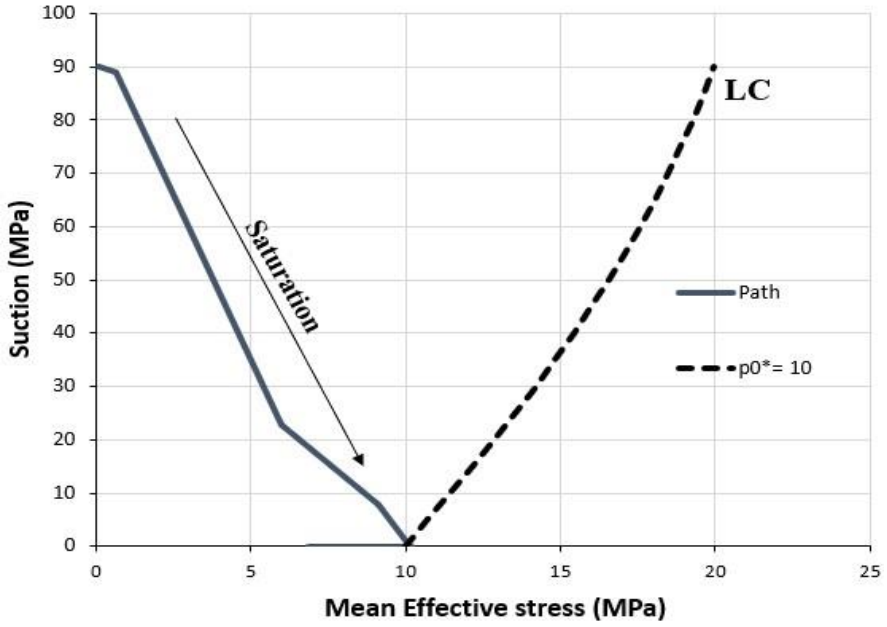

Figure 4-45 Suction path with respect to the mean effective stress in the canister-clay system.

As indicated above, before shearing, the bentonite was saturated with distilled water through the surrounding filters using low water pressure and allowed to soak for three months. The swelling pressure was continuously measured. For model validation, three months was thought to be sufficient time to achieve the steady-state conditions in swelling pressure according to results in Börgesson (1986). The comparison between the swelling pressure calculated in numerical modeling by CODE_BRIGHT and measured in the experiment is shown in Figure 4-46. Despite the difficulty of the models and the complexities in calculating stresses and strains during the saturation phase, the findings indicate an

agreement between modeled and tested results. Before one month, there is a tiny discrepancy in swelling pressure between the simulation and the experiment due to the value of the hydraulic conductivity, which seems to be overestimated in the model, but after that, the calculated swelling pressure is very close to the measured value.

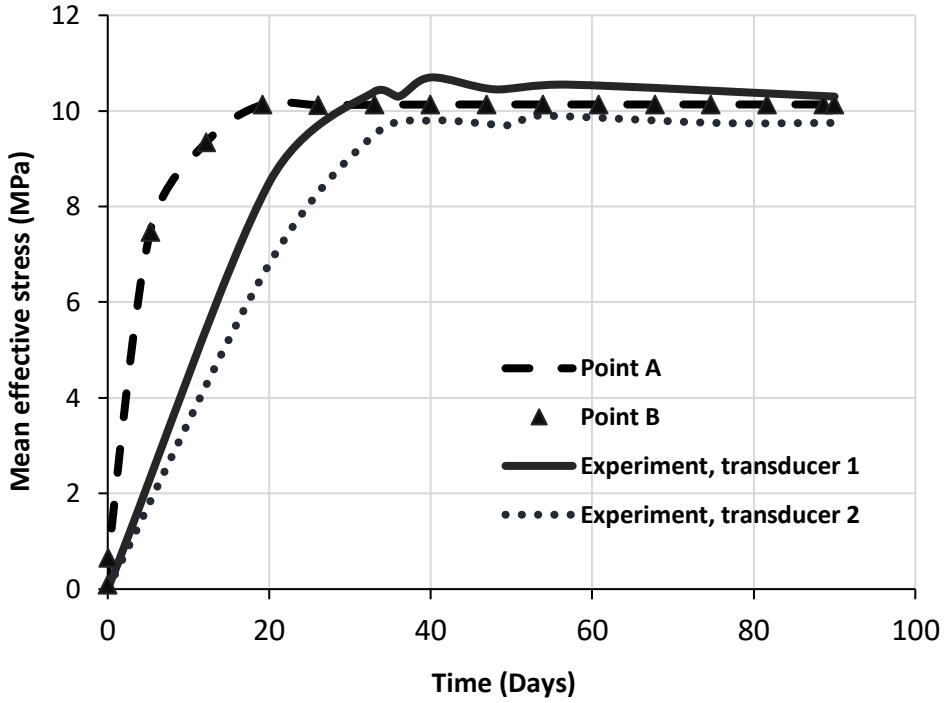

Figure 4-46 Mean effective stress-time curves from the beginning of the saturation phase of Test 1 until the end of the saturation phase (three months) in numerical modeling and experimental test.

Figure 4-47 depicts the stress path for locations A and B (Figure 4-44). The saturation phase occurs from the mean effective stress of zero to 10 MPa. Some deviatoric stresses develop in this phase but they vanish as full saturation is achieved, indicating that this process leads to a final state quite isotropic.

The shearing phase begins at mean effective stress of about 10 MPa. Under shearing conditions, the stress path reaches the critical state line (failure envelope), and the Cam-Clay ellipse follows the stress path during the shearing phase and illustrates the intersection point between the stress path and the failure envelope.

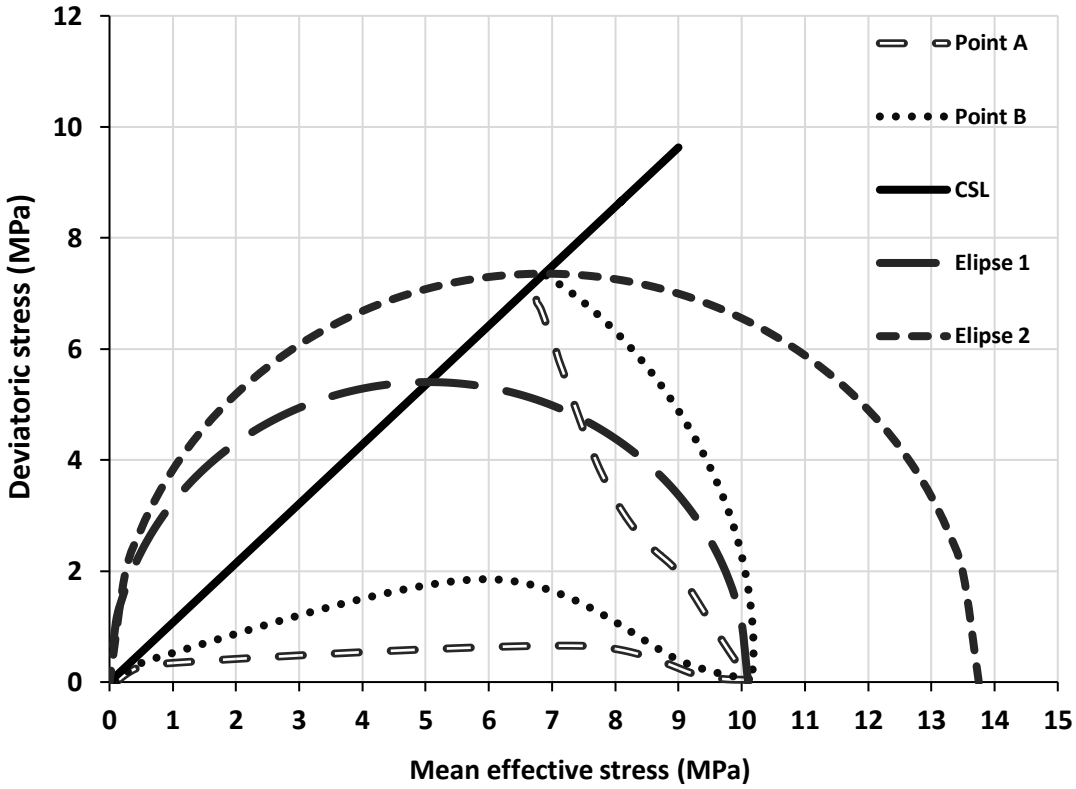

Figure 4-47 Stress path in points A and B in deviatoric stress-mean effective stress curves.

According to Figure 4-48, the radial stress in bentonite was measured in three spots on the surface of the copper canister and three points on the surface of the steel tube (rock). Two different properties of copper were considered for the simulated shear tests in CODE_BRIGHT at small strains conditions. The reference model uses the parameters from Bodner-Partom, 1975 and the calibrated model (calibrated refers only to copper parameters), the properties of the copper obtained from the test presented in Börgesson and Hernelind, 2010. The sensitivity analysis of calculated (Reference model and calibrated model) and measured radial stresses in Test 1 are shown in Figure 4-49 and according to the calculations, the transducers 7 and 9 do not differ significantly and they roughly coincide with the corresponding measurements in Test 1.

It should be noted, as Börgesson (1986) stated, that these measurements are difficult to make since the bentonite is highly stiff and is not permitted to swell during the rapid shear and valve formations at the transducer's contact point are possible. So according to difficulties involved with this sort of measurement, it's remarkable that the agreement between measured and modelled stresses is so good.

As it is shown in Figure 4-48, the strain gauges were glued axially to the canister surface. The calculated and measured strain in the canister surface as a function of shear displacement is

shown in Figure 4-50. According to the measurements and calculations, the only transducers that appear to operate properly are numbers 16, 17, and 18.

When graphing the strain in the copper bar surface vs. total shear displacement using strain gauges 16, 17, and 18, we can observe that the form and amplitude of the curves correspond extremely well between modeled and measured conclusions.

The displacement of the simulated canister in relation to the simulated rock was measured in 4 cm from the canister's end. Figure 4-51 depicts a comparison between calculated and measured relative displacement for this test.

Despite being 5 mm apart, the modeled and measured curves correspond quite well. The inclination and the form of the curve (straight line) are almost similar. The observed tilting (relative displacement) does not begin until after 5 mm shear displacement, but the modeling results show that the tilting begins immediately.

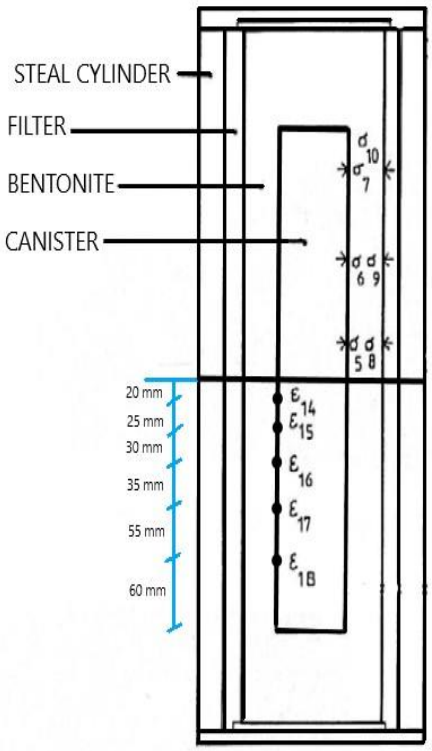

Figure 4-48 Location and numbering of the strain gauges glued to the canister surface (ε_{14}-ε_{18}) and pressure transducers (σ_7-σ_{10}) (located 3, 11, and 19 cm from top of the copper canister).

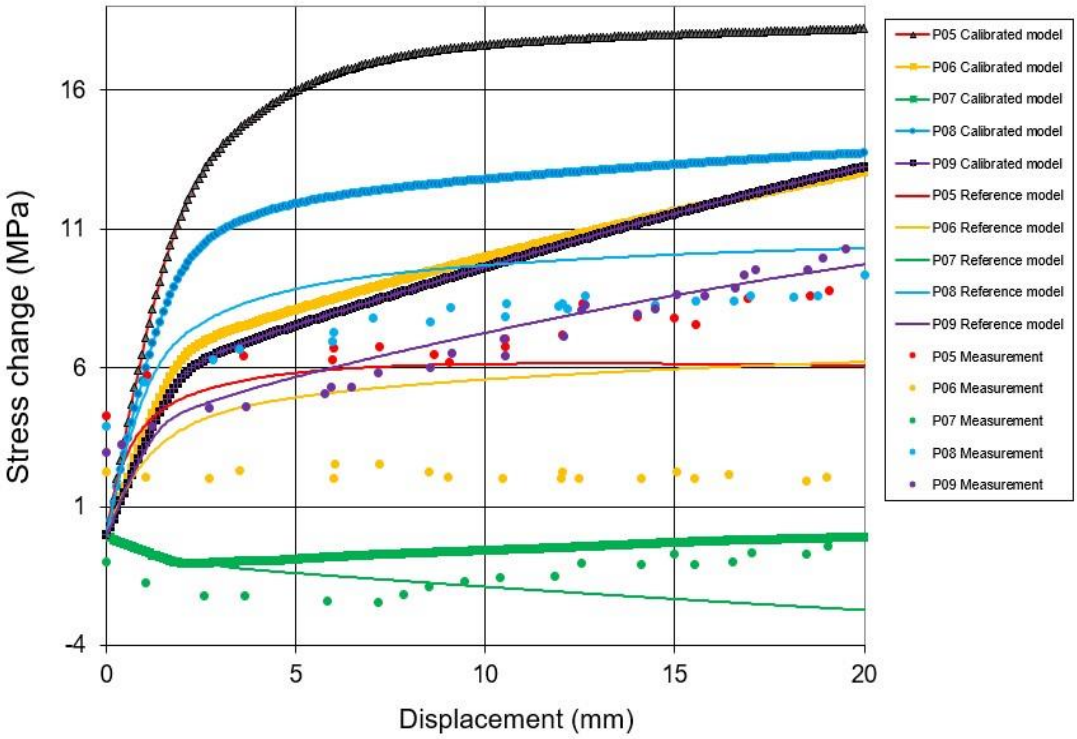

Figure 4-49 Sensitivity analysis of model calibrated and reference model and measured radial stress change in the buffer for Test 1.

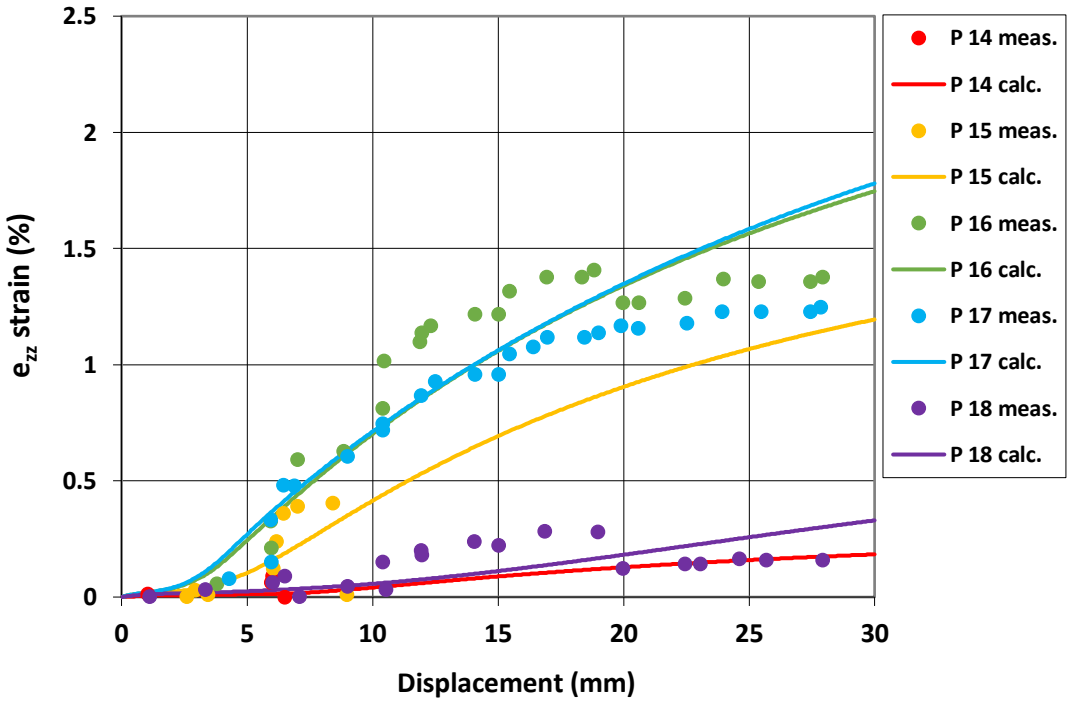

Figure 4-50 Modeled (Reference model) and measured axial strain in the canister surface for Test 1.

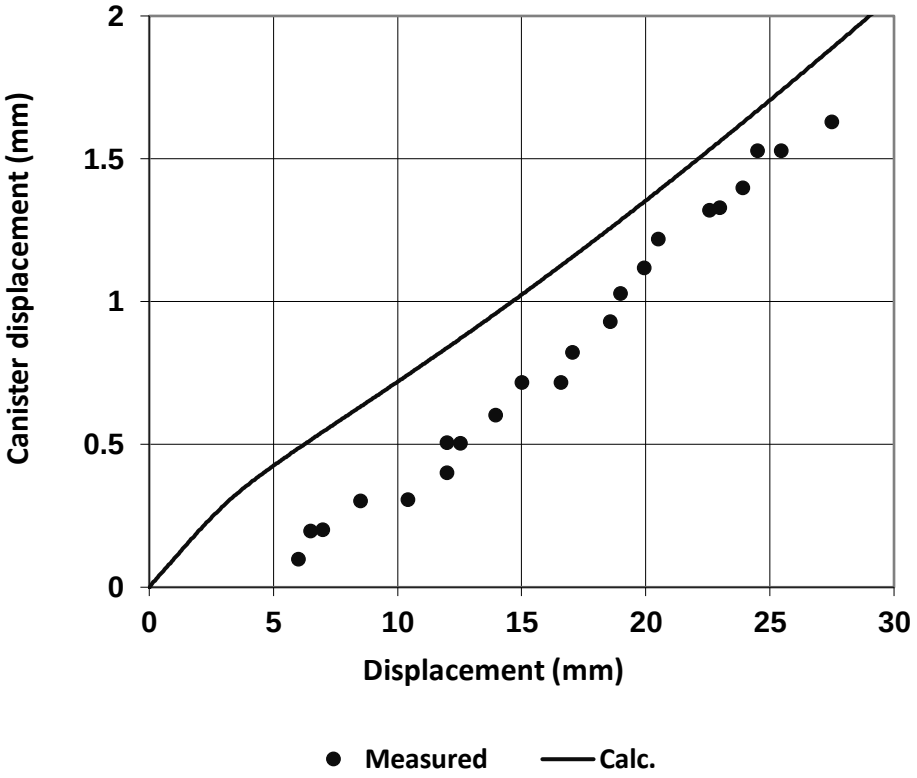

Figure 4-51 Comparison between the calculated (Reference model) and measured relative displacement of the canister end and the rock surface for Test 1.

The geometries after the shear tests and the total forces with respect to displacements in numerical modeling are compared with experimental measurements. In this section, the shear tests were almost equal with exception of the shear rates. The shear rates in tests 1, 2, 3 are 1.9 mm/min (0.0317 mm/s), 1.9 mm/s, 160 mm/s, respectively. The shear test was made at room temperature.

After the calculations, the results of CODE_BRIGHT (a finite element analysis) are related to experimental data (Börgesson, 1986). Comparisons between the CODE_BRIGHT modeling and experiment regarding the geometries are shown at the end of the test in Figure 4-52, Figure 4-53, and Figure 4-54.

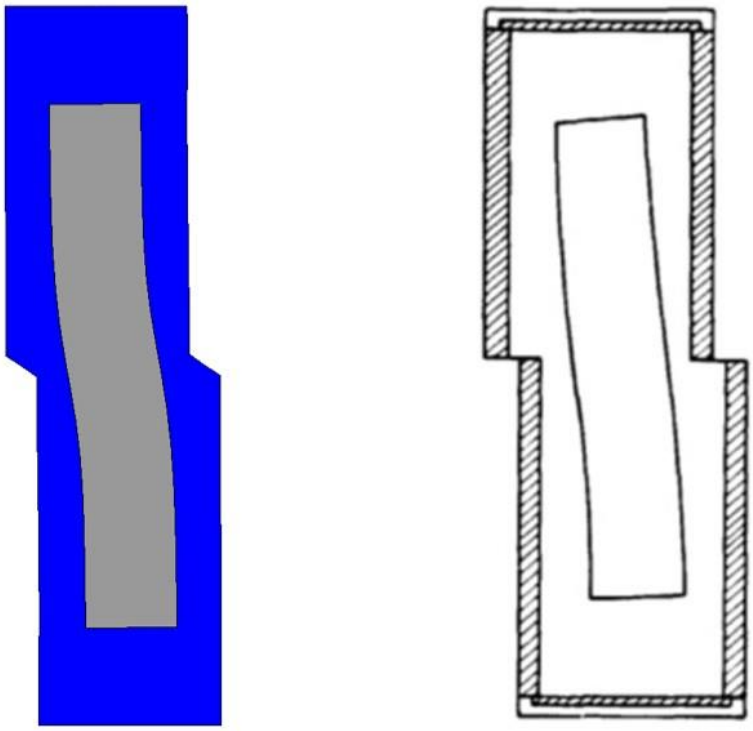

Figure 4-52 The geometries of canister-clay deformation in numerical modeling (left) and experimental test (right) for Test 1.

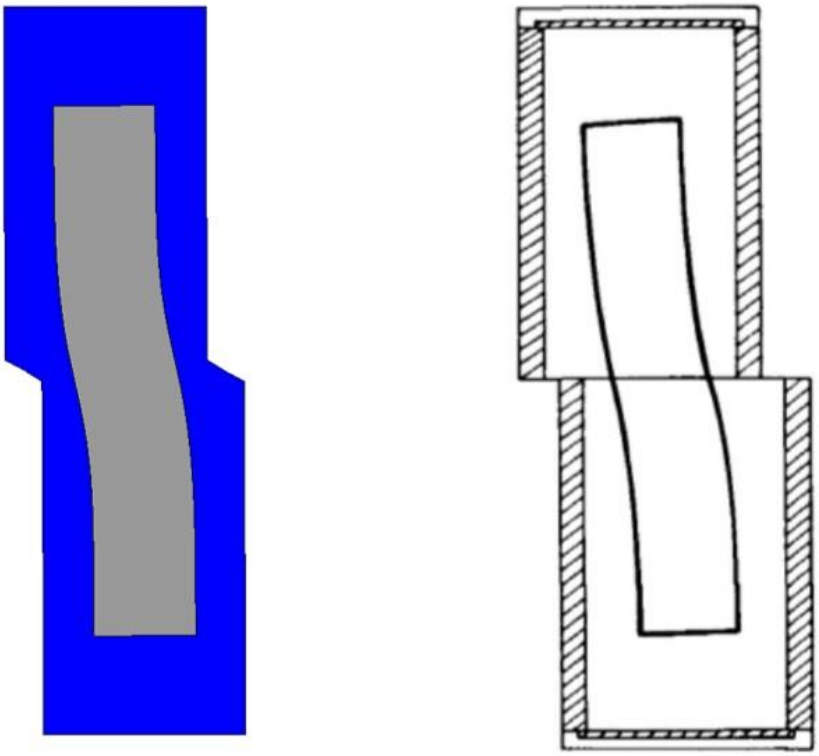

Figure 4-53 The geometries of canister-clay deformation in numerical modeling (left) and experimental test (right) for Test 2.

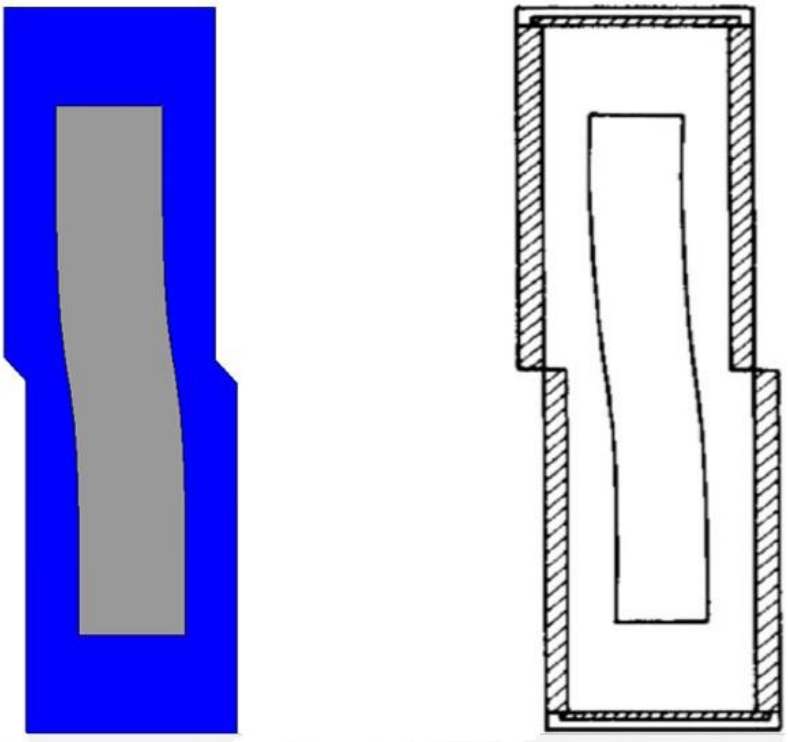

Figure 4-54 The geometries of canister-clay deformation in numerical modeling (left) and experimental test (right) for Test 3.

Finally, total forces in the canister-clay system concerning the displacements in three types of shear tests are compared. The total forces calculated in the simulations are close to the measurements obtained from the experiment for three shear tests in Figure 4-55, Figure 4-56, and Figure 4-57.

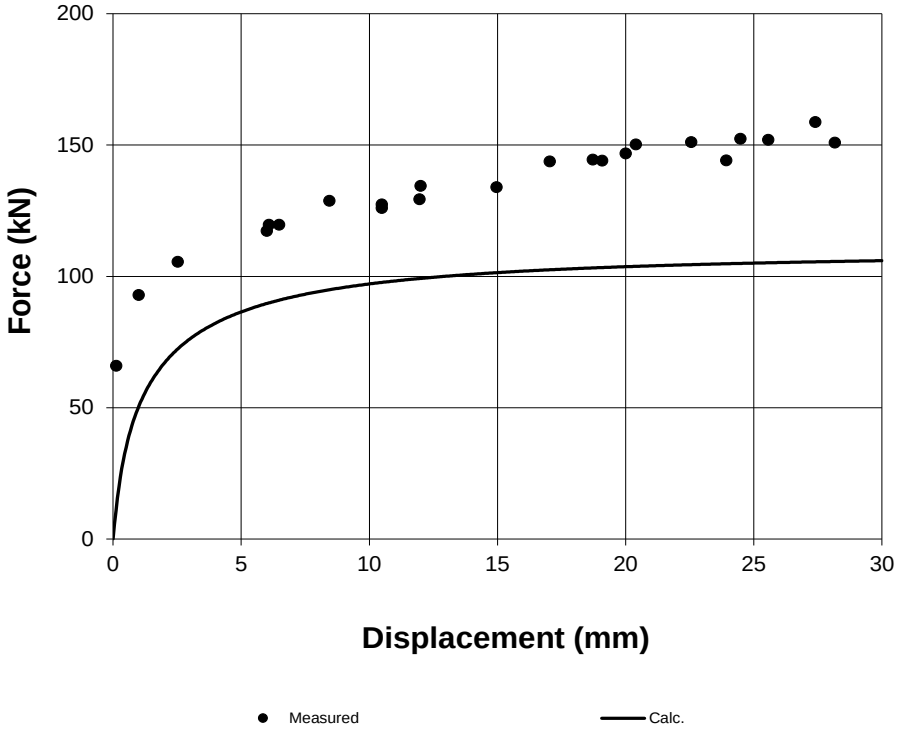

Figure 4-55 Total force-displacement curves for Test 1 in numerical modeling and experimental test.

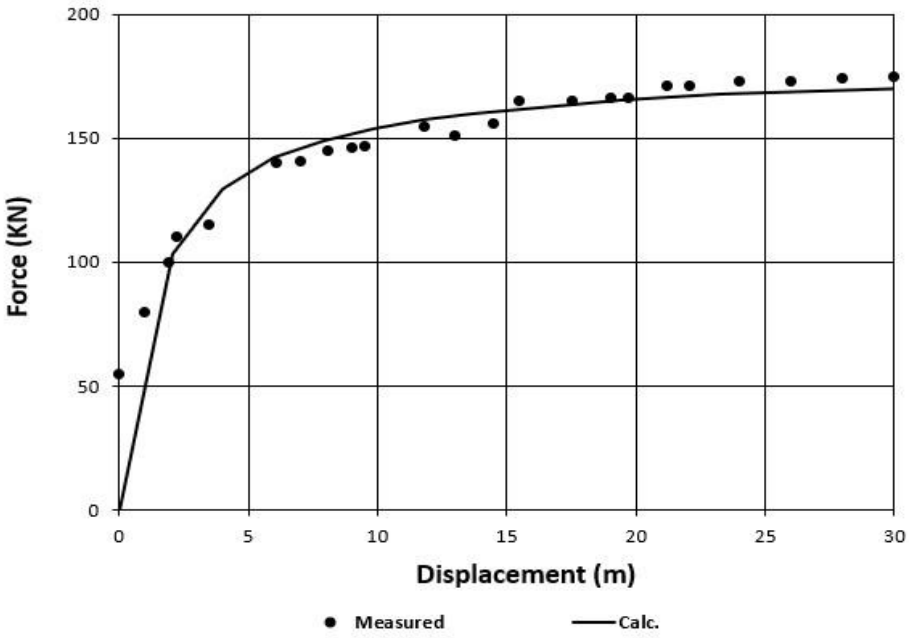

Figure 4-56 Total force-displacement curves for Test 2 in numerical modeling and experimental test.

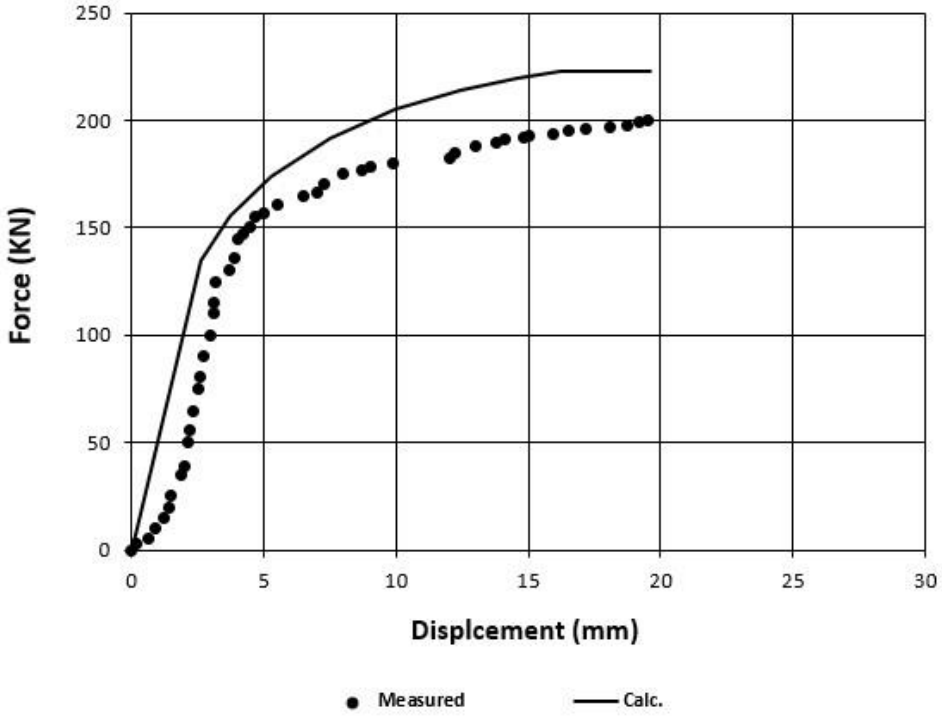

Figure 4-57 Total force-displacement curves for Test 3 in numerical modeling and experimental test.

According to the results obtained by CODE_BRIGHT, the difference between the tests is:

- This difference is visible in the behavior of the copper canister, which is substantially tilted in Test 1 in the opposite to in Test 3. The explanation for this difference is the greater stiffness of the bentonite in Test 3 because of the higher shear rate compared to Test 1.
- From Test 1 to Test 3, the plastic strain in the copper decreases, while the plastic strain in the buffer is strongly increased.
- The strain rate of the copper canister is very low especially for Test 1.

The shear tests can also be well simulated if the initial effective stress is considered to be 10 MPa, avoiding the saturation process simulation. The results are similar as the calculated stress distribution in bentonite produced during saturation is almost uniform. The outcomes of the shearing phase simulation with and without the simulation of the saturation phase are compared for Test 1 in Figure 4-58.

The parameters were calculated from a tensile test carried out in a copper sample (Börgesson and Hernelind, 2010). The test (carried out at a strain rate of 0.0031 s^{-1}) and the simulation of the test with the Bodner-Partom model and calibrated from the test with HPOF (high purity oxygen free) copper (Börgesson and Hernelind, 2010) are presented in Figure 4-59 and the parameters are referred to in Table 4-7.

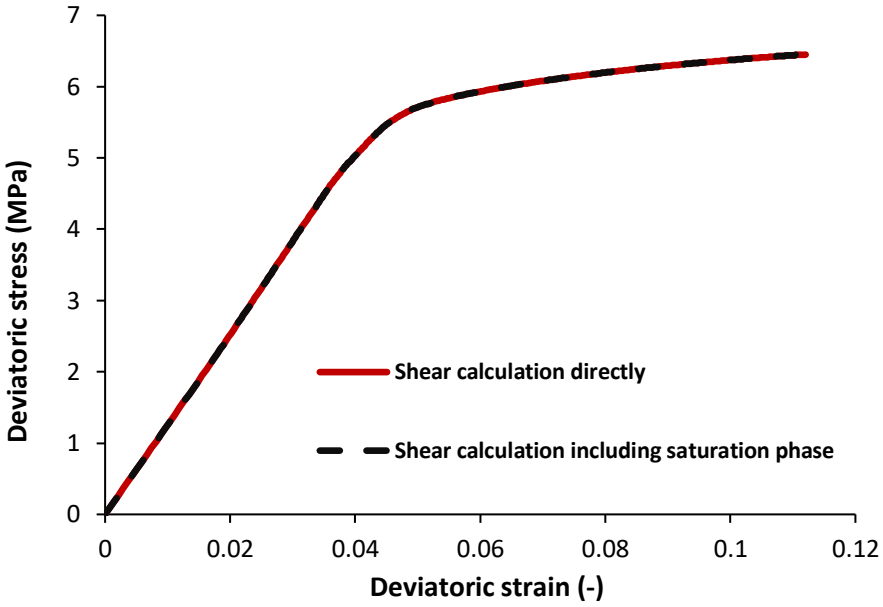

Figure 4-58 Comparison between the calculation of the shearing phase directly and the shearing phase including the saturation phase in deviatoric stress-deviatoric strain curve for bentonite (Test 1, Point A in Figure 4-44).

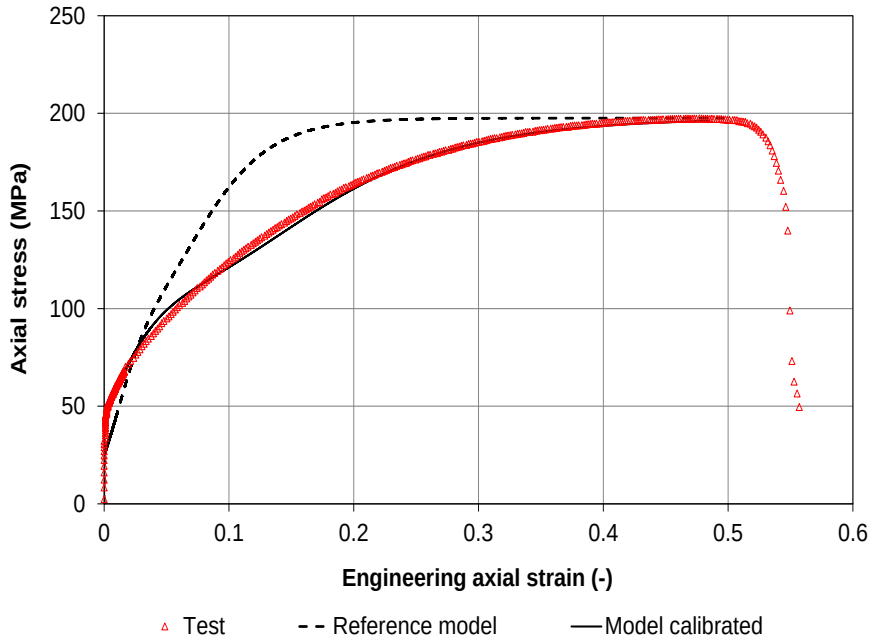

Figure 4-59 Measured and calibrated model (Börgesson and Hernelind, 2010) and simulated stress-relation of a copper sample.

4.5 Shear test modeling using total stress approach in 3D

4.5.1 Full-scale

Mechanical modeling (stress equilibrium) has been verified in total stress, and the time interval is 30 seconds. The total stress modeling in 3D has the same height and width as the total stress modeling in 2D, and the shear thickness is also 10 cm. The element type is hexahedral and the number of elements and nodes are 2349 and 2640, respectively (Figure 4-61). Points A and B were chosen for bentonite and copper, respectively (Figure 4-60). Figure 4-62 and Figure 4-63 have been shown the assumed initial porosity and displacement field. The Drucker-Prager model was used to model MX-80 bentonite clay, and the parameters were described in Table 4-1 and Table 4-2.

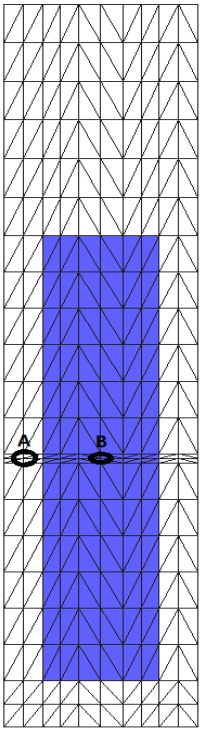

Figure 4-60 Cut in direction of x-z.

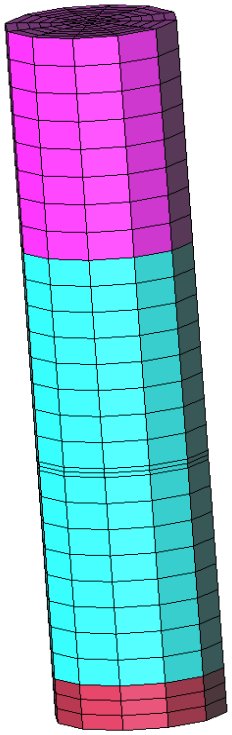

Figure 4-61 Canister-clay shear test in full-scale.

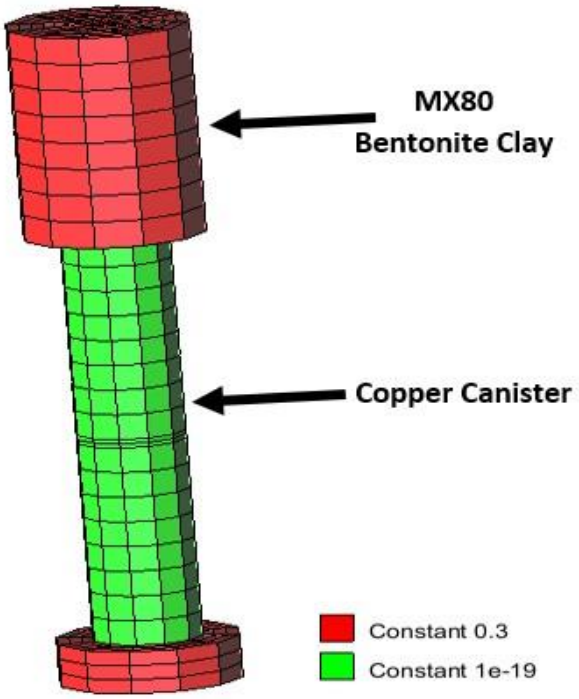

Figure 4-62 Initial porosity of canister-clay shear test.

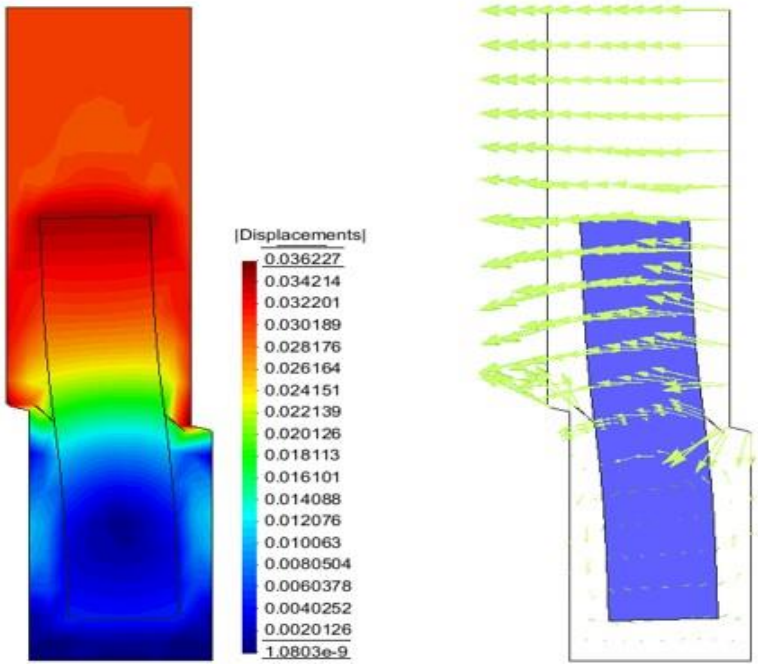

Figure 4-63 Displacement field and display vector of canister-clay shear test in 3D.

4.5.1.1 Sensitivity analysis of dimension in 3D

For deviatoric stress-strain, a comparison of the full-scale and the mock-up scale was performed. The deviatoric stress in both models for bentonite is almost identical, but in copper, the mock-up model has higher deviatoric stress than the full-scale model. Figure 4-64 and Figure 4-65 display the respective graphs.

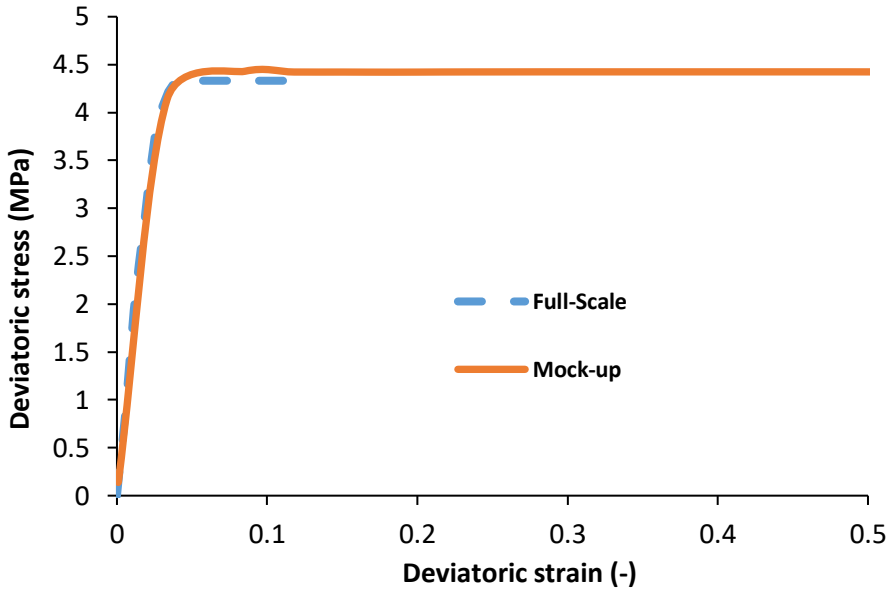

Figure 4-64 Deviator stress-strain curves in full-scale and mock-up scale for bentonite (Point A).

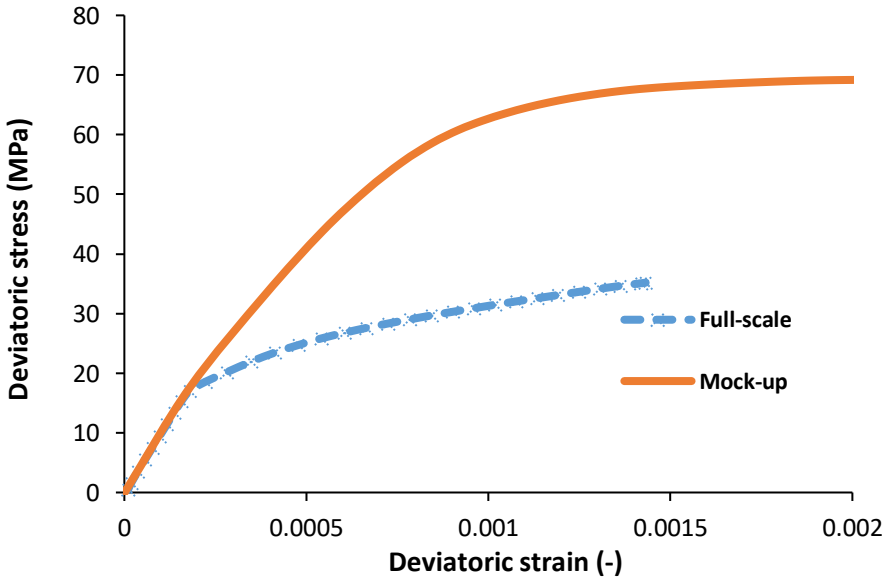

Figure 4-65 Deviator stress-strain curves in full-scale and mock-up scale for copper (Point B).

4.5.1.2 Sensitivity analysis of Γ_0 in 3D

The effect of clay parameter Γ_0 (Fluidity = 1/viscosity) on the stress-strain curve of clay and copper has been investigated in a mock-up scale. In copper and clay, deviatoric stress for Γ_0 of 10^{-3} are higher than the deviatoric stresses for Γ_0 of 10^{+3} and 1. Finally the deviatoric stresses for Γ_0 of 10^{+3} and 1 are equal. The results are shown in Figure 4-66 and Figure 4-67.

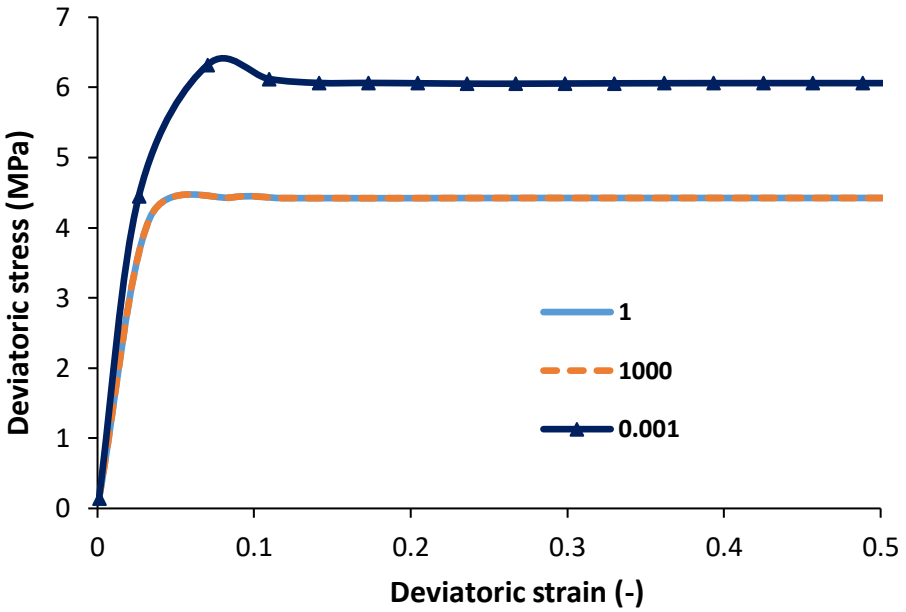

Figure 4-66 Deviatoric stress-strain curves in different Γ_0 for bentonite (Point A).

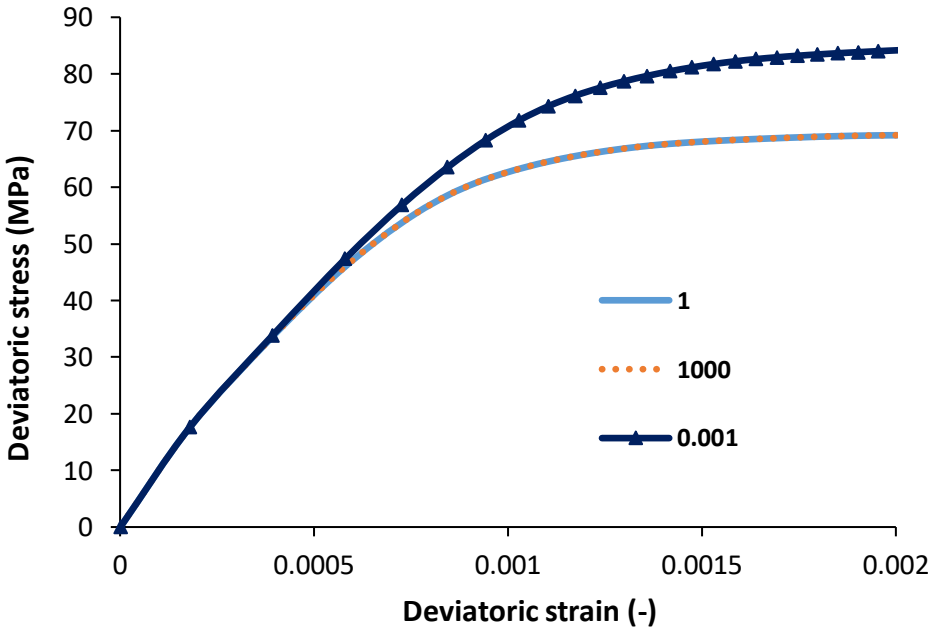

Figure 4-67 Deviatoric stress-strain curves in different Γ_0 for Copper (Point B).

4.5.1.3 Comparison between 2D and 3D modeling in total stress approach

According to the results obtained in the mock-up scale seen in Figure 4-68 and Figure 4-69, the deviatoric stress in two-dimensional modeling is greater than the deviatoric stress in three-dimensional modeling for copper, but the deviatoric stress in both models is the same for bentonite.

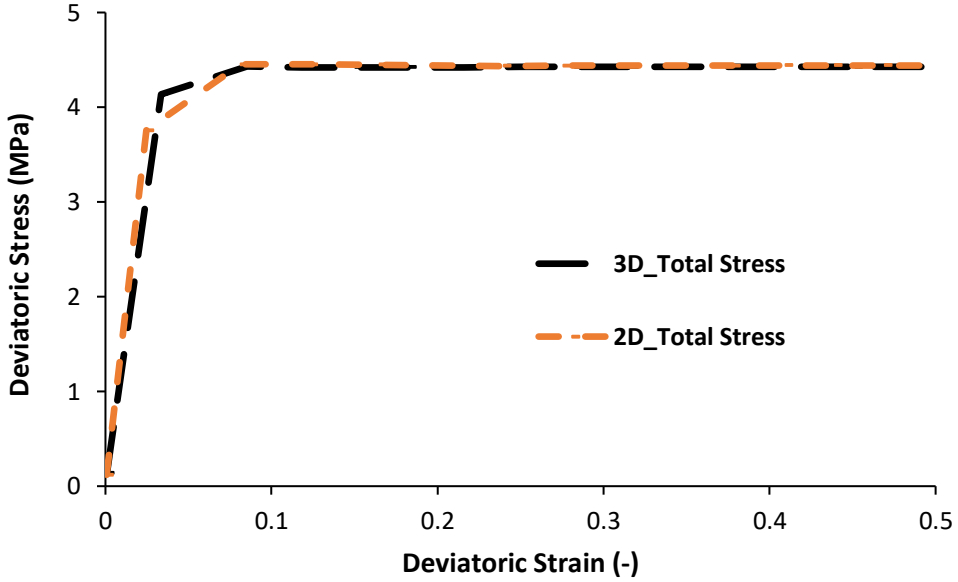

Figure 4-68 Deviator stress-strain curves of total stress in 2D and 3D for bentonite (Point A).

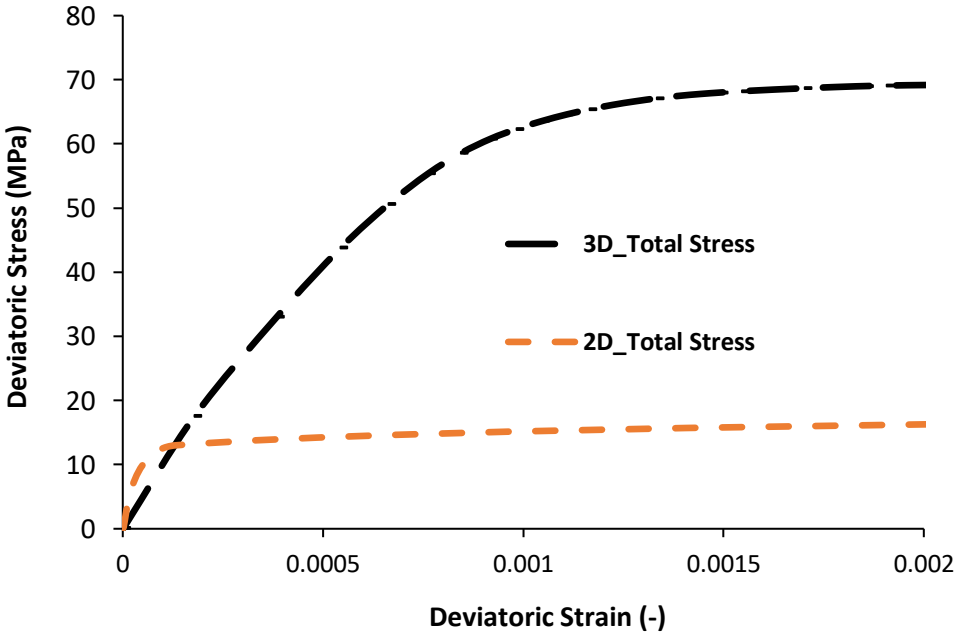

Figure 4-69 Deviator stress-strain curves of total stress in 2D and 3D for copper (Point B).

4.5.1.4 Sensitivity analysis of mesh

In the total stress approach, the quadratic tetrahedral mesh is compared to the hexahedra mesh for Full scale. The number of nodes and elements in a tetrahedral mesh are 1353 and 864, respectively, while the number of nodes and elements in a hexahedra mesh is 2640 and 2349, respectively. The deviatoric stress in bentonite is the same, except in copper, the deviatoric stress in hexahedra mesh is higher than the deviatoric stress in the quadratic tetrahedral mesh. They are depicted in Figure 4-70 and Figure 4-71.

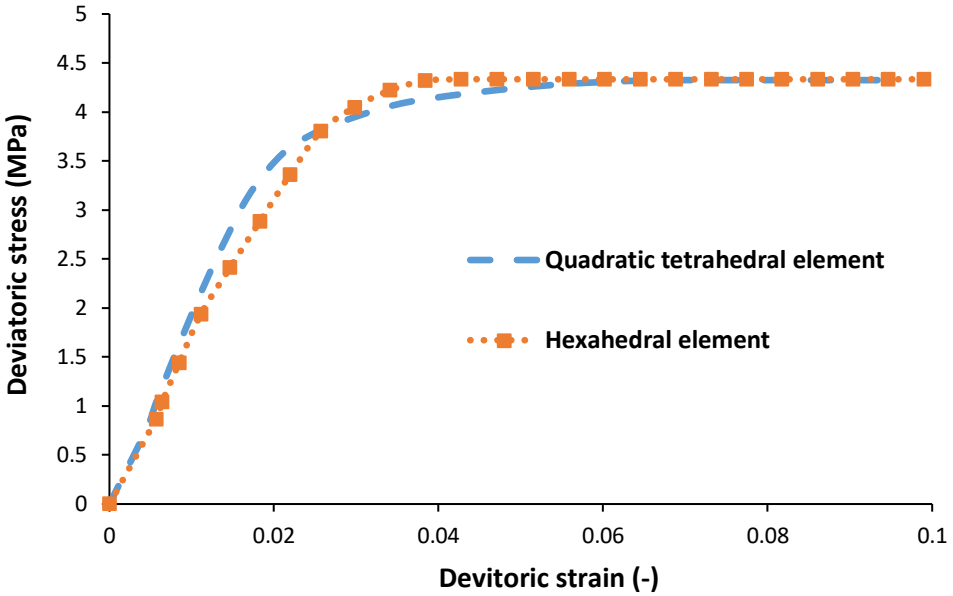

Figure 4-70 Deviator stress-strain curves in different mesh for bentonite.

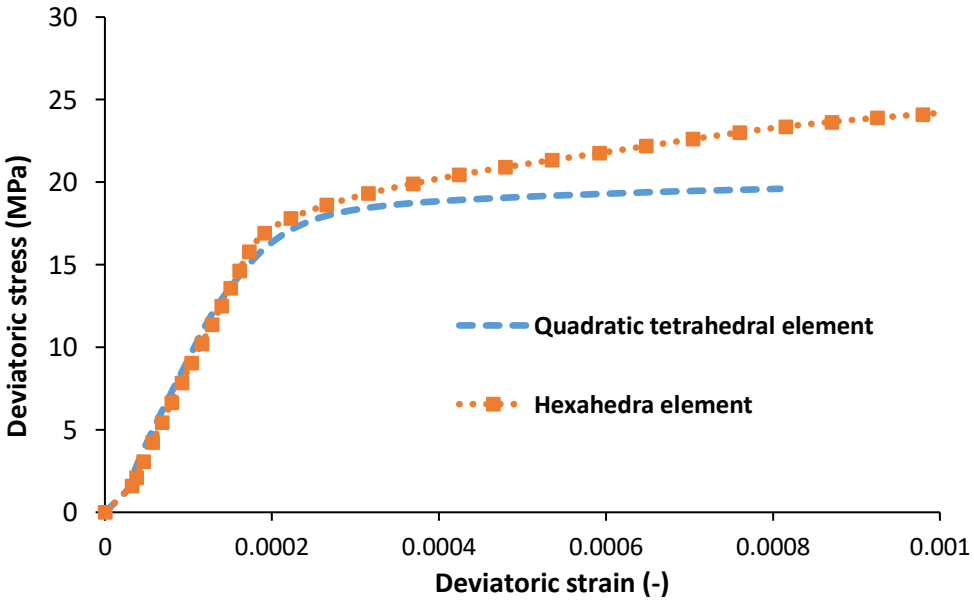

Figure 4-71 Deviator stress-strain curves in different mesh for copper.

4.6 Shear test modeling using effective stress approach in 3D

4.6.1 Full-Scale

The element type is hexahedral and the number of elements and nodes are 792 and 943 in respectively. The buffer geometry is based on the work of Juvankoski (Juvankoski & Marcos, 2010). BBM is used to model MX-80 bentonite clay. Table 4-4 lists their parameters. Figure 4-73 and Figure 4-74 demonstrate contour fill and the liquid pressure progression at the end of the test (30 Seconds) as the bentonite is saturated. Figure 4-77 shows the generation of deviatoric stresses in the buffer due to swelling. To avoid excessive isotropic pressures on the canister, the swelling pressure should not exceed 15 MPa.

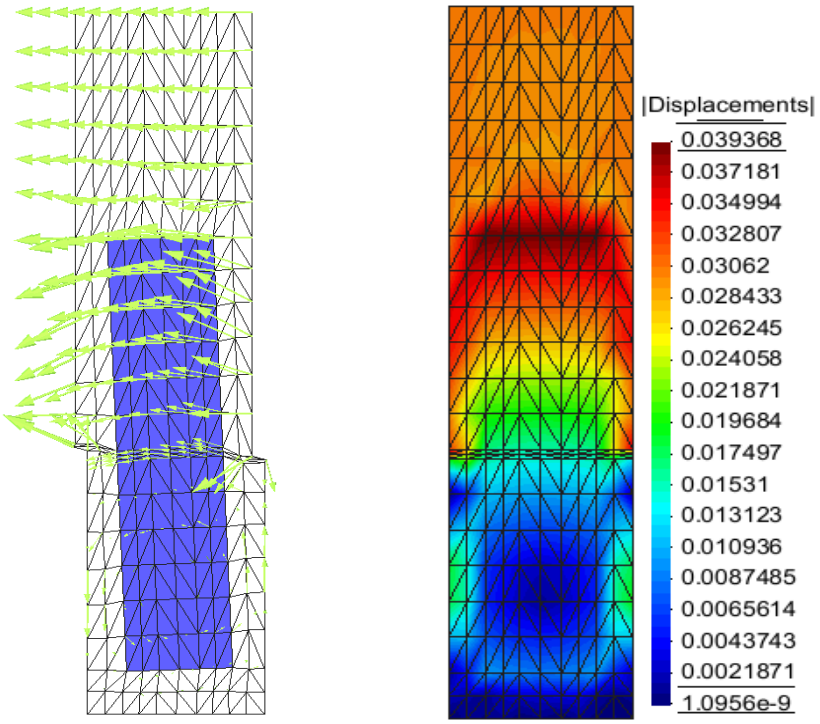

Figure 4-72 Displacements field (Right) and display vector (Left) of canister-clay shear test in three dimensional.

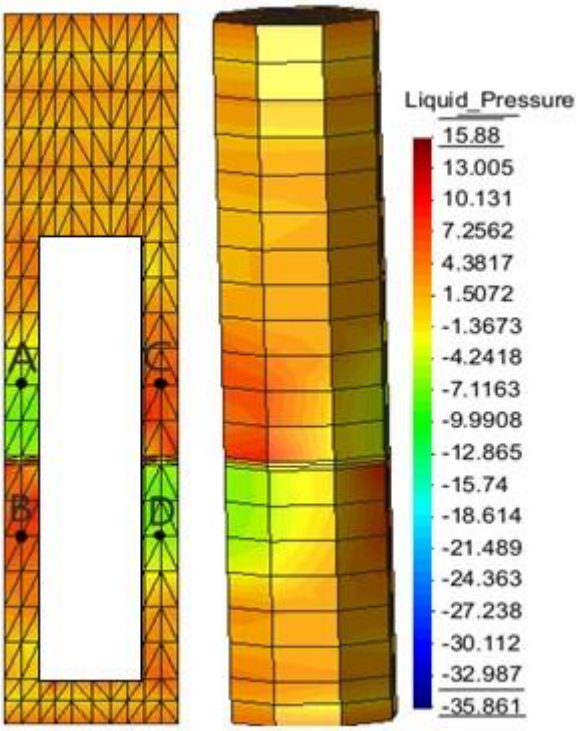

Figure 4-73 Contour fill of liquid pressure.

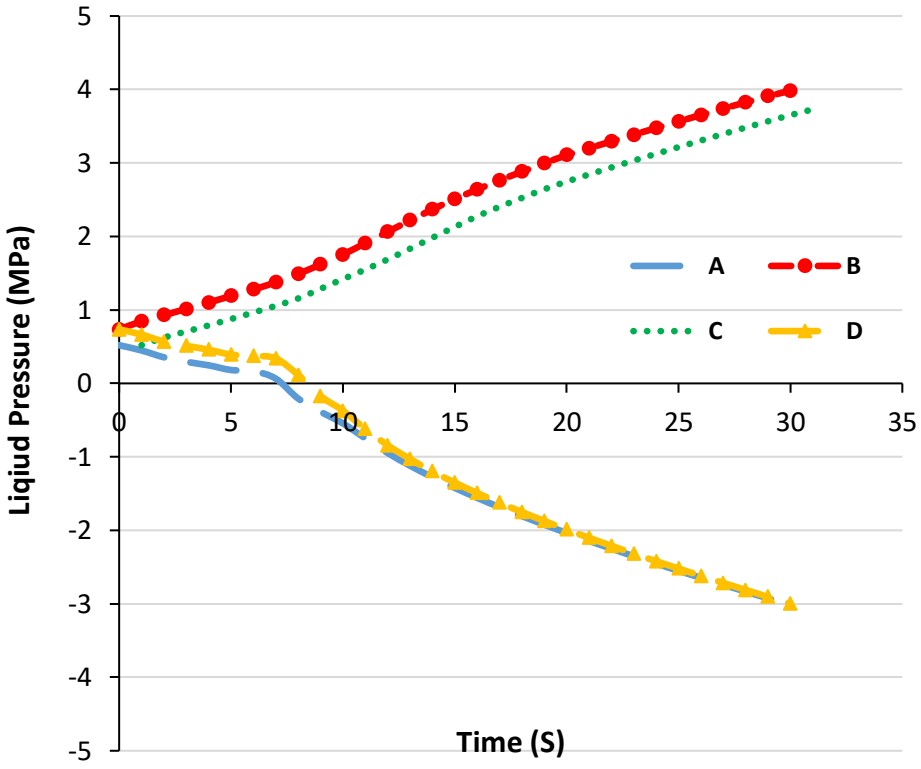

Figure 4-74 Evolution of liquid pressure.

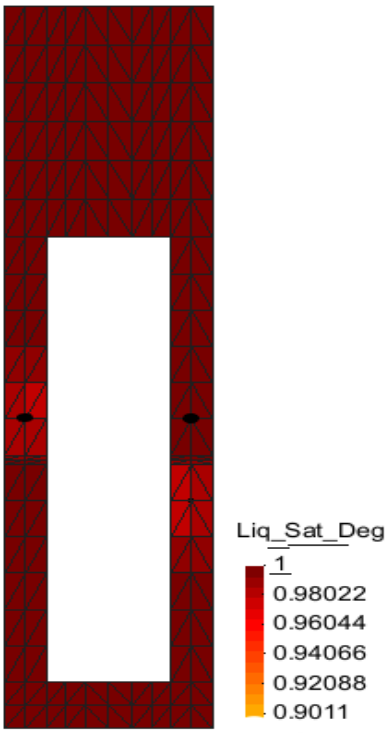

Figure 4-75 Contour fill of degree of saturation at the end of the shear test.

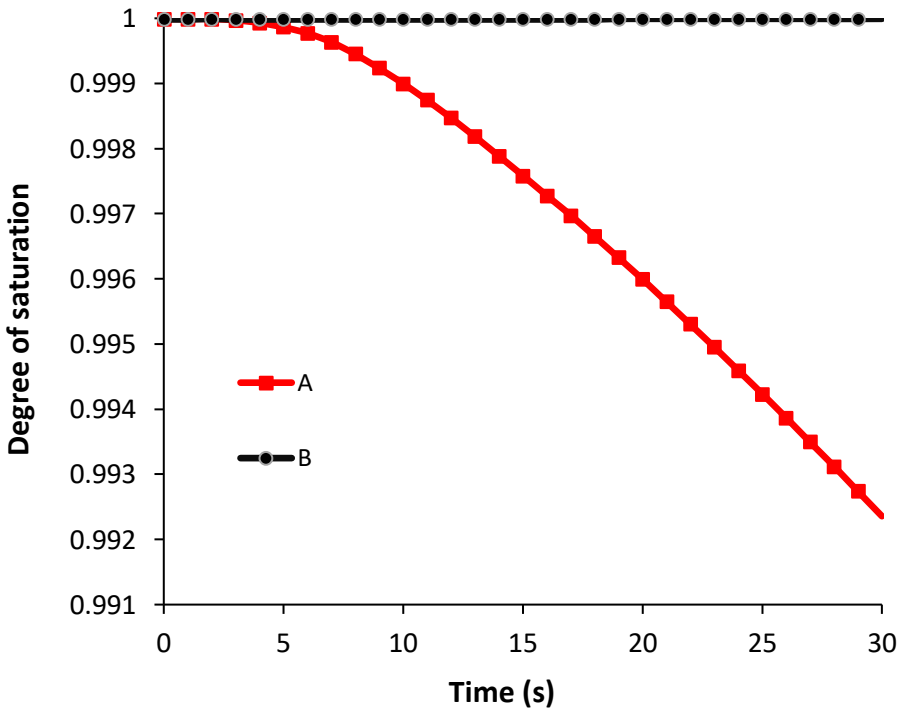

Figure 4-76 Evolution of degree of saturation.

Curves of deviator stress-strain for bentonite and copper are depicted in Figure 4-77 and Figure 4-78. Points A and B in Figure 4-60 are chosen for bentonite and copper, respectively.

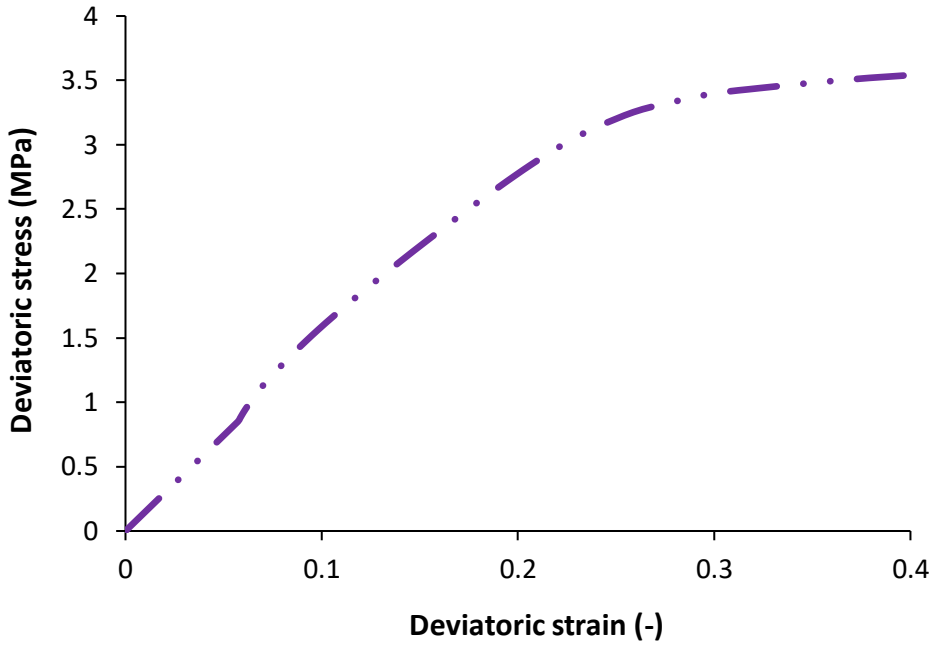

Figure 4-77 Deviator stress-strain curves for bentonite (Point A).

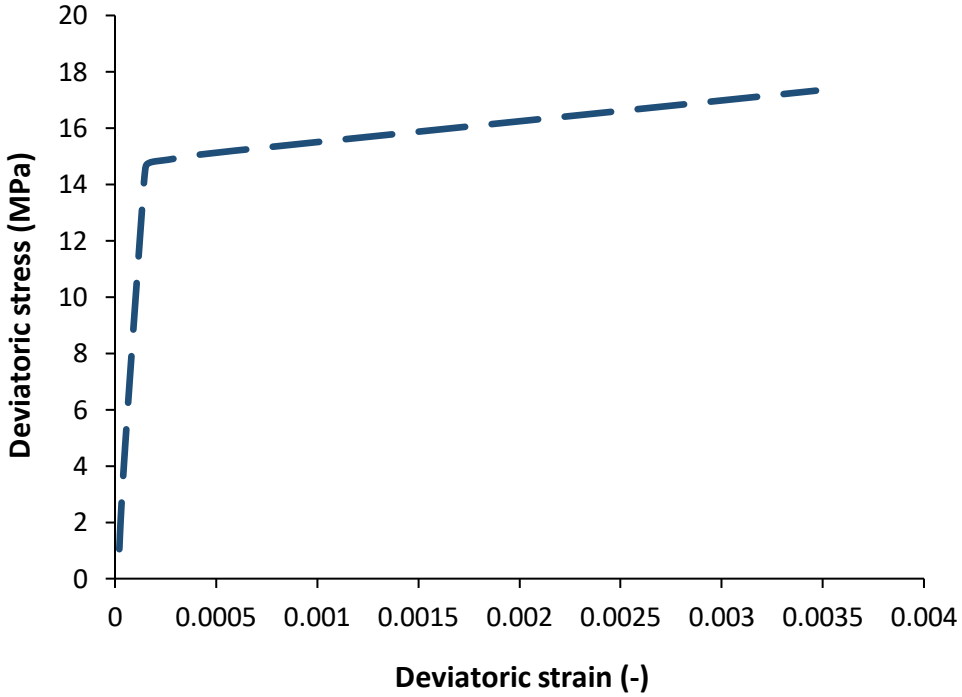

Figure 4-78 Deviator stress-strain curves for copper.

Then, curves of porosity-deviatoric strain and preconsolidation stress-deviatoric strain for bentonite are depicted in Figure 4-79 and Figure 4-80.

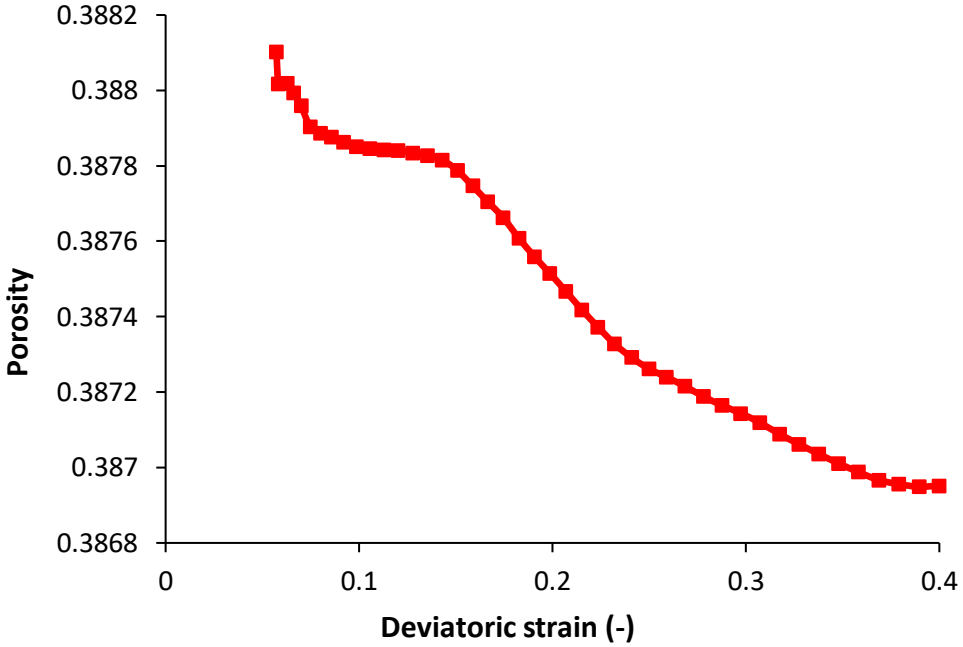

Figure 4-79 Porosity-Deviatoric strain curve for bentonite (Point A).

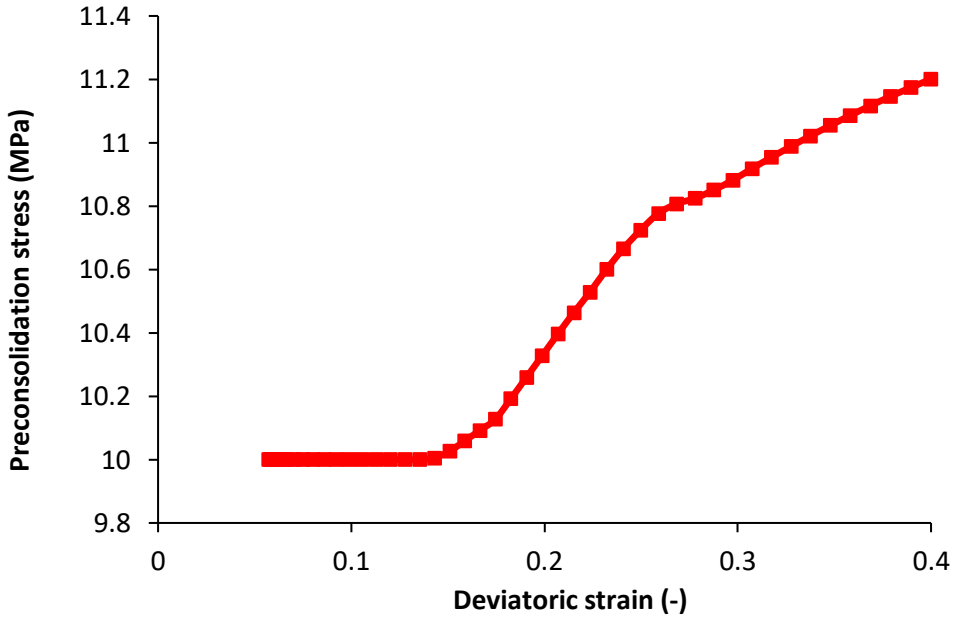

Figure 4-80 Preconsolidation stress-deviatoric strain curve for bentonite (Point A).

4.6.1.1 Sensitivity analysis of permeability in 3D

Permeabilities of 5.59×10^{-19}, 5.59×10^{-20} and 5.59×10^{-21} (Toprak et al., 2017) have been investigated in full-scale. In the deviatoric stress-deviatoric strain curves in Figure 4-81 and Figure 4-82, It has a negligible effect on the results and deviatoric stress in three permeabilities is equal for copper and bentonite.

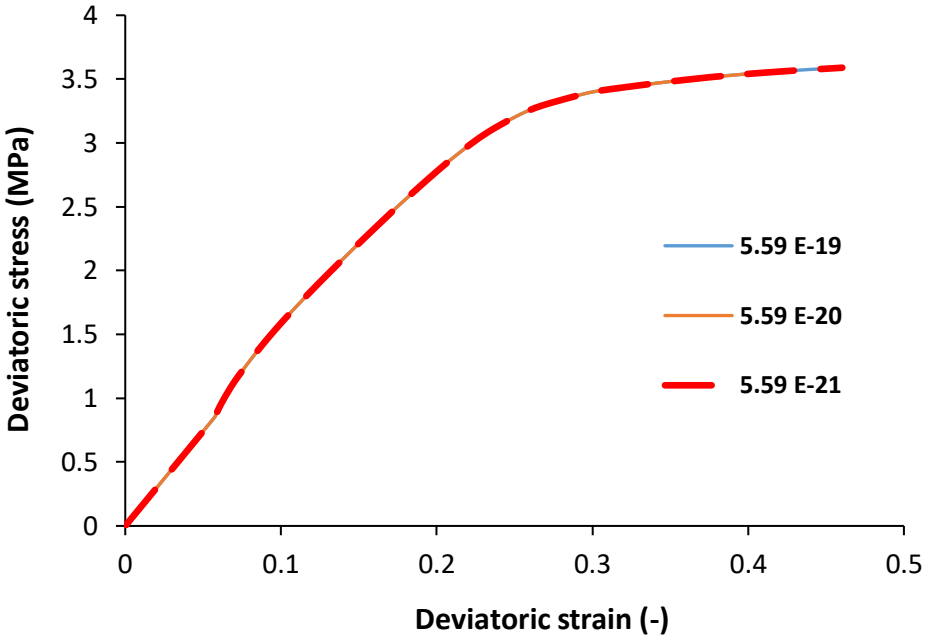

Figure 4-81 Deviatoric stress-strain curves of permeabilities for bentonite (Point A).

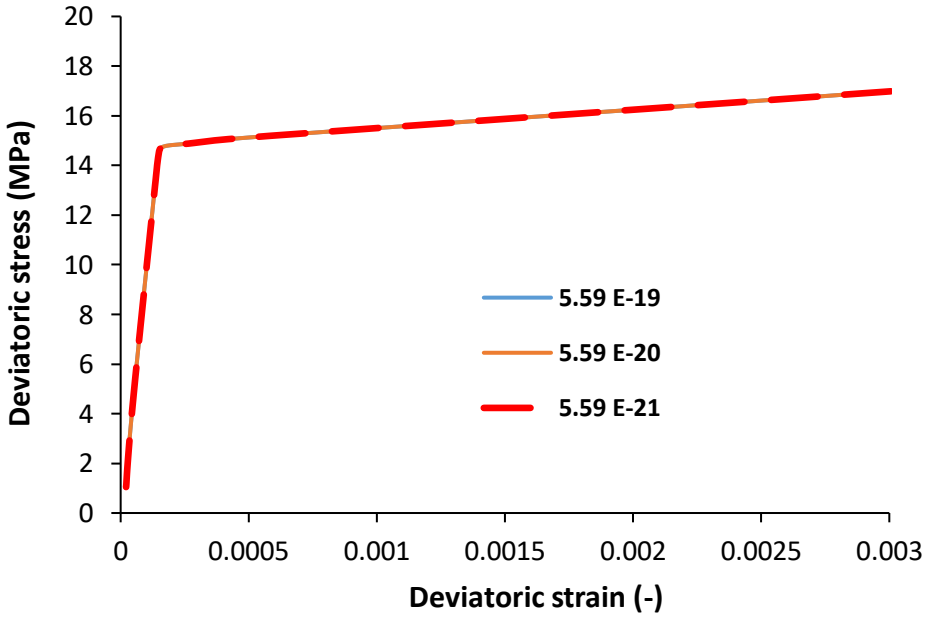

Figure 4-82 Deviator stress-strain curves of permeabilities for copper (Point B).

4.6.1.2 Comparison between 2D and 3D modeling in effective stress approach

In terms of the results are captured in the full-scale that is shown in Figure 4-83 and Figure 4-84, the deviatoric stress in three-dimensional modeling is greater than the deviatoric stress in two-dimensional modeling for copper but for bentonite, the deviatoric stress in both models is similar. Preconsolidation stress and porosity in three-dimensional modeling are less than preconsolidation stress and porosity in two-dimensional modeling for effective stress.

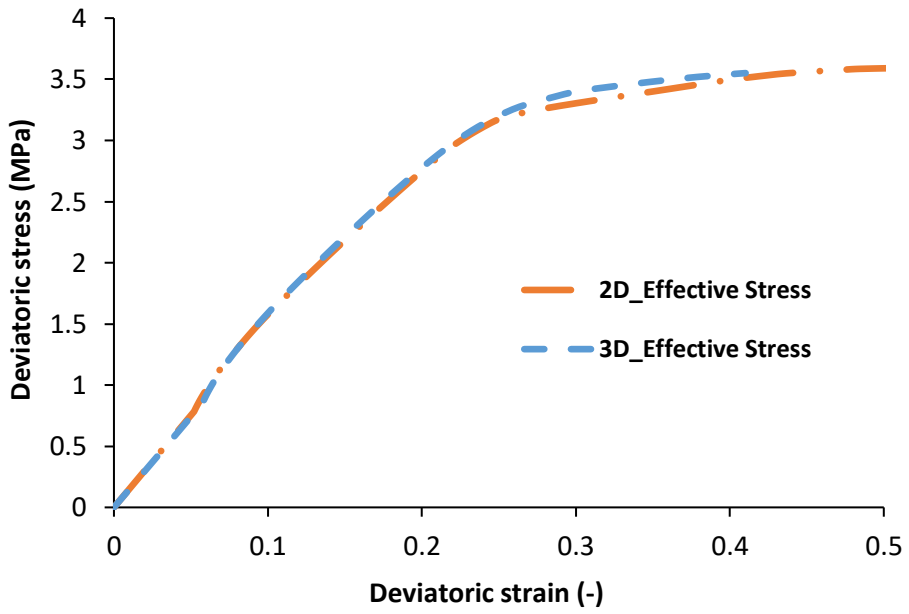

Figure 4-83 Deviatoric stress-strain curves for bentonite (Point A).

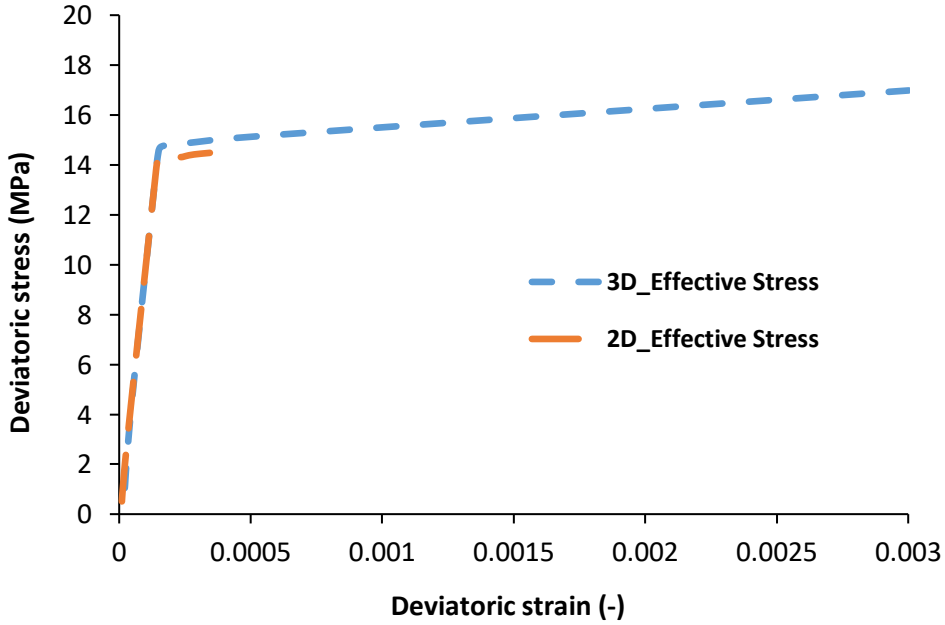

Figure 4-84 Deviatoric stress-strain curves for copper (Point B).

4.6.1.3 Sensitivity analysis of dimension in 3D

For deviatoric stress-strain, the distinction between the full-scale and the mock-up scale has been checked. For bentonite, the deviatoric stress in the mock-up scale is less than the deviatoric stress in the full-scale, and the deviatoric stress in the full-scale is higher for copper. The corresponding charts are referred to Figure 4-85 and Figure 4-86.

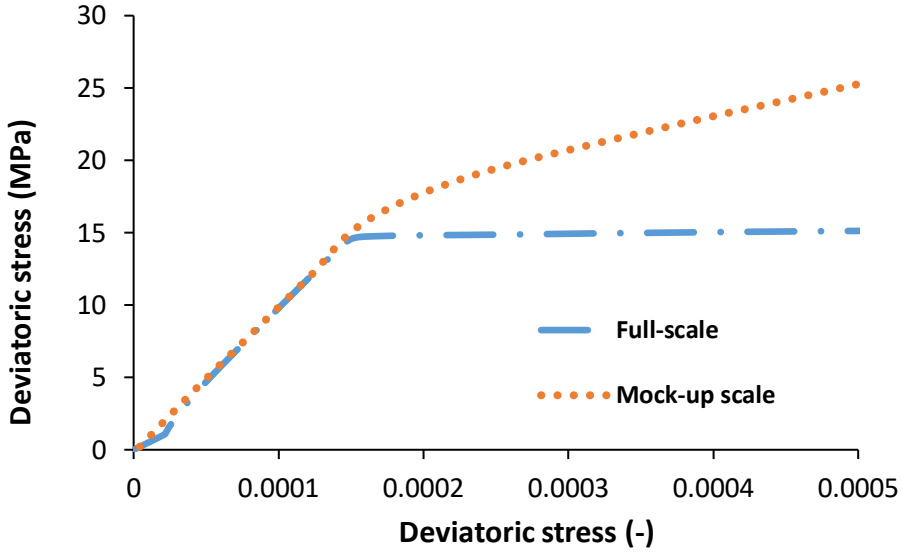

Figure 4-85 Deviatoric stress-strain curves in the full-scale and the mock-up scale for copper (Point B).

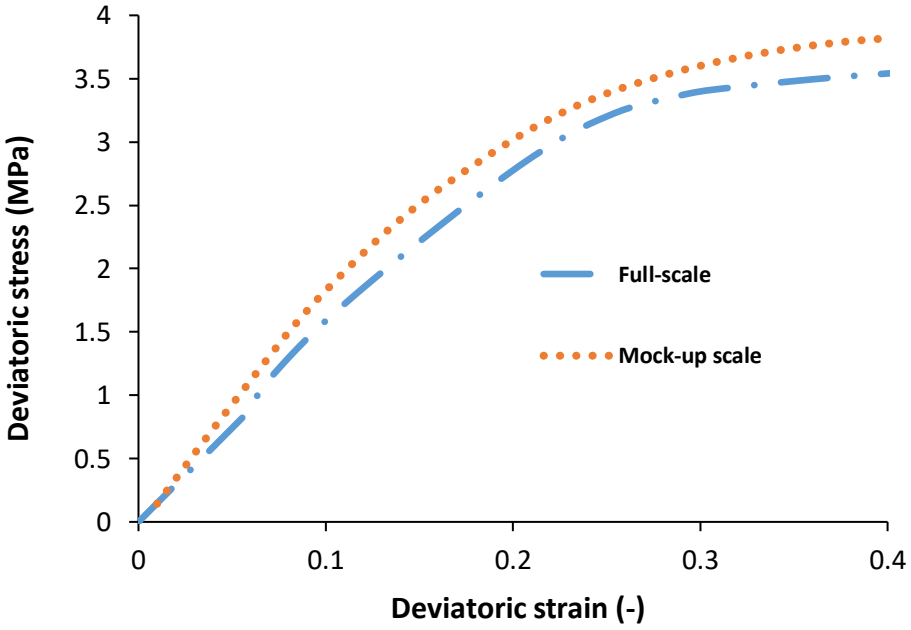

Figure 4-86 Deviatoric stress-strain curves in the full-scale and the mock-up scale for bentonite (Point A).

CHAPTER 5

5 Influence of discontinuity in a canister-clay shear test

5.1 Application of Discontinuity in 2D Numerical Modelling

5.1.1 Full-scale

The canister-clay system has been surrounded by discontinuous rock. The model is divided into two parts, one of which (bottom half) is set fixed and the other of which (upper half) can be displaced perpendicularly to the axial direction. In boundary condition, on the part corresponding to the mobile half (upper half) of the model, a displacement rate of X is applied and equal to -0.001 m/s (the vertical displacements were held to zero) and on the part corresponding to the fixed half (bottom half) of the model, has a uniform field of 0. There is a thin zone between those parts which has a discontinuity in the rock and a transition zone in canister-clay and has a thickness of 10 cm. In CODE_BRIGHT, elastoplastic material models are accompanied by plane strain conditions, which allow for dimension reduction from 3D to 2D. At the top of geometry, vertical stress of -10.57 MPa is applied.

The mesh used in this model is structured and the element type is linear quadrilateral by means of the modification of the matrix B (Hughes, 1980) with 4 integration points. The number of elements and nodes are 2412 and 2516 in respectively. The initial stresses for rock and discontinuity changed linearly as follows (Table 5-1):

Table 5-1 The initial stress for rock and discontinuity (Toprak et al., 2017).

From	Until
Height = 0	Height=37.71
$\boldsymbol{\sigma_1 = -10.57\ \mathbf{MPa}}$	$\sigma_1 = -11.55$ MPa
$\boldsymbol{\sigma_2 = -6.83\ \mathbf{MPa}}$	$\sigma_2 = -7.81$ MPa
$\boldsymbol{\sigma_3 = -6.83\ \mathbf{MPa}}$	$\sigma_3 = -7.81$ MPa

The initial stress for canister and clay is -8 MPa (Figure 5-2) and the system is confined due to the swelling pressure and the stresses in rock and EBS are not in equilibrium. The mesh and dimension of the canister-clay system are depicted in Figure 5-1.

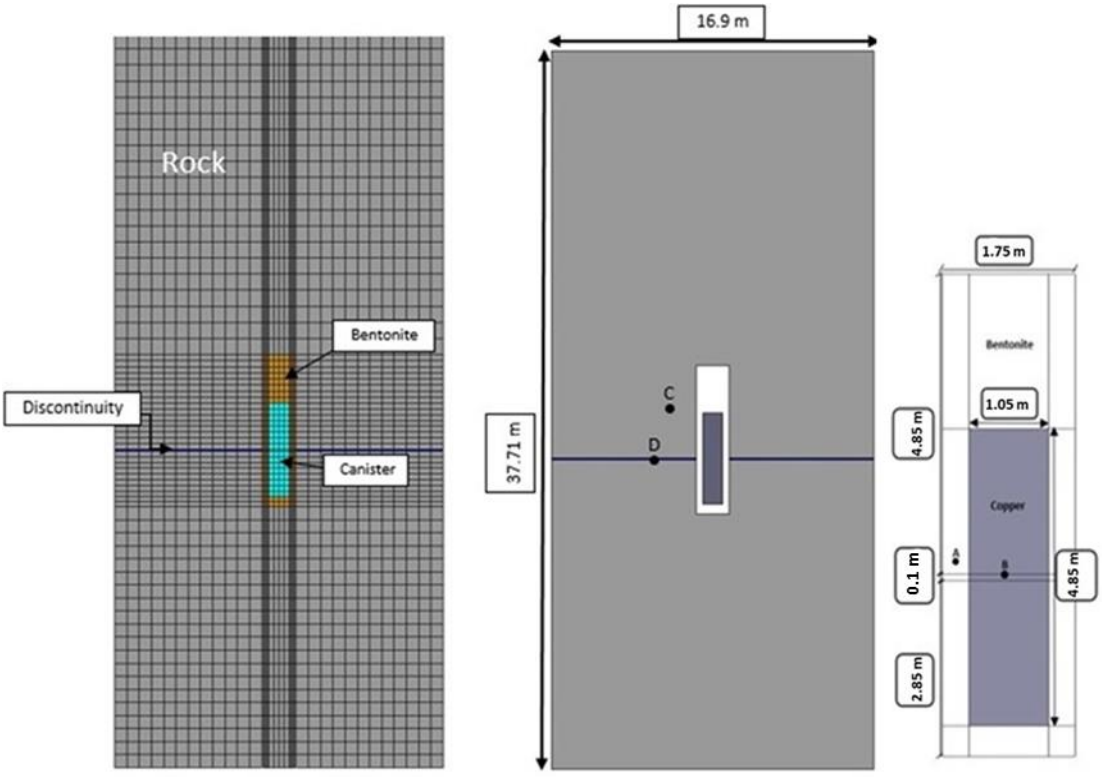

Figure 5-1 Mesh and dimensions of the shear test model.

Initial stress and initial porosity of the canister-clay system are shown in Figure 5-2 and Figure 5-3, respectively.

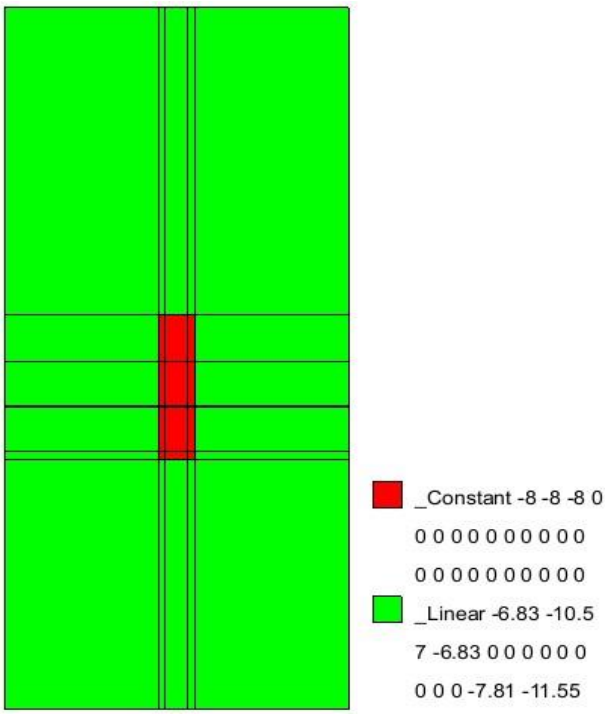

Figure 5-2 Initial stress for the canister-clay system.

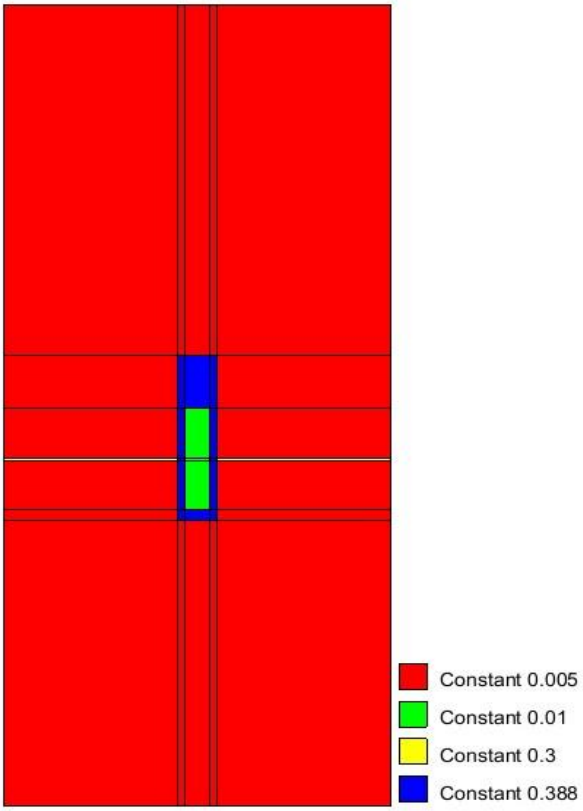

Figure 5-3 Initial total porosity.

Two models are presented, mechanical analysis (M) and hydro-mechanical coupling (HM). In two models, linear elasticity for all materials and Viscoplasticity Drucker-Prager based on Mohr-Coulomb for rock and discontinuity as shown in Table 5-2 and Table 5-3. Viscoplasticity Bodner-Partom model (Bodner & Merzer, 1978; Bodner & Partom, 1975; Khadivipanah et al., 2020) for copper in Table 4-1 are used but the difference between them is plasticity modeling of bentonite, in mechanical modeling, the Drucker-Prager criterion is applied and in the hydro-mechanical coupling, Barcelona Basic Model (BBM) (Alonso et al., 1990) is performed. The undrained situation which is realistic in clayey soils is used in the mechanical analysis.

Table 5-2 Input parameters of the Rock (Drucker & Prager, 1952; Hoek et al., 1992; Toprak et al., 2013; Toprak et al., 2017).

Linear Elasticity	ν	-	0.25	Poisson's Ratio
	E	MPa	9000	Young modulus
Drucker-Prager viscoplasticity	Γ_0	$s^{-1}MPa^{-m}$	10^{-3}	Fluidity = 1/Viscosity
	m		3	Stress power
	c	MPa	3.5	Cohesion
	M	-	1.33	The slope in p-q

Table 5-3 Input parameters of the discontinuity (Drucker & Prager, 1952; Hoek et al., 1992; Toprak et al., 2013; Toprak et al., 2017).

Linear Elasticity	ν	-	0.49	Poisson's Ratio
	E	MPa	1400	Young modulus
Drucker-Prager viscoplasticity	Γ_0	$s^{-1}MPa^{-m}$	10^{-3}	1/Viscosity
	m		3	Stress power
	M	-	0.94	The slope in *p-q*
	C	MPa	0.55	Cohesion

For the canister, the linear elasticity model and Bodner-Partom Viscoplasticity model (Bodner & Merzer, 1978; Bodner & Partom, 1975; Khadivipanah et al., 2020) are used. It is shown in Table 5-4.

Table 5-4 Input parameters of the copper (Bodner & Partom, 1975; Toprak et al., 2017).

Linear Elasticity	ν	-	0.35	Poisson's Ratio
	E	MPa	133000	Young modulus
Bodner-Partom Viscoplasticity	D_0	s^{-1}	10^4	Limiting strain rate
	Z_0	MPa	31	Initial value of the internal state variable
	Z_1	MPa	237	Saturated value of the internal state variable
	m_0	$(MPa)^{-1}$	0.15	Initial value of hardening parameter
	m_1	$(MPa)^{-1}$	0.25	Saturated value of hardening parameter
	α	$(MPa)^{-1}$	0.50	A material constant

5.1.1.1 Shear test modeling using mechanical analysis in 2D

The stress equilibrium is taken into account in a mechanical study. The study is performed under isothermal conditions, and the temperature is around 20° C. The linear elasticity model and Drucker–Prager viscoplasticity model (Drucker & Prager, 1952) are used for bentonite in Table 5-5. Figure 5-4 depicts the displacements field for a full-scale simulation of a deposition hole in plane strain, as well as the displacement vectors when the amplification factor is set to 10.

Table 5-5 Input parameters of the bentonite in mechanical analysis (DIT-UPC, 2021; Drucker & Prager, 1952; Toprak et al., 2013; Toprak et al., 2017).

Linear elasticity	ν	-	0.49	Poisson's Ratio
	E	MPa	304	Young modulus
Drucker-Prager viscoplasticity	Γ_0	$s^{-1}MPa^{-m}$	10^{-3}	1/Viscosity
	m	-	3	Stress power
	c_u	MPa	3.672	Undrained shear strength

Bentonite has a height of 7.8 meters and a width of 1.75 meters in the main model of the canister-clay system seen in Figure 5-1, while copper has a height of 4.8 meters and a width of 1.05 meters. The model employs continuum elements with no contact elements, and the fracture thickness in rock is set at 10 cm.

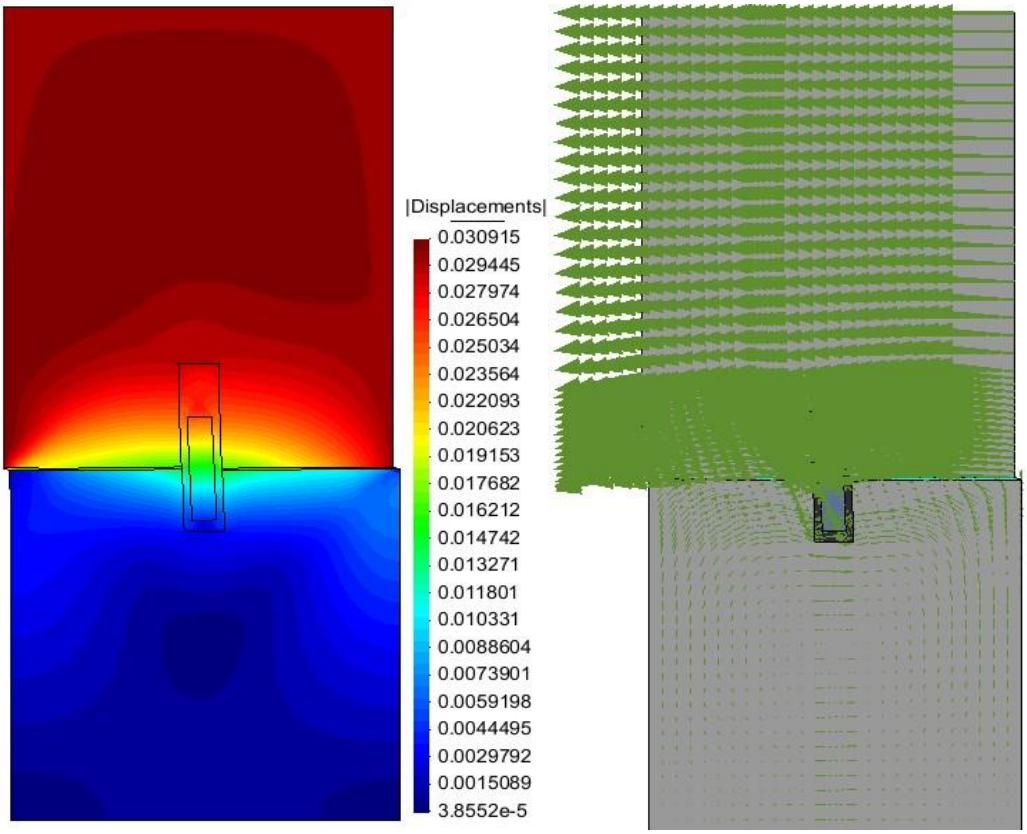

Figure 5-4 Displacements and display vector of the shear test.

5.1.1.2 Sensitivity analysis of width in mechanical analysis

For analysis, two different widths of 16.9 m (Figure 5-1) and 3.75 m (Figure 5-5) are considered. The first geometry (width of 16.9 m) was explained in section 5.1.1, and the second geometry (width of 3.75 m) has all of the same conditions as the first geometry (structure mesh and quadrilateral element), except the number of nodes and elements are 2872 and 2752, respectively, and the elements are structured and quadrilateral.

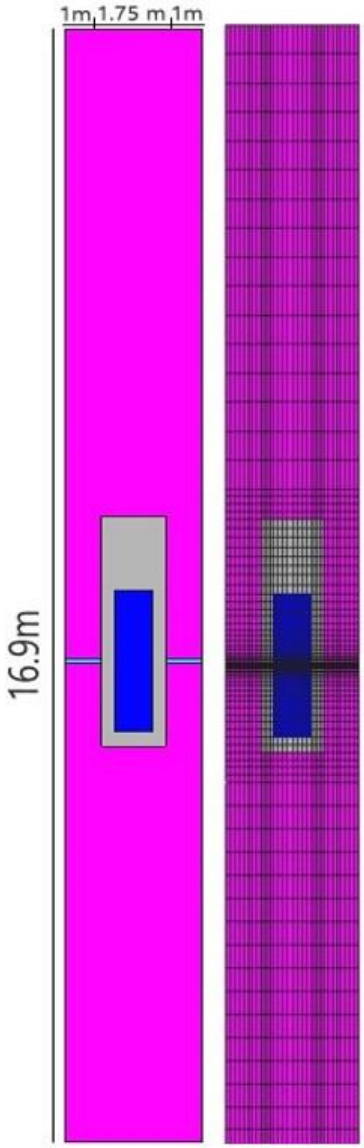

Figure 5-5 Geometry (left, width = 1m) and mesh (right) of the full-scale simulation.

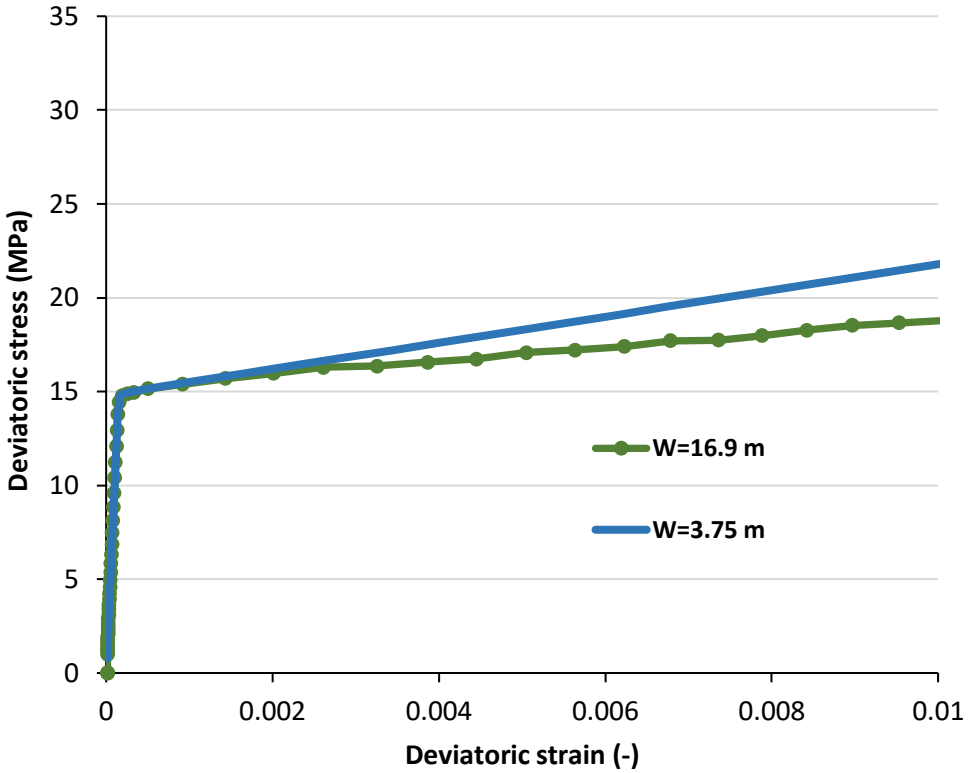

Figure 5-6 Deviatoric stress-strain curves in different widths for copper (B).

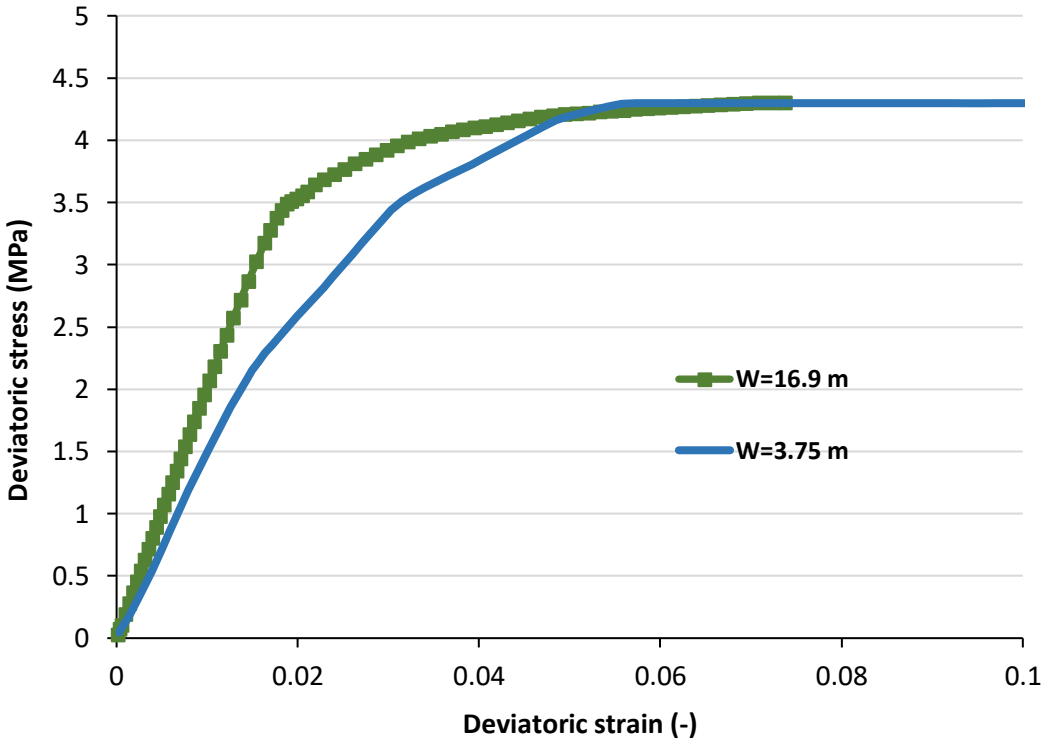

Figure 5-7 Deviatoric stress-strain curves in different widths for bentonite (A).

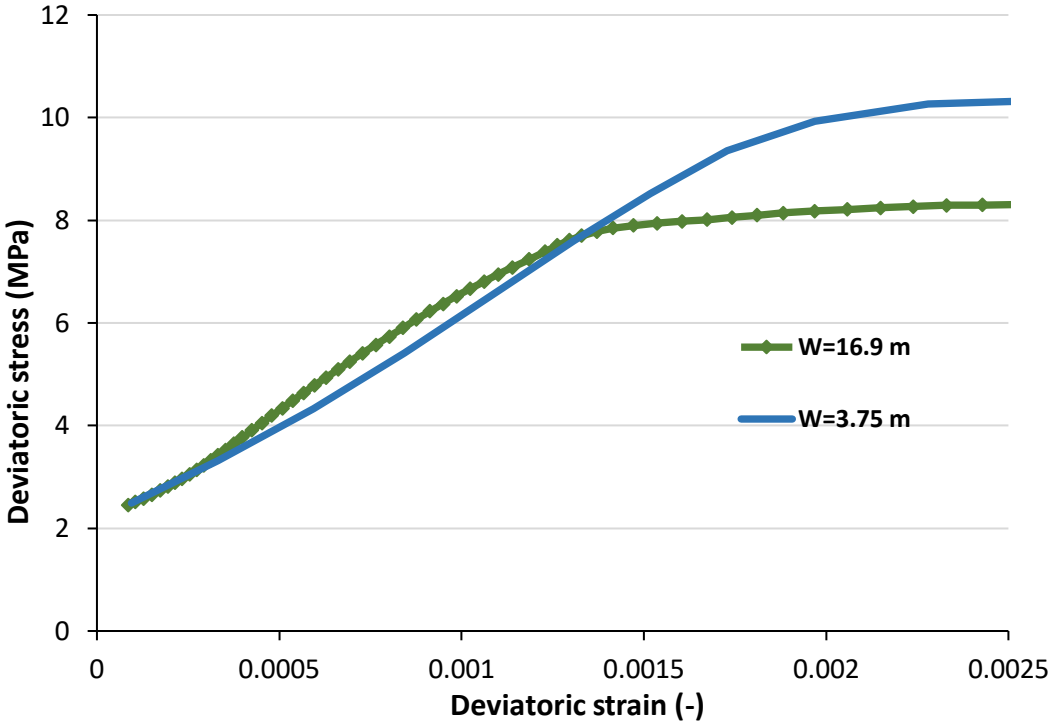

Figure 5-8 Deviatoric stress-strain curves in different widths for rock (Point C).

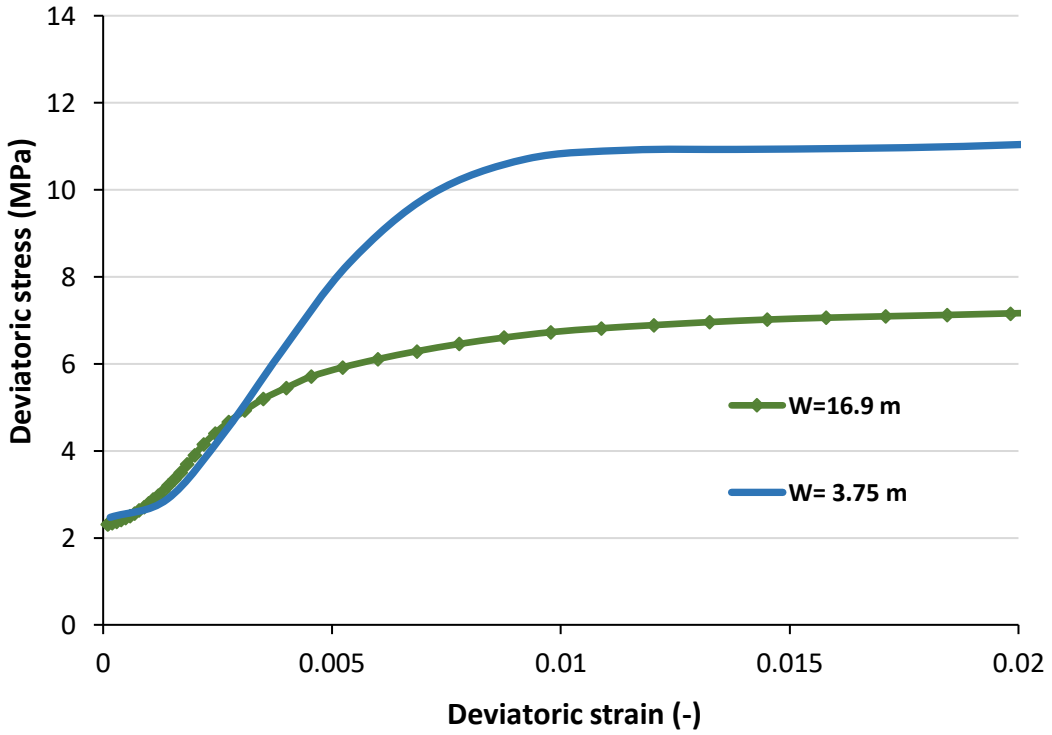

Figure 5-9 Deviatoric stress-strain curves in different widths for discontinuity (Point D).

In consequence:

- Both widths have the same deviatoric stress in the elastic part for copper, but the green line (w=16.9 m) has more deviatoric stress in the plastic part than the blue line (w=3.75 m) (Figure 5-6).
- For bentonite, the green line (w=16.9 m) has higher deviatoric stress than the blue line (w=3.75 m) before the 0.05 deviatoric strain. After that, the deviatoric stress in widths is almost identical (Figure 5-7).
- The blue line (w=3.75 m) has less deviatoric stress than the green line (w=16.9 m) for rock before 0.0014. Following that, the green line (w=16.9 m) has less deviatoric stress than the blue line (w=3.75 m) (Figure 5-8).
- For discontinuity, deviatoric stress in both widths is roughly the same until the deviatoric strain of 0.004, and then the blue line (w=3.75 m) has greater strength than the green line (w=16.9 m) in proceeding (Figure 5-9).

5.1.1.3 Difference between rock or without a rock in 2D shear test modeling

According to Figure 5-5, a full-scale canister and clay system with rock has been mechanically analyzed, and the findings have been compared to the canister-clay simulation without rock.

Points A and B in Figure 4-21 are chosen for bentonite and copper analysis, respectively. Deviatoric stress-strain curves demonstrate in Figure 5-10 and Figure 5-11.

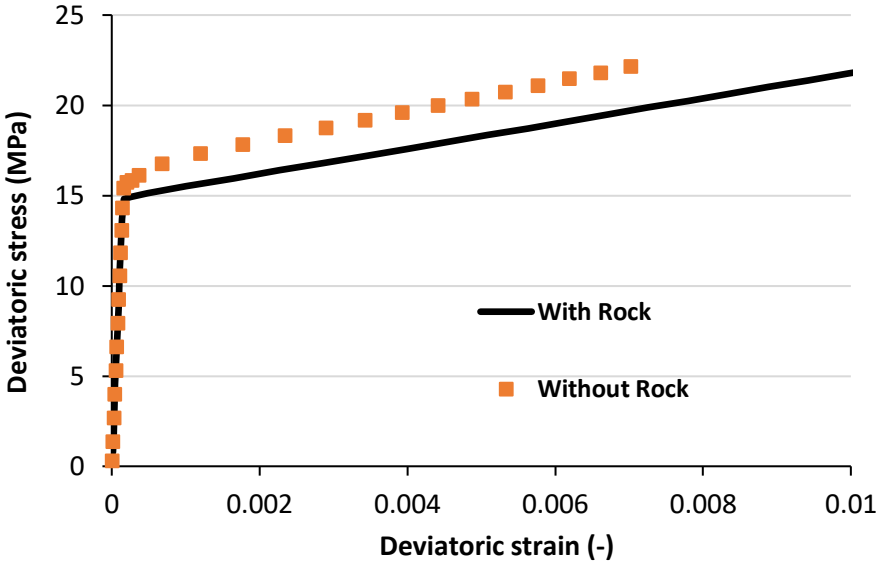

Figure 5-10 Comparison between shear test with rock and without rock for copper (Point B).

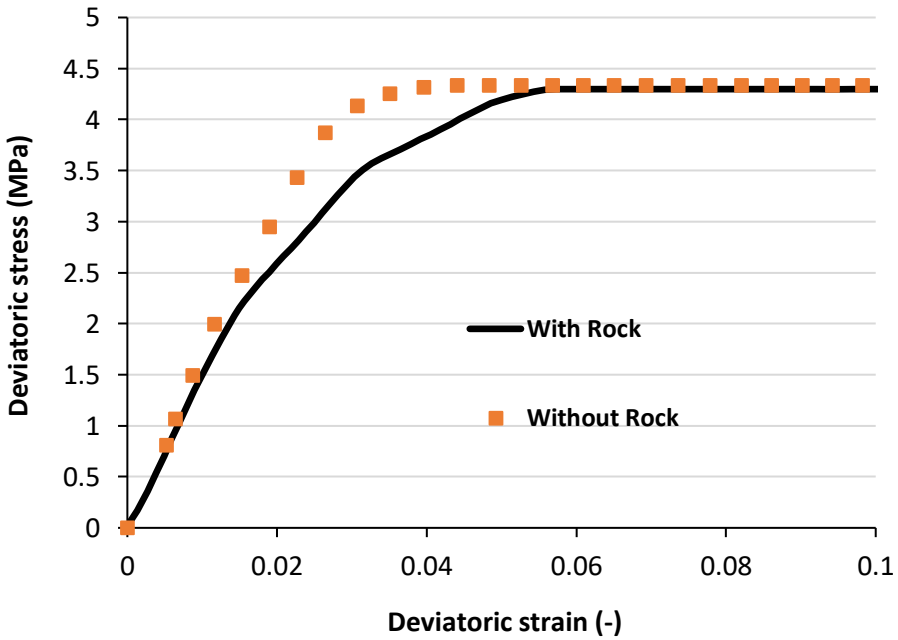

Figure 5-11 Comparison between full-scale shearing with rock and without rock for bentonite (Point A).

According to Figure 5-10 for copper, deviatoric stress in the shear test with rock is lesser than deviatoric stress without rock but for bentonite in Figure 5-11, the variation in deviatoric stress is very small.

5.1.1.4 Full-scale shear modeling using hydro-mechanical coupling in 2D

A coupled hydro-mechanical method has been used to model the behavior of porous geological media, and it is also applicable to modeling coupled HM processes in rock and discontinuities.

It is essential to consider the coupled hydro-mechanical (HM) behavior of a porous medium when evaluating future bentonite, rock, and discontinuity for the disposal of high-level radioactive waste.

Table 5-6 Input parameters of the bentonite in HM coupling (Alonso et al., 1990; DIT-UPC, 2021).

BBM Model	ν	-	0.3	Poisson's Ratio
	K_{min}	MPa	10	Minimum bulk modulus
	κ_{s0}	-	0	The initial elastic slope for specific volume-suction
	κ_{i0}	-	0.05	The initial elastic slope for specific volume-mean stress
	λ(0)	-	0.15	The slope of void ratio-mean stress curve at zero suction
	r	-	0.8	Parameter defining the maximum soil stiffness
	β	$(\mathrm{MPa})^{-1}$	0.02	Parameter controlling the rate of increase of soil stiffness with suction
	p^c	MPa	0.1	Reference pressure
	p_0^*	MPa	10	Initial preconsolidation mean stress for saturated soil
	M	-	1.07	Critical state line parameter

To simulate the complex coupling mechanism, a coupled hydro-mechanical model for porous media is needed, which is based on solving the mass balance equation with Darcy's law for advective fluid flow and Fick's law for non-advective fluid flow, as well as the equation of stress equilibrium for complex plastic and viscoplastic constitutive models. Porous media has been considered for all materials in CODE BRIGHT, and the porous medium in this work is homogeneous and isotropic. The bentonite, rock, and discontinuity have all reached saturation. Throughout the domain, there is local thermal equilibrium. The BBM model for bentonite is also used.

Dimensions and boundary conditions in HM modeling are identical to dimensions and boundary conditions in mechanical analysis. There is no flow at the hydraulic boundary condition (impervious boundary). At first, the MX-80 bentonite clay is fully saturated. The degree of saturation is proportional to the amount of water present, as well as the dry density and solids density (Villar & Lloret, 2008). The porosity is related directly to the dry density (Ghrieb et al., 2014; Herrmann & Bucksch, 2014; Stange & Horn, 2005).

$$S_r = \frac{{}^{w}/_{\rho_w}}{{}^{1}/_{\rho_d} - {}^{1}/_{\rho_{solid}}} \tag{5.1-1}$$

$$\phi = 1 - \frac{\rho_d}{\rho_{solid}} \tag{5.1-2}$$

In CODE_BRIGHT, assuming that the canister is treated as a porous material and it is provided with extremely low porosity (ϕ) and intrinsic permeability (k_{ii}). The values of porosity and intrinsic permeability are 0.01 and 10^{-27} ($k_{11} = k_{22} = k_{33}$), respectively. The liquid pressure in copper is equal to -35.4 MPa and this is due to the fact that liquid cannot enter into the canister and liquid pressure for bentonite is equal to 4 MPa. On the other hand, the liquid pressure of the canister-clay interface is 4 MPa because the water is out of the copper, and the copper is under the liquid pressure of the bentonite. According to Figure 5-13, it is assumed the liquid pressure on top of the geometry is 4 MPa because this model is placed underground and has a high depth ($\sim 400\ m$).

The liquid pressure for rock and discontinuity changed linearly as follows:

Table 5-7 Liquid pressure of rock and discontinuity.

From	Until
Height = 0	Height=37.71
$\boldsymbol{P_l = 4\ \mathbf{MPa}}$	$P_l = 4.37$ MPa

The liquid pressure for a canister is -35.4 MPa and the system is confined due to the swelling pressure. It is shown in Figure 5-13. Neither the air balance equation nor the energy balance equation is solved, so gas pressure and temperature are constant. The gas pressure is fixed in 0.1 MPa and temperature in $20^{\circ}C$. Initial porosity for all materials is referred to in Figure 5-14.

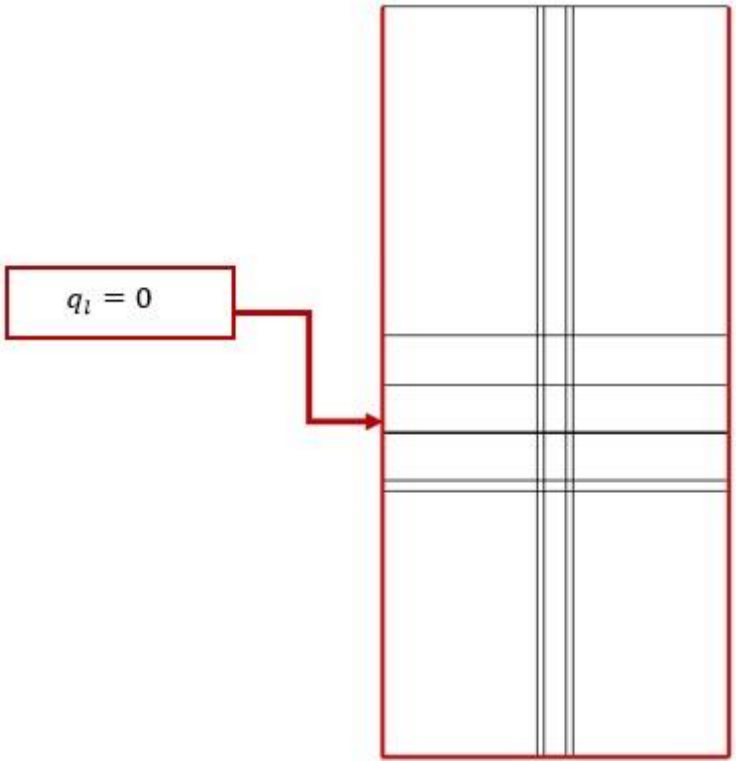

Figure 5-12 Flux boundary condition.

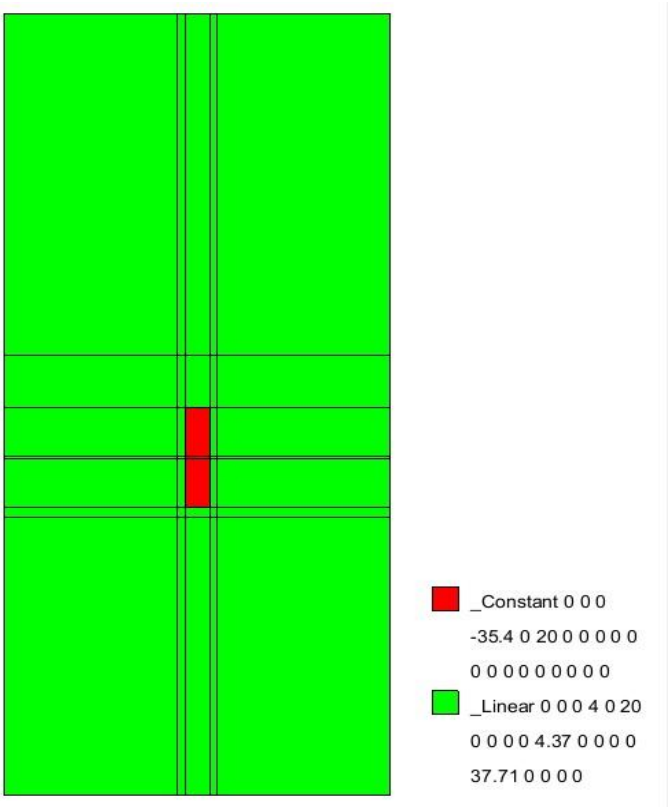

Figure 5-13 The liquid pressure (P_l) in the initial unknown.

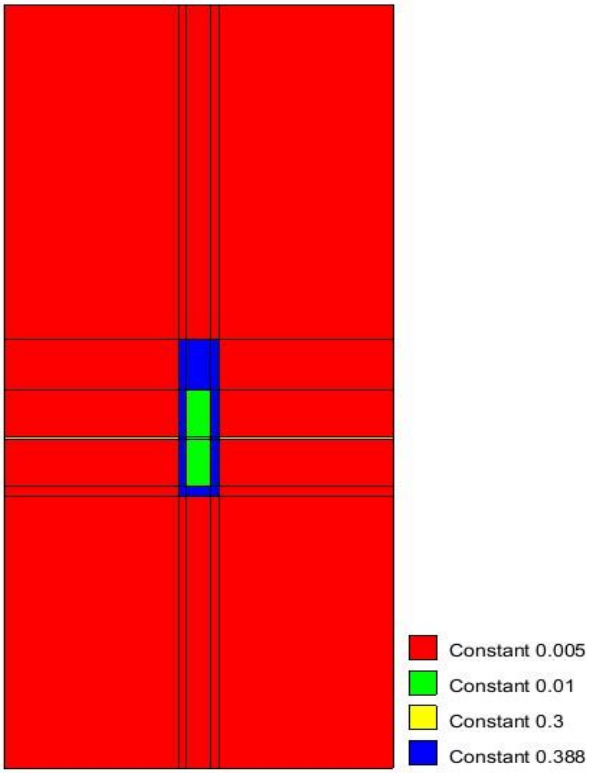

Figure 5-14 Initial Porosity in the canister-clay system.

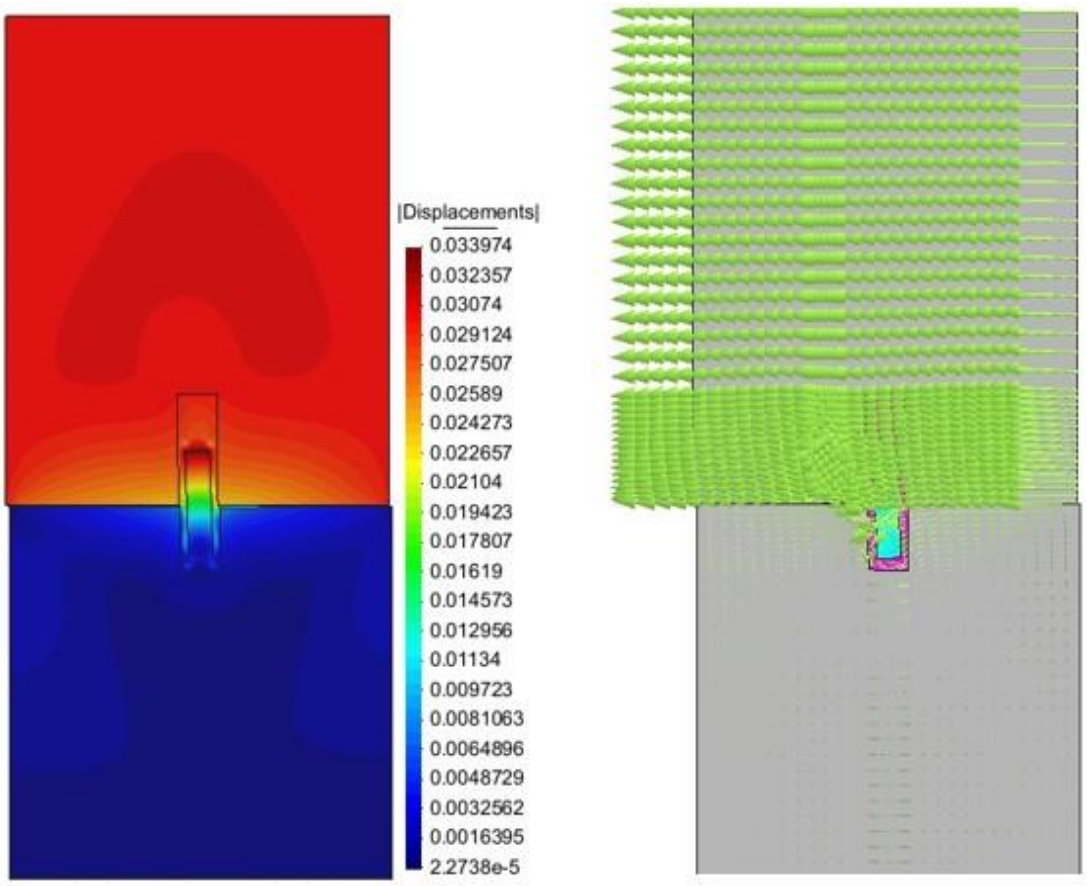

Figure 5-15 Displacement field and display vectors of the model in hydro-mechanical modeling at the end of the test.

Figure 5-15 shows the contour fill of Displacement and Display Vector of the canister-clay system in coupled hydro-mechanical with the amplification factor of 5.0.

5.1.1.5 Sensitivity analysis of permeability

In the hydro-mechanical coupling, for rock and bentonite, the sensitivity analysis of the permeability has been done and described the effects of variation of permeability parameters. Figure 5-17 depicts different Points of A, B, C, and D for analysis of the rock.

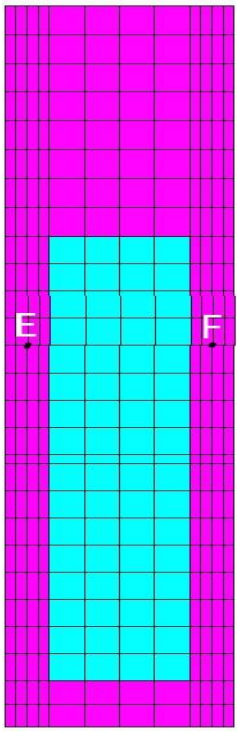

Figure 5-16 Analytical points of bentonite.

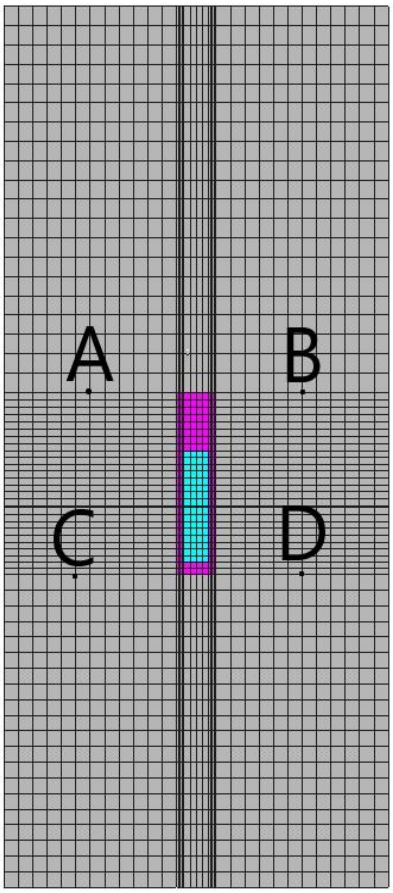

Figure 5-17 Analytical points of rock.

In the beginning, sensitivity analysis on the bentonite permeability in rock and bentonite (Antonio Gens et al., 2009; Toprak et al., 2013; Toprak et al., 2017) is analysed. Points of E and F are shown in Figure 5-16 for analysis of bentonite. With all bentonite permeabilities, the rock permeability is 1.52×10^{-19}. First, liquid pressure with respect to the time in the bentonite permeability of 5.59×10^{-17} is demonstrated in Figure 5-18 and Figure 5-19.

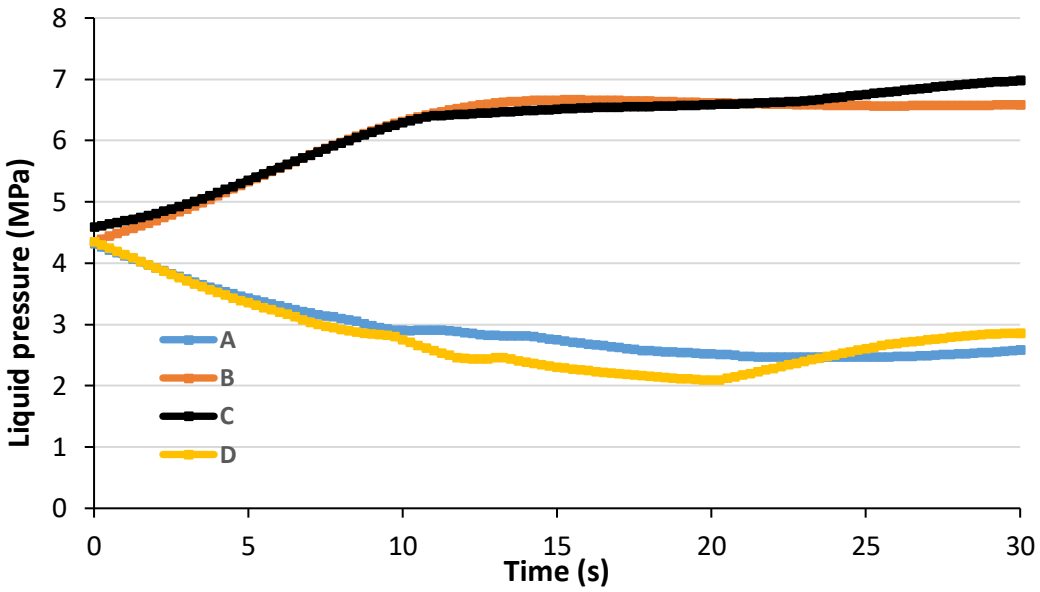

Figure 5-18 Liquid pressure-time curves in rock influenced by the permeability of 5.59×10^{-17} m^2 (bentonite).

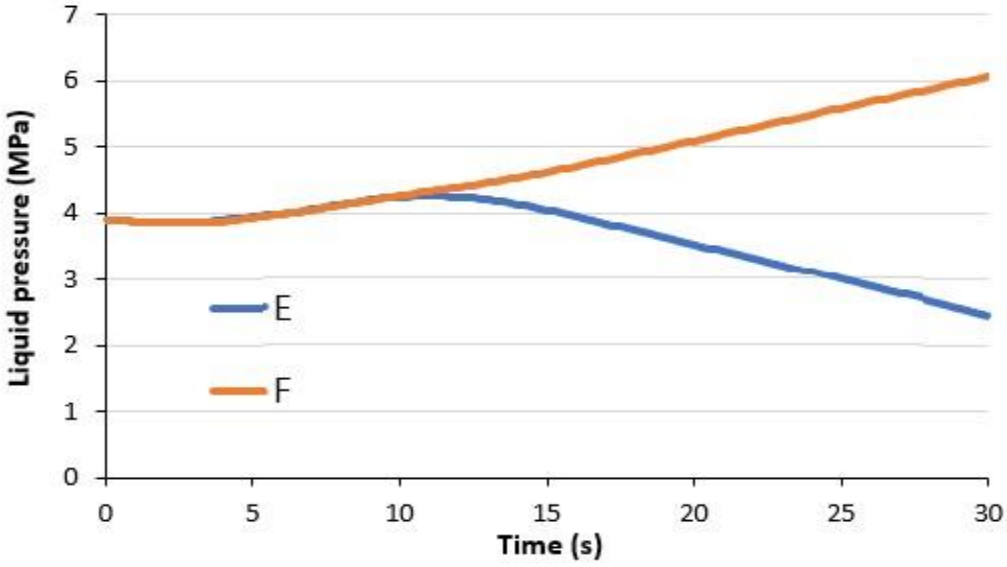

Figure 5-19 Liquid pressure-time curves in bentonite with the permeability of 5.59×10^{-17} m^2.

Then, rock (the rock permeability is 1.52×10^{-19} (Posiva, 2012)) and bentonite with the permeability of 5.59×10^{-18} m^2 are investigated in Figure 5-20 and Figure 5-21, respectively.

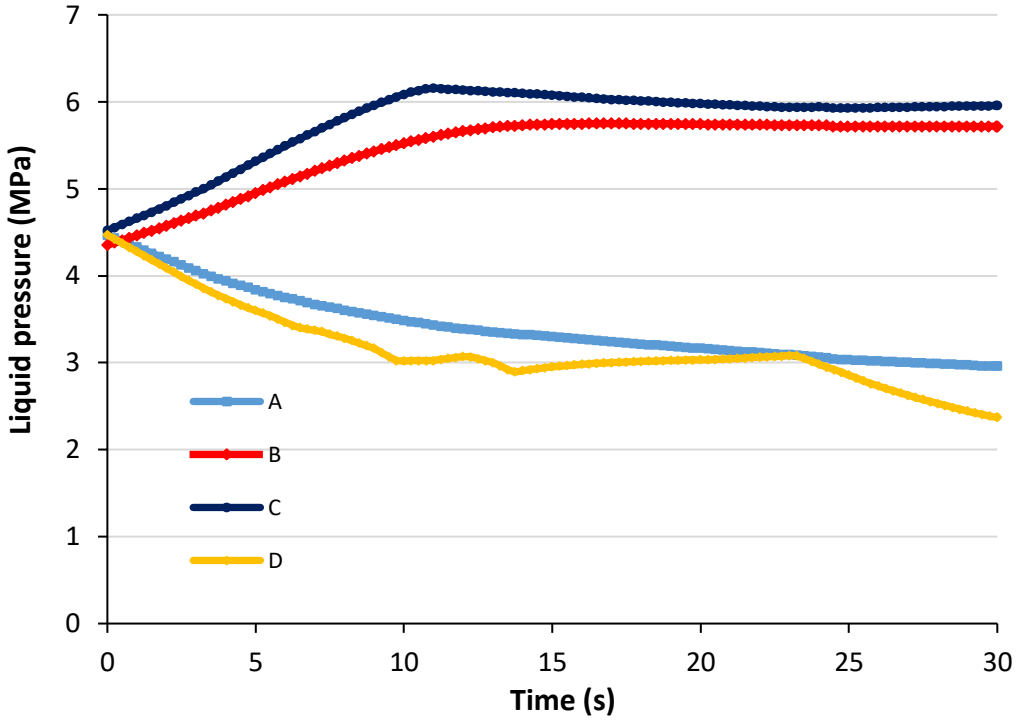

Figure 5-20 Liquid pressure-time curves in rock influenced by the permeability of $5.59\times10^{-18}m^2$ (bentonite).

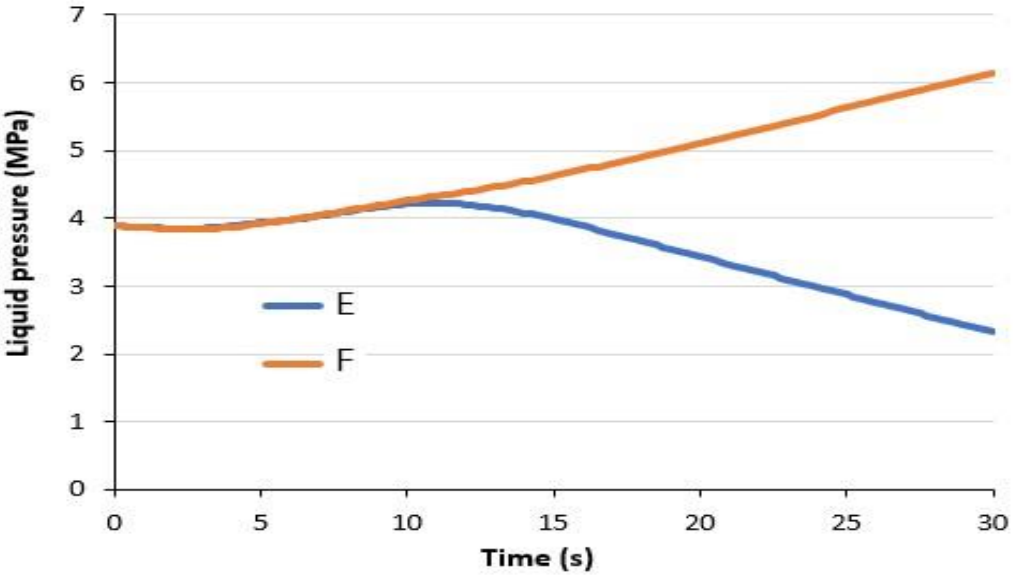

Figure 5-21 Liquid pressure-time curves in bentonite with the permeability of $5.59\times10^{-18}m^2$.

Rock (the rock permeability is 1.52×10^{-19}) and bentonite with the permeability of 5.59×10^{-19} m^2 are checked in Figure 5-22 and Figure 5-23 respectively.

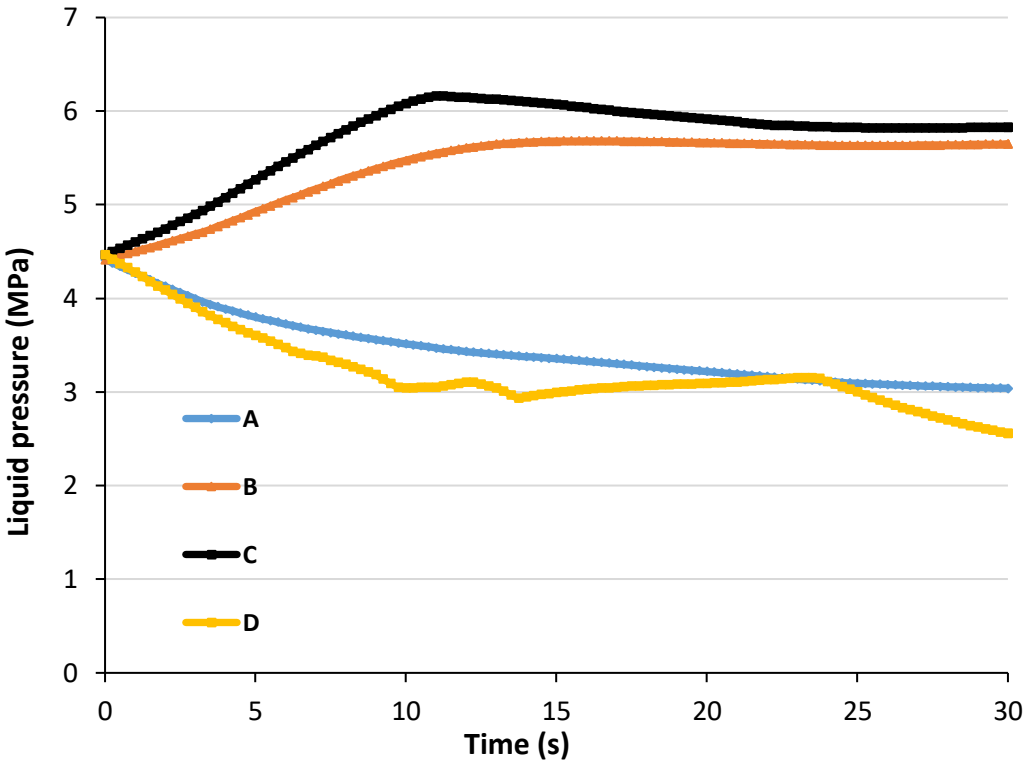

Figure 5-22 Liquid pressure-time curves in rock influenced by the permeability of $5.59\times10^{-19}m^2$ (bentonite).

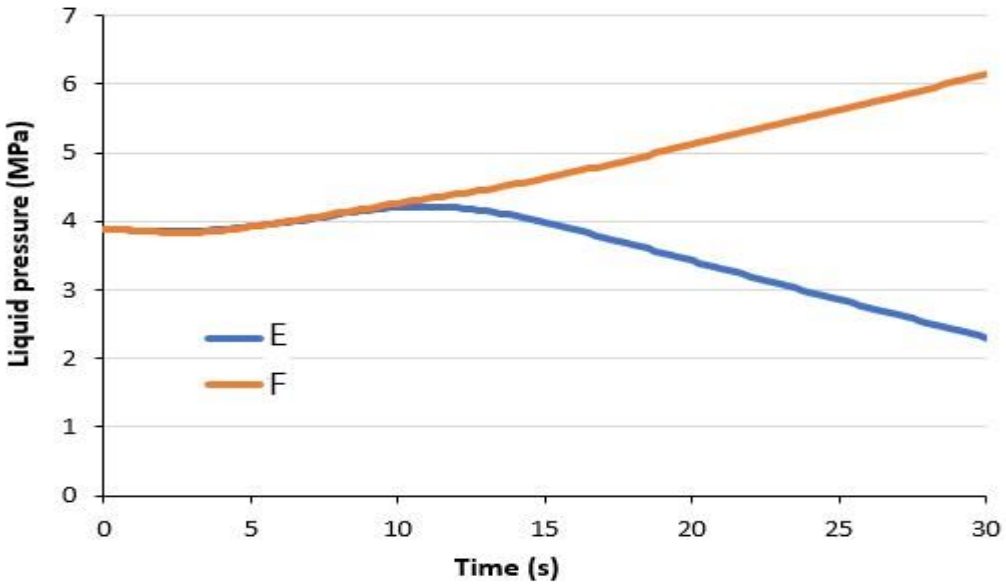

Figure 5-23 Liquid pressure-time curves in bentonite with the permeability of $5.59\times10^{-19}m^2$.

Finally, rock (the rock permeability is 1.52×10^{-19}) and bentonite with the permeability of 5.59×10^{-20} m^2 are analyzed in Figure 5-24 and Figure 5-25 respectively.

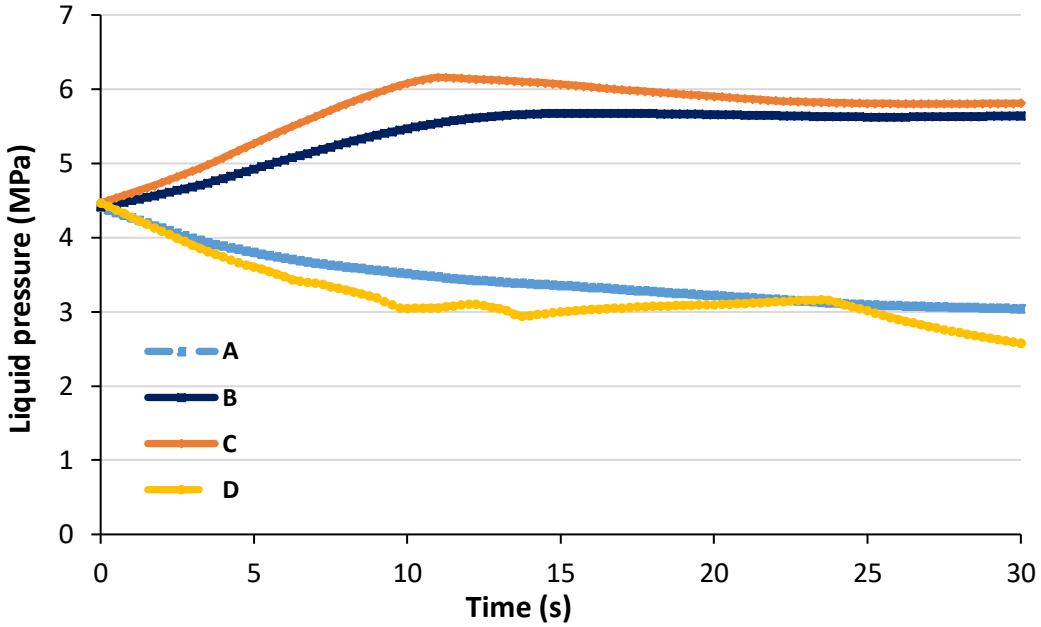

Figure 5-24 Liquid pressure-time curves in rock influenced by the permeability of $5.59\times10^{-20}m^2$ (bentonite).

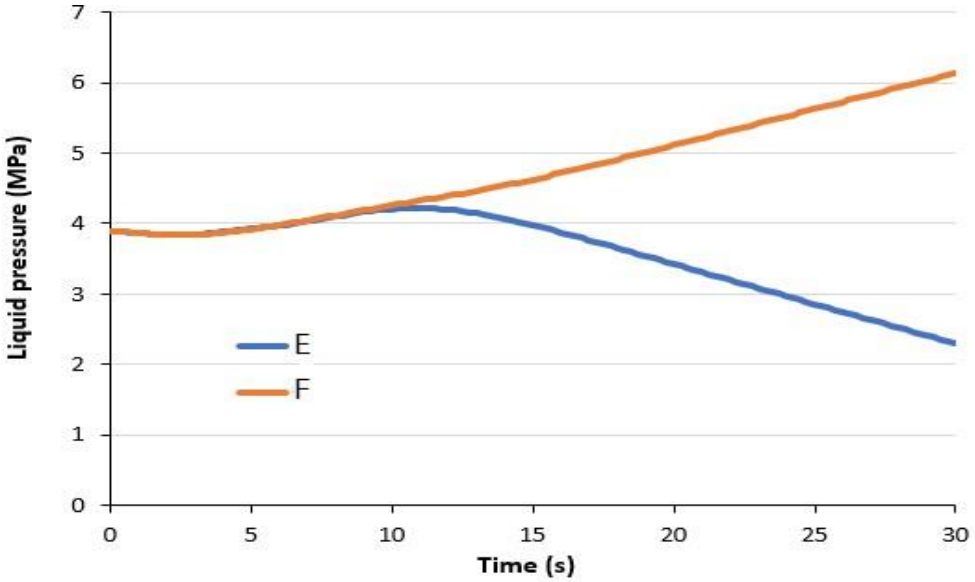

Figure 5-25 Liquid pressure-time curves in bentonite with the permeability of $5.59\times10^{-20}m^2$.

As a result, the three different permeabilities of bentonite, in this case, have a negligible effect on liquid pressure concerning the time on rock and bentonite.

In continuous. sensitivity analysis of rock permeability for 4 points has been done and it is exposed in Figure 5-26, Figure 5-27, Figure 5-28, and Figure 5-29, respectively (Toprak et al.,

2013; Toprak et al., 2017). The bentonite permeability of 5.59×10^{-19} is considered for this sensitivity.

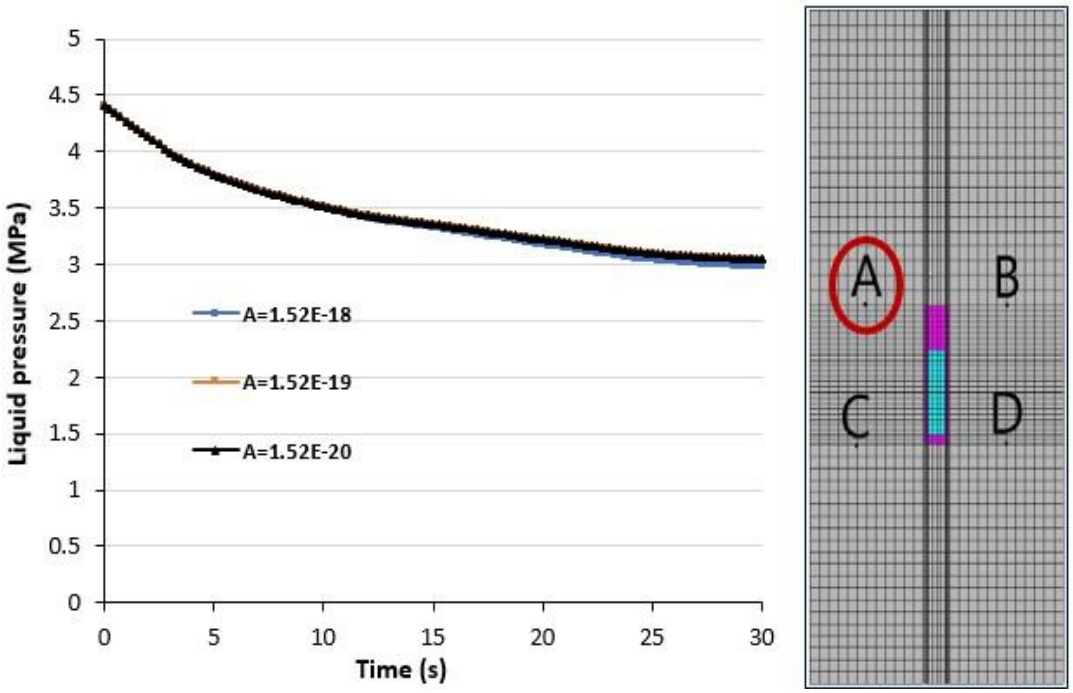

Figure 5-26 Liquid pressure-time curves for all permeabilities (point A).

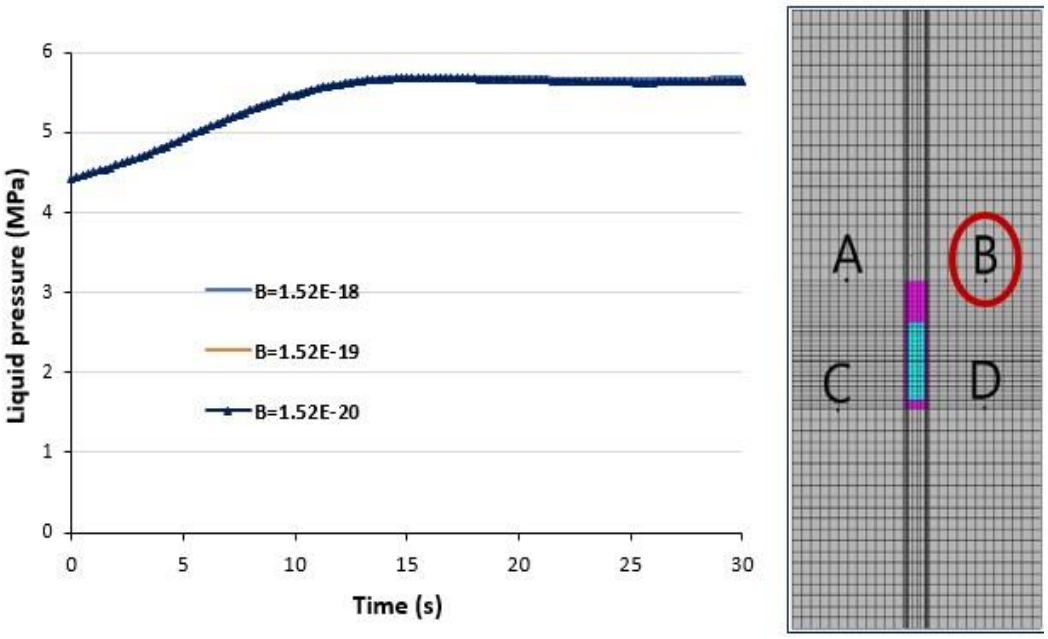

Figure 5-27 Liquid pressure-time curves for all permeabilities (point B).

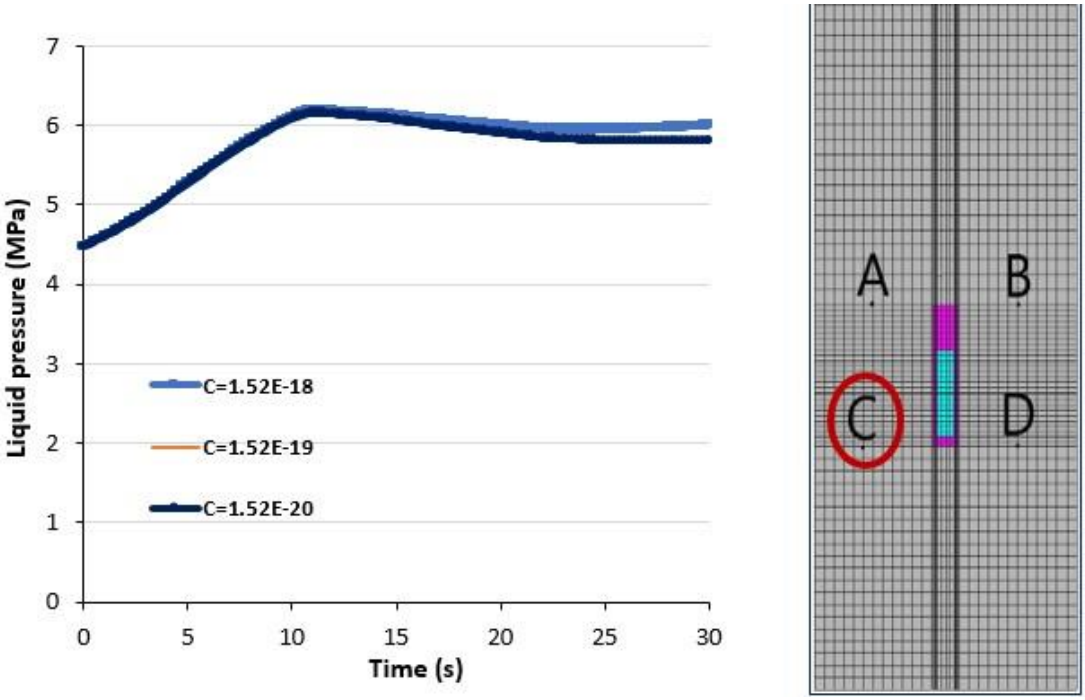

Figure 5-28 Liquid pressure-time curves for all permeabilities (point C).

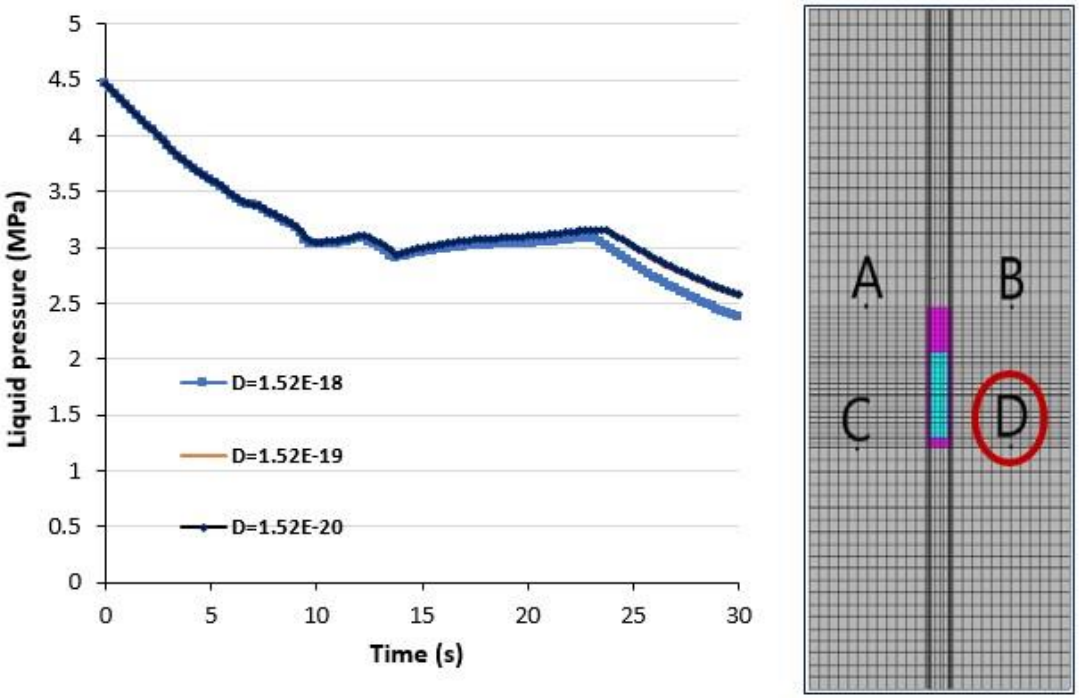

Figure 5-29 Liquid pressure-Time curves for all permeabilities (point D).

In conclusion, it is expected that liquid pressure on different points is not equal. In points A and D, by increasing the time the liquid pressure becomes low but for points, B and C is inverse when the time is increasing then the liquid pressure is increasing as well. All

permeabilities in rock have the same liquid pressure at the same point and in continuous, the liquid pressure curves in the same point for different permeabilities are shown.

5.1.2 Comparison between the mechanical analysis and hydro-mechanical coupling in 2D

In this section, a comparison between the mechanical analysis and the coupled hydro-mechanical analysis in the view of the deviatoric stress has been investigated in full-scale. In the mechanical analysis, Γ_0 is equal to 10^{-3} for rock, bentonite, and discontinuity, and in the hydro-mechanical coupling, the permeability is equal to 5.59×10^{-20} m^2, 1.52×10^{-20} m^2, 1.52×10^{-16} m^2 (Gens et al., 2009; Toprak et al., 2013; Toprak et al., 2017) for bentonite, rock, and discontinuity, respectively. Points A, B, C, and D in Figure 5-1 for bentonite, copper, rock, and discontinuity are being sorted out to check analysis in respectively. In mesh, the number of elements and nodes are 2412 and 2516 in respectively.

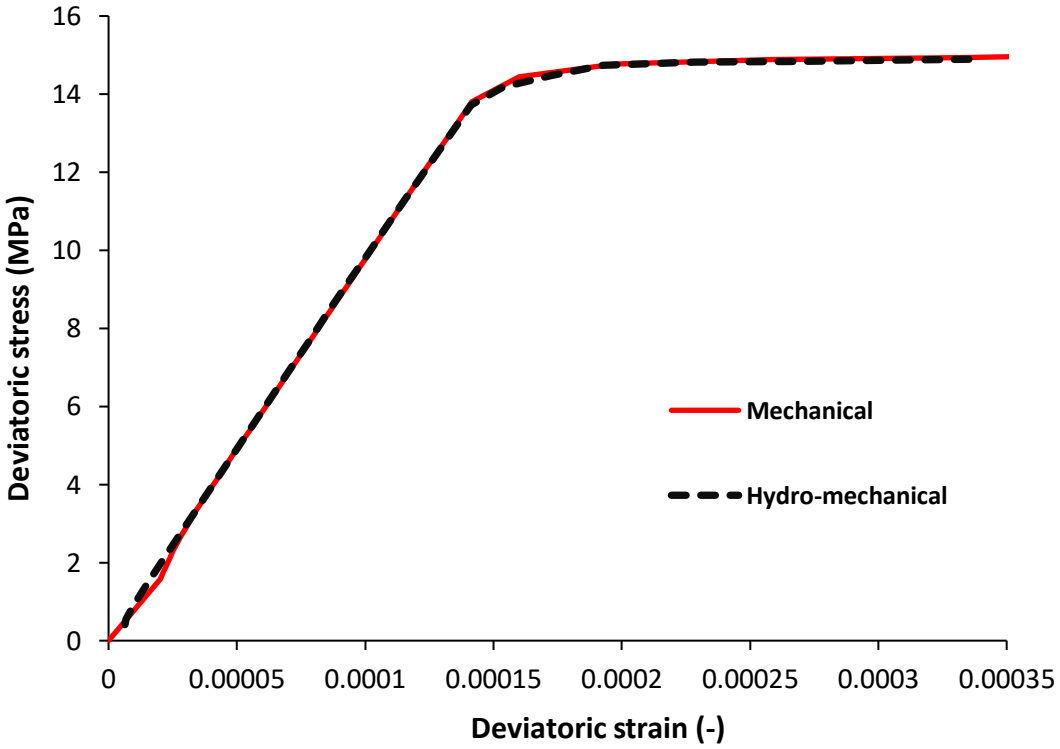

Figure 5-30 Deviatoric stress- deviatoric strain curves for copper (Point B).

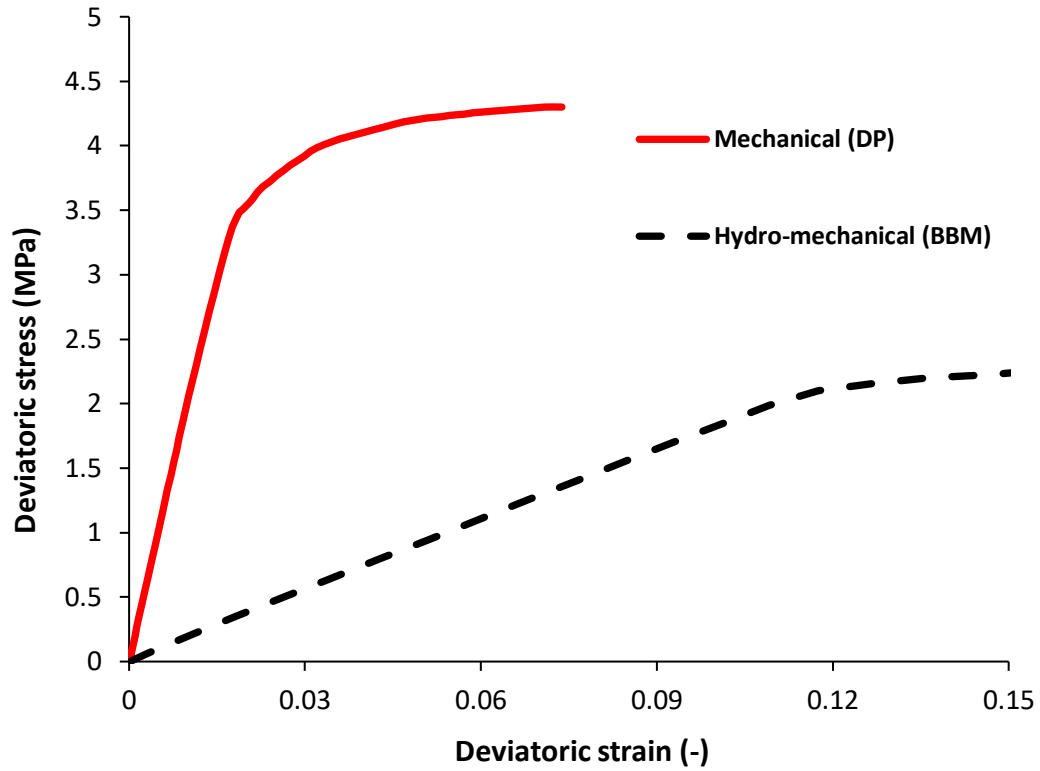

Figure 5-31 Deviatoric stress- deviatoric strain curves for bentonite (Point A).

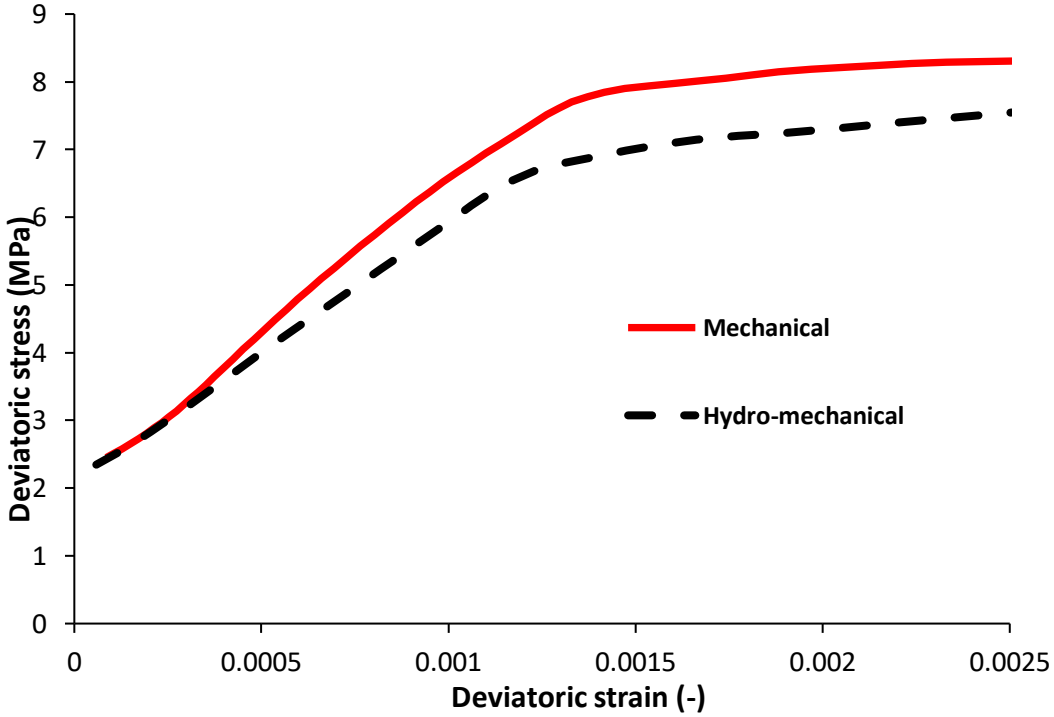

Figure 5-32 Deviatoric stress- deviatoric strain curves for rock (Point C).

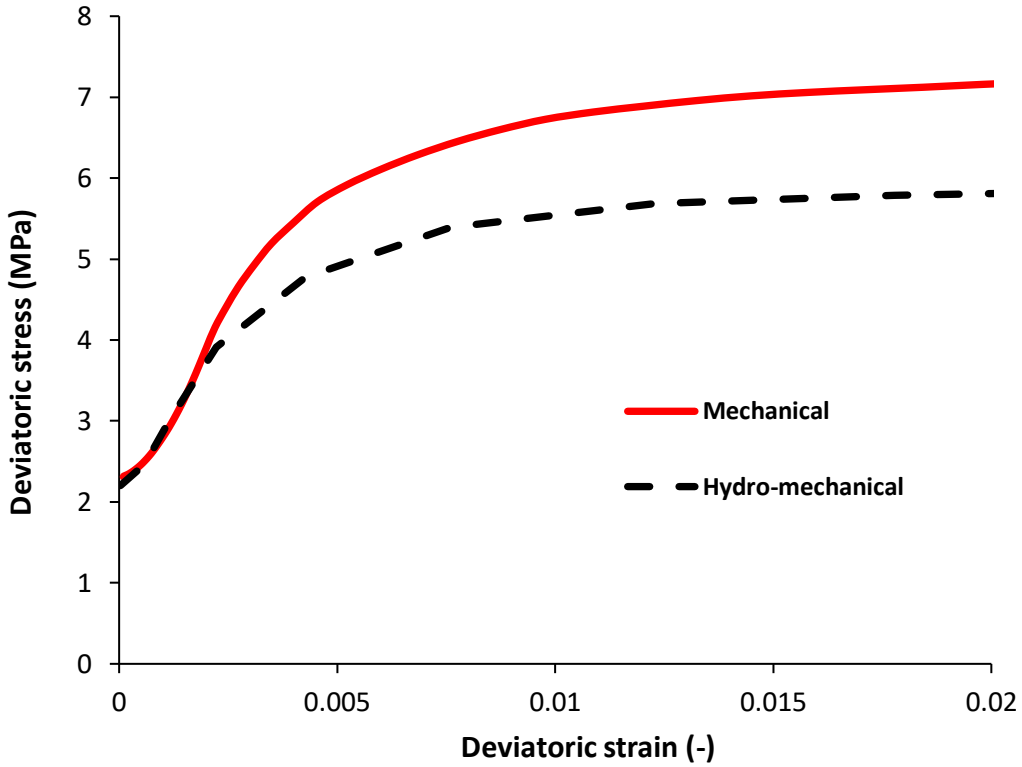

Figure 5-33 Deviatoric stress- deviatoric strain curves for discontinuity (Point D).

In conclusion, deviatoric stress in copper (Figure 5-30) for mechanical analysis and coupled hydro-mechanical analysis is the same but for rock (Figure 5-31), bentonite (Figure 5-32), and discontinuity (Figure 5-33), the deviatoric stress in the mechanical analysis is more than the deviatoric stress in hydro-mechanical coupling.

5.2 Application of Discontinuity in 3D Numerical Modelling of Shear Test

5.2.1 Full-scale

The full-scale shearing has been simulated in three dimensions. Mechanical and coupled hydro-mechanical analyses are considered and compared together. Shearing in 30 seconds and height, width, and boundary conditions are the same as two-dimensional modeling. The thickness of discontinuity (it is a fracture and is not used contact elements) in rock and transition zone between two parts (mobile half and fix half) in bentonite and copper is 10 cm.

The element type is linear tetrahedra with analytical integration and the number of elements and nodes are 21840 and 4755 in respectively. In Figure 5-35, the points A, B, C, and D are chosen for copper, bentonite, rock, and discontinuity in respectively. The assumed initial porosity and initial stress are the same as 2D modeling and they are shown in Figure 5-36 and Figure 5-37 in respectively. Finally, the results in view of plane strain modeling (2D) and 3D modeling have been compared. The geometry is depicted in Figure 5-34.

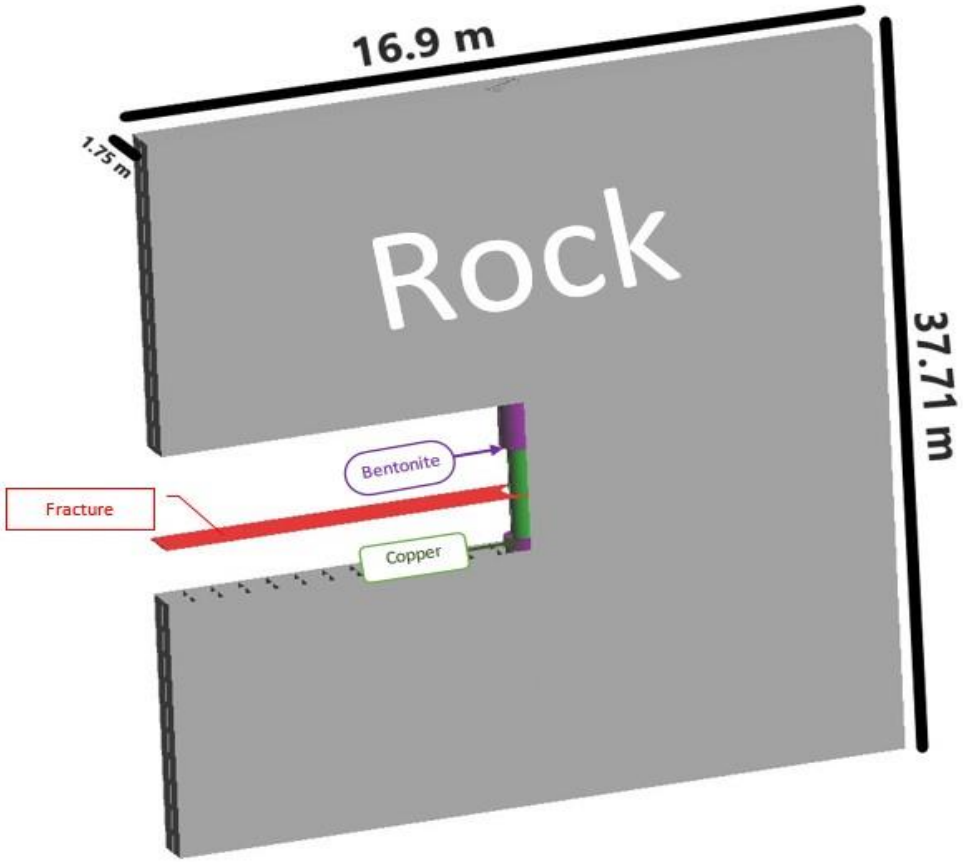

Figure 5-34 The geometry of the shear test.

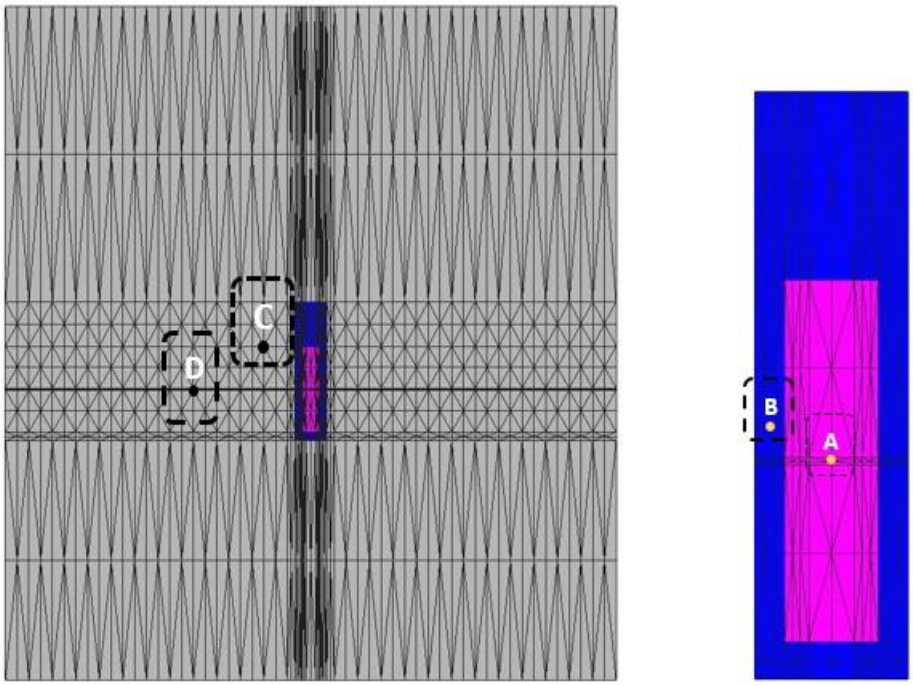

Figure 5-35 Cut in direction of x-z in rock (left shape) and bentonite (right shape).

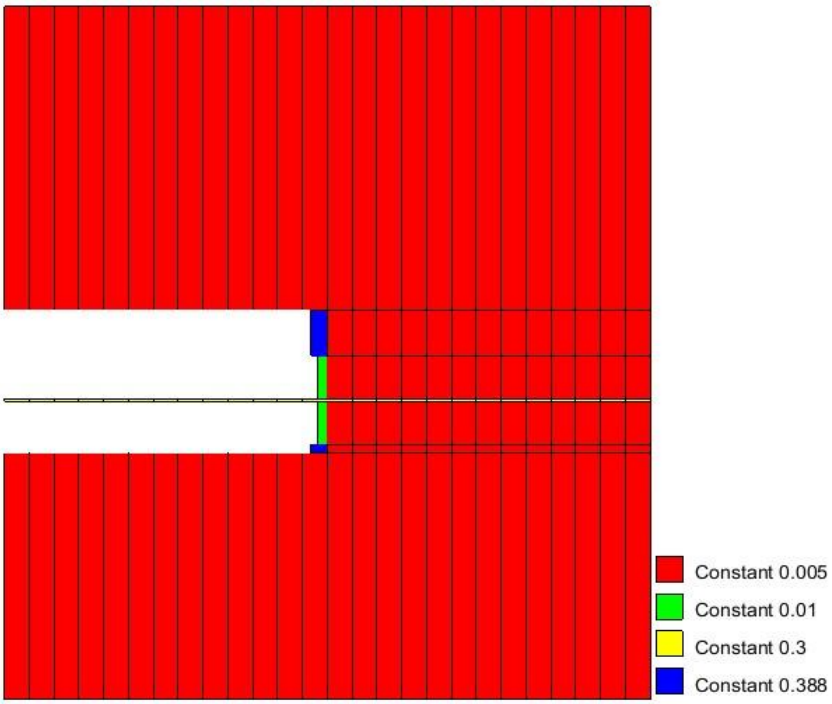

Figure 5-36 Initial porosity of Shear Test.

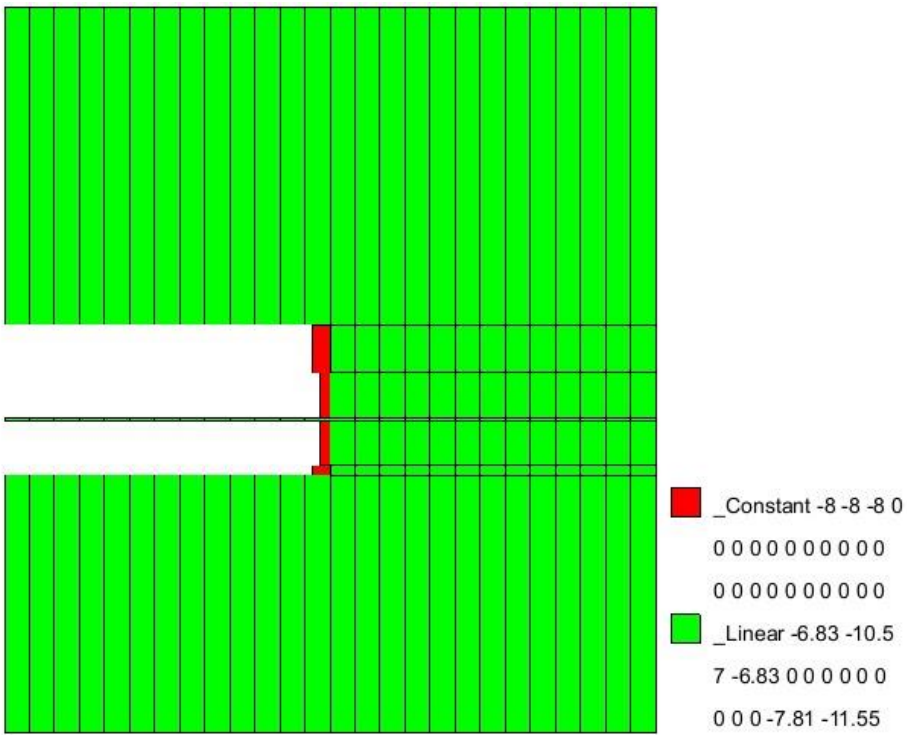

Figure 5-37 Initial stress of Shear Test.

5.2.1.1 Full-scale shear modeling using mechanical analysis in 3D

In the mechanical analysis, stress equilibrium is considered. Contour fill of displacement and display vector with an amplification factor of 10 is referred to in Figure 5-38. Charts of deviator stress-strain for rock, discontinuity, bentonite, and copper are shown in Figure 5-39, Figure 5-40, Figure 5-41, and Figure 5-42 in respectively. The copper takes more deviatoric stress due to high its stiffness and strength. In Figure 5-35, the points A, B, C, and D are selected for copper, bentonite, rock, and discontinuity respectively.

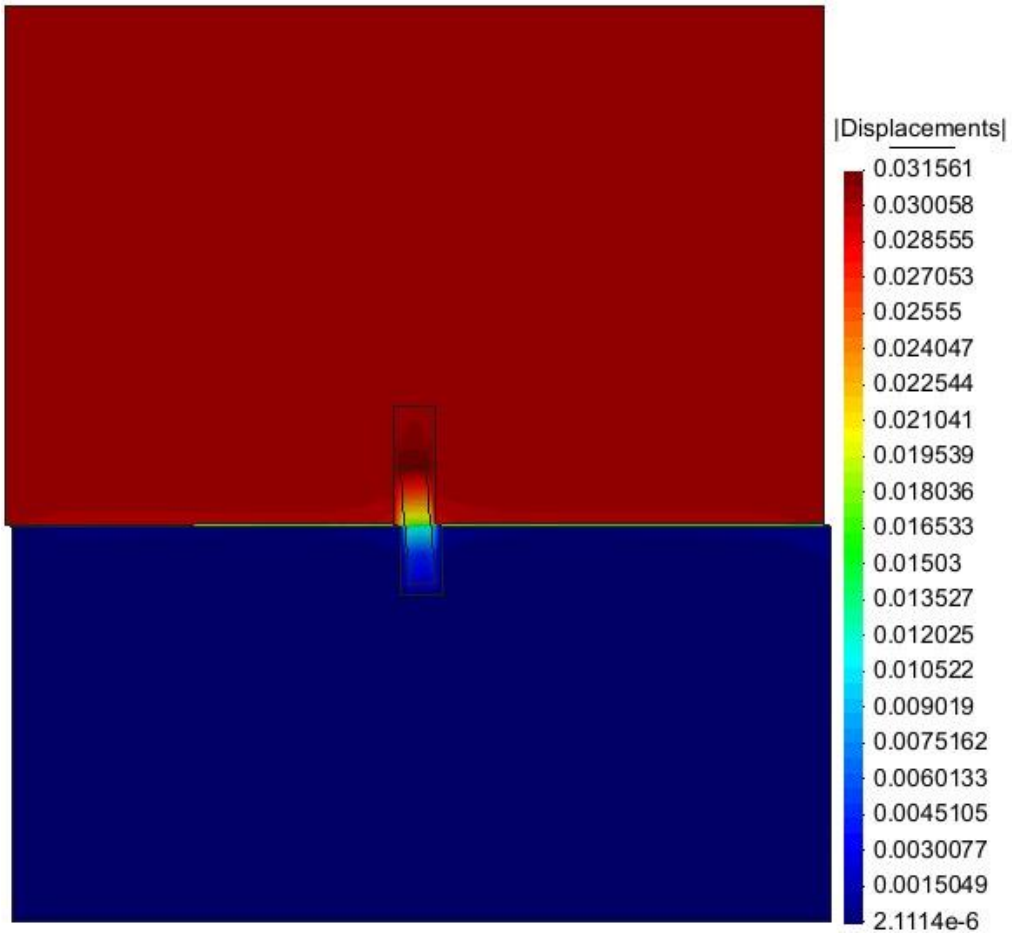

Figure 5-38 Displacements field of the shear test in 3D.

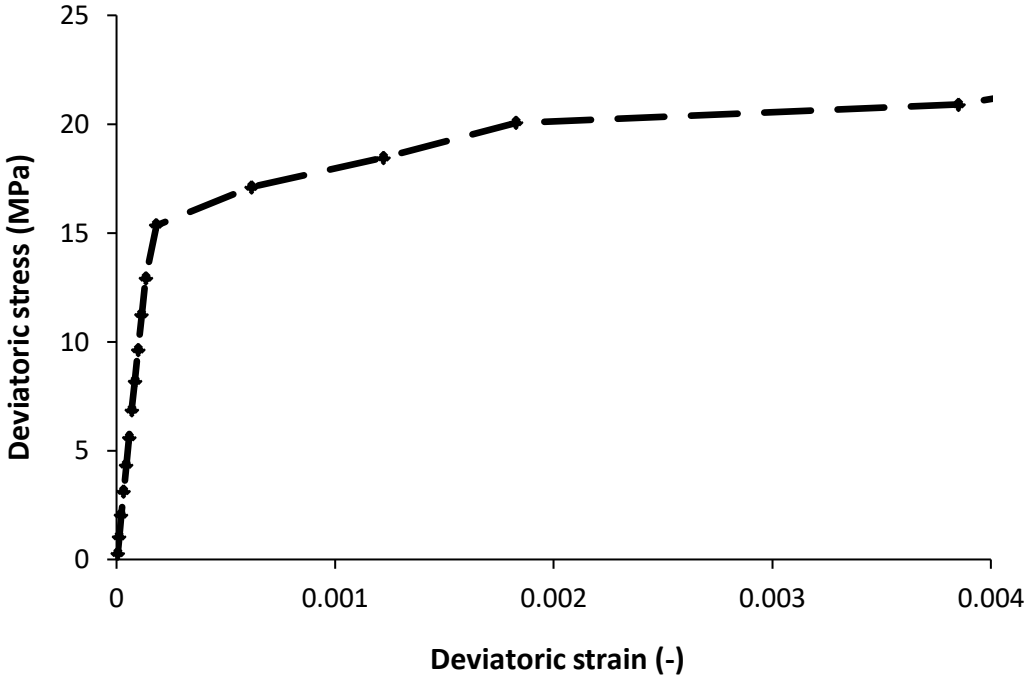

Figure 5-39 Deviator stress-strain curve in real scale for copper (Point A).

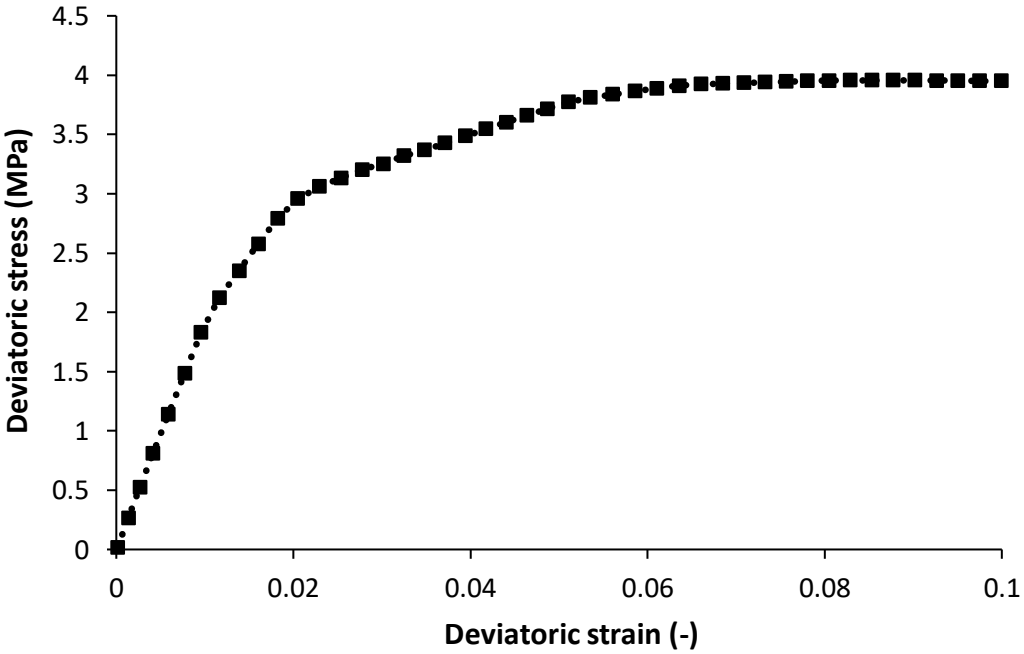

Figure 5-40 Deviatoric stress-strain curve in real scale for bentonite (Point B).

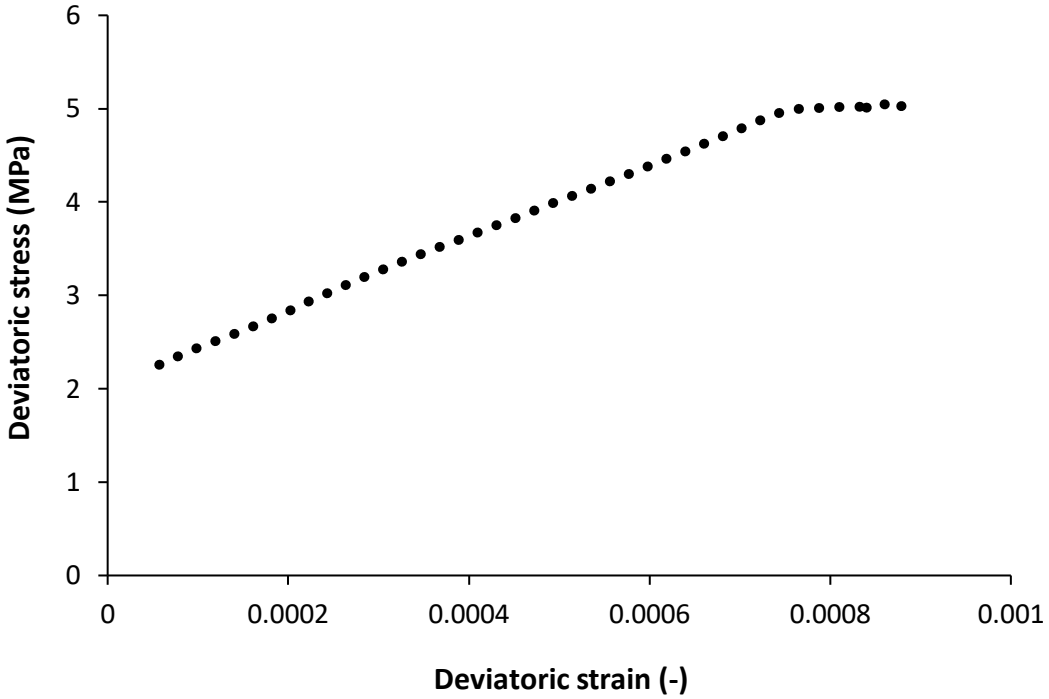

Figure 5-41 Deviatoric stress-strain curve in real scale for rock (Point C).

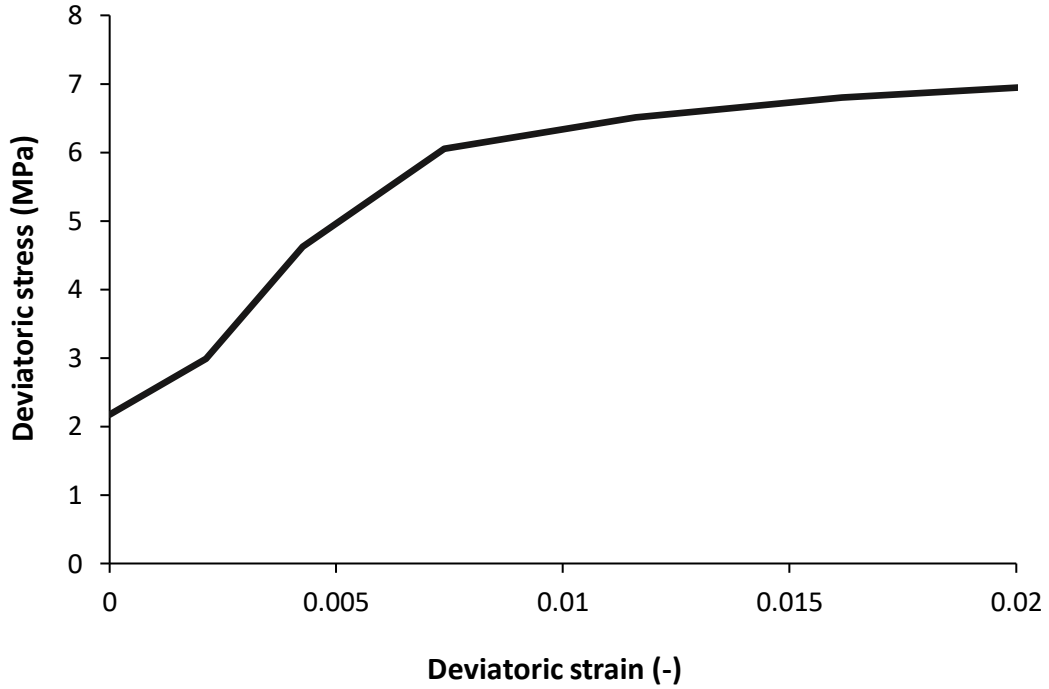

Figure 5-42 Deviatoric stress-strain curve in real scale for discontinuity (Point D).

5.2.1.2 Sensitivity analysis of width in the Y direction

The purpose is to understand the response of deviatoric stress-strain in a different dimension. The two different shear tests in the view of width in the Y direction have been done. According to Figure 5-43, the first shear test has a width of 16.9 m and the number of nodes and elements (hexahedra element) are 48805 and 44856 respectively. The second one has a width of 1.75 m and it is shown in Figure 5-34.

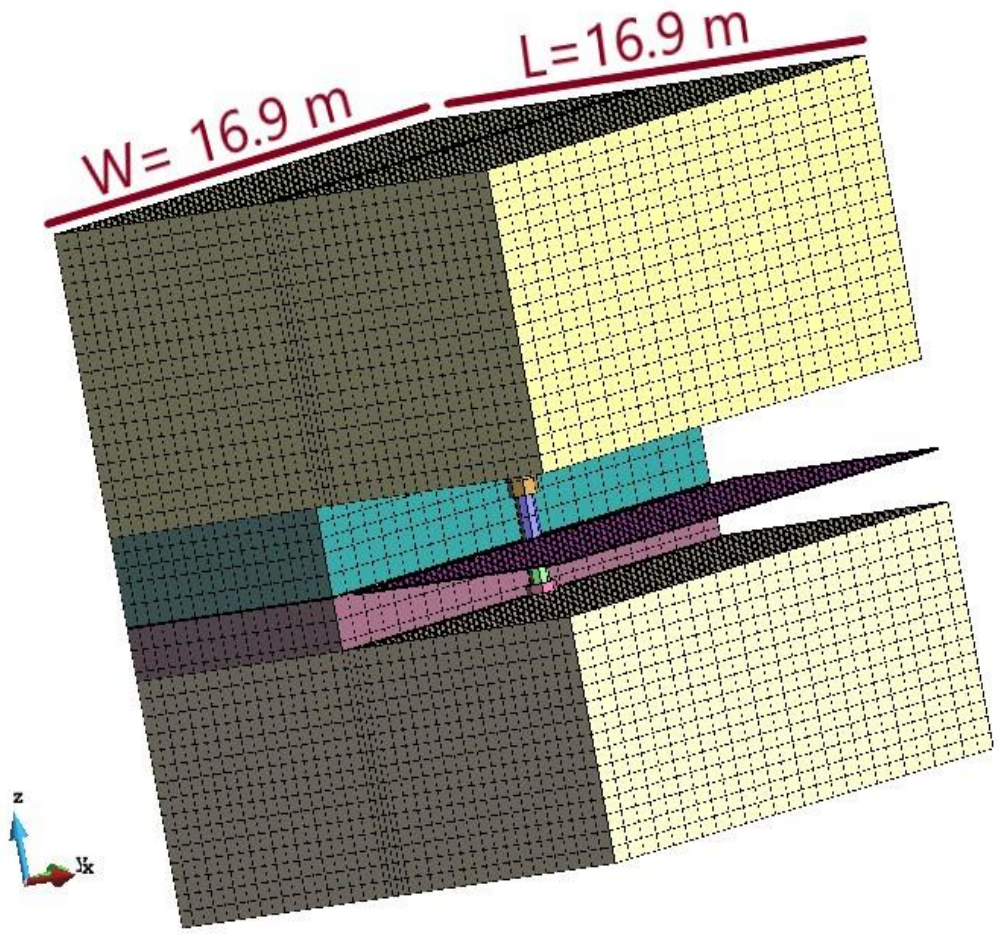

Figure 5-43 Geometry (width = 16.9 m) and mesh of shear test.

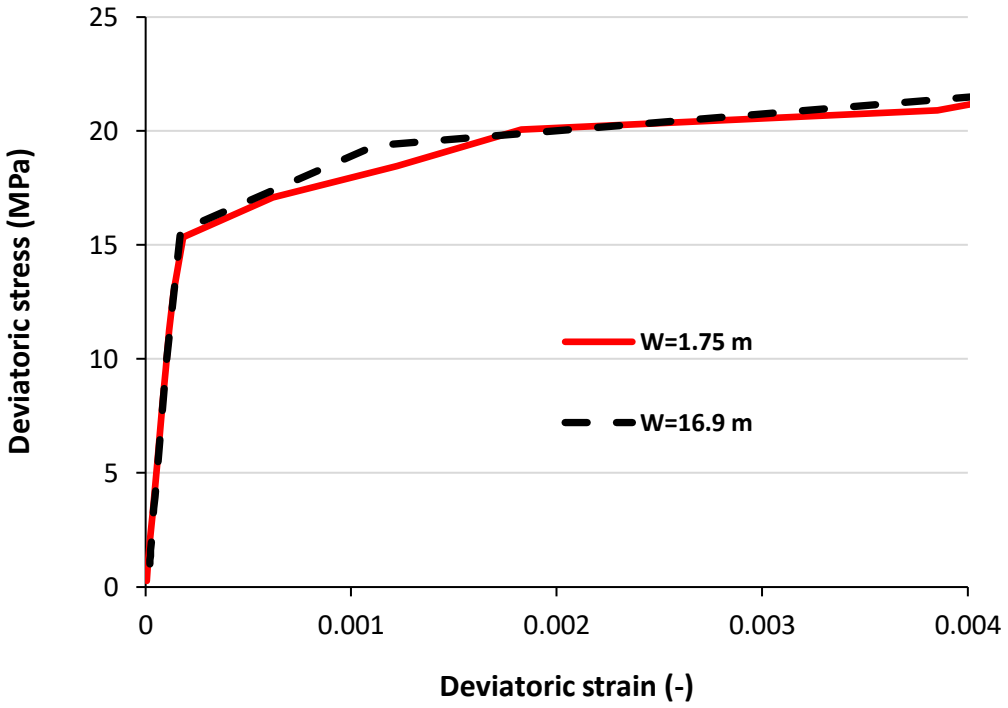

Figure 5-44 Deviatoric stress-strain curves in different widths for copper (Point A).

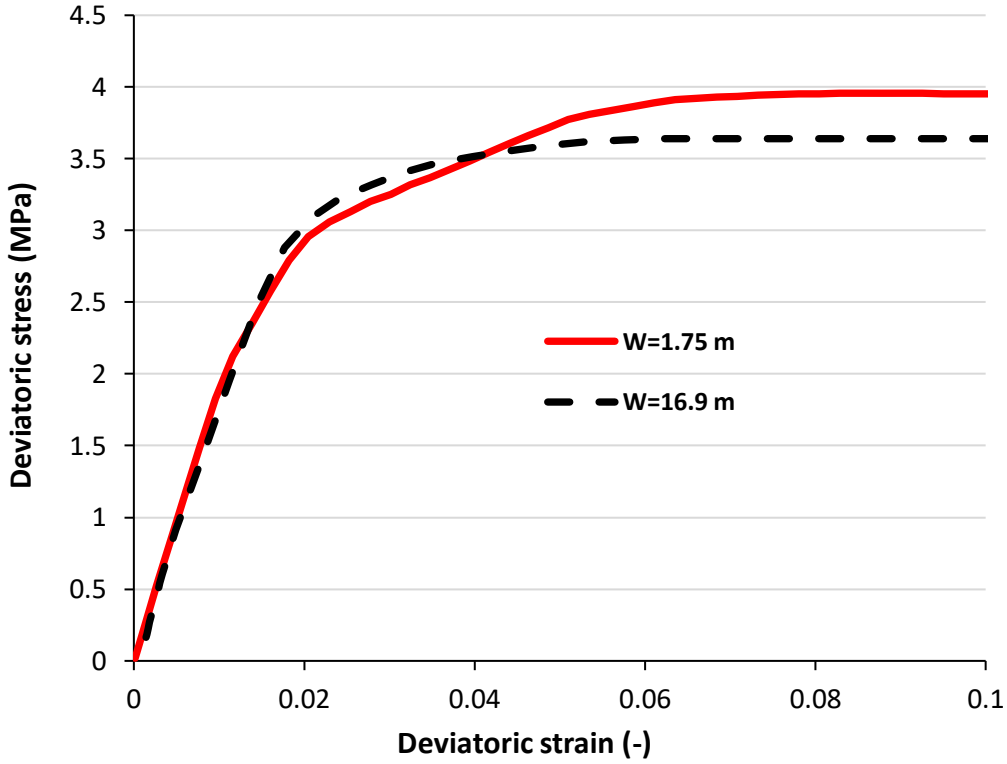

Figure 5-45 Deviatoric stress-strain curves in different widths for bentonite (Point B).

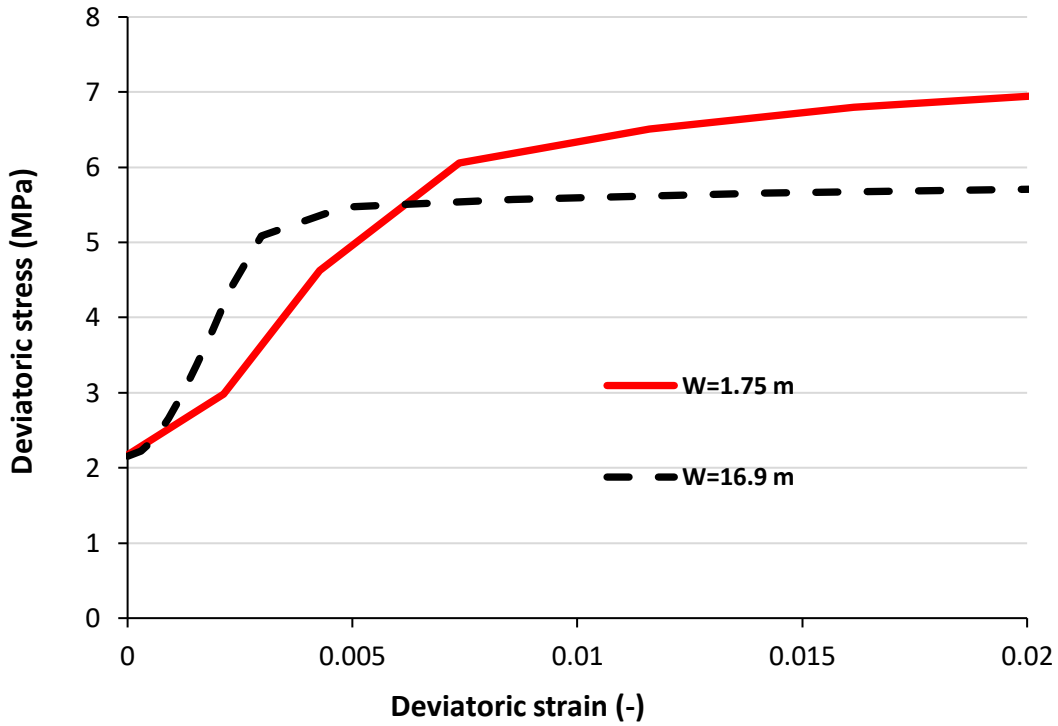

Figure 5-46 Deviatoric stress-strain curves in different widths for discontinuity (Point D).

According to Figure 5-44, deviatoric stress for copper in both models is approximately the same and for bentonite in Figure 5-45, deviatoric stress until the deviatoric strain of 0.04 is equal but more than 0.04, deviatoric stress in width=1.75 m is more than the deviatoric stress in width=16.9 m. Finally, for discontinuity, deviatoric stress in width=16.9 m less than the deviatoric stress in width=1.75 m and it is shown in Figure 5-46.

5.2.1.3 Comparison between 2D and 3D modeling in Mechanical analysis

In a computer workspace, two and three dimensions correspond to the real dimensions. When the horizontal and vertical (X and Y) dimensions are used, the image has just two dimensions and becomes a line when rotated to the side. The depth (Z) dimension of 3D geometry is added. The third dimension enables rotation and representation from a variety of angles.

In present work, deviatoric stress with respect to deviatoric strain is considered in full-scale shear modeling and the obtained results in 2D and 3D are compared together and they are depicted for each material (copper, bentonite, rock, and discontinuity) in Figure 5-47, Figure 5-48, Figure 5-49 and Figure 5-50 in mechanical analysis. In the deviatoric stress-deviatoric strain curves, deviatoric stresses in 3D are more than deviatoric stresses in 2D for copper but in the rock, discontinuity, and bentonite, the deviatoric stresses in 3D are less than the deviatoric stresses in 2D.

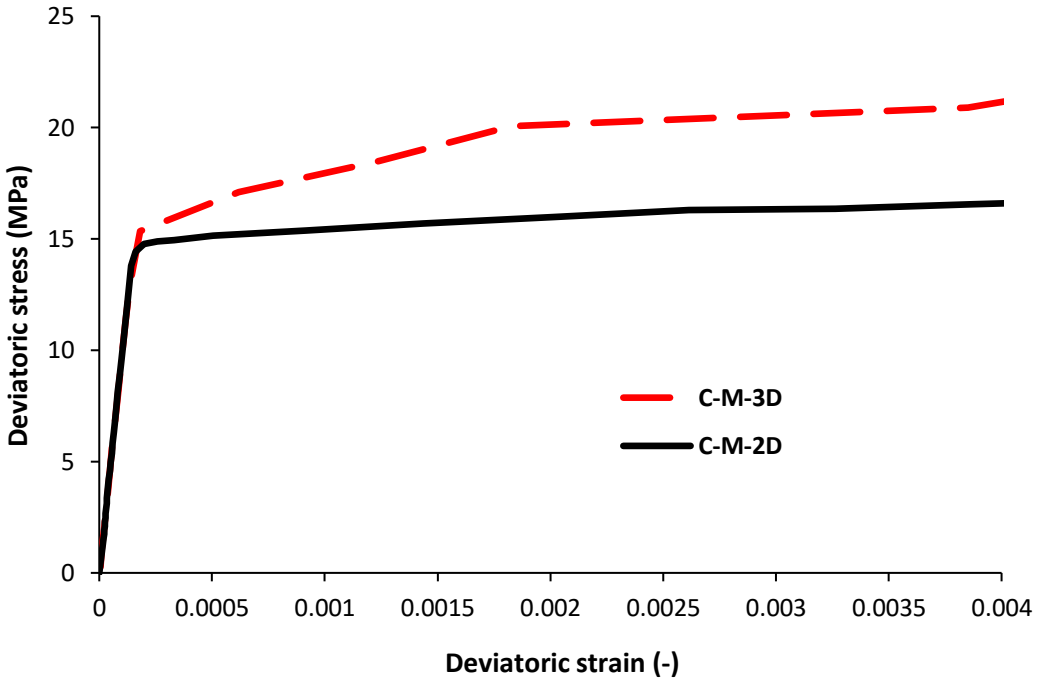

Figure 5-47 Deviatoric stress-strain curves in 2D and 3D for copper (Point A).

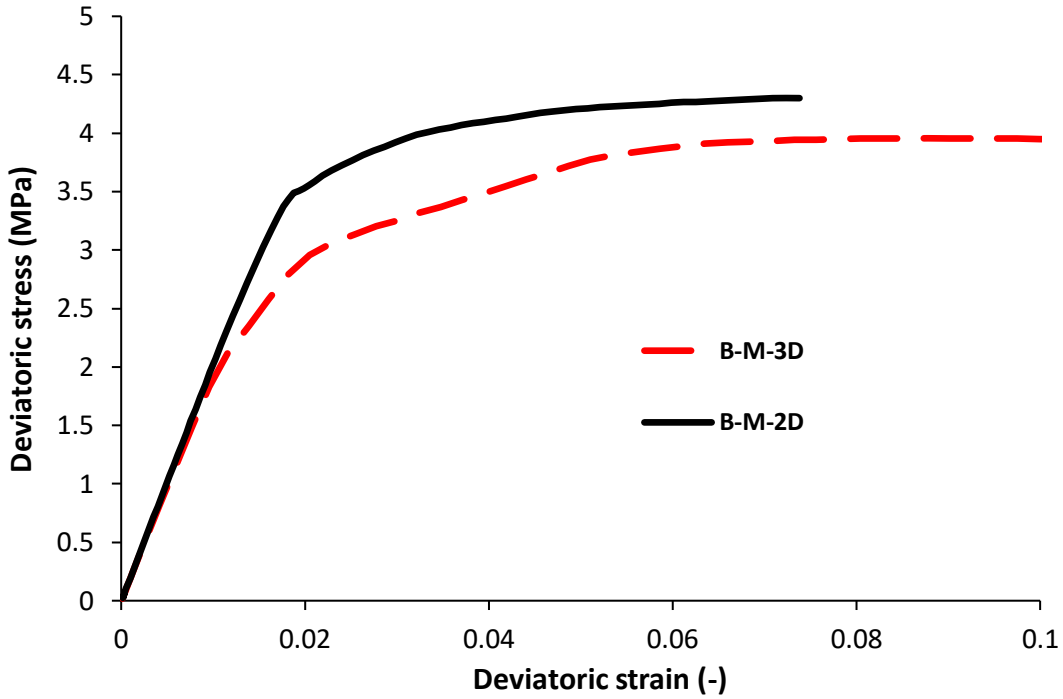

Figure 5-48 Deviatoric stress-strain curves in 2D and 3D for bentonite (Point B).

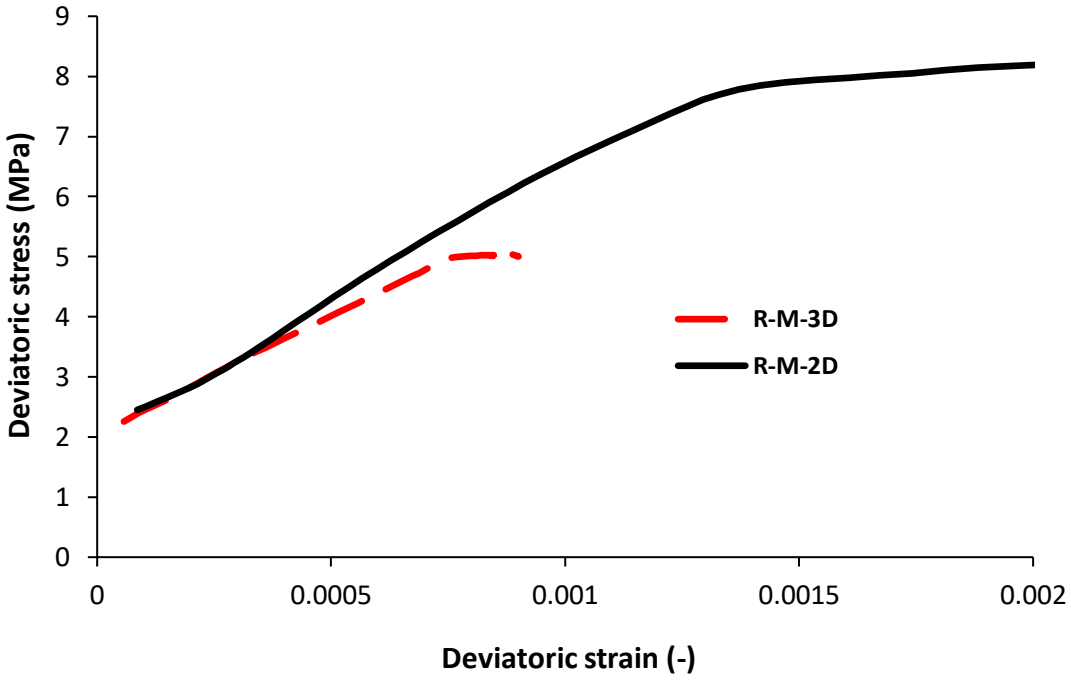

Figure 5-49 Deviatoric stress-strain curves in 2D and 3D for rock (Point C).

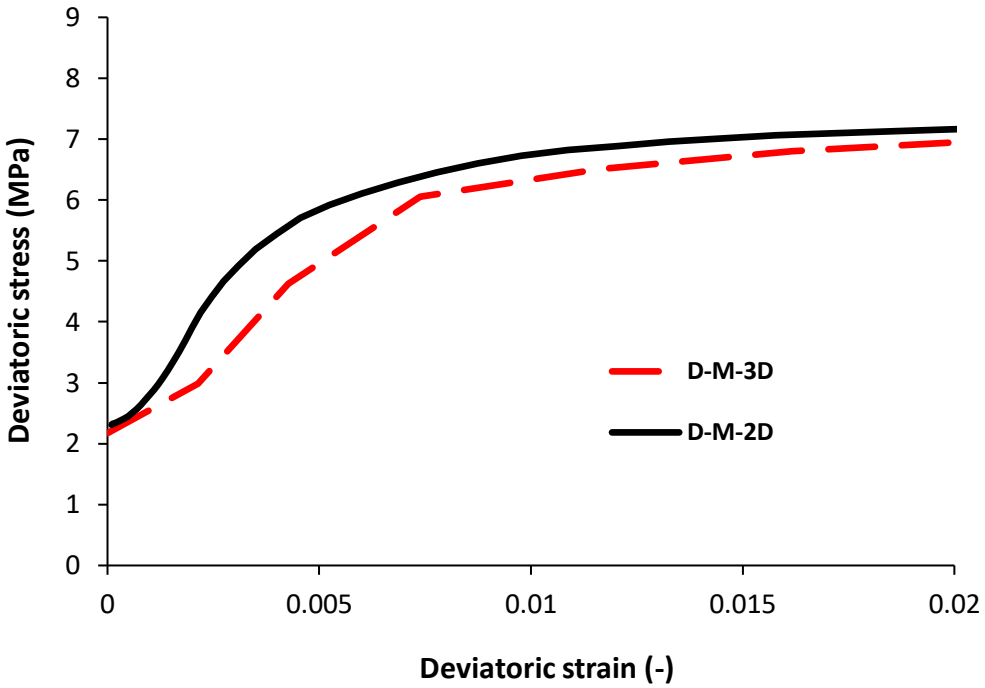

Figure 5-50 Deviatoric stress-strain curves in 2D and 3D for discontinuity (Point D).

5.2.1.4 Full-scale shear modeling using hydro-mechanical coupling in 3D

In this section, modeling of hydro-mechanical coupling processes of geomaterials with the multiphase fluid flow is presented. The governing equations are based on the theory of mixture applied to the multiphysics of porous media, considering solid phase deformation, multiphase fluid flow in CODE_BRIGHT.

The deformation of the shear test is shown in Figure 5-51 and the buffer geometry is derived from Juvankoski (Juvankoski & Marcos, 2010). Figure 5-36 shows the initial porosity for all components. Equations are solved with the finite element method (FEM). The system is confined. MX-80 bentonite clay is modeled with BBM and their parameters are given in Table 5-6. Figure 5-52 and Figure 5-53 show contour fill and the evolution of liquid pressure at the end of the test (30 Seconds) and the bentonite is saturated.

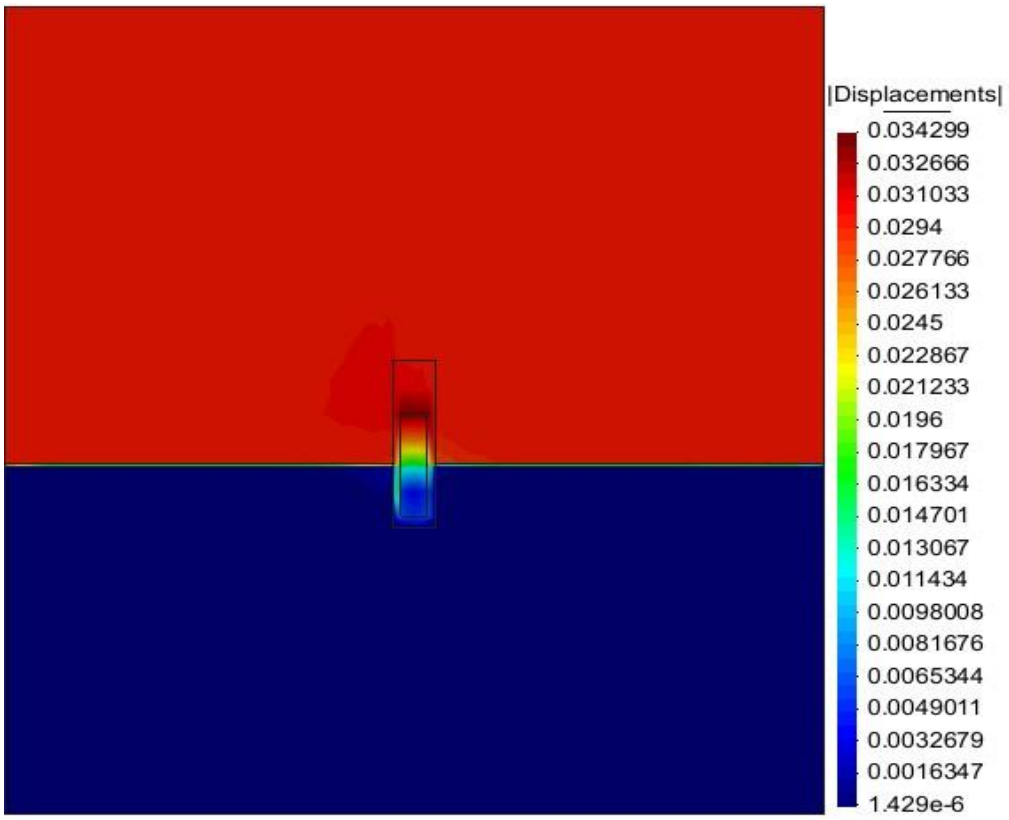

Figure 5-51 Contour fill of displacements in 3D.

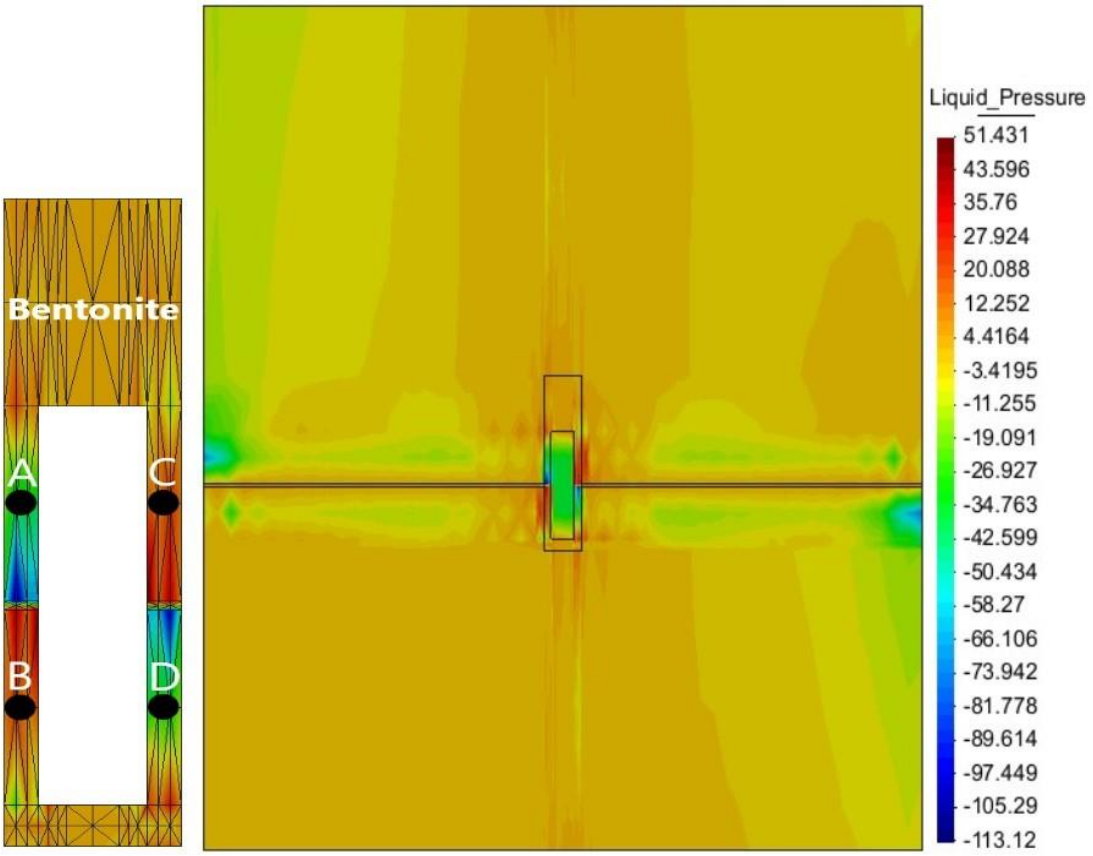

Figure 5-52 Contour fill of liquid pressure.

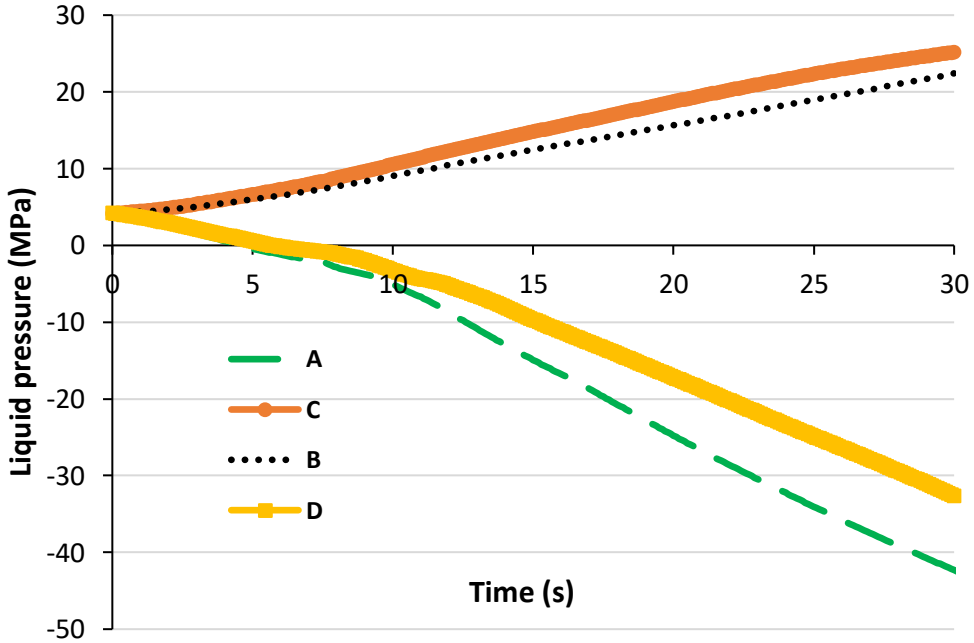

Figure 5-53 Evolution of liquid pressure in bentonite.

Figure 5-54, Figure 5-55, Figure 5-56, Figure 5-57 show the generation of deviatoric stresses with respect to deviatoric strain in copper, bentonite, rock, and discontinuity respectively. In

Figure 5-35, the points A, B, C, and D are chosen for copper, bentonite, rock, and discontinuity respectively.

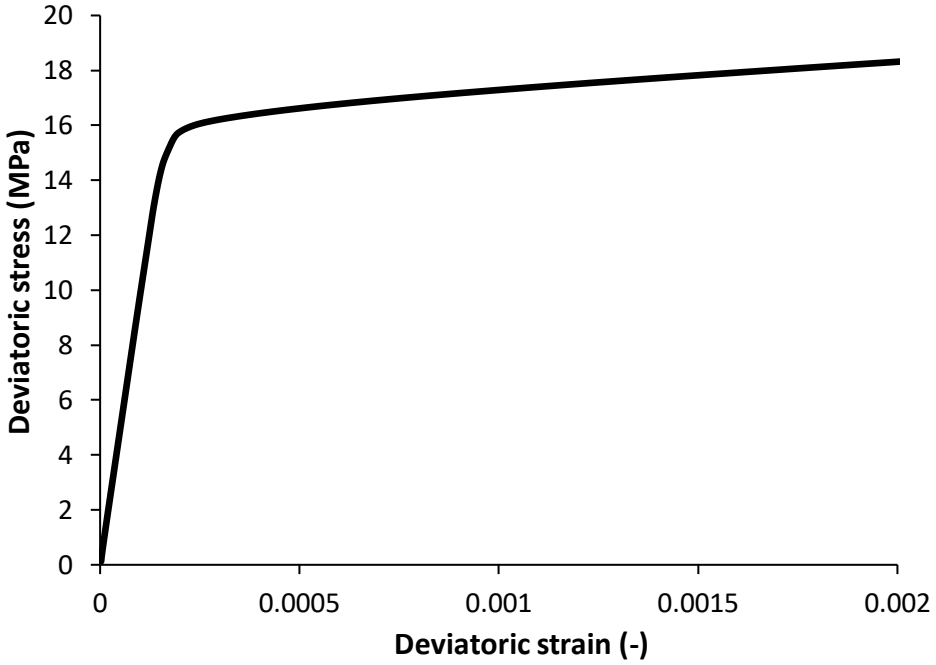

Figure 5-54 Deviatoric stress-strain curve in real scale for copper (Point A).

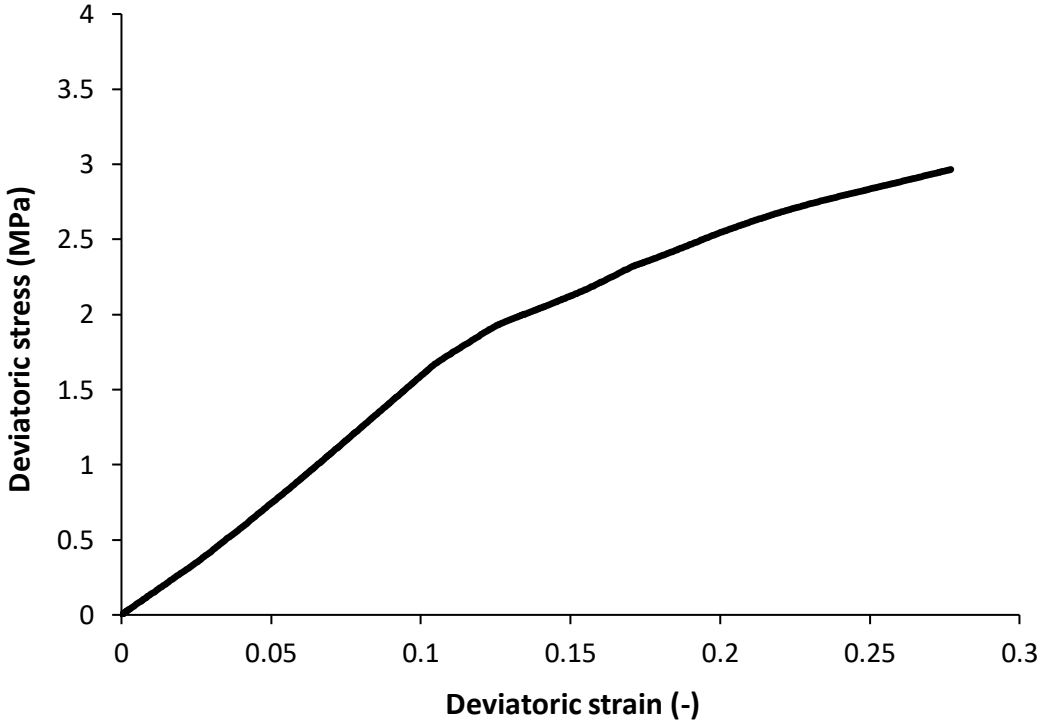

Figure 5-55 Deviatoric stress-strain curve in real scale for bentonite (Point B).

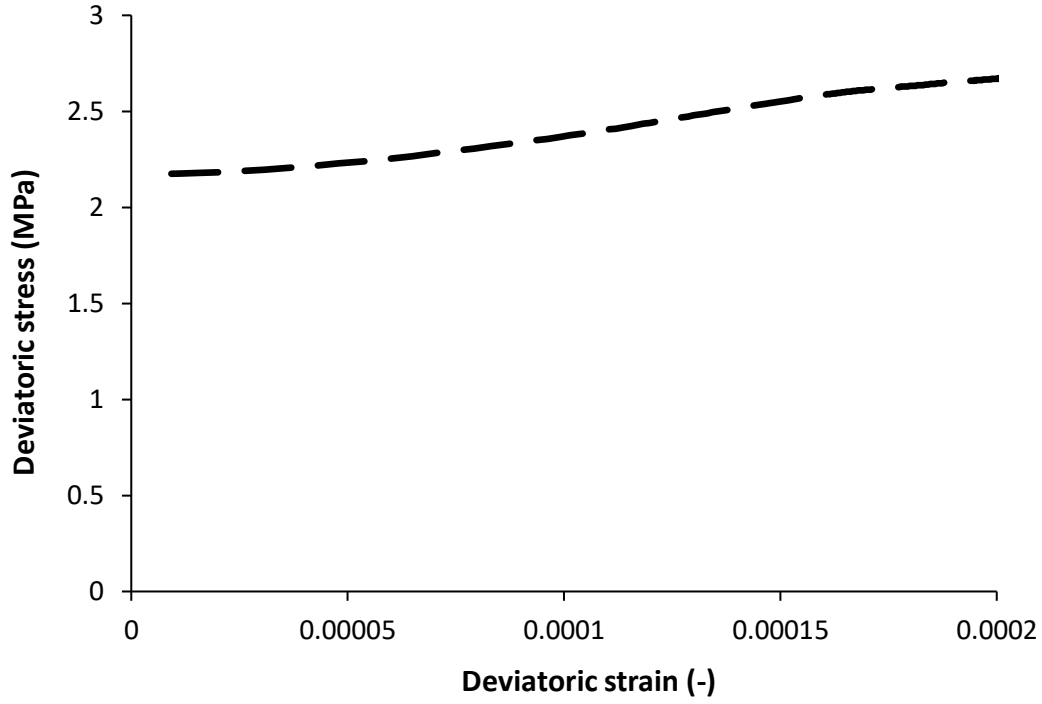

Figure 5-56 Deviatoric stress-strain curve in Full scale for rock (Point C).

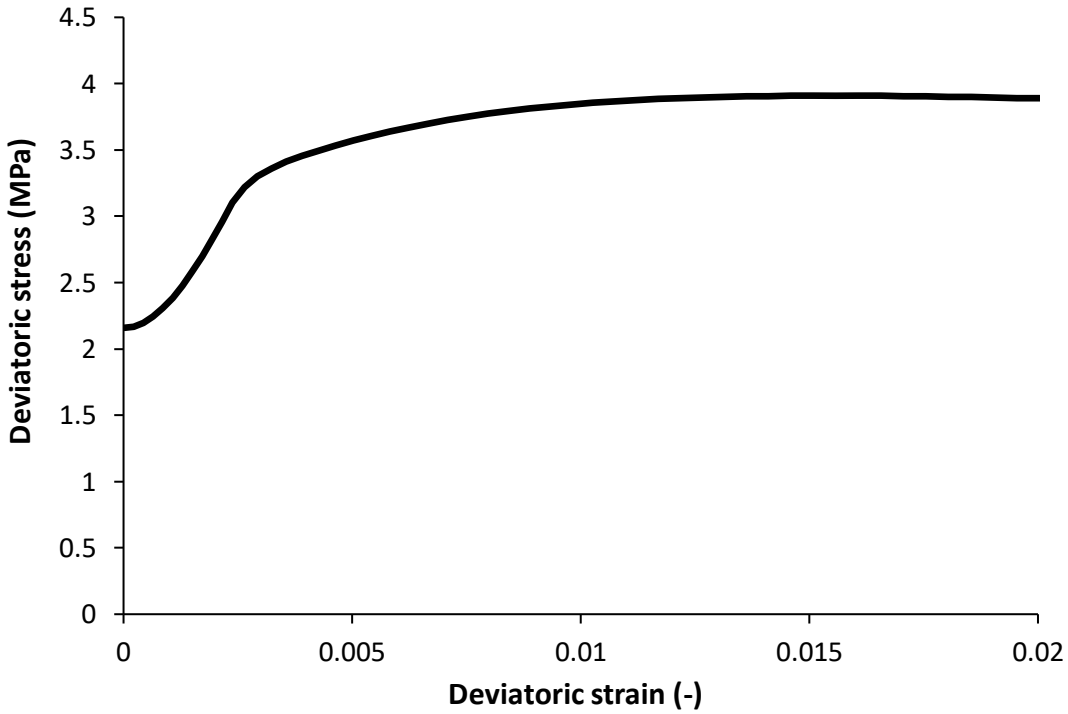

Figure 5-57 Deviatoric stress-strain curve in Full scale for discontinuity (Point D).

5.2.1.5 Comparison between 2D and 3D modeling in the hydro-mechanical analysis

A coupled hydro-mechanical (HM) finite element method is presented for shear test modeling. Fractures are modeled as surface discontinuities within three-dimensional and line discontinuities in the two-dimensional matrix. The temperature in shear test materials is defined and coupled to hydro-mechanical analysis. Hexahedral elements for 3D modeling and quadrilateral elements for 2D modeling are used for the shear test in full-scale. Deviatoric stress-strain results for copper, bentonite, and discontinuity are shown in Figure 5-58, Figure 5-59 and Figure 5-60.

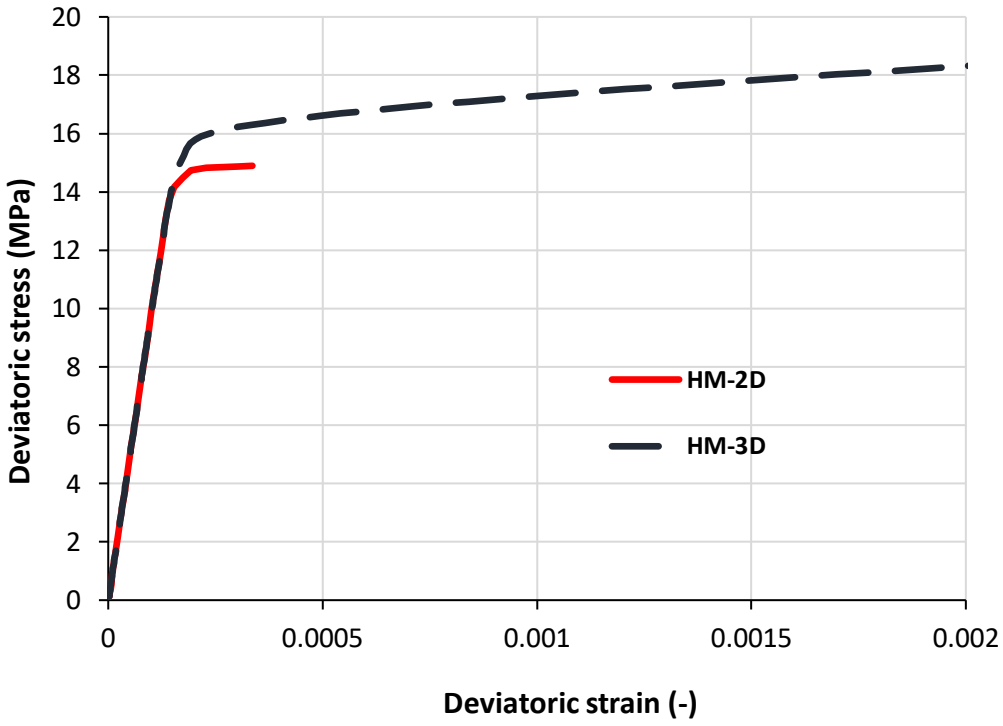

Figure 5-58 Deviatoric stress-strain curves in 2D and 3D for copper (Point A).

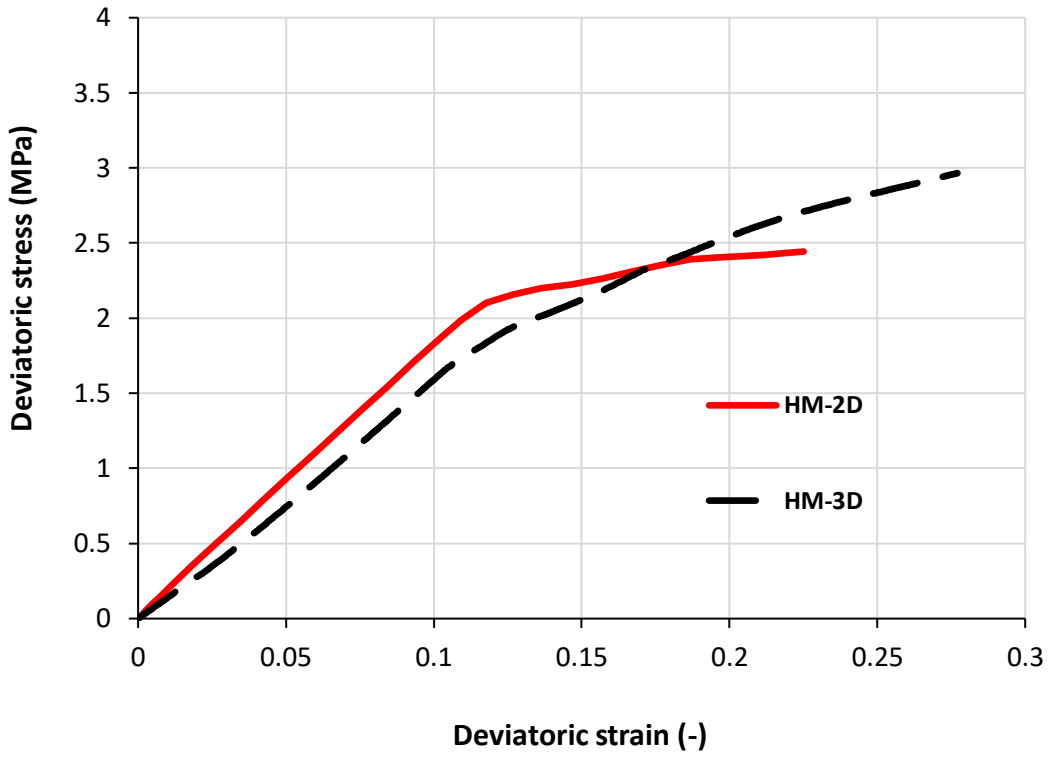

Figure 5-59 Deviatoric stress-strain curves in 2D and 3D for bentonite (Point B).

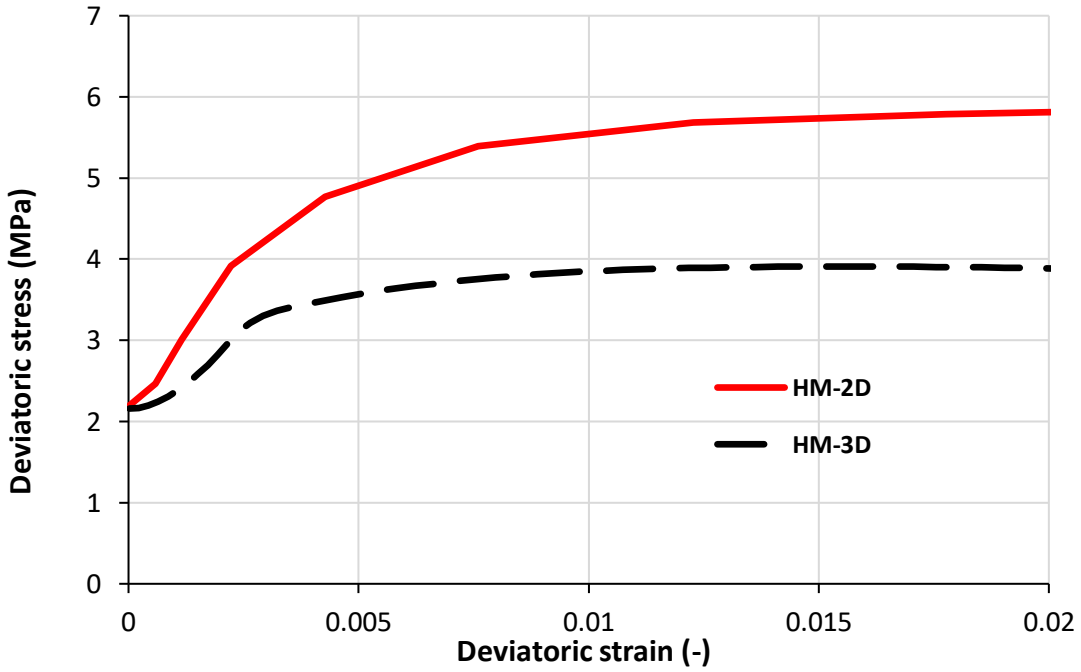

Figure 5-60 Deviatoric stress-strain curves in 2D and 3D for discontinuity (Point D).

The deviatoric stress in two-dimensional modeling is greater than the deviatoric stress in three-dimensional modeling for bentonite (Figure 5-59) and discontinuity (Figure 5-60) but for copper in Figure 5-58, its inverse, and the deviatoric stress in two-dimensional modeling is less than the deviatoric stress in three-dimensional modeling.

5.2.1.6 Difference between rock or without a rock in 3D full-scale shear modeling

A full-scale distinction was made between considering rock and not considering rock. Since the mechanical and hydraulic activity of rock masses is highly influenced by current discontinuities, a coupled hydro-mechanical analysis is used.

Figure 5-61 and Figure 5-62 depict the outcomes. The deviatoric stress with rock is greater than the deviatoric stress without rock for copper but for bentonite, the deviatoric stress in both models is similar.

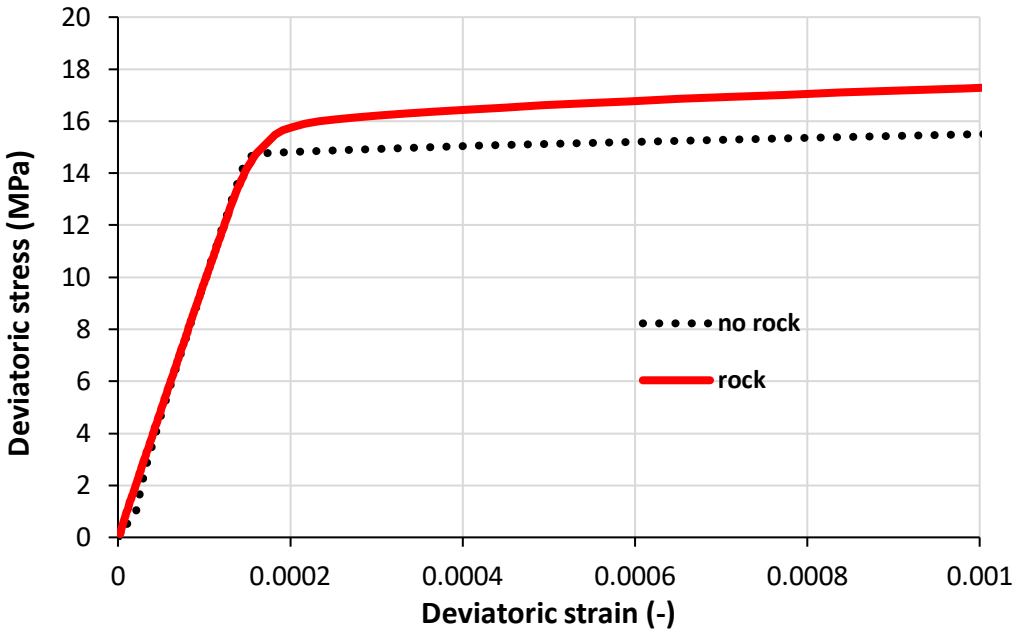

Figure 5-61 Comparison between shear test with rock and no rock for copper (Point A).

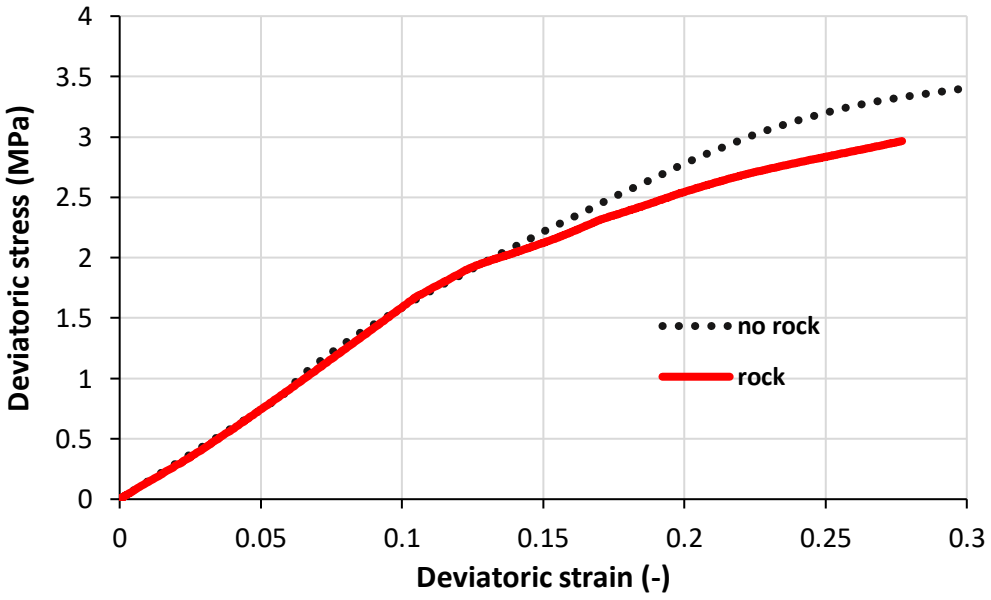

Figure 5-62 Comparison between shear test with rock and no rock for bentonite (Point B).

CHAPTER 6

6 Conclusions and Future work

6.1 Conclusions

The models implemented in CODE_BRIGHT were developed in the past for rocks and soils. They have specific features for unsaturated geomaterials under non-isothermal conditions. However, none of the existing models was adequate for model metal based canisters.

The two main components of the metal canister present significant hardening and are temperature and time-dependent. So, it is important to implement the behaviour accordingly after reaching the yield stress in order to be able to simulate the real behavior of the canister when the loads and strain rates are significant. The implementation of the Bodner-Partom model allows using CODE_BRIGHT when the strain rates and loads on the canister are important. The test presented by Börgesson (1986) clearly has the copper yielded, so it is not sufficient to model the canister elastically as it is usually done in standard THM simulations.

The main advantages of the Bodner and Partom based on a state variable are:

- To incorporates a number of important features including the modeling of a broad range of loading histories.
- To be suitable for its implementation within the finite element method.
- To provide with parameters that are easily obtained from high strain rate experiments.

For the validation of the numerical solutions of the elasto-viscoplastic response of the copper, the calculated results have been compared with experimental results, and a good correlation between numerical and experimental results has been observed. Applied boundary conditions appeared also to be appropriate in the inelastic range of deformation.

The Bodner and Parton model is used to verify the response of copper to change of strain rate for the copper element with CODE_BRIGHT subroutines. CODE_BRIGHT with Bodner-Partom constitutive equations has been verified against Stealth Finite Difference Code and semi-analytical solutions.

For a hydro-mechanical calculation, it is necessary to solve the water balance equation and the equilibrium equation (Olivella et al., 1996) but it is possible to avoid the solution of the water balance equation when the water does not flow out of the porous media (undrained conditions). This happens when the load is sufficiently fast and the porous media has low

hydraulic conductivity. In this case, total stresses (mechanical behavior) and undrained parameters (undrained Young modulus, undrained Poisson ratio and undrained shear strength) are used in shear test modeling.

Due to the fact that the analysis in undrained conditions depends only on the initial conditions, it is possible to use the von Mises constitutive model, which is equivalent to the Drucker-Prager model when the mean effective stresses remain constant. In this case, the von Mises cylinder which represents the yield surface, and the cone that represents the Drucker-Prager yield surface define the same circumference that defines the plane orthogonal to the hydrostatic axis where the mean effective stress remains constant. It should be taken into account that if the mean effective stress changes, the parameter that defines the von Mises yield stress (the c_u) should change.

The undrained conditions that occur during fast loading permit to study the problem using total stress provided that specific parameters are considered. When the coupled effective stress analysis is carried out, sensitivity to the permeability of the bentonite permits the assessment of whether the undrained conditions are satisfied. Only for bentonite with relatively high permeability, shear will produce internal volumetric deformations linked with water movement.

6.1.1 Outcomes of shear test modeling using the mechanical analysis in 2D

The results of the sensitivity analysis on bentonite and copper have evidenced the following:

6.1.1.1 Mock-up scale

- In a fluidity Γ_0 (1/viscosity) sensitivity analysis, when fluidity is very small, the deviatoric stresses increase in the bentonite and copper.
- In a mesh sensitivity analysis, there is no significant effect on the bentonite deviatoric stresses as well as in the copper. Essentially, the deviatoric stresses are the same for the meshes considered.
- In all cases, strength reduction of the clay leads to less deviatoric deformation of the canister. This is explained by the fact that the solid rigid movement of the canister is facilitated by the higher deformability of the surrounding clay, so displacements are bigger but deformations smaller.
- Results for undrained shear strength c_u = 3 MPa (obtained with parameters presented by Toprak et al., 2016) and c_u = 1 MPa (obtained with results presented by Börgesson et al., 1995) for MX-80 bentonite, have been presented.

- The fixed mesh method and updated Lagrangian method practically do not show differences.
- Limiting plastic strain rate (D_0) is the limiting value of plastic work strain rate in shear and one of the important parameters in viscoplastic constitutive equations of the Bodner-Partom model for copper. In a sensitivity analysis of limiting plastic strain rate, the variation of deviatoric stress for different values of D_0 is very small.

6.1.1.2 Full-scale

- In a sensitivity analysis of limiting plastic strain rate, the values of D_0 possess no notable influence on the copper and the bentonite.
- In the comparison between the full-scale and mock-up scale for the bentonite in both models, the deviatoric stresses are approximately the same but in copper, the deviatoric stresses in the full-scale are larger than in the mock-up scale.

6.1.2 Outcomes of shear test modeling using the coupled hydro-mechanical analysis in 2D

Sensitivity analysis of important parameters and mesh for copper and bentonite and also the comparison between the mechanical and hydro-mechanical analysis has evidenced the following:

6.1.2.1 Mock-up scale

In the mesh sensitivity analysis, the deviatoric stress in a rough mesh (225 nodes and 224 elements) is higher than the deviatoric stress for a medium mesh (425 nodes and 384 elements) and a fine mesh (731 nodes and 672 elements) for bentonite. For copper, the deviatoric stress in rough and medium meshes is similar but the deviatoric stress in the fine mesh is somewhat greater than the other meshes.

For the effective stress analysis, the decrease of M value causes stiffness reduction in clay. Effective and total stress analyses are consistent with what is obtained for different strengths. Actually, the two approaches must tend to be equivalent for low permeability conditions.

In a sensitivity analysis of permeability, it has been observed that when the permeability values are close to undrained condition (sufficiently low), the results in the effective stress analysis are, in terms of strength, very close and consistent with what is obtained for the total stress analysis.

6.1.2.2 Full-scale

A coupled hydro-mechanical analysis of Full-Scale and Mock-up scale was carried out and roughly provide similar values of the deviatoric stress in copper and bentonite in both dimensions is roughly the same.

In the comparison between the total stress (mechanical analysis) and the effective stress (coupled hydro-mechanical analysis) in 2D, the deviatoric stress in the total stress approach is somewhat greater than the deviatoric stress in the effective stress approach. For copper, the deviatoric stress in total stress is the same as the deviatoric stress in effective stress.

This can be explained by the fact that the effective stress model permits some local changes in porosity thus causing some heterogeneity along with the clay. In contrast, the total stress model is solved as uniform plastic deformation and the canister takes more deviatoric stress due to its higher stiffness and strength as compared with the clay.

6.1.3 Consequences of the canister-clay system using mechanical analysis in 3D

The comparison between full-scale and mock-up scale was done for deviatoric stress-strain in 3D. For bentonite in both models, the difference of deviatoric stresses between both models is very small but for copper, the deviatoric stress in mock-up scale is higher than in the full-scale.

In the sensitivity analysis of fluidity parameter (Γ_0), the deviatoric stress for $\Gamma_0=10^{-3}$ is higher than the deviatoric stresses in $\Gamma_0=10^{3}$ and 1. Finally the deviatoric stresses in $\Gamma_0=10^{3}$ and 1 are equal in the full-scale model.

In the mechanical analysis of full-scale model, it is observed that the deviatoric stress in the two-dimensional model is greater than the deviatoric stress in the three-dimensional modeling for copper. For bentonite, the deviatoric stress in both models is quite similar.

The comparison between the quadratic tetrahedral mesh and hexahedra mesh for the full-scale model, shows that the deviatoric stress in hexahedra mesh is greater than the deviatoric stress in the quadratic tetrahedral mesh in the case of copper.

6.1.4 Consequences of the canister-clay system using coupled hydro-mechanical analysis in 3D

The sensitivity analysis of permeability performed in the full-scale considers permeabilities of 5.59×10^{-19}, 5.59×10^{-20} and 5.59×10^{-21} (Toprak et al., 2013; Toprak et al., 2017). In this

comparison, the deviatoric stress obtained for all permeabilities is roughly the same for copper and bentonite.

The comparison between the full-scale and the mock-up scale is checked out for deviatoric stress-strain. For bentonite, the deviatoric stress in the mock-up scale is lesser than the deviatoric stress in the full-scale, and in the copper, the deviatoric stress in the mock-up test is greater than for the full-scale.

For the validation of the models, an experimental solution of the canister-clay shear test by Börgesson (1986) has been compared to the results of the numerical model using the CODE_BRIGHT. For the canister-clay system in the three types of tests, the total forces obtained by numerical modeling are approximately the same as the results obtained in the experiments (Börgesson, 1986). Implementation is correct as the results are reproduced with the same parameters. The buffer can be plastically deformed without extra stresses when the shear strength is achieved. The higher the shear strength of the buffer has the higher stresses in the canister.

According to the results obtained by mock-up tests (The difference in shear rate), for copper canister, Test 1 (shear rate of 0.0317 mm/s) appears to be strongly tilted. This is opposite to what happens in Test 3 (shear rate of 160 mm/s). The higher shear rate in Test 3 leads to a higher stiffness in the bentonite as compared to Test 1. The shear rate only has effects on stress-strain relation and this difference is obvious for each test.

6.1.5 Conclusions from a full-scale shear test with mechanical analysis based on the impact of discontinuity

In the sensitivity analysis of discontinuity width in 2D, deviatoric stress for *w=3.75 m* is greater than deviatoric stress for *w=16.9 m.*

Regarding the presence of rock in the canister-clay system in 2D, for copper, the deviatoric stress is greater than in the situation in which rock is nonexistent; but for bentonite, the variation in deviatoric stress is very small in both cases.

In the sensitivity analysis of width in the Y direction in 3D, deviatoric stress for copper in both cases is approximately the same. For bentonite, deviatoric stress until the deviatoric strain of 0.04 is equal. The deviatoric stress for a width=1.75 m is greater than the deviatoric stress for a width=16.9 m. Finally, for the discontinuity, deviatoric stress for a width=16.9 m is less than the deviatoric stress for a width=1.75 m.

The comparison between 2D and 3D modeling in Mechanical analysis shows that deviatoric stresses in 3D are higher than deviatoric stresses in 2D for the copper but for the rock, the discontinuity, and the bentonite, deviatoric stresses in 3D are lesser than the deviatoric stresses in 2D in full-scale.

6.1.6 Conclusions from a full-scale shear test with hydro-mechanical analysis based on the impact of discontinuity

In the sensitivity analysis of permeability, in conclusion, it is expected that liquid pressure on different points is not equal. In some points which are under tension, by increasing the time the liquid pressure becomes low but for other points which are in compression, when the time is increasing then the liquid pressure is increasing as well. All permeabilities in the rock have the same liquid pressure at the same point.

A comparison between the mechanical analysis and the hydro-mechanical coupling in 2D indicates that deviatoric stress in copper for mechanical analysis and coupled hydro-mechanical analysis are the same. In contrast, for rock, bentonite, and discontinuity, the deviatoric stress in the mechanical analysis is greater than the deviatoric stress in hydro-mechanical coupling.

According to the simulation of 3D full-scale shear modeling with the presence of fracture in rock and concerning the variation of deviatoric stress, copper has higher stiffness than the canister-clay system without rock. But for bentonite, the variation of stiffness is very small in both models. Evaluation of the discontinuity effect in the canister-clay system in 2D and 3D indicates that the deviatoric stress in 2D is higher than in 3D for copper, but in contrast, the alteration of deviatoric stress in bentonite has a negligible effect in both dimensions.

6.2 Future work

The Bodner-Partom model is a powerful tool for the simulation of metal components but cannot simulate other phenomena that are taken into account in canister design like excessive plastic deformation or creep deformation in copper or buckling tendency or crack initiation or stable crack growth in cast iron (Jonsson et al., 2018). The simulation of these loading types is out of the scope of the thesis but can be considered in future work.

CODE_BRIGHT formulation was implemented in small strains and has the option to use the updated Lagrangian method. Other programs, like for instance PLAXIS (PLAXIS, 2019) or Abaqus (Abaqus, 2020), have large strain formulations implemented. It would be of some interest to compare the results obtained with CODE_BRIGHT incorporating the updated Lagrangian formulation with the results obtained with others that use the large strains in the canister-clay shear test and evaluate if it is necessary to go further in implementing a large deformation approach.

3D THM simulations of the full-scale canister-clay shear test. Understanding the effect of energy balance (thermal) on the copper-canister system can be a future contribution.

Dynamic analysis can be a domain to explore as the effect of seismic actions in this problem can be of special relevance. Actually, the Bodner-Partom model is prepared for this type of condition as it was developed originally to study the impact of copper projectiles.

The copper must be considered as porous material when hydro-mechanical modeling is performed and improving the code locking the solution of the water mass balance equation (and also air) in metals can be done for a contribution in the future.

Appendix

A.1 Undrained shear strength for bentonite material

The Cam-Clay model and the extension to unsaturated soil model BBM are critical state models. Both share some concepts, for instance regarding failure, which is based on the critical state theory for soils. For a critical state model, the invariants (q and p') at the critical state point satisfy:

$$q_{cs} = Mp'_{cs} \tag{A1}$$

Where *M* is a strength parameter. It can be determined from laboratory results. It can also be calculated from a friction angle. The void ratio at the critical state can be calculated as:

$$e_{cs} = e_0 - \lambda \ln p'_{cs} \tag{A2}$$

And, taking into account that the undrained shear strength and the deviatoric stress at failure are simply related by definitions, it is possible to calculate:

$$c_u = \frac{q_{cs}}{2} = \frac{M}{2p'_{cs}} = \frac{M}{2}\exp\left(\frac{e_{cs} - e_0}{\lambda}\right) \tag{A3}$$

This equation is difficult to apply as the estimation of the void ratio in a triaxial test can be difficult. Following the results from Mayne (1980), an alternative equation, in terms of mean effective stress and preconsolidation mean effective stress, can be written as:

$$c_u = p'\frac{M}{2}\left(\frac{p'_o}{2p'}\right)^{\frac{\lambda-\kappa}{\lambda}} \tag{A4}$$

The application of this equation to the parameters for bentonite (Table 4-4) leads to:

$$c_u = p'\frac{M}{2}\left(\frac{p'_o}{2p'}\right)^{\frac{\lambda-\kappa}{\lambda}} = 8 \times \frac{1.07}{2}\left(\frac{1}{2}\right)^{\frac{0.15-0.05}{0.15}} \cong 3\ \text{MPa} \tag{A5}$$

where $p' = p'_0 = 8$ MPa is assumed for the swelling pressure of the bentonite. It is assumed that the swelling pressure has already been achieved at the moment of shearing because of the saturation of the bentonite.

For a lower strength the calculated value is lower (see sensitivity to *M* in the corresponding section):

$$c_u = p' \frac{M}{2} \left(\frac{p'_o}{2p'} \right)^{\frac{\lambda-\kappa}{\lambda}} = 8 \times \frac{0.369}{2} \left(\frac{1}{2} \right)^{\frac{0.15-0.05}{0.15}} \cong 1 \text{ MPa} \quad \text{A6}$$

These two values have been used for the sensitivity under total stress analysis.

References

AB, S. K. (2010a). Buffer, backfill and closure process report for the safety assessment SR-Site.

AB, S. K. (2010b). Design, production and initial state of the closure.

Åkesson, M., Börgesson, L., & Kristensson, O. (2010). SR-Site Data report. THM modelling of buffer, backfill and other system components.

Alonso, E. E., Gens, A., & Josa, A. (1990). A constitutive model for partially saturated soils. *Geotechnique*, *40*(3), 405-430. https://doi.org/10.1680/geot.1990.40.3.405

Ávila, A. F., & Krishina, T. K. (1999). Non-linear analysis of laminated metal matrix composites by an integrated micro/macromechanical model. *Revista Brasileira de Ciencias Mecanicas/Journal of the Brazilian Society of Mechanical Sciences*, *21*(4), 622-640. https://doi.org/10.1590/S0100-73861999000400006

Bodner, S., & Merzer, A. (1978). Viscoplastic constitutive equations for copper with strain rate history and temperature effects.

Bodner, S. R., & Partom, Y. (1975). Constitutive equations for elastic-viscoplastic strain-hardening materials. *Journal of Applied Mechanics, Transactions ASME*, *42*(2), 385-389. https://doi.org/10.1115/1.3423586

Bodner, S. R., & Rajendran, A. M. (1995). On the strain rate and temperature dependence of hardening of copper. *Proceedings of the Conference on Shock Compression of Condensed Material*(1), 499-502.

Boergesson, L. (1986). *Model shear tests of canisters with smectite clay envelopes in deposition holes*. http://inis.iaea.org/search/search.aspx?orig_q=RN:19006046

Boergesson, L., & Hernelind, J. (2006). *Earthquake induced rock shear through a deposition hole Influence of shear plane inclination and location as well as buffer properties on the damage caused to the canister* (1404-0344). http://www.skb.se/upload/publications/pdf/TR-06-43webb.pdf

http://inis.iaea.org/search/search.aspx?orig_q=RN:38056909

Börgesson, L. (1986). Model shear tests of canister with smectite clay envelopes in deposition holes. *Model Shear Tests of Canisters with Smectite Clay Envelopes in Deposition Holes*.

Börgesson, L., Dueck, A., & Hernelind, J. (2018). Earthquake-induced rock shear through a deposition hole: Laboratory tests on bentonite-material models and modelling of three scale tests. *Clay Minerals*, *53*(2), 213-235. https://doi.org/10.1180/clm.2018.15

Börgesson, L., & Hernelind, J. (2010). *Earthquake induced rock shear through a deposition hole. Modelling of three model tests scaled 1: 10. Verification of the bentonite material model and the calculation technique*.

Börgesson, L., Johannesson, L., Sandén, T., & Hernelind, J. (1995). *Modelling of the physical behaviour of water saturated clay barriers. Laboratory tests, material models and finite element application*.

Brunnengraeber, A., & Schreurs, M. (2015). Nuclear Energy and Nuclear Waste Governance Perspectives after the Fukushima Nuclear Disaster. 47-78. https://doi.org/10.1007/978-3-658-08962-7_2

Chan, K. S., Lindholm, U. S., & Bodner, S. R. (1988). Constitutive modeling for isotropic materials (HOST). *Constitutive Modeling for Isotropic Materials (HOST)*.

Chen, G., Ledesma, A. J. J. o. g., & engineering, g. (2009). Coupled thermohydromechanical modeling of the full-scale in situ test “prototype repository”. *135*(1), 121-132.

Deng, F., Li, Y., Lin, H., Miao, J., & Liang, X. (2020). A BWM-TOPSIS Hazardous Waste Inventory Safety Risk Evaluation. *International journal of environmental research and public health*, *17*(16), 5765. https://doi.org/10.3390/ijerph17165765

Desai, C., Zhang, D. J. I. J. f. N., & Geomechanics, A. M. i. (1987). Viscoplastic model for geologic materials with generalized flow rule. *11*(6), 603-620.

DIT-UPC. (2021). CODE_BRIGHT, a 3-D program for thermo-hydro-mechanical analysis in geological media: User's guide. In: Centro Internacional de Métodos Numéricos en Ingeniería (CIMNE) Barcelona, Spain.

Drucker, D. C., & Prager, W. (1952). Soil mechanics and plastic analysis or limit design. *Q. Appl. Math.*, *10*(2), 157-165.

Dueck, A., Börgesson, L., & Johannesson, L.-E. (2010). *Stress-strain relation of bentonite at undrained shear. Laboratory tests to investigate the influence of material composition and test technique*.

Dueck, A., & Nilsson, U. (2010). Thermo-Hydro-Mechanical properties of MX-80. Results from advanced laboratory tests.

Dvořáková, M., Vencl, M., & Bečvaříková, T. (2015, 27-30 May 2015). Deep geological repository for disposal of nuclear waste in the Czech Republic. 2015 5th International Youth Conference on Energy (IYCE),

François, B., & Laloui, L. (2008). Unsaturated soils under non-isothermal conditions: Framework of a new constitutive model. In *GeoCongress 2008: Characterization, Monitoring, and Modeling of GeoSystems* (pp. 1077-1083).

François, B., Laloui, L. J. I. j. f. n., & geomechanics, a. m. i. (2008). ACMEG-TS: A constitutive model for unsaturated soils under non-isothermal conditions. *32*(16), 1955-1988.

Fyfe, W. F., Babuska, V., Price, N. J., Schmid, E., Tsang, C. F., Uyeda, S., & Velde, B. (1984). The geology of nuclear waste disposal. *Nature*, *310*(5978), 537-540. https://doi.org/10.1038/310537a0

Fyfe, W. S. (1999). Nuclear waste isolation: an urgent international responsibility. *Engineering Geology*, *52*(3), 159-161. https://doi.org/https://doi.org/10.1016/S0013-7952(99)00003-4

Gallipoli, D., Gens, A., Sharma, R., & Vaunat, J. J. G. (2003). An elasto-plastic model for unsaturated soil incorporating the effects of suction and degree of saturation on mechanical behaviour. *53*(1), 123-135.

Gens, A., & Alonso, E. E. (1992). A framework for the behaviour of unsaturated expansive clays. *Canadian Geotechnical Journal*, *29*(6), 1013-1032. https://doi.org/10.1139/t92-120

Gens, A., Garitte, B., Olivella, S., Vaunat, J. J. E. j. o. e., & engineering, c. (2009). Applications of multiphysical geomechanics in underground nuclear waste storage. *13*(7-8), 937-962.

Gens, A., Sánchez, M., Guimarães, L. D. N., Alonso, E. E., Lloret, A., Olivella, S., Villar, M. V., & Huertas, F. (2009). A full-scale in situ heating test for high-level nuclear waste disposal: Observations, analysis and interpretation. *Geotechnique*, *59*(4), 377-399. https://doi.org/10.1680/geot.2009.59.4.377

Ghrieb, A., Mitiche-Kettab, R., & Guettala, S. (2014). Relationship between Porosity, the Maximum Dry Density and the Mechanical Behavior of Stabilized Dune Sands. *Global Journal of Researches in Engineering: E (Civil and Structural Engineering)*, *14*, 29-38.

Karnland, O., Olsson, S., & Nilsson, U. (2006). *Mineralogy and sealing properties of various bentonites and smectite-rich clay materials* (No. SKB-TR--06-30). Swedish Nuclear Fuel and Waste Management Co..

Hedin, A., Andersson, J., Kautsky, U., Morén, L., Munier, R., Nyström, C., Näslund, J.-O., Pers, K., Puigdomenech, I., Sellin, P., Selroos, J.-O., Skagius, K., Spahiu, K., Vahlund, F., &

Werme, L. (2008). *Safety assessment for licensing a spent nuclear fuel repository in Sweden*.

Hernelind, J. (2010). Modelling and Analysis of Canister and Buffer for Earthquake Induced Rock Shear and Glacial Load: SKB TR-10-34. *Modelling and Analysis of Canister and Buffer for Earthquake Induced Rock Shear and Glacial Loads. SKB Technical Report TR-10-34*.

Herrmann, H., & Bucksch, H. (2014). dry density. In. https://doi.org/10.1007/978-3-642-41714-6_44473

Hoek, E., Wood, D., & Shah, S. (1992). A modified Hoek–Brown failure criterion for jointed rock masses. Rock Characterization: ISRM Symposium, Eurock'92, Chester, UK, 14–17 September 1992,

Hughes, T. J. R. (1980). Generalization of selective integration procedures to anisotropic and nonlinear media. *International Journal for Numerical Methods in Engineering*, *15*(9), 1413-1418. https://doi.org/10.1002/nme.1620150914

Ji, W., Waas, A. M., & Bazant, Z. P. J. J. o. A. M. (2013). On the importance of work-conjugacy and objective stress rates in finite deformation incremental finite element analysis. *80*(4).

Johannesson, L. E., Börgesson, L., Goudarzi, R., Sandén, T., Gunnarsson, D., & Svemar, C. (2007). Prototype repository: A full scale experiment at Äspö HRL. *Physics and Chemistry of the Earth*, *32*(1-7), 58-76. https://doi.org/10.1016/j.pce.2006.04.027

Jonsson, M., Emilsson, G., & Emilsson, L. (2018). Mechanical Design Analysis for the Canister: Posiva SKB Report 04.

Juvankoski, M., & Marcos, N. (2010). Design basis for buffer components. *Working Report 2009-132*.

Khadivipanah, P., Pintado, X., Olivella, S., & Vaunat, J. (2020). Copper canister shearing in spent nuclear fuel repository using Bodner–Partom model. *Geomechanics for Energy and the Environment*, *22*, 100171. https://doi.org/https://doi.org/10.1016/j.gete.2019.100171

Kiviranta, L., & Kumpulainen, S. (2011). *Quality control and characterization of bentonite materials*.

Manual, Abaqus Users. (2020). Abaqus user manual. *Abaqus*.

Martín, P., Barcala, J., & Villar, M. (2014). Behaviour of a bentonite barrier under thermal and hydraulic gradients: FEBEX mock-up test, 16 years of operation. Unsaturated Soils: Research and Applications-Proceedings of the 6th International Conference on Unsaturated Soils, UNSAT,

Mayne, P.W. 1980, Cam-clay predictions of undrained strength. Journal of Geot. Engrg 106 (11): 1219-1242.

Milly, P. C. D. J. W. R. R. (1982). Moisture and heat transport in hysteretic, inhomogeneous porous media: A matric head-based formulation and a numerical model. *18*(3), 489-498.

Olivella, S., Carrera, J., Gens, A., & Alonso, E. E. (1994). Nonisothermal multiphase flow of brine and gas through saline media. *Transport in Porous Media*, *15*(3), 271-293. https://doi.org/10.1007/BF00613282

Olivella, S., Gens, A., Carrera, J., & Alonso, E. E. (1996). Numerical formulation for a simulator (CODE_BRIGHT) for the coupled analysis of saline media. *Engineering Computations*, *13*(7), 87-&. https://doi.org/10.1108/02644409610151575

Olivella, S., & Gens, A. J. T. i. P. M. (2000). Vapour transport in low permeability unsaturated soils with capillary effects. *40*(2), 219-241.

Perzyna, P. (1966). Fundamental problems in viscoplasticity. In *Advances in applied mechanics* (Vol. 9, pp. 243-377). Elsevier.

Pintado, X., Hassan, M. M., & Martikainen, J. (2013). *Thermo-hydro-mechanical tests of buffer material*.

Pintado, X., Kristensson, O., Malmberg, D., Åkesson, M., Olivella, S., & Puig, I. J. E., Finland. Posiva working report. (2016). TH and THM modelling for a KBS-3H deposition drift. *25*.

Pintado, X., Schatz, T., García-Siñeriz, J. L., & Kronberg, M. J. E. G. (2019). Full-scale test for KBS-3H spent nuclear fuel repository alternative in Sweden. *7*(2), 121-136.

PLAXIS. (2019). PLAXIS 2D Reference Manual; Bentley Systems International Limited, Dublin, Ireland.

Oy, Posiva. (2011). Olkiluoto site description 2011. *Report POSIVA*, *2*.

Oy, Posiva. (2012). Safety case for the disposal of spent nuclear fuel at Olkiluoto. Synthesis, 2012-12.

Pruess, K. J. U. o. C., Berkeley, CA. (1987). TOUGH user's guide, Lawrence Berkeley Laboratory.

Raiko, H. (2012). *Canister design 2012*. Posiva.

Raiko, H., Sandström, R., Rydén, H., & Johansson, M. (2010). Design analysis report for the canister. *Design Analysis Report for the Canister*.

Raiko, H. J. P. r. (2005). Disposal canister for spent nuclear fuel–design report. *2*(61), 1-61.

Rajendran, A., & Grove, D. (1987). Bodner-Partom viscoplastic model in STEALTH finite difference code. *Report AFWAL-TR-86-4098*.

Rajendran, A. M., & Bless, S. J. (1986). Use of the Bodner-Partom viscoplastic constitutive model to describe HY100 steel. *Shock Waves in Condensed Matter*.

Rubin, M. B. (1989). A time integration procedure for plastic deformation in elastic-viscoplastic metals. *ZAMP Zeitschrift für angewandte Mathematik und Physik*, *40*(6), 846-871. https://doi.org/10.1007/BF00945807

Sellin, P., & Leupin, O. X. (2013). The Use of Clay as an Engineered Barrier in Radioactive-Waste Management a Review. *Clays and Clay Minerals*, *61*(6), 477-498. https://doi.org/10.1346/CCMN.2013.0610601

Sjöberg, L. (2004). Explaining Individual Risk Perception: The Case of Nuclear Waste. *Risk Management*, *6*(1), 51-64. http://www.jstor.org/stable/3867934

Stange, C. F., & Horn, R. J. V. Z. J. (2005). Modeling the soil water retention curve for conditions of variable porosity. *4*(3), 602-613.

Terzaghi, K. J. F. D., Leipzig, Germany. (1925). Earthwork mechanics on the basis of groundphysics (Erdbaumechanik, in German).

Thegerstroem, C., & Laarouchi Engstroem, S. (2013). Deep geological disposal of nuclear waste in the Swedish crystalline bedrock. *Atw Internationale Zeitschrift fuer Kernenergie*, *58*(6), 359-363. http://inis.iaea.org/search/search.aspx?orig_q=RN:51088117

Toprak, E., Mokni, N., Olivella, S., & Pintado, X. (2013). *Thermo-hydro-mechanical modelling of buffer, synthesis report*.

Toprak, E., Olivella, S., & Pintado, X. (2017). Coupled THM modelling of engineered barriers for the final disposal of spent nuclear fuel isolation. In *Geological Society Special Publication* (Vol. 443, pp. 235-251).

Van Genuchten, M. T. J. S. s. s. o. A. j. (1980). A closed-form equation for predicting the hydraulic conductivity of unsaturated soils. *44*(5), 892-898.

Villar, M. (2005). MX-80 bentonite. Thermo-hydro-mechanical characterisation performed at CIEMAT in the context of the Prototype Project. Informes Técnicos CIEMAT 1053. CIEMAT, Madrid, 39 pp. Febrero 2005.

Villar, M., & Lloret, A. (2008). Influence of dry density and water content on the swelling of a compacted bentonite. *Applied Clay Science*, *39*, 38-49. https://doi.org/10.1016/j.clay.2007.04.007

Wimelius, H., & Pusch, R. (2008). Backfilling of KBS-3V deposition tunnels-possibilities and limitations.

Wood, D. M. (1990). *Soil behaviour and critical state soil mechanics*. Cambridge university press.

Yao, X. X., & Sandström, R. (2000). Study of Creep Behavior in P-Droped Copper with Slow Strain Rate Tensile Stress: SKB report TR-00-09. *Study of Creep Behaviour in P-doped Copper with Slow Strain Rate Tensile Tests, SKB TR-00-09*.